

Srd66/63

1004896

Università degli Studi di Trieste

XV CICLO DEL DOTTORATO DI RICERCA IN FISICA

Titolo Tesi di Dottorato:

DARK MATTER IN EARLY-TYPE GALAXIES WITH
X-RAY HALOES. A SPECTROSCOPIC STUDY OF
DYNAMICS AND ABUNDANCE INDICES

Dottorando

Srdjan Samurović 166

62

Coordinatore del Collegio dei Docenti

Chiar.mo Prof. Gaetano Senatore

Università degli Studi di Trieste

GA

Relatore

Chiar.mo Prof. John Danziger

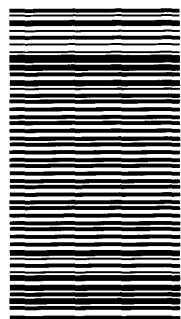
Osservatorio Astronomico di Trieste

Correlatore

Chiar.ma Prof. Maria Francesca Matteucci

Università degli Studi di Trieste

BIB. GENERALE
UNIV. TS
DR 6
0063



N. INV. : 066 63

ABSTRACT

In this thesis the existence of dark matter in the early-type galaxies with and without X-ray haloes was explored. I used high quality long-slit spectra obtained from various sources related to the field, binary, group and cluster galaxies from which, after the reduction procedure, full line-of-sight velocity profiles were extracted. The analyzed spectra extend from the center out to one to three effective (half-light) radii. Some published data from the literature related to the kinematical and photometric parameters were also used.

The velocity profiles were modeled as a truncated Gauss-Hermite series, taking into account velocity, velocity dispersion, and Gauss-Hermite parameters, h_3 and h_4 , that describe asymmetric and symmetric departures from the Gaussian, respectively. Comparison of velocity profiles with the predictions of different dynamical models which were constructed: two-integral Jeans model and three-integral Schwarzschild's numerical orbital superposition model was done. From the two-integral modeling it is inferred that some galaxies could not be fitted with this approach thus leading to the conclusion that their distribution function depends on three integrals of motion. This kind of modeling, however, provided useful constraints on the mass-to-light ratios in these galaxies.

A general conclusion is that, while some galaxies can be fitted without the inclusion of dark matter in their haloes, one cannot reject its existence, because the models are marginally consistent at larger radii with this assumption. X-ray haloes, when they are present, show the similar trend of increasing mass-to-light ratio as in the case of two-integral modeling. The three-integral models that were constructed permitted me to explore stellar orbits in different potentials: spherical, axisymmetric and flattened triaxial. For each analyzed galaxy a discussion was presented about which potential is the most appropriate and comparison of results with the results obtained with the two-integral modeling technique (where available) was done.

Absorption features present in the integrated stellar spectra of early-type galaxies that provide information on the chemical evolution of these objects were also studied. Using the aforementioned long-slit spectra absorption line indices were extracted and compared with the available models of chemical evolution of galaxies.

*This thesis is dedicated
to the Living Memory
of my father,
Svetozar Samurović*

Dear friend, all theory is grey,
And green the golden tree of life.
Goethe, *Faust*

ACKNOWLEDGMENTS

I would like to thank my thesis advisors John Danziger and Francesca Matteucci for their help, encouragement and support. They provided guidance and posed interesting and important problems yet allowing me a large amount of freedom in solving them.

I would like to thank the following colleagues from the Trieste Observatory and the Department of Astronomy of the University of Trieste for numerous discussions and advice: Simone Zaggia for the help in obtaining spectra of galaxies from the Fornax sample and the help in the data reduction, Antonio Pipino for calculation of different photo-chemical evolution models, Francesco Calura for stimulating discussions about different aspects of elliptical galaxies, Piercarlo Bonifacio for the help with the data reduction. I thank Fabio Mardirossian for his continual help while he was the Director of both institutions. I express my gratitude to the late Giuliano Giuricin who helped me in the initial phases of this work.

I thank Eduardo Simonneau for useful discussions regarding different observational aspects of elliptical galaxies.

I would especially like to thank the following two colleagues from the Belgrade Astronomical Observatory for numerous interesting discussions: Milan M. Ćirković and Slobodan Ninković. Big thanks goes to Milan S. Dimitrijević and Zoran Knežević in their role as Director of the Belgrade Astronomical Observatory for their understanding and help. I also thank Luka Č. Popović for his help.

I am grateful to Giuseppe Furlan, the head of the ICTP TRIL (Training and Research in Italian Laboratories) program and Elena Dose, the secretary of the ICTP TRIL program for their continual help during the work on this thesis.

This research has made use of the NASA/IPAC Extragalactic Database (NED) (<http://nedwww.ipac.caltech.edu/>) is operated by the Jet Propulsion Laboratory, California Institute of Technology, under contract with the National Aeronautics and Space Administration. This research has also made use of the HyperLeda information system (<http://leda.univ-lyon1.fr>). The usage of the ESO archive (<http://archive.eso.org/>) is also acknowledged.

The spectra of several galaxies were obtained courtesy of Marcella Carollo and Kenneth C. Freeman. Olivier Hainout kindly provided photometry data for IC3370. Nicola Caon kindly provided Fornax galaxies photometry data in machine readable form. I acknowledge the use of the Gauss-Hermite Fourier Fitting Software developed by R.P. van der Marel and M. Franx and the use of the Two-integral Jeans Modeling Software developed by R.P. van der Marel and J.J. Binney.

I would like to thank my parents, Ljiljana and Svetozar, and brother, Rastko, for their help, support and encouragement. To my great sorrow, my father, Svetozar, lawyer and painter, died during the work on this thesis, on June 14, 2001. His keen interest in my work and Science was always of great importance to me. I dedicate this thesis to the living memory of him using his favorite quotation from Goethe's *Faust*.

I thank my wife, Hana Ovesni, for her patience, understanding and interest for my work. I am grateful to Kristinka Ovesni, Darinka Ovesni and Goran Miličić for their encouragement and help.

CONTENTS

Abstract	iii
Acknowledgements	vii
Introduction	1
1. Theoretical Concepts, Observations and Reductions	1
1.1 Stellar Kinematics: Theoretical Approach	11
1.2 Observations	15
1.2.1 General Remarks	15
1.2.2 Sample 1 (IC3370, IC1459)	16
1.2.3 Sample 2 (galaxies from the Fornax cluster: NGC1336, NGC1339, NGC1373, NGC1374, NGC1379, NGC1399, NGC1404, NGC1419)	23
1.2.3 Sample 3 (NGC4339, NGC3379, NGC4105)	26
1.2.4 Sample 4 (NGC2434, NGC3706, NGC5018)	28
2. Dynamical Modeling of Early-Type Galaxies	47
2.1 Two-Integral Modeling	47
2.1.1 Theoretical Introduction	47
2.1.2 Modeling Results	50
2.1.2.1 Sample 1 (IC3379, IC1459)	50
2.1.2.2 Sample 3 (NGC2434, NGC3706, NGC5018)	55
2.2 Three-Integral Modeling	60
2.2.1 Theoretical Introduction	60
2.2.2 Galaxies With Isophotal Twist	66
2.2.3 Modeling Results	72
2.2.3.1 Sample 1 (IC3370, IC1459)	72
2.2.3.2 Sample 2 (galaxies from the Fornax cluster: NGC1336, NGC1339, NGC1373, NGC1374, NGC1379, NGC1399, NGC1404, NGC1419)	74
2.2.3.3 Sample 3 (NGC4339, NGC33379, NGC4105)	84

2.2.3.4 Sample 4 (NGC2434, NGC3706, NGC5018)	87
3. Galaxies with X-ray haloes	95
4. Line strength indices	105
4.1 Measurements	105
4.2 Modeling	109
5. Conclusions	125
6. Appendices	133
1 Ill-Posed Problems and Regularization	133
2 Non-Negative Least Squares (NNLS)	141
3 Orbits	143
4 Self-Organizing Maps (SOMs)	159
5 Tables	165
5.1 Stellar kinematics	165
5.2 Line strength indices	182
List of Figures	195
List of Tables	199

Introduction

Galaxies are large systems that contain stars, gas, dust, planets and, most probably, dark matter. A large galaxy can contain approximately $10^{11} - 10^{12}$ stars. The amount of gas and dust can vary from a few percent of the total stellar mass (as in lenticular galaxies) to about ten percent for the most gas-rich objects (spiral galaxies). As noted by Binney & Tremaine (1987), in reply to the statement of Sandage made in 1961 that "galaxies are to astronomy what atoms are to physics", some analogy between galaxies and atoms indeed exists: galaxies are relatively isolated systems and they maintain their identity throughout their lives, except for occasional collisions and mergers with other galaxies. Also, a galaxy is a dynamical and chemical unit. However, there are some differences: for galaxies the laws from the world of atoms do not hold: a huge number of processes in some galaxy may, but not necessarily, be present in some other galaxy. That is why Binney & Tremaine suggested a more appropriate analogy: the relationship between galaxies and astronomy should be regarded as the relationship between ecosystems and biology — this analogy takes into account their complexity, their relative isolation and their ongoing evolution.

Galaxies can be classified according to the Hubble's classification system (see Figure 1) into four main types: ellipticals, lenticulars, spirals and irregulars. Early-type (elliptical and lenticular) galaxies belong to the left-hand end of the Hubble's tuning-fork diagram. The original suggestion of E. Hubble was that galaxies evolve from the left-hand end to the right. This suggestion has now been abandoned.

Elliptical galaxies have the surface brightness that falls off smoothly with radius, and in most cases can be fitted by $R^{1/4}$ or de Vaucoulers law:

$$I(R) = I(0) \exp(-kR^{0.25}) \equiv I_e \exp\{-7.67[(R/R_e)^{0.25} - 1]\}, \quad (1)$$

where R_e is the effective radius, that is the radius of the isophote containing half of the total luminosity and I_e is the surface brightness at R_e . The shape of elliptical galaxies varies in form from round to elongated. One can use the simple formula $n = 10[1 - (b/a)]$, where (b/a) denotes the apparent axial ratio, to write the type of these galaxies: En . Therefore, E0 are round galaxies, and E6 are highly elongated systems as seen projected on the sky. Research over the last 20 years has brought new knowledge about ellipticals and we now know that these galaxies are much more complex systems that they seemed. The elliptical galaxies contain little or no gas or dust. The old stars that are prevalent are cool, evolved, and therefore of late spectral type. In the middle of the Hubble's diagram there is a class of galaxies designated as type S0, known as lenticular galaxies. They have a smooth central brightness condensation similar to an elliptical galaxy that is surrounded by a large region of less steeply declining brightness. They have disks that do not show

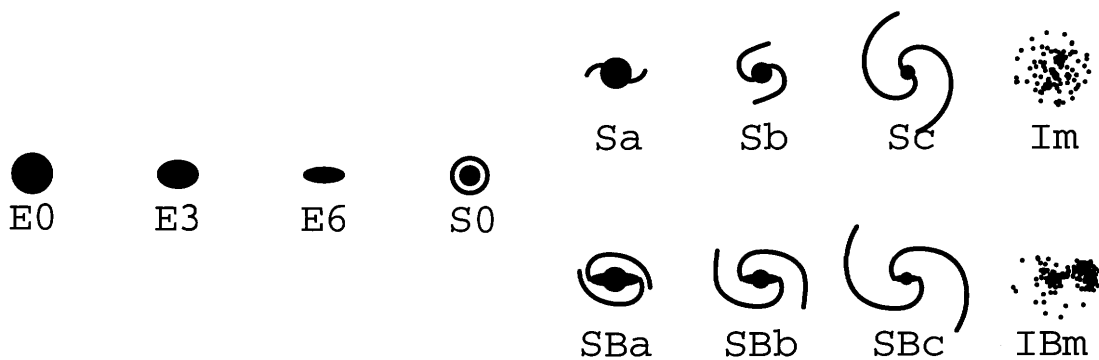


Figure 1: The Hubble tuning-fork diagram. On the left-hand end there are elliptical galaxies, in the middle there are lenticulars (S0) and on the right-hand end there spirals (Sa \rightarrow Sc) and irregulars. Lower part of the right-hand end is occupied by galaxies with bars (letter "B").

any conspicuous structure. Because of their appearance, and also because of their stellar content (e.g., spectral type), they look more like ellipticals rather than spiral galaxies. The problems may arise in the classification of S0 galaxies. For example, for a close well-studied galaxy NGC3379 it is not certain whether it is a bona fide normal elliptical or a face-on lenticular galaxy. The example of IC3370 also presented in this thesis provides another case of a problematic classification (its distance is ~ 42 Mpc, for the Hubble constant $h_0 \sim 0.7$). The remark of Gregg et al. (2003) therefore seems appropriate: "If after such detailed investigations, we are unable to discern the morphological type of NGC3379, at a distance of only 10 Mpc, then it is practically impossible to establish the true morphology of other early type galaxies at greater distances in clusters such as Coma, let alone at high redshift".

Spiral galaxies (including our own, Milky Way) consist of three main parts: spheroid, thin disk and dark halo. Spirals contain a prominent disk that is composed of Population I stars, gas, and dust. The disk also contains spiral arms, in which are embedded bright O and B stars, gas, and dust – this is a place in which the stars are currently forming. Hubble divided spirals into a sequence of four classes (types), called Sa, Sb, Sc, and Sd. Along this sequence (Sa \rightarrow Sd) the relative luminosity of the spheroid (that contains older Population II stars) decreases, the relative mass of the gas increases, and the spiral arms become more loosely wound. The Milky Way is sometimes classified as Sbc, expressing the fact that its Hubble type is between Sb and Sc. Rotation curves of spirals are typically flat, a fact that is of importance for the dark matter studies (see below).

Irregular galaxies are galaxies for which one cannot easily distinguish a particular pattern. The majority of irregulars are low-luminosity gas-rich system such as the Magellanic Clouds (see Fig. 1 – the letters "I" and "m" refer to irregulars of the type similar to that of the Magellanic Clouds).

1. DARK MATTER PROBLEM IN EARLY-TYPE GALAXIES

The problem of the dark matter in galaxies remains perhaps the most important astrophysical problem in contemporary cosmology and extragalactic astronomy. Although its nature is still unknown, general opinion is that it exists and that it is a necessary ingredient of every viable cosmological model (see recent overview of the dark matter problem in galaxies in Binney (2003): in this paper

the problems of the cold dark matter (CDM) and MOND theory are presented).¹ The existence of the dark matter in spiral galaxies (late-type galaxies), like our own, Milky Way is rather clear mainly because of existence of cool gas which provides a powerful tool for obtaining rotation curves (that provide dependence of circular speed on radius from the center of the galaxy), that are, for most spirals, nearly flat thus indicating presence of dark mass in their outer parts – dark haloes (see, e.g., Binney & Tremaine 1987). There are problems in the determination of its shape, but observations tend to conclude that the dark halo is flattened (see, e.g., Samurović, Ćirković & Milošević-Zdjelar 1999).

However, the problem of dark matter in elliptical galaxies (early-type galaxies) is more complicated – it is more difficult to confirm the presence of dark haloes around ellipticals. Since elliptical galaxies contain little or no cool gas usually one cannot use 21-cm observations to trace kinematics of neutral hydrogen out to large radii, as is possible in the case of spirals. The support against gravitational collapse in ellipticals comes from essentially random motions rather than ordered rotation. In an attempt to check whether ellipticals have dark haloes one can use stellar kinematics, but since their outer parts are very faint, it is usually difficult to obtain spectra to constrain kinematics at large radii. An additional problem is related to the fact that one does not *a priori* know anything about the orbits of stars in ellipticals. Current investigations lead to the conclusion that there is less unambiguous evidence for the dark matter in ellipticals than in the case of spirals. Moreover, there are hints that in ellipticals the dark matter is not needed at all or, more precisely, not needed in some early-type galaxies, out to a given observed distance from the galactic center.

Recent reviews on the dark matter problem in elliptical galaxies can be found for example in Danziger (1997), Binney & Merrifield (1998) and Bertin (2000). I here briefly present different approaches that can be used in order to determine the presence of the dark haloes around early-type galaxies. As in Danziger (1997) I split the different methodological approaches in three large groups that are then subdivided: gas, test particles and lensing methods.

(a) GAS The gas in the early type-galaxies can be found in the X-ray haloes, this is a *hot gas* with temperature $T \sim 10^7$ K. Studies of X-ray haloes strongly suggest the existence of dark matter out to large distances from the center (review in Mathews & Brighenti 2003). I refer the reader to Chapter 3 where I present relevant calculations and apply them to the galaxies from my samples that posses X-ray haloes. The gas can also be *warm*, with $T \sim 10^4$ K. This is ionized hydrogen that includes emission line gas and $H\alpha + [\text{NII}]$ regions (e.g. Buson et al. 1993, Zeilinger et al. 1996). Pizzella et al. (1997) analyzed the velocity fields of ionized gas disks in four ellipticals and derived mass-to-light ratios as a function of radial distance. Using triaxial mass distribution they found that M/L ratio changes within individual galaxies, although there is no systematic increase with radius. The mean value for the B-band that was found is $\sim 5M_{\odot}/L_{B\odot}$ out to one effective radius (note that $h_0 = 0.5$ was used). This technique is limited to the inner regions of galaxies. *Cold gas* has been detected in several early-type galaxies out to large distances ($\geq 10R_e$). Bertola et al. (1993) found that variation of mass-to-light ratio in the B-band, $M_{\odot}/L_{B\odot}$ (in this thesis abbreviated to M/L_B), in ellipticals is similar to that of spiral galaxies. They showed that in spirals and ellipticals there exists a radius where the density of the dark matter is equal to that of

¹ In this thesis all the calculations were done in the framework of the classical Newtonian dynamics – no attempts were made to perform calculations within alternative theories (e.g. MOND theory of Milgrom 1983).

the visible matter. Expressed in units of effective radius, R_e , this distance is at $1.2 R_e$. Morganti et al. (1995) studied the example of elliptical galaxy NGC5266 and found that a disk of neutral hydrogen extends out to $10 R_e$. They discovered that there was an increase of mass-to-light ratio in the B-band from a value of $M/L_B \sim 2 - 3$ in the inner region to $M/L_B \sim 12$ at the most distant measured point at $\sim 9 R_e$. Thus they concluded that there is a hint of a dark matter halo. Oosterloo et al. (2002) studied five dust lane elliptical galaxies and found that in the case of NGC3108 the regular distribution and kinematics of the HI allowed them to derive the mass-to-light ratio: they calculated the value of $M/L_B \sim 18$ at $6 R_e$. The very recent result of radio and optical observations of the same galaxy of Jozsa, Oosterloo & Morganti (2003) suggests that the mass-to-light ratio out to $6R_e$ is $\sim 15 M_\odot/L_{V\odot}$ (in the V-band) (corresponds to $M/L_B \sim 22$ in the B-band). They reached the conclusion that this galaxy possesses a dark halo similar to that observed in spirals.

(b) TEST PARTICLES *Planetary nebulae (PNe)* are very a promising tool for dark matter research because they are detectable even in moderately distant galaxies through their strong emission lines. Hui, Freeman & Dopita (1995) found that the mass-to-light ratio in the central region of a giant elliptical galaxy NGC5128 is ~ 3.9 and that out to $\sim 5 R_e$ it increases to ~ 10 (in the B-band), thus indicating the existence of the dark halo. In an extension of this work, very recently, Peng, Ford & Freeman (2003) presented their results of an imaging and spectroscopic survey for PNe in NGC5128. They detected 1141 PNe, out of which they confirmed 780. They found that PNe exist at distances out to 80 kpc ($\sim 15R_e$) making this study the largest kinematic study of an elliptic galaxy to date, both in the number of velocity tracers and in radial extent. They found that the dark matter is necessary to explain the observed stellar kinematics, but their value of M/L_B is *much* lower than that expected from determinations that use X-ray haloes: within 80 kpc they found the total dynamic mass $\sim 5 \times 10^{11} M_\odot$ with $M/L_B \sim 13$. According to the paper of Bahcall, Lubin & Dorman (1995) that is based on the compilation of the mass-to-light ratios from the literature, at 80 kpc one should expect $M/L_B \sim 112 \pm 28$. It was already found by Hui et al. (1995) that the dynamical mass that they measured within 25 kpc was systematically lower than that measured by Forman, Jones & Tucker (1985) from ROSAT data who calculated a total mass of $1.2 \times 10^{12} M_\odot$ within 20 kpc. Also, van Gorkom et al. (1990) estimated the dynamical mass of NGC5128 using HI synthesis observations and found that it is much lower than that obtained using X-ray halo: they found that the total mass is $2.5 \times 10^{11} M_\odot$, and the mass within $1.2R_e$ is $1.2 \times 10^{11} M_\odot$. Thus, they found that there exists a constant mass-to-light ratio (that is equal to 3.1) out to at least 8.7 kpc. An interesting example of usage of PNe methodology in dark matter research is that of galaxy NGC3379. Ciardullo, Jacoby & Dejonghe (1993) used 29 PNe (out to $3.8 R_e$) to draw the conclusion that the mass-to-light ratio $M/L_B \sim 7$ and that there is no need for the dark matter. Recently, Romanowsky et al. (2003) observed PNe in three galaxies (NGC821, NGC3379 and NGC4494) and confirmed this conclusion for NGC3379 using much larger sample of 109 PNe (out to $\sim 5.5 R_e$). I analyzed this galaxy in some detail using different available data (photometry, long-slit spectra, X-ray data) in Chapters 1 and 2 and I reached the same conclusions, although I stress that some doubts still remain.

Globular clusters can also be used as tracers of dark matter in the early-type galaxies: Mould

et al. (1990) obtained optical multislit spectra of two giant elliptical galaxies M49 and M87 from the Virgo cluster. They found that the velocity dispersion profiles of the cluster systems were flat, thus suggesting the existence of an isothermal halo of dark matter in these elliptical galaxies. Grillmair et al. (1994) studied the radial velocities of 47 globular clusters in NGC1399 in the Fornax cluster. Under the assumption that the clusters were on purely circular orbits, they gave a lower limit on a globally constant mass-to-light (M/L) ratio of 79 ± 20 in the B-band. Their result suggesting that M/L is several times larger than values of mass-to-light ratio determined from the stellar component closer to the core implies that M/L must increase substantially with radius. This galaxy has been analyzed in Chapter 2 of this thesis. Côté et al. (2003) studied M49 (= NGC4472) galaxy and showed that the globular clusters radial velocities and density profiles provide "unmistakable evidence" for a massive dark halo. Very recently, Bridges et al. (2003) presented their results obtained using Gemini/GMOS spectrograph of several early-type galaxies. It is important to note that they have observed 22 globular clusters in the aforementioned galaxy NGC3379 and found no evidence of the dark matter out to $6 R_e$: they, in fact, in their preliminary analysis reached the conclusion that the mass-to-light ratio *decreases* (from ~ 8 at $2 R_e$ to ~ 4 at $\sim 6 R_e$, in the V-band, see Fig. 3 in Chapter 3 that includes this result transformed to the B-band).

A large set of dark matter investigations in early-type galaxies is made of studies of *integrated stellar light*. Since this is one of the main subjects of my thesis in subsequent chapters I will provide more details later. Here I present briefly the history of observations and modeling procedures. Binney, Davies & Illingworth (1990) in their seminal paper established a two-integral axisymmetric modeling based on the photometric observations. They analyzed galaxies NGC720, NGC1052, and NGC4697 and modeled velocities and velocity dispersions out to $\sim 1 R_e$. van der Marel et al. (1990) applied this approach to NGC3379 (out to $\sim 1 R_e$), NGC4261 (out to $\sim 1 R_e$), NGC4278 (out to $\sim 1 R_e$) and NGC4472 (out to $0.5 R_e$). Cinzano & van der Marel (1994) modeled the galaxy NGC2974 out to $0.5 R_e$ introducing a new moment – modeling of the Gauss-Hermite moments (for definitions see Chapter 1) defined previously in van der Marel & Franx (1993). All these modeling procedures did not take into account dark matter, because they dealt with the regions in which dark matter was not expected to make a significant contribution. In this case they showed that this method can provide a hint on the embedded stellar disk. Bertin, Saglia & Stiavelli (1992) and Saglia, Bertin & Stiavelli (1992) developed self-consistent two-component models of ellipticals. They fitted the models to observed photometric and kinematic profiles of individual galaxies and found that the amount of dark matter within one effective radius is not too large (it is of similar order to the luminous mass). In the case of NGC4472 (under their physical assumptions) it was found that dark matter must be present.

Saglia et al. (1993) presented a kinematical and line strength profiles of NGC4472, IC4296 and NGC7144 and from their dynamical modeling (quadratic programming) concluded that there is a strong evidence for dark matter in these galaxies. Carollo et al. (1995) observed and modeled a set of elliptical galaxies (NGC2434, NGC2663, NGC3706 and NGC5018). They used two-integral modeling procedure to model the stellar line-of-sight velocity distribution (using velocity dispersion and Gauss-Hermite h_4 parameter) out to two effective radii. They concluded that the massive dark matter haloes must be present in three of the four galaxies (they were analyzed in this thesis using a three-integral modeling procedure), and in case of NGC2663 there was no evidence of the dark matter. In 1997 Rix et al. used the Schwarzschild (1979) method for construction of axisymmetric and triaxial models of galaxies in equilibrium without explicit knowledge of the

integrals of motion. They introduced into the analysis velocity, velocity dispersion and Gauss-Hermite parameters h_3 and h_4 . They used the galaxy NGC2434 (from Carollo et al. 1995) to perform a detailed dynamical modeling in order to conclude that this galaxy contains a lot of dark matter: they found that about half of the mass within one effective radius is dark.

Statler et al. (1996) studied stellar kinematical fields of the post-merger elliptical galaxy NGC1700 out to four effective radii. In a subsequent paper Statler et al. (1999) found, using two-integral axisymmetric models as well as three-integral quadratic programming models that NGC1700 must have a radially increasing mass-to-light ratio, and that NGC1700 "appears to represent the strongest stellar dynamical evidence to date for dark halos in elliptical galaxies". Unfortunately, as noted by Statler et al., this galaxy has not been observed in the X-ray domain. Saglia et al. (2000) modeled the galaxy NGC1399 using two-integral models (major photometric axis only) out to $\sim 2.5 R_e$. They marginally detected the influence of the dark component that starts from $1.5 R_e$.

Gerhard et al. (1998) modeled NGC6703 using two-integral approach out to $2.6 R_e$ and found that dark halo must exist and that dark matter contributes about equal mass at $2.6 R_e$ to that from stars. Kronawitter et al. (2000) modeled a large sample of 21 elliptical galaxies out to $1-2 R_e$: for three of them (NGC2434, NGC7507, NGC7626) they found that models based on luminous matter should be ruled out. De Bruyne et al. (2001) modeled NGC4649 and NGC7097 using a three-integral quadratic programming method and found that in the case of NGC4649 a constant mass-to-light ratio ($M/L_V = 9.5$) fit can provide good agreement with the data and that a marginally better fit can be obtained including 10% of dark matter at $1.2 R_e$. In the case of NGC7097 both kinematic and photometric data can be fitted out to $1.6 R_e$ using a constant mass-to-light ratio ~ 7.2 . Cretton et al. (2000) modeled the giant elliptical galaxy NGC2320 using the Schwarzschild orbit superposition method and found that the models with radially constant mass-to-light ratio and logarithmic models with dark matter provide comparably good fits to the data and have similar dynamical structure (but note that the mass-to-light in the V-band is rather large: ~ 15 for the mass-follows-light models and ~ 17 for the logarithmic models).

The Schwarzschild method can be applied in modeling of the central parts of the early-type galaxies, see for example, the paper by van der Marel et al. (1998) in which M32 was analyzed, the Cretton & van der Bosch (1999) paper in which axisymmetric models of NGC4342 were presented, the Gebhardt et al. (2000) paper in which a black hole in the center of NGC3379 was modeled, the Gebhardt et al. (2003) paper with the sample of 12 ellipticals that were analyzed using axisymmetric approach. Finally, I mention the paper of Cappellari et al. (2002) that modeled in detail, using the Schwarzschild formalism, internal parts of one early-type galaxy that is also a subject of this thesis, IC1459.

A new, promising, avenue in studies of integrated light from the early-type galaxies is usage of new integral field spectrographs (like, for example, SAURON, cf. Bacon et al. 2001, de Zeeuw et al. 2002) that should provide information on line-of-sight velocity distribution and spectral indices in two dimensions improving the limitations of long-slit spectroscopy that is limited by time to few position angles. Unfortunately, this technique is at the moment limited to the interior parts of the galaxies (out to $\sim 1 R_e$, Emsellem, 2002, priv. communication). Therefore, long-slit spectroscopy with its long exposures still remains a necessary tool in dark matter studies.

There are numerous studies of early-type dwarf galaxies in the Local Group that investigate the *internal dynamics* of dwarf ellipsoidal galaxies. A successful fit to the data is obtained when

one assumes that they are embedded in a dark halo with mass of $\sim 10^7 M_\odot$, and a luminous mass component with a mass-to-light ratio in V-band $M/L_V = 2.5$ (see, e.g. Mateo 1998).

(c) LENSING METHODS

In this group of methods, I include weak gravitational lensing that enables determination of the dependence of the velocity dispersion on the luminosity of the lensing galaxies and is suitable for studies of the dark matter in outer part of galaxies. It was found that a Navarro-Frenk-White (NFW) profile provides a good fit to the data (Kleinheinrich et al. 2003). Strong gravitational lenses can also be used for probing of the galaxy haloes, but only in the inner regions of galaxies (few tens of kiloparsecs) (see, for example, Prada et al. 2003). I also mention the Lenses Structure and Dynamics (LSD) Survey that gathers kinematic data for distant (up to $z \sim 1$) early-type galaxies that are gravitational lenses (review in Treu et al. 2003). The results of this survey suggest that extended dark matter haloes are detected in the early-type galaxies and that the dark matter contributes 50-75% to the total mass within the Einstein radius (cases of the lens galaxies MG2016+112 in Treu & Koopmans (2002) and 0047-281 in Koopmans & Treu 2003).

2. THE AIM OF THIS THESIS

This thesis is dedicated to the detailed study of the kinematics of the early-type galaxies that is extracted from the integrated spectra of their stars. Since the existence of dark matter in the early-type galaxies can be established only in a study that takes into account all available observational data, the observational data that I had were then used in combination with the photometry data and the X-ray data in cases where galaxies possess X-ray haloes. A substantial part of the thesis is devoted to the construction of realistic dynamical models of the early-type galaxies: a publicly available code for two-integral modeling (van der Marel 2003) was used and I built my own package for three-integral dynamical modeling (based on the Schwarzschild (1979) method and Rix et al. (1997) paper) that I describe in detail. A reduction of long-slit spectra of all of the galaxies that I had at my disposal (except for three galaxies from Carollo et al. (1995) sample for which I took the data from literature) was made. Some photometric data from the literature was also used. Comparison of my results with the results of other aforementioned techniques in cases where such data existed revealed both agreement and discrepancies. Finally, in an attempt at making a link between the dynamics and chemical evolution I calculated abundance indices and compared them with the up-to-date chemical evolution models (Matteucci 2001, Pipino & Matteucci 2003)

REFERENCES

- Bacon, R., Copin, Y., Monnet, G., Miller, B.W., Allington-Smith, J.R., Bureau, M., Carollo, C.M., Davies, R.L., Emsellem, E., Kuntschner, H., Peletier, R.F., Verolme, E.K. & Tim de Zeeuw, P.T.: 2001, MNRAS, 326, 23
- Bahcall, N.A., Lubin, L.M. & Dorman, V.: 1995, ApJ, 447, L81

- Bertin, G.: 2000, *Dynamics of Galaxies*, Cambridge University Press
- Bertin, G., Saglia, R.P. & Stiavelli, M.: 1992, ApJ, 384, 423
- Bertola, F., Pizzella, A., Persic, M. & Salucci, P.: 1993, ApJ, 416, L45
- Binney, J.J., Davies, R.D. & Illingworth, G.D.: 1990, ApJ, 361, 78
- Binney, J.J. & Merrifield, M.R.: 1998, *Galactic Astronomy*, Princeton University Press
- Binney, J.J. & Tremaine, S.: 1987, *Galactic Dynamics*, Princeton University Press
- Binney, J.J.: 2003, to appear in IAU Symposium 220, "Dark Matter in Galaxies", S. Ryder, D.J. Pisano, M. Walker & K. Freeman (eds.), preprint astro-ph/0310219
- Bridges, T., Beasley, M., Faifer, F., Forbes, D., Forte, J., Gebhardt, K., Hanes, D., Sharples, R. & Zepf, S.: 2003, in press, in "Joint Discussion 6: Extragalactic Globular Clusters and their Host Galaxies", IAU General Assembly, July 2003. T. Bridges and D. Forbes (eds.), preprint astro-ph/0310324
- Buson, L.M., Sadler, E.M., Zeilinger, W.W., Bertin, G., Bertola, F., Danzinger, I.J., Dejonghe, H., Saglia, R.P. & de Zeeuw, P. T.: 1993, A&A, 280, 409
- Cappellari, M., Verolme, E.K., van der Marel, R.P., Verdoes Kleijn, G.A., Illingworth, G.D., Franx, M., Carollo, C.M. & de Zeeuw, P.T.: 2002, ApJ, 578, 787
- Carollo, C.M., de Zeeuw, P.T., van der Marel, R.P., Danziger, I.J. & Qian, E.E.: 1995, ApJ, 441, L25
- Ciardullo, R., Jakoby, G.H. & Dejonghe, H.G.: 1993, ApJ, 414, 454
- Cinzano, P. & van der Marel, R.P.: 1994, MNRAS, 270, 325
- Côté P., McLaughlin, D.E., Cohen, J.G. & Blakeslee, J.P.: 2003, 591, 850
- Cretton, N. & van der Bosch, F.C: 1999, ApJ, 514, 704.
- Cretton, N., Rix, H-W. & de Zeeuw, P.T.: 2000, ApJ, 536, 319
- Danziger I.J.: 1997, *Dark and Visible Matter in Galaxies*, ASP Conference Series, Vol. 117, Massimo Persic & Paolo Salucci (eds.), 28
- De Bruyne, V., Dejonghe, H., Pizzella, A., Bernardi, M. & Zeilinger, W.W.: 2001, ApJ, 546, 903
- de Zeeuw, P.T., Bureau, M., Emsellem, E., Bacon, R., Carollo, C.M., Copin, Y., Davies, R.L., Kuntschner, H., Miller, B.W., Monnet, G., Peletier, R.F. & Verolme, E.K.: 2002, MNRAS, 329, 513
- Forman, W., Jones, C. & Tucker, W.: 1985, ApJ, 293, 102
- Gebhardt, K., Richstone, D., Kormendy, J., Lauer, T.R., Ajhar, E.A., Bender, R., Dressler, A., Faber, S.M., Grillmair, C., Magorrian, J. & Tremaine, S.: 2000, AJ, 119, 1157
- Gebhardt, K., Richstone, D., Tremaine, S. Lauer, T.R., Bender, R., Bower, G., Dressler, A. Faber, S.M., Filippenko, A.V., Green, R., Grillmair, C., Ho, L.C., Kormendy, J., Magorrian, J. & Pinkney, J.: 2003, ApJ, 583, 92
- Gerhard, O., Jeske, G., Saglia, R.P. & Bender, R.: 1998, MNRAS, 295, 197
- Gregg, M.D, Ferguson, H.C., Minniti, D., Tanvir, N. & Catchpole, R.: 2003, AJ, in press, preprint astro-ph/0312158
- Grillmair, C.J., Freeman, K.C., Bicknell, G.V., Carter, D., Couch, W.J., Sommer-Larsen, J. & Taylor, K.: 1994, ApJ, 422, L9
- Hui, X., Ford, H.C., Freeman, K.C., Dopita, M.A.: 1995, ApJ, 449, 592
- Jozsa, G., Oosterloo, T. & Morganti, R.: 2003, in Proceedings of "Dark Matter in Galaxies", International Astronomical Union, Symposium no. 220, held 22-25 July, 2003 in Sydney

- Kleinheinrich, M., Schneider, P., Erben, T., Schirmer, M., Rix, H-W., Meisenheimer, K. & Wolf, C.: 2003, to appear in the Proceedings of the Meeting on "Gravitational Lensing : A unique Tool for Cosmology" held in Aussois, France, 5-11 Jan. 2003, preprint astro-ph/0304208
- Koopmans, L.V.E. & Treu, T.: 2003, ApJ, 583, 606
- Kronawitter, A, Saglia, R.P., Gerhard, O. & Bender, R: 2000, A& AS, 144, 53
- Mateo, M.L.: 1998, ARAA, 36, 435
- Mathews, W.G. & Brighenti, F.: 2003, ARAA, 41, 191
- Matteucci, F.: 2001, *Chemical Evolution of the Galaxy*, Kluwer Academic Publishers, Dordrecht
- Milgrom, M.: 1983, ApJ, 270, 365
- Morganti, R., Pizzella, A., Sadler, E.M. & Bertola, F.: 1995, PASA, 12, 143
- Mould, J.R., Oke, J.B., de Zeeuw, P.T. & Nemec, J.M.: 1990, AJ, 99, 1823
- Oosterloo, T. A., Morganti, R. Sadler, E. M., Vergani, D. & Caldwell, N.: 2002, AJ, 123, 729
- Peng, E.W., Ford, H.C. & Freeman, K.C.: 2003, ApJ, in press, preprint astro-ph/0311236
- Pipino, A. & Matteucci, F.: 2003, MNRAS, in press, preprint astro-ph/0310251
- Pizzella, A., Amico, P., Bertola, F., Buson, L.M., Danziger, I.J., Dejonghe, H., Sadler, E.M., Saglia, R.P., de Zeeuw, P.T., & Zeilinger, W.W.: 1997, A& A, 323, 349
- Prada, F., Vitvitska, M., Klypin, A., Holtzman, J.A., Schlegel, D.J., Grebel, E.K., Rix, H-W., Brinkmann, J., McKay, T.A. & Csabai, I.: 2003, ApJ, in press, astro-ph/0301360
- Rix, H.-W., de Zeeuw, P.T., Cretton, N., van der Marel, R.P. & Carollo, C.M.: 1997, ApJ, 488, 702
- Romanowsky, A.J., Douglas, N.G., Arnaboldi, M., Kuijken, K., Merrifield, M.R., Napolitano, N.R., Capaccioli, M. & Freeman, K.C.: 2003, Science, 5640, 1696
- Saglia, R.P., Bertin, G. & Stiavelli, M.: 1992, ApJ, 384, 433
- Saglia, R. P., Bertin, G., Bertola, F., Danziger, I. J., Dejonghe, H., Sadler, E. M., Stiavelli, M., de Zeeuw, P. T. & Zeilinger, W. W.: 1993, ApJ, 403, 567
- Saglia, R.P., Kronawitter, A., Gerhard, O. & Bender, R.: 2000, AJ, 119, 153
- Samurović, S., Ćirković, M.M. & Milošević-Zdjelar, V.: 1999, MNRAS, 309, 63
- Schwarzschild, M.: 1979, ApJ, 232, 236
- Statler, T., Smecker-Hane, T. & Cecil, G.: 1996, AJ, 111, 1512
- Statler, T., Dejonghe, H., & Smecker-Hane, T.: 1999, ApJ, 117, 126
- Treu, T., Koopmans, L.V.E., Sand, D.J., Smith, G.P. & Ellis, R.S: 2003, to appear in the proceedings of IAU Symposium 220 "Dark matter in galaxies", S. Ryder, D.J. Pisano, M. Walker, and K. Freeman (eds.), preprint astro-ph/0311052
- Treu, T. & Koopmans, L.V.E.: 2002, ApJ, 575, 87
- van der Marel, R.P. & Franx, M.: 1993, ApJ, 407, 525
- van der Marel, R.P., Binney, J. & Davies, R.L.: 1990, MNRAS, 245, 582
- van der Marel, R.P., Cretton, N., de Zeeuw, P.T. & Rix, H-W.: 1998, ApJ, 493, 613
- van der Marel, R.P.: 2003, homepage at : <http://www-int.stsci.edu/~marel/>
- van Gorkom, J. H., van der Hulst, J. M., Haschick, A. D. & Tubbs, A. D.: 1990, AJ, 99, 1781
- Zeilinger, W.W., Pizzella, A., Amico, P., Bertin, G., Bertola, F., Buson, L. M., Danziger, I.J., Dejonghe, H., Sadler, E.M., Saglia, R.P. & de Zeeuw, P.T.: 1996, A&AS, 120, 257

1

THEORETICAL CONCEPTS, OBSERVATIONS AND REDUCTIONS

1.1 STELLAR KINEMATICS: THEORETICAL APPROACH

Stars are moving in a given galaxy under the influence of a potential $\Phi(\mathbf{x}, t)$. If one wants to give a full description of the state of a collisionless system such as galaxy at any time t , one can use the number of stars $f(\mathbf{x}, \mathbf{v}, t)d^3\mathbf{x}d^3\mathbf{v}$ that have positions in the small volume $d^3\mathbf{x}$ that is centered on \mathbf{x} and have velocities in the small range $d^3\mathbf{v}$ that is centered on \mathbf{v} . The function $f(\mathbf{x}, \mathbf{v}, t)$ is called the distribution function (or phase-space density) of the system. This is obviously a non-negative function: $f \geq 0$.

In the case of all external galaxies, one cannot obtain data necessary for the reconstruction of the distribution function directly: one can observe line-of-sight velocities and angular coordinates. Since individual stars cannot be resolved, one has to deal with integrated stellar light that represents the average of the stellar properties of numerous unresolved stars that lie along each line of sight (LOS). Each star will have a slightly different LOS velocity, and therefore its spectral features will be shifted by a different amount: $\Delta u = c\Delta\lambda/\lambda = v_{\text{LOS}}$. The final galaxy spectrum will be shifted and broadened, as shown in Fig. 1.

The first step in the analysis of the shifts and broadenings is to define the line of sight velocity distribution (LOSVD, also called velocity profile, VP): this is a function $F(v_{\text{LOS}})$ that defines the fraction of the stars that contribute to the spectrum that have LOS velocities between v_{LOS} and $v_{\text{LOS}} + dv_{\text{LOS}}$ and is given as $F(v_{\text{LOS}})dv_{\text{LOS}}$. Now, if one assumes that all stars have identical spectra $S(u)$ (where u is the spectral velocity in the galaxy's spectrum), then the intensity that is received from a star with LOS velocity v_{LOS} is $S(u - v_{\text{LOS}})$. When one sums over all stars one gets:

$$G(u) \propto \int dv_{\text{LOS}} F(v_{\text{LOS}}) S(u - v_{\text{LOS}}). \quad (1)$$

This relation represents the starting point for a study of stellar kinematics in external galaxies (cf. Binney & Merrifield 1998, hereafter BM98). The observer gets $G(u)$ for a LOS through a galaxy by obtaining its spectrum. If the galaxy is made of certain type of stars, one can estimate $S(u)$ using a spectrum of a star from the Milky Way galaxy (see Fig. 1, lower part).

The solution of Eq. (1) seems rather simple. It would be enough to take its Fourier transform:

$$\tilde{F}(k) \propto \frac{\tilde{G}(k)}{\tilde{S}(k)} \quad (2)$$

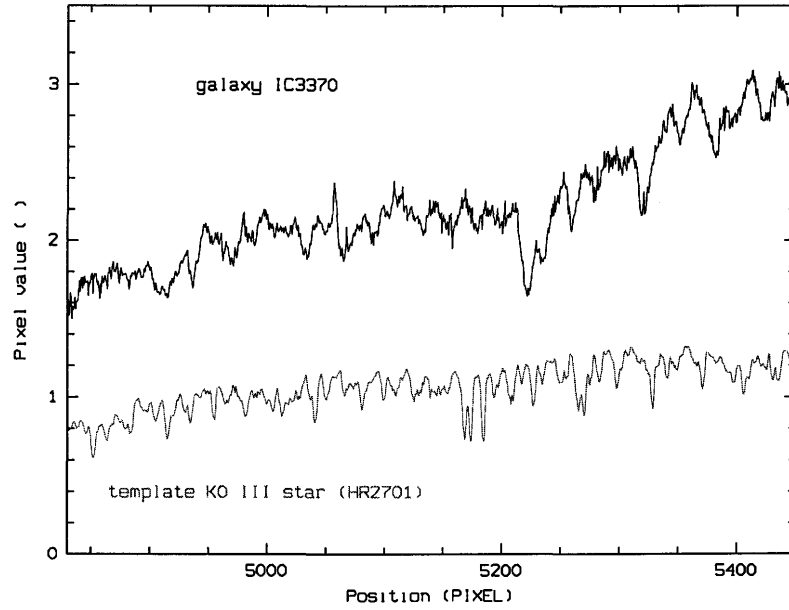


Figure 1: Reduced central spectrum of the galaxy IC3370 (above) and template star (below). Spectra have been wavelength calibrated: x axis is in Angstroms. Note effects of velocity dispersion and redshift in the case of the galaxy; y axis is in arbitrary units.

where quantities with tilde sign are the Fourier transforms of the original functions. This is however a very difficult task, since $\frac{\tilde{G}(k)}{\tilde{S}(k)}$ will be plagued by large errors that vary from point to point and the simple derivation of $F(v_{\text{LOS}})$ will not be easy (for details, see BM98). Therefore, less direct methods have been invented to solve this problem.

First we can define the simplest properties of a LOSVD. Its mean value is given as:

$$\bar{v}_{\text{LOS}} = \int dv_{\text{LOS}} v_{\text{LOS}} F(v_{\text{LOS}}). \quad (3)$$

Its dispersion is given as:

$$\sigma_{\text{LOS}}^2 = \int dv_{\text{LOS}} (v_{\text{LOS}} - \bar{v}_{\text{LOS}})^2 F(v_{\text{LOS}}). \quad (4)$$

One possible solution is to assume that the LOSVD has the Gaussian form. Sargent et al. (1977) invented the method known as Fourier Quotient Method, that has a problem of large errors for the ratio $\frac{\tilde{G}(k)}{\tilde{S}(k)}$ that vary from point to point. The cross-correlation method based on the calculation of the cross-correlation function between the galaxy and the stellar spectra was pioneered by Simkin (1974) and developed further by Tonry and Davis (1979) and Statler (1995).

The LOSVD can be modeled as truncated Gauss-Hermite (F_{TGH}) series that consists of a Gaussian that is multiplied by a polynomial (van der Marel & Franx 1993, also Gerhard 1993):

$$F_{\text{TGH}}(v_{\text{LOS}}) = \Gamma \frac{\alpha(w)}{\sigma} \exp\left(-\frac{1}{2}w^2\right) \left[1 + \sum_{k=3}^n h_k H_k(w)\right] \quad (5)$$

here Γ represents the line strength, $w \equiv (v_{\text{LOS}} - \bar{v})/\sigma$, $\alpha \equiv \frac{1}{\sqrt{2\pi}} \exp(-w^2/2)$, where \bar{v} and σ are free parameters. h_k are constant coefficients and $H_k(w)$ is a Gauss-Hermite function, that is a polynomial of order k . I will truncate the series at $k = 4$ (although higher values are also possible), for which the polynomials are:

$$\begin{aligned} H_0(w) &= 1, \\ H_1(w) &= \sqrt{w}, \\ H_2(w) &= \frac{1}{\sqrt{2}}(2w^2 - 1), \\ H_3(w) &= \frac{1}{\sqrt{6}}(2\sqrt{2}w^3 - 3\sqrt{2}w), \end{aligned} \tag{6}$$

and

$$H_4(w) = \frac{1}{\sqrt{24}}(4w^4 - 12w^2 + 3).$$

It can be shown (van der Marel & Franx 1993) that $H_l(w)$ (in this case, $l = 0, \dots, 4$) are orthogonal with respect to the weight function $\alpha^2(w)$.

Now the LOSVD can be calculated by varying the values of \bar{v} , σ , h_3 and h_4 until the convolution of the function $F_{TGH}(v_{\text{LOS}})$ with a template star spectrum best reproduces the observed galaxy spectrum. The optimal fit is then reached using a non-linear least-squares fitting algorithm. If the form of the LOSVD is close to the Gaussian form, then \bar{v} and σ will be approximately equal to $\overline{v_{\text{LOS}}}$ and σ_{LOS} . Parameters h_3 and h_4 are important because they measure asymmetric and symmetric departures from the Gaussian. If one detects a positive (negative) value of the h_3 parameter that would mean that the distribution is skewed towards higher (lower) velocities with respect to the systemic velocity. On the other hand, if one detects $h_4 > 0$ this means that the distribution is more peaked than the Gaussian at small velocities with more extended high-velocity tails; for $h_4 < 0$ the distribution is more flat-topped than the Gaussian. In the study of the dark matter in the early type galaxies the value of the h_4 parameter plays a crucial role because it is constraining the level of tangential anisotropy which is extremely important since it is well known that the excess of tangential motions can mimic the existence of the dark matter haloes in these galaxies (Danziger 1997, Gerhard 1993). The influence of changes in their values on the form of the LOSVD is given in Fig. 2.

For the extraction of the stellar kinematics I used van der Marel's freely available "Gauss-Hermite Fourier Fitting Software". Since this package was written for the Sun FORTRAN compiler for the Sun UNIX platform, initial testing was done using Sun Sparc (Sun-Blade-100) platform. Later, it was modified and ported to the x86 GNU/Linux PC platform that uses a GNU FORTRAN compiler. Detailed tests were done, and it was found that the results obtained in two different environments were in the excellent agreement. All the results presented in this thesis were obtained in the GNU/Linux environment.

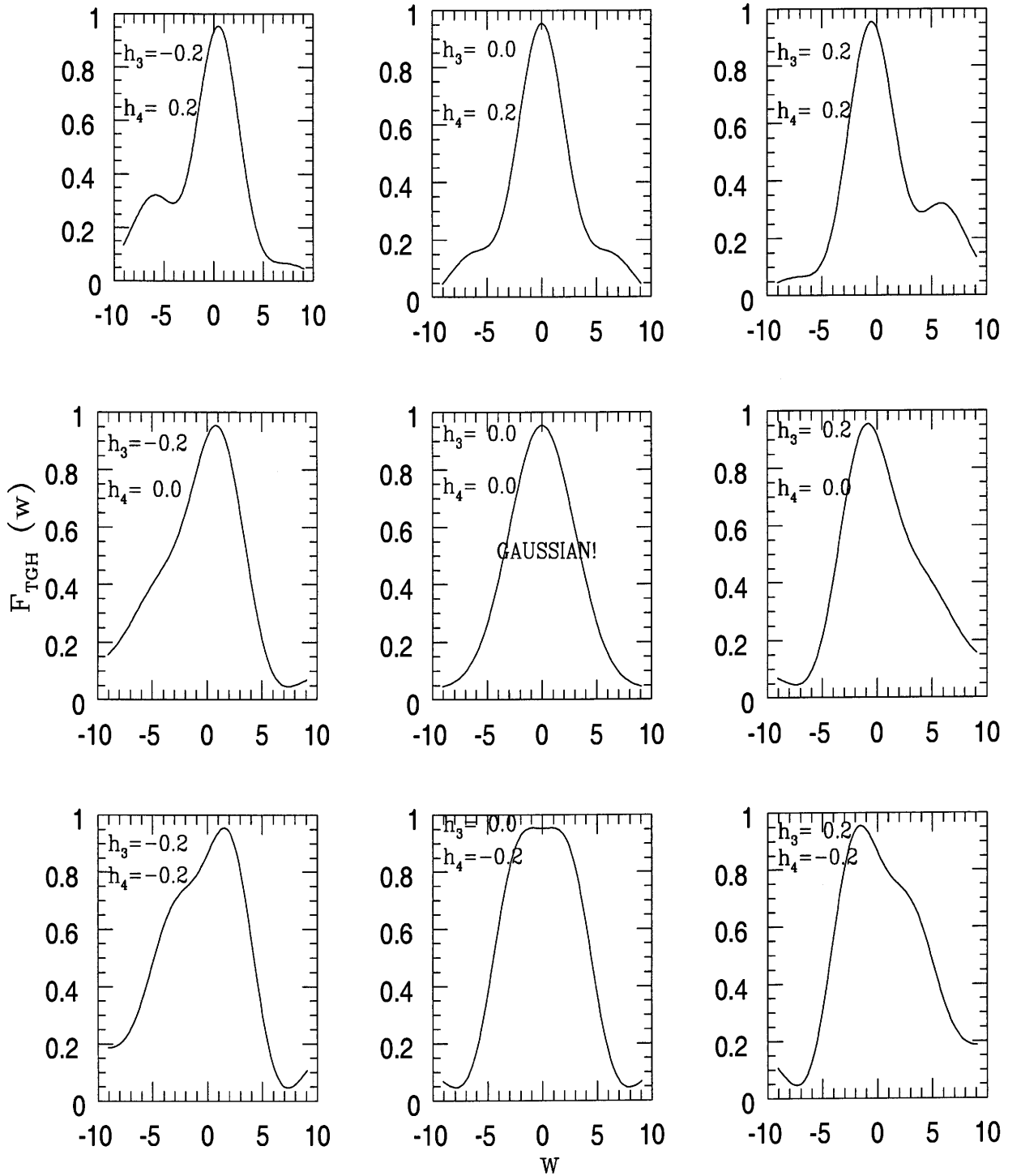


Figure 2: Plots demonstrating various combinations of h_3 and h_4 on the shape of the function $F_{\text{TGH}}(w)$. Pure Gaussian is in the center (both h_3 and h_4 are equal to zero). h_3 parametrizes the skewness of the line profile, while h_4 measures whether the profile is more or less peaked than a Gaussian. Units of the variable w are arbitrary.

1.2 OBSERVATIONS

1.2.3 General remarks

I have used different long-slit data obtained from different sources that will be called *Samples* hereafter. They are:

Sample 1. Observations obtained courtesy of J. Danziger (ESO NTT was used) which include spectra of IC1459 and IC3370.

Sample 2. Observations obtained courtesy of A. Graham and S. Zaggia (Double Beam Spectrograph attached to the Australian National University 2.3 m telescope at Siding Springs Observatory was used) which include the spectra of the following galaxies: NGC1336, NGC1339, NGC1373, NGC1374, NGC1379, NGC1399, NGC1404 and NGC1419 (from Fornax cluster – see Graham et al. (1998)).

Sample 3. Observations obtained courtesy of M. Carollo and K. Freeman (again Double Beam Spectrograph attached to the Australian National University 2.3 m telescope at Siding Springs Observatory was used) which include NGC3379 and NGC4339. Galaxy NGC4105 was observed using ESO 2.2 m telescope with EFOSC.

Details of the instrumental setup will be given in detail when each sample will be analyzed. Here I present the details of the reduction procedures that are common for all the observations. Note that in this thesis I will also deal with *Sample 4* which includes three galaxies taken from the literature: NGC2434, NGC3706 and NGC5018 (Carollo et al. 1995). For all galaxies for which I had the observational data I extracted stellar kinematic parameters (velocity, velocity dispersion, h_3 and h_4 parameters) and spectral indices.

All the reduction procedures of the long-slit spectra were done using the ESO MIDAS package¹. All the standard MIDAS commands and the commands from the context long were used, and where necessary small routines were written using MIDAS command language, MCL. First, I combined the spectra taken under the same conditions using COMBINE/LONG command. This was a very efficient way to remove the cosmic particle hits from the raw data. The bias, that is composed of a DC offset that is noiseless, and a noise component generated by the process of CCD readout, was subtracted: I have made a combined bias frame out of all available bias frames. A correction for the dark current was not made. For flat-fielding which performs the corrections for variations in pixel sensitivity across the CCD array, I combined available flat-field frames into a single flat-field frame which was normalized to unity. Frames of interest (galaxy's and stellar) were then divided by this single frame. For the purpose of the wavelength calibration I used spectra of different lamps (for example Helium-Argon) which were available for each observation. Interactive identification of lines was done using MIDAS commands that were embedded in a small MCL script: typical RMS uncertainty was $\sim 0.03 \text{ \AA}$. Sky subtraction was of a crucial importance because the outer parts of the galaxies are very faint, and sky removal had to be done very carefully. The command

¹ MIDAS is developed and maintained by the European Southern Observatory.

SKYFIT/LONG was used taking an average of ~ 30 rows near the edges of the exposure frames. For the extraction of the kinematical parameters of the galaxies rebinning into a logarithmic scale was done using simple MIDAS commands. Finally, the frames were trimmed by removing the rows and columns near the edges of the frames. In some cases I will present comparisons of my extracted kinematical parameters with those taken from literature (see below). The agreement is typically very good.

I used IRAF² for extraction of photometric profiles and for conversion of the MIDAS format into the IRAF format required by the Fourier Fitting package.

1.2.4 Sample 1

IC3370

GENERAL INFORMATION

IC3370 is a bright galaxy, classified as E2-E3 (elliptical) galaxy, absolute blue magnitude -21.4, heliocentric radial velocity $2930 \pm 24 \text{ km s}^{-1}$ (taken from the LEDA database). It covers 2.9×2.3 arcmin on the sky (RC3). However, it is a rather unusual elliptical galaxy and according to Jarvis (1987, hereafter referred to as J87) it should be classified as S0pec (see below). One arcsec in the galaxy corresponds to $\sim 203.02 \text{ pc}$. The effective radius is $35''$ ($=7.10 \text{ kpc}$).

PHOTOMETRIC OBSERVATIONS

I used frames kindly provided by O. Hainaut using ESO NTT and EMMI in the RILD mode on July 3-4, 2002 in the B-band. The photometry of IC3370 is very interesting and it is given in detail in J87. I present here some additional elements that are complementary to that study and are of importance for the analysis that I am undertaking.

One should note that J87 took for the major axis the position angle (PA) of 40° , Carollo, Danziger & Buson (1993) took for the same axis P.A. of 51° , while the spectra in this study were taken using P.A. = 60° . The reason for these differences lies in a very particular photometry of this galaxy that has strong isophotal twisting as shown in J87 and in Fig. 3 (see position angle (P.A.) plot). This may be evidence for the fact that this galaxy is triaxial, because the isophotes of an axisymmetric system must always be aligned with one another (see, for example, BM98). Fasano & Bonoli (1989) using a sample of 43 isolated ellipticals found that the twisting observed in these galaxies is intrinsic (triaxiality). Jarvis has taken the mean position angle of isophotes to be equal to $40 \pm 2^\circ$ which is true for the data up to $80''$. However, at larger radii the PA tends to increase, so the usage of larger value of 60° (and 150° for the minor axis) is justified (see Fig. 3).

In Fig. 3 I present relevant photometric data obtained using IRAF task `ellipse`: ellipticity, magnitude in the B-band for major axis (filled circles) and minor axis (open circles), a_4 parameter (fourth harmonic deviations from ellipse) and the position angles, as a function of distance. The value of a_4 is positive up to one effective radius (for almost all values of radius), thus indicating that the isophotes are disk-like, while beyond one effective radius, the isophotes become boxy since a_4 is negative. Since a_4 increases rapidly up to $\sim 5''$ this can lead to the conclusion of the embedded disk. The existence of the stellar disk was shown in J87. The photometric data in the case of

² IRAF is distributed by NOAO, which is operated by AURA Inc., under contract with the National Science Foundation.

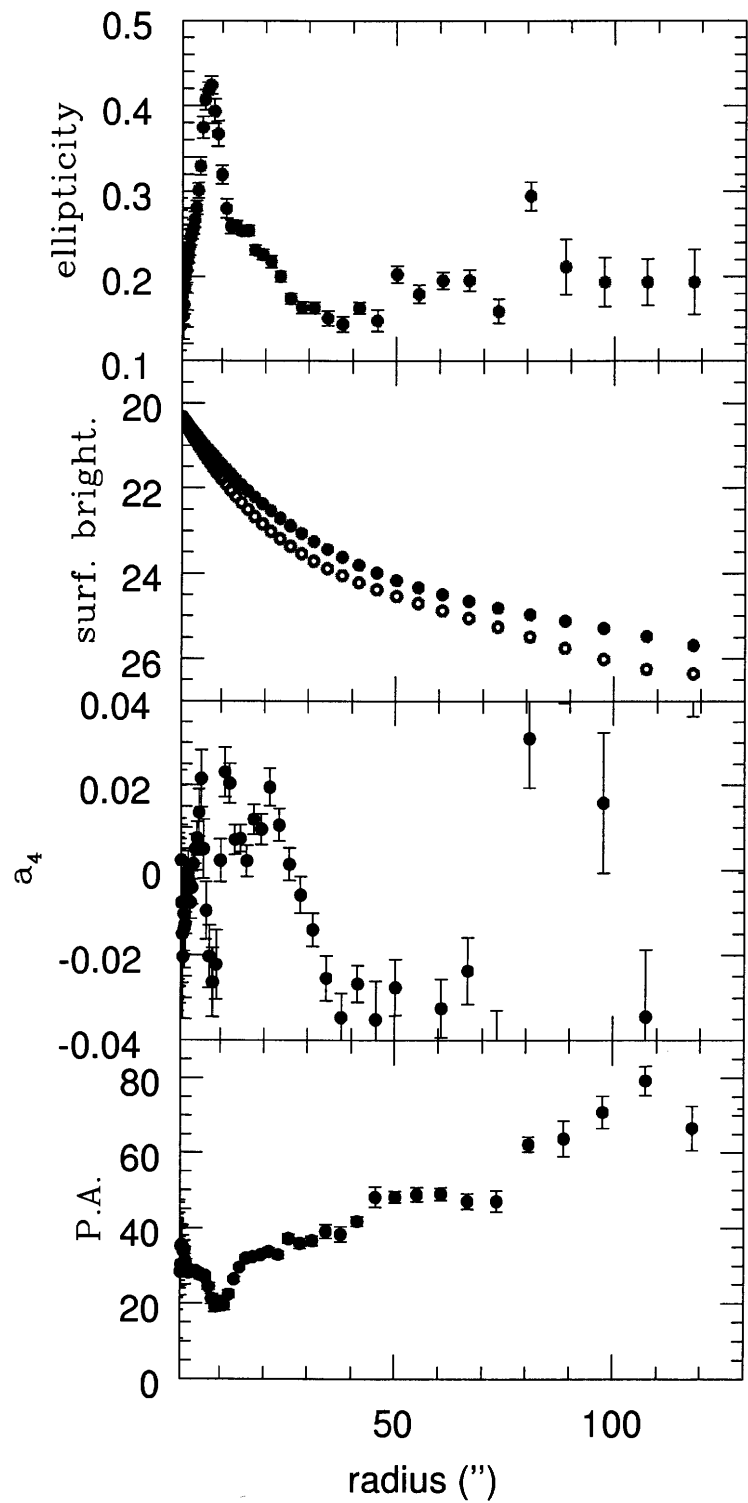


Figure 3: Photometric profiles for IC3370 (in the B-band). From top to bottom: ellipticity, surface brightness for the B filter in mag arcsec⁻² (for major axis: full circles; for minor axis: open circles), a_4 parameter and position angle.

IC3370, as well as in case of other galaxies that I present here, will be necessary for the dynamical modeling that will be given in the next Chapter.

LONG-SLIT SPECTRA

Long-slit spectra observations provided by J. Danziger were taken during 1998 March 1-3, using ESO NTT and EMMI in the Red Medium Spectroscopy mode. The central wavelength was chosen to be near the Mg_2 feature: $\sim 5150 \text{ \AA}$ with a range of $\sim 700 \text{ \AA}$. Several exposures were taken for three different position angles: for the galactic major axis (P.A. = 60°) total exposure of 21,600 s, for the minor axis (P.A. = 150°) total exposure of 7,200 s. Also, the spectra of the intermediate axis were taken (P.A. = 20°), and the total exposure time was 14,400 s. The spectra were rebinned at the telescope over 2 pixels giving a scale of $0.56 \text{ arcsec pixel}^{-1}$. I did the standard data reduction procedures in ESO MIDAS, as described previously. Wavelength calibration was done using the Helium-Argon comparison lamp spectra. Sky subtraction was done by taking an average of 30 rows near the edges of the exposure frames. Finally the spectra were rebinned on a logarithmic scale. Also, spectra of several template stars were reduced as described above, continuum divided, and averaged over several rows in order to obtain one stellar template spectrum of high signal-to-noise ratio (S/N). In Fig. 1 I showed a central galactic spectrum and a template star spectrum (K0 III star HR2701). The instrumental dispersion was $\sim 3.5 \text{ \AA}$ ($\sim 190 \text{ km s}^{-1}$) and was determined using a Helium-Argon spectrum in a region $\sim 5000 \text{ \AA}$. This is important for the conversion of the abundance indices to the Lick system discussed in Chapter 4.

In Fig. 4 I show the major axis kinematic parameters. This galaxy indeed shows behaviour that is characteristic for an S0 galaxy: for example, its major axis kinematics can be compared to that of NGC1461, lenticular galaxy from the Fisher (1997) sample. Note the usual behaviour of h_3 parameter: when the velocity rises, h_3 decreases, and vice versa. In Fig. 5 I present intermediate and minor axis kinematic profiles: IC3370 has minor axis rotation that provides an additional hint (apart from the isophotal twist) of the triaxiality. Note the small values (consistent with zero) of h_3 and h_4 at the large distances from the center for the major axis and their generally small values in the two other cases – they provide evidence of the lack of excessive tangential motions, that may mimic the dark matter in the outer parts of the galaxy.

IC1459

GENERAL INFORMATION

IC1459 is a giant E3 elliptical galaxy. Its absolute blue magnitude is -20.52, heliocentric radial velocity $1663 \pm 74 \text{ km s}^{-1}$ (taken from the LEDA database). It covers $5.2 \times 3.8 \text{ arcmin}$ on the sky (RC3). One arcsec in the galaxy corresponds to $\sim 117.16 \text{ pc}$. The effective radius is $33''$ ($=3.87 \text{ kpc}$). One of its most characteristic features is a fast counterrotating stellar core (Franx & Illingworth 1988). It has other peculiarities: twisted isophotes (Williams & Schwarzschild 1988), a dust lane and patches near the nucleus (Sparks et al. 1986) and an ionized gaseous disk at the core that rotates along the major axis in the same direction as the majority of stars in the galaxy – this is the opposite direction to that of the stellar core (Forbes et al. 1995). The nucleus of IC1459 has a strong (1Jy) compact radio source (Slee et al 1994). Recently, Fabbiano et al. (2003) observed this galaxy with *Chandra* ACIS-S.

Verdoes Klein et al. (2000) analyzed kinematical observations of the nuclear gas disk, and found a central black hole of mass $M_{\text{BH}} = (2 - 6) \times 10^8 M_\odot$. Cappellari et al. (2002) observed IC1459 using several slit positions and constructed axisymmetric three-integral models of this

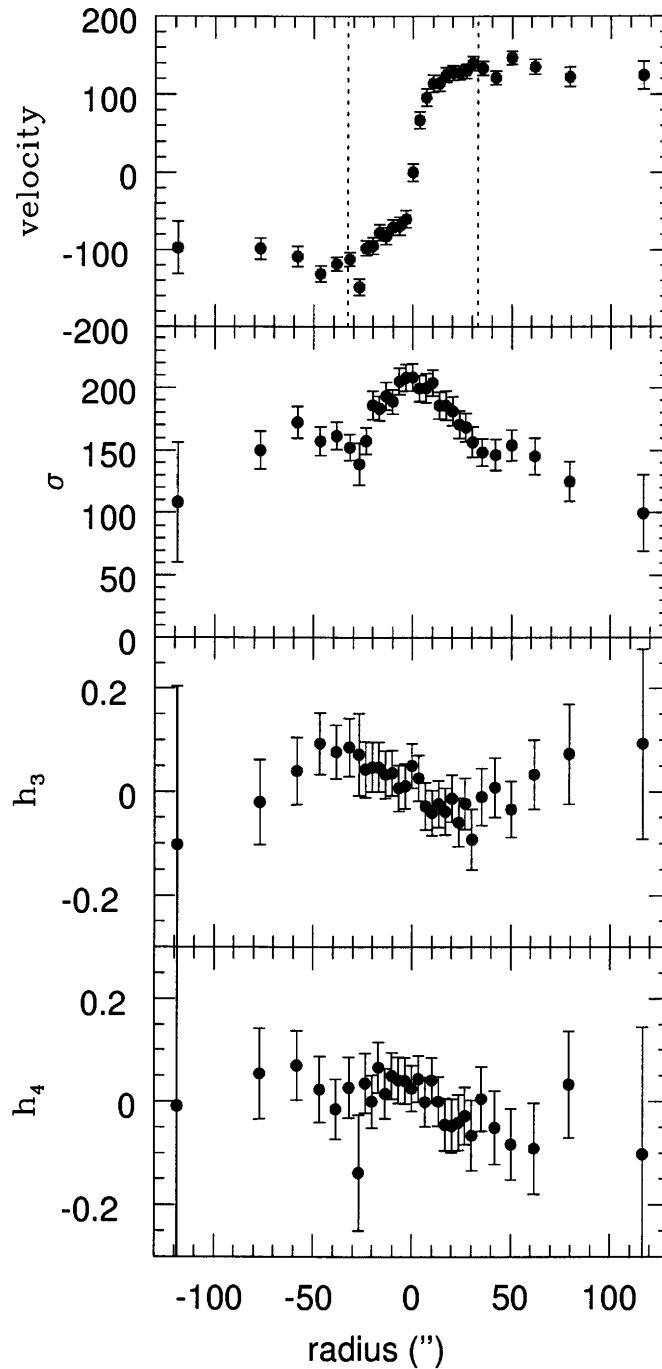


Figure 4: Kinematic profiles for the major axis of IC3370 (P.A.= 60°). From top to bottom: velocity, velocity dispersion, h_3 and h_4 parameters. One effective radius is plotted using dashed lines.

galaxy using the Schwarzschild orbit superposition method. They found, using stellar and gas kinematics, that $M_{\text{BH}} = (1.1 \pm 0.3) \times 10^9 M_\odot$.

PHOTOMETRIC OBSERVATIONS

Photometric observations made by J. Danziger during 1997 August 28-30 using the ESO NTT and EMMI in the Red Medium Spectroscopy mode in the V-band were used. I present the results ob-

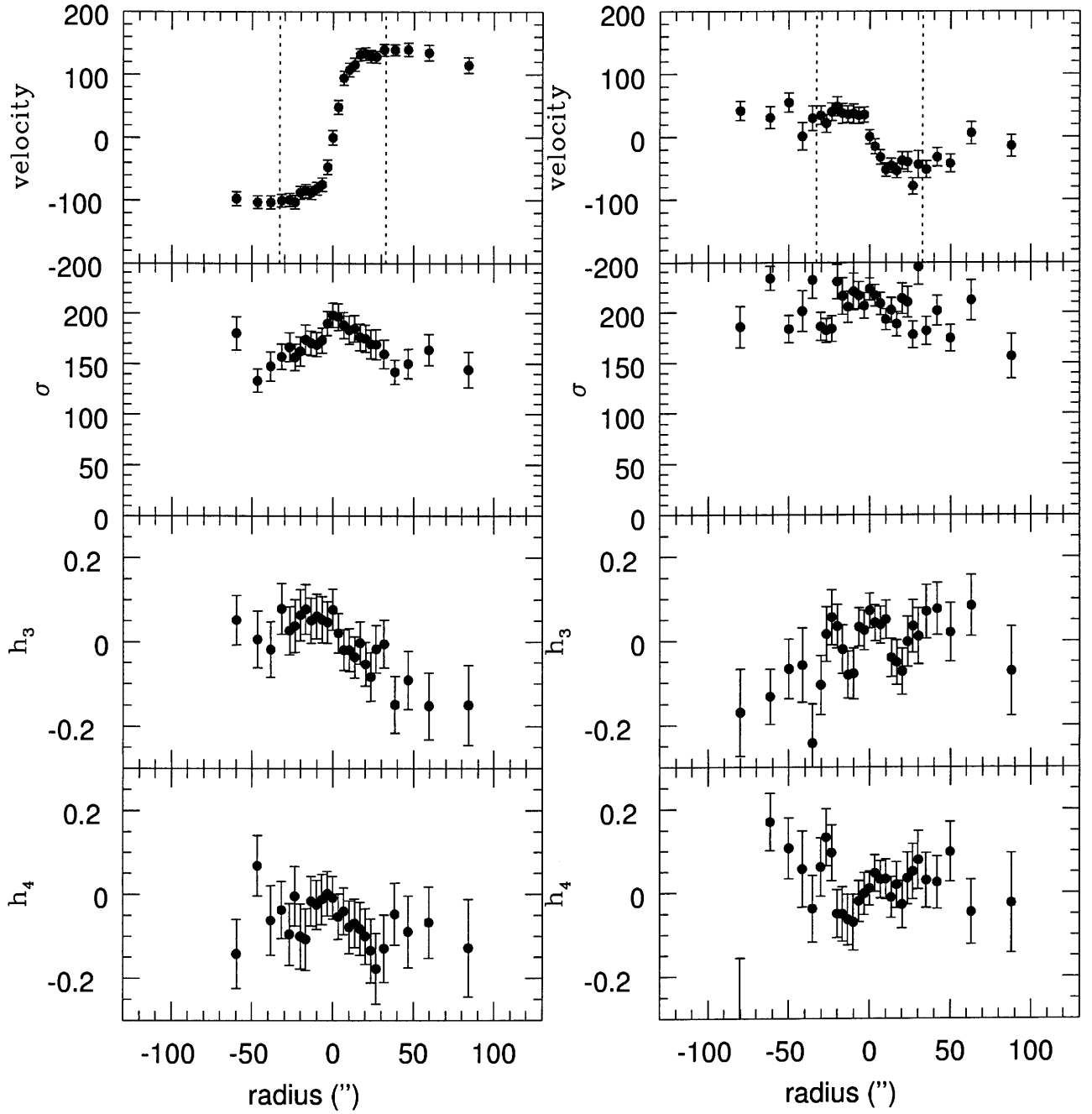


Figure 5: Kinematic profiles for the intermediate (P.A.= 150° , left) and minor (P.A.= 20° , right) axes of IC3370. From top to bottom: velocity, velocity dispersion, h_3 and h_4 parameters. One effective radius is plotted using dashed lines.

tained using the aforementioned IRAF routine in Fig. 6 where surface brightness was transformed to the B-band using relation $B - V = 0.99$ taken from the LEDA database. The photometric profile was compared with that of Franx & Illingworth (1988) and it was found that they were in a good agreement.

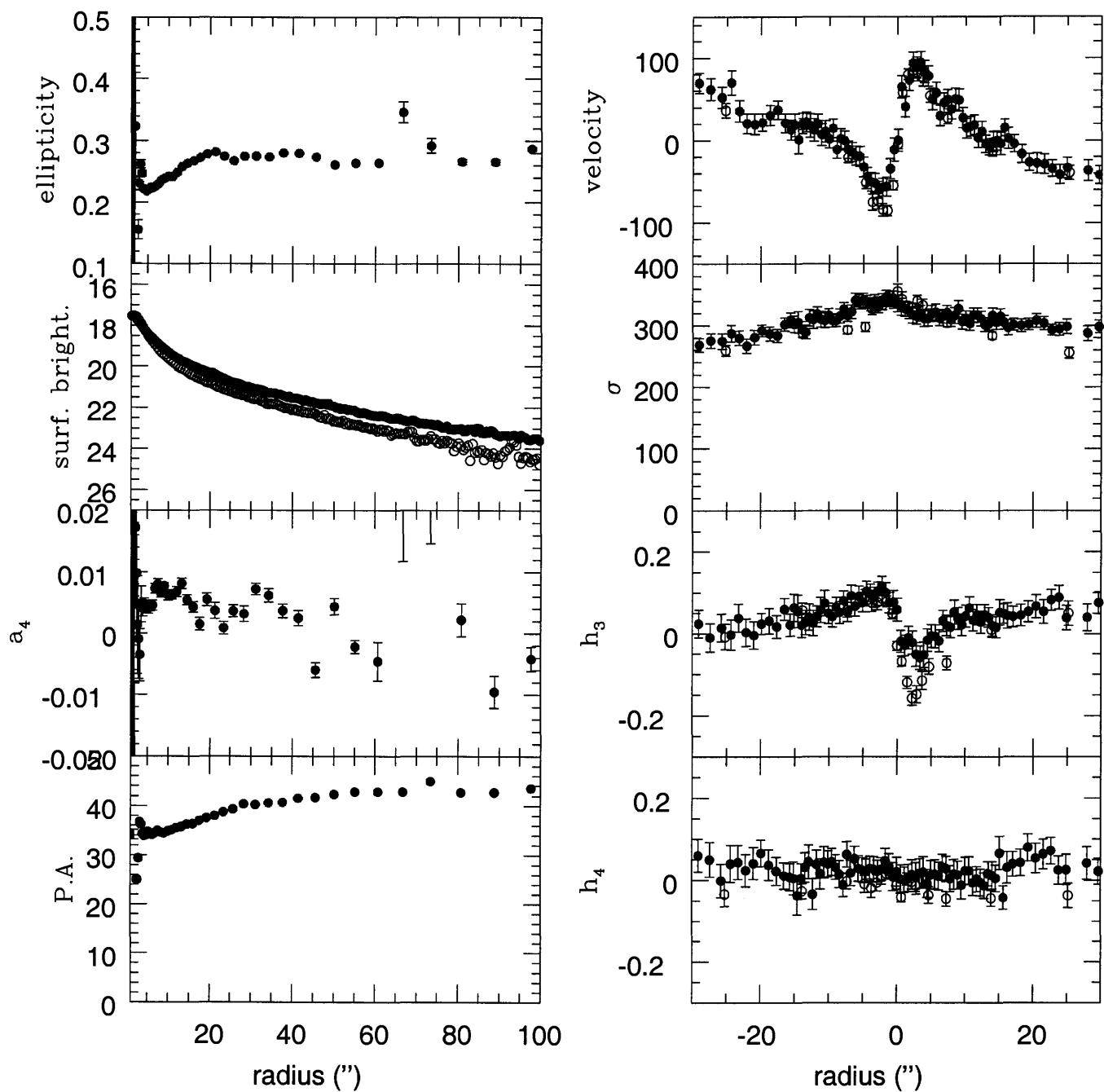


Figure 6: Left: Photometric profiles for IC1459 (in V-band). From top to bottom: ellipticity, surface brightness for the B filter (see text) in mag arcsec⁻² (for major axis: full circles; for minor axis: open circles), a_4 parameter and position angle. Right: Comparison of the kinematic profiles for the major axis of IC1459 (P.A.= 40°, black circles) and the data taken from Cappellari et al. (2002) (P.A.= 39°, open circles). From top to bottom: velocity, velocity dispersion, h_3 and h_4 parameters.

LONG-SLIT SPECTRA

Long-slit spectra observations provided by J. Danziger were done during the same nights using the same telescope and setup as in the case of IC3370. The central wavelength was chosen to be near the Mg_2 feature: $\sim 5150 \text{ \AA}$. The range that was covered was $\sim 700 \text{ \AA}$. Several exposures were taken for two different position angles: for the galactic major axis (P.A. = 40°) total exposure of 35,100 s, and for the minor axis (P.A. = 130°) total exposure of 3,600 s. Because of the fact that only one exposure was available for the minor axis, the removal of the cosmic ray hits was not successful and I have taken the minor axis stellar kinematics from Cappellari et al. (2002). I compared the results for the major axis and plot the comparison in Fig. 6. Cappellari et al. (2002) used the Cerro Tololo Inter-American Observatory (CTIO). The agreement is good, except for the velocity and h_3 parameter near the galactic center where some discrepancy exists. Note, however, that Cappellari et al. (2002) used P.A.= 39° and observations that I had were made at P.A.= 40° . In the outer parts agreement is excellent for the whole velocity profile. The spectra were rebinned at the telescope over 2 pixels giving a scale of $0.56 \text{ arcsec pixel}^{-1}$. I made standard reduction procedures in ESO MIDAS, as described previously. Wavelength calibration was done using a Helium-Argon comparison lamp spectra. Finally the spectra were rebinned on the logarithmic scale. Again, spectra of several template stars were reduced as described above, continuum divided, and averaged over several rows in order to obtain one stellar template spectrum of high signal-to-noise ratio (S/N). This time the template star HR5852 was used. The instrumental dispersion was $\sim 3.5 \text{ \AA}$ ($\sim 190 \text{ km s}^{-1}$) and was determined using Helium-Argon spectrum in a region $\sim 5000 \text{ \AA}$.

In Fig. 7 I show the major and minor axis kinematic parameters. Major axis data show the rapid increase of velocity in the inner $\sim 3''$: velocity rises to $\sim 100 \text{ km s}^{-1}$ (note however a small asymmetry in my determination of velocity). Velocity dispersion is large at the centre: $\sim 350 \text{ km s}^{-1}$, and decreases rapidly to $\sim 240 \text{ km s}^{-1}$ (at $\sim 40''$). There is a plateau in velocity dispersion between $\sim 20''$ and $30''$ after which velocity dispersion decreases. The h_3 parameter shows a typical behaviour, i.e. it rises (falls) when velocity rapidly increases (decreases). In the outer parts it shows small departures from zero. The h_4 parameter shows very small departures from zero in the inner parts, and in the outer parts there is an increase of its value, suggesting existence of the radial anisotropy. Minor axis data provide evidence of small velocities, and larger central velocity dispersion ($\sim 380 \text{ km s}^{-1}$). Both h_3 and h_4 parameters show very small departures from zero throughout the observed parts of the galaxy.

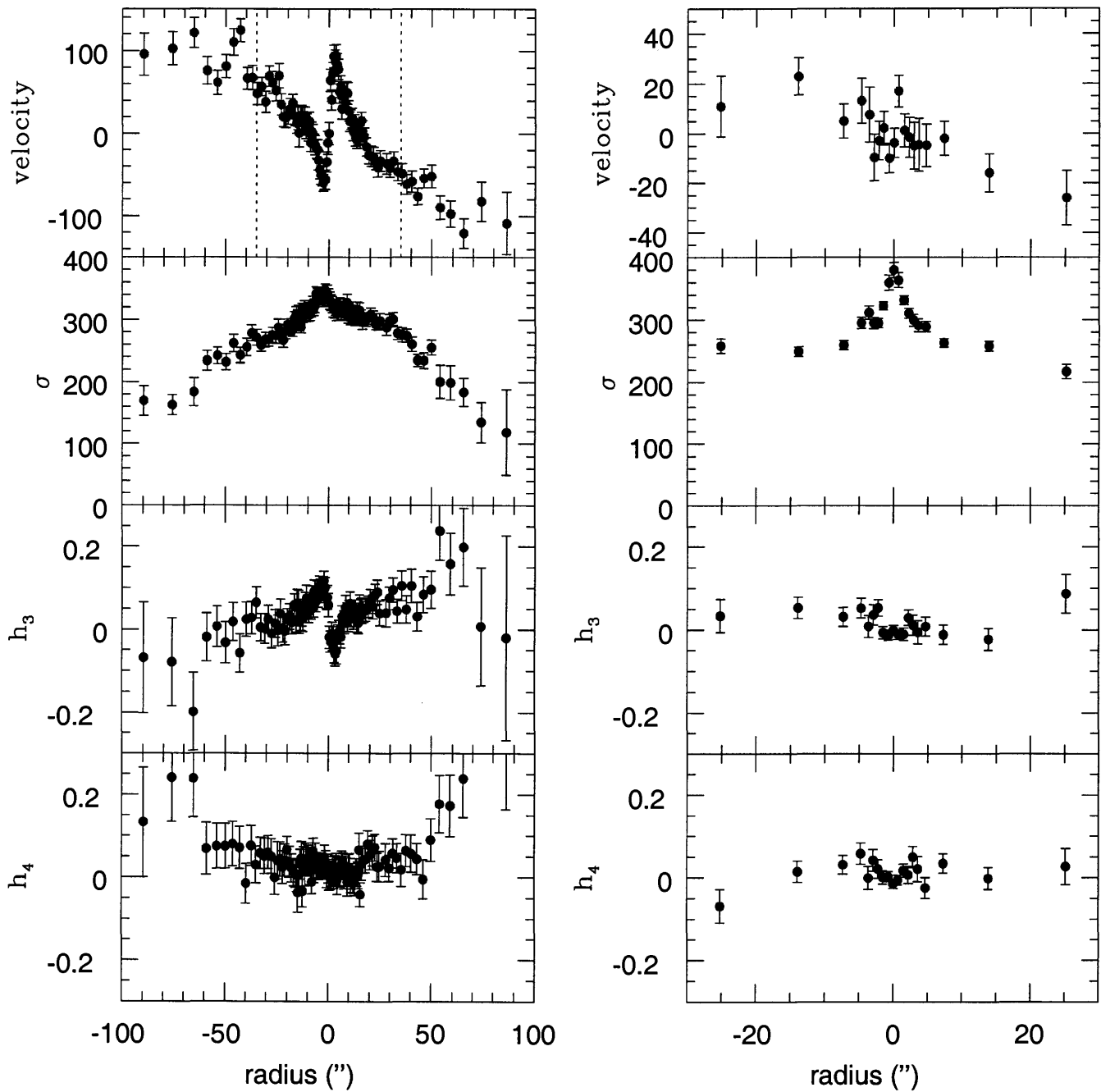


Figure 7: Stellar kinematics of IC1459. Left: major axis data. Right: minor axis data (taken from Cappellari et al. 2002). From top to bottom: velocity, velocity dispersion, h_3 and h_4 parameters. One effective radius in case of the major axis is plotted using dashed line. Note that in case of the minor axis it is out of scale.

1.2.5 Sample 2

In this subsection I will describe the sample and present the stellar kinematic results for the early-

type galaxies in the Fornax cluster obtained courtesy from A. Graham and S. Zaggia. These observations include 13 galaxies (major axes data) and represent a sample of 86% of Fornax galaxies brighter than $B_T = 15$ mag. From the observed galaxies I chose 8 galaxies for which I could extract the full velocity profiles and whose spectra extend to the distances larger than one effective radius (except for NGC1336, see below). A detailed description of the observations is given in Graham et al. (1998) (hereafter G98) and here I provide only some details that will be of importance for the modeling procedures. In TABLE 1-1 I give the basic observational data of Sample 2.

TABLE 1-1
GRAHAM ET AL. (1998) SAMPLE

Name	α_{1950} (h m s)	δ_{1950} (° ' ")	Type	v_{hel} km s^{-1}	B_T (mag)	r_e (")	$\frac{r_{\text{obs}}}{r_e}$	μ_e	P.A. °	Exp (hr)
NGC1336	3 24 35.9	-35 53 10	E4	1444 ± 66	13.3	30	0.8	23.6	20	1
NGC1339	3 26 06.1	-32 27 26	E4	1356 ± 48	12.7	15	2.0	21.5	175	2
NGC1373	3 33 03.3	-35 20 06	E3	1373 ± 34	14.2	11	2.0	22.4	140	3.5
NGC1374	3 33 21.1	-35 23 29	E0	1331 ± 36	11.9	26	1.5	22.3	120	1
NGC1379	3 34 08.7	-35 36 22	E0	1365 ± 46	12.0	24	2.0	22.0	7	0.75
NGC1399	3 36 34.2	-35 36 46	E0	1446 ± 36	10.0	42*	2.0	24.2	112	3
NGC1404	3 36 57.3	-35 45 17	E2	1942 ± 44	10.9	26	3.0	21.2	160	2.5
NGC1419	3 38 50.3	-37 40 09	E0	1649 ± 220	13.6	9	2.0	21.7	50	1

NOTE: Column (1): name, columns (2) and (3) coordinates (R.A. and Dec.), column (4): morphological type (according to Ferguson (1989)), column (5): heliocentric radial velocity (from LEDA database), column (6): total apparent blue magnitude, column (7) effective radius in arcsecs, column (8) approximate radial range of the kinematical data (in units of effective radius), column (9) blue surface brightness at 1 effective radius given in (mag/sq.arcsec.), column (10) major axis position angle, column (11): total exposure time (in hours). (*) Note that the effective radius for NGC1399, as in Kronawitter et al. (2000), was taken from Bicknell et al. (1989) (see Chapter 2).

The spectra were obtained during two runs in November and December 1996. The blue arm of the Double Beam Spectrograph was attached to the Australian National University's 2.3 m telescope at Siding Spring Observatory. The spatial scale on the chip was $0.91 \text{ arcsec pixel}^{-1}$. A spectrograph slit width of 2 arcsec on the sky with a length greater than the spatial extent of the CCD was used. FWHM for the arc lines of was found to be equal to 2.7 pixels or 1.50 \AA , giving a resolution of 86 km s^{-1} at 5200 \AA . I did the whole reduction procedure (explained in section 1.2.3 of this Chapter). The Neon-Argon lamp frames were used for the wavelength calibration. The spectra of several template stars were reduced and used for the extraction of the full velocity profiles. The template star HD4128 was used in extracting the stellar kinematics of the following galaxies: NGC1336, NGC1379, NGC1374, NGC1399 and NGC1419. The template star HD4188 was used in case of these galaxies: NGC1339, NGC1373 and NGC1404. Note that in the presentation of the photometric data I used Caon et al. (1994) data that give the cos4 parameter that represents the amplitude of the residual cos4 coefficient (multiplied by 100) of the isophotal deviation from the best fitting ellipse. In all the plots of this *Sample*, East (E) side is given with the

positive values of the radius (right hand side), and the west side (W) is given with the negative values of the radius (left hand side).

NGC1336 (Fig. 8)

One arcsec in this galaxy corresponds to ~ 100 pc. The effective radius is $30''$ ($=3.00$ kpc). The velocity has a slow increase and does not reach large values (maximum of 50 km s^{-1} , with large error bars). Velocity dispersion profiles show a lack of symmetry and have a decreasing trend (error bars are large, so this should be taken with caution). G98 suggested the existence of a bar – note the large $\cos 4$ parameter in the photometric profile inside $10''$, and also the small positive values of h_4 in this region.

NGC1339 (Fig. 9)

One arcsec in the galaxy corresponds to ~ 93.95 pc and the effective radius is $15''$ ($=1.41$ kpc). The data for the rotation curve extend to $\sim 2R_e$ and the velocity remains constant. The velocity dispersion falls from the central value of $\sim 170 \text{ km s}^{-1}$ to $\sim 100 \text{ km s}^{-1}$ (at $\sim 1R_e$) and then begins to rise: at the last measured point $\sigma \approx 125 \text{ km s}^{-1}$. The parameter h_3 behaves as usual when the galaxy has such a rotation curve: it rises when velocity rises, and declines when velocity declines. h_4 shows signs of an increase: only in the very internal part its value is consistent with zero.

NGC1373 (Fig. 10)

One arcsec in the galaxy corresponds to ~ 95.13 pc. The effective radius is $11''$ ($=1.05$ kpc). The rotation curve is rather symmetric and with a small degree of rotation. On the contrary, the velocity dispersion shows clear signs of asymmetry. Also, there is a trend of rising velocity dispersion values in the outer parts. From h_3 and h_4 it is difficult to draw conclusions. There is a hint that h_4 has small positive values throughout the observed regions of the galaxy.

NGC1374 (Fig. 11)

One arcsec in the galaxy corresponds to ~ 92.22 pc. The effective radius is $26''$ ($=2.40$ kpc). The rotation curve is another example of the steep increase of the velocity in the inner parts ($\sim 5''$). As noted by G98, although the overall velocity profile is symmetric there are important departures from symmetry, which are also visible in the velocity dispersion profiles: when the plateau of $\sigma \sim 150 \text{ km s}^{-1}$ is reached at $\sim 10''$ the velocity dispersion changes behavior beyond one effective radius. h_3 and h_4 profiles also show a lack of symmetry.

NGC1379 (Fig. 12)

One arcsec in the galaxy corresponds to ~ 94.58 pc. The effective radius is $24''$ ($=2.27$ kpc). This galaxy has a slow rotation (the value of the maximum velocity: $\sim 40 \text{ km s}^{-1}$). Velocity profiles show a lack of symmetry twice: first, near the central region and, second, in the outer regions – on the E side velocity approaches zero, and on the W side it tends to be constant $\sim 30 - 40 \text{ km s}^{-1}$. The velocity dispersion does not show a tendency to decline beyond one effective radius.

NGC1399 (Fig. 13)

One arcsec in the galaxy corresponds to ~ 100.19 pc. The effective radius is $42''$ ($=4.21$ kpc); note, however that this value might be problematic: Caon et al.(1994) calculated a value of $127''$ ($=12.72$ kpc) by fitting their extended photometry (see the note related to this galaxy in the next Chapter). This is the largest galaxy in the Fornax cluster and is positioned in the center of the cluster. The rotation curve shows evidence for a kinematically distinct inner component. The velocity reaches (at W side) at $\sim 20''$ a value of $\sim 30 \text{ km s}^{-1}$ which then steadily falls to zero (at $\sim 50''$). At the E side the velocity remains constant at $\sim 30 \text{ km s}^{-1}$ (starting from $10''$). The velocity dispersion is very high at the center $\sim 320 \text{ km s}^{-1}$ and quickly declines to $\sim 250 \text{ km s}^{-1}$ (at $10''$) and then remains approximately flat. The h_3 parameter remains slightly positive throughout the whole observed galaxy. The h_4 parameter shows small departures from zero but which can be considered to be consistent with zero throughout the whole observed galaxy.

NGC1404 (Fig. 14)

One arcsec in the galaxy corresponds to ~ 134.55 pc. The effective radius is $26''$ ($=3.50$ kpc). This galaxy shows a steep gradient of velocity: it rises to $\sim 100 \text{ km s}^{-1}$ within $10''$. Note, however, that there is a flattening at the inner $\sim 2''$ (note the different binning used in extracting stellar kinematics for this galaxy with respect to the other galaxies in the Fornax cluster). The velocity remains constant beyond one effective radius, $v \sim 80 \text{ km s}^{-1}$ and the profile looks symmetric with respect to the center. The velocity dispersion profiles are in general symmetric, too. There are two local maxima at $\pm 2''$ from the center. Beyond these two points the velocity dispersion decreases at a nearly constant rate until it reaches a plateau at $\sim 12''$. Departures from symmetry can be seen in the outer parts of the galaxy ($\sim 3R_e$). In these outer regions the velocity dispersion again becomes $\sigma \sim 200 \text{ km s}^{-1}$. The h_3 parameter shows the usual behaviour for the case of the galaxy with rapidly increasing velocity (see the note for NGC1339) and is consistent with zero at large distances from the center ($\sim 3R_e$). h_4 is slightly negative, but within the error bars it is consistent with zero throughout the whole observed galaxy.

NGC1419 (Fig. 15)

One arcsec in the galaxy corresponds to ~ 114.25 pc, and the effective radius is $9''$ ($=1.03$ kpc). As noted by G98 the velocity and dispersion profiles of this galaxy are very similar to those of NGC1336. The velocity is small and is almost consistent with zero in the inner parts. The velocity dispersion is approximately constant ($\sigma \sim 100 \text{ km s}^{-1}$) within the observed parts of this galaxy. Not much can be said about h_3 and h_4 : in the outer regions they appear to be consistent with zero.

1.2.6 Sample 3

These are observations of early-type galaxies obtained courtesy of M. Carollo and K. Freeman. Galaxies NGC3379 and NGC4339 were observed using the Double Beam Spectrograph attached to the Australian National's University 2.3 m telescope at Siding Springs Observatory. Galaxy NGC4105 was observed using ESO 2.2 m telescope with EFOSC.

For NGC4339 the long slit observations of the major axis (P.A.=20°) were taken on March 14, 1997, and the total exposure time was 20,000 s. For NGC3379 the long slit spectra of the major axis (P.A.=70°) were taken on March 13-14, 1997 and the total exposure time was 6,000 s. In both cases: (i) the scale was 0.59 arcsec pixel⁻¹, (ii) wavelength calibration was done using Neon-Argon lamp, and (iii) the template star was cpd-43. The instrumental dispersion was $\sim 2 \text{ \AA}$ ($\sim 100 \text{ km s}^{-1}$) and was determined using a Neon-Argon spectrum in a region $\sim 5000 \text{ \AA}$. For NGC4339 the photometry data were taken from the paper of Caon et al. (1994) (see Fig. 15). For NGC3379 the surface brightness was taken from the paper of Capaccioli et al. (1990), whereas ellipticity, a_4 parameter and position angle as function of radius using images from the ESO archive (I band) were extracted using standard IRAF commands (see Fig. 17).

NGC4339 (Fig. 16)

NGC4339 is an E0 galaxy, with heliocentric radial velocity of 1292 km s^{-1} , and absolute B magnitude -19.25. One arcsec in the galaxy corresponds to $\sim 89.31 \text{ pc}$. The effective radius is $16''$ ($=1.43 \text{ kpc}$). The rotation shows a rapid increase: within inner $5''$ velocity rises to $\sim 70 \text{ km s}^{-1}$ and stays approximately constant out to $30''$ ($\sim 2R_e$). The velocity dispersion profile shows flat top in the inner $5''$ (of approximately 120 km s^{-1}) and then declines rapidly out to $60''$ (at $\sim 1R_e$). Beyond one effective radius there are no signs of further decline of velocity dispersion. h_3 and h_4 do not show large departures from zero. The h_4 parameter remains slightly positive throughout the observed parts of the galaxy.

NGC3379 (Fig. 17, Fig. 18)

NGC3379 is a bright E0 galaxy (note however the ellipticity $\epsilon \approx 0.15$ in Fig. 17; there are still some doubts whether this is a bona fide normal elliptical or a face-on lenticular galaxy, cf. Gregg et al. 2003), with heliocentric radial velocity of 911 km s^{-1} , and absolute B magnitude -20.57. One arcsec in the galaxy corresponds to $\sim 63.12 \text{ pc}$. The effective radius is $35''$ ($=2.22 \text{ kpc}$).

Since I had only major axis (P.A.=70°) data, I have taken data from Statler & Smecker-Hane (1999) for the major and the minor axis (P.A.=340°). I compared the results for the inner region which I have in common for the major axis and found that they are in an excellent agreement (see Fig. 17 (right)). The data that I had extend out to $\approx 30''$, so in the modeling procedures (see next Chapter) I will use Statler & Smecker-Hane (1999) measurements because their data extend to a larger radius ($80''$ that is $\approx 2 R_e$) and are also available for the minor axis.

This galaxy shows steep increase of velocity: it rises to $\sim 60 \text{ km s}^{-1}$ in the inner $20''$. After a plateau between $\sim 20''$ and $\sim 60''$ the velocity shows a tendency to decrease. The velocity dispersion peaks at $\sim 230 \text{ km s}^{-1}$ and then decreases rapidly. There is a plateau between $\sim 20''$ and $\sim 50''$. One can see that there is an obvious asymmetry at $\sim 80''$. However, other observations show that there is a decreasing trend out to $6 R_e$ (see next Chapter). The h_3 parameter is small out to $\sim 50''$, but shows departures from zero at $\sim 70''$. h_4 remains small throughout the whole observed galaxy, except in the outer parts for which there is a hint of departures from zero, but since error bars are large, it is difficult to draw firm conclusions. Minor axis data suggest that NGC3379 does not show significant rotation on the minor axis. The velocity dispersion profile is similar to

that of the minor axis. The h_3 and h_4 parameters are small throughout the whole observed galaxy on the minor axis (see Fig. 18).

NGC4105 (Fig. 19, Fig. 20)

GENERAL INFORMATION

NGC4105 is an E galaxy, with heliocentric radial velocity of 1918 km s^{-1} , and absolute B magnitude -20.72 . One arcsec in the galaxy corresponds to $\sim 134.14 \text{ pc}$. The effective radius is $11''$ ($\approx 1.48 \text{ kpc}$).

PHOTOMETRIC OBSERVATIONS

Photometric data were extracted from frames obtained courtesy of M. Carollo & K. Freeman using standard IRAF routines (Fig. 19). Note that the surface brightness is given in the R-band.

LONG-SLIT SPECTRA

Long slit spectra were obtained on March 9-13, 1994 using ESO 2.2 m telescope with EFOSC. The total exposure time for the major axis (P.A. $\approx 150^\circ$) was 27,900 s. The total exposure time for the minor axis (P.A. $\approx 60^\circ$) was 14,400 s. The scale was $0.336 \text{ arcsec pixel}^{-1}$. The wavelength calibration was done using Helium-Argon lamp. The template star was HR5582. The instrumental dispersion was $\sim 4.2 \text{ \AA}$ ($\sim 280 \text{ km s}^{-1}$) and was determined using Helium-Argon spectrum in a region $\sim 5000 \text{ \AA}$.

On the major axis this galaxy shows a maximum value of the velocity $\sim 60 \text{ km s}^{-1}$ (see Fig. 20, left). Note that there is a hint of a counterrotating stellar core in the inner $3''$. In general, there is a lack of symmetry about the galaxy center. The central value of the velocity dispersion is large: $\sim 320 \text{ km s}^{-1}$. It declines in the inner $\sim 5''$ after which there is a tendency that to remain constant (out to $2R_e$). h_3 also shows a hint of the effects of the counterrotating stellar core in the inner $3''$. At the larger radii the value of h_3 is consistent with zero. The h_4 parameter remains small (slightly negative, but consistent with zero) throughout the whole observed galaxy. On the minor axis NGC4105 shows rather complex behaviour and again a lack of symmetry is evident (see (Fig. 20). The velocity dispersion decreases from the central value of $\sim 320 \text{ km s}^{-1}$ to $\sim 200 \text{ km s}^{-1}$. Not much can be said about h_3 and h_4 parameters, except that they show asymmetries.

1.2.7 Sample 4

In this sample I include three galaxies from Carollo et al. (1995) for which these authors found an indication of existence of a dark halo: NGC2434 (a galaxy studied in detail also in Rix et al. 1997, see next chapter), NGC3706 and NGC5018. The details concerning these galaxies are given in the above two papers for each galaxy. Stellar kinematics for all galaxies are given in Carollo et al. (1995). Here, I give only a brief overview and present kinematical data (see related Figures) which I obtained in electronic form courtesy of M. Carollo:

NGC2434 (Fig. 21)

This is E0-1 galaxy, with heliocentric radial velocity $v = 1390 \pm 27 \text{ km s}^{-1}$ (taken from the NED database). Total apparent corrected B-magnitude is 11.29 (taken from the LEDA database). Details on photometry can be found in Carollo & Danziger (1994a). One arcsec in the galaxy corresponds to $\sim 96.31 \text{ pc}$. The effective radius is $24''$ ($\approx 2.31 \text{ kpc}$). This galaxy possesses a strong isophotal twisting in the inner $\sim 10''$. Isophotes are disky in the inner $\sim 3''$. The velocity does not reach large values: at $\sim 2R_e$ it is $\sim 30 \text{ km s}^{-1}$. The velocity dispersion peaks at $\sim 260 \text{ km s}^{-1}$, and then declines rapidly. Note that from $\sim 15''$ outwards it remains constant. h_3 parameters have small values throughout the observed galaxy. Note, however, that the velocity data in combination with the h_3 data may indicate the existence of the counterrotating stellar core (a case similar to that of NGC4105). Apart from small positive values in the inner region, the h_4 parameter is zero in the outer regions thus providing (in combination with the flat velocity dispersion profile) a strong indication of the existence of the dark halo.

NGC3706 (Fig. 22)

This is an E galaxy (according to the LEDA database), with heliocentric radial velocity $3215 \pm 150 \text{ km s}^{-1}$ (taken from NED database). The total corrected apparent B-magnitude is 12.32 (taken from the LEDA database). Details on photometry can be found in Carollo & Danziger (1994a). One arcsec in the galaxy corresponds to $\sim 222.75 \text{ pc}$. The effective radius is $27''$ ($\approx 6.01 \text{ kpc}$). This galaxy does not show strong isophotal twisting: the P.A. decreases slowly from $\sim 80^\circ$ (at $\sim 2''$) to $\sim 70^\circ$ (at $\sim 100''$). The rotation curve (and h_3 behaviour) is very similar to that of galaxies NGC1339 and NGC1404. The central velocity dispersion is rather high: 340 km s^{-1} and declines rapidly in the inner $\sim 20''$. At $\sim 2R_e$ it does show a plateau (albeit only on one side – data on the opposite side are unfortunately unavailable). The h_4 parameter has small positive values in the inner region and in the outer regions small negative values (that deviate from zero).

NGC5018 (Fig. 23)

This is an E-SO galaxy (according to LEDA database), with heliocentric radial velocity 2897 km s^{-1} . The total corrected apparent B-magnitude is 11.7 (all data are from ESO Lauberts & Valentijn catalog, as quoted in Carollo & Danziger (1994b). Details of photometry can be found in Carollo & Danziger (1994b). The galaxy does not show an isophotal twist. Note the asymmetry in velocity: maximum on one side $\sim 100 \text{ km s}^{-1}$, and on the other side maximum $\sim 50 \text{ km s}^{-1}$. The velocity dispersion has a double peaked maximum values (at $\sim 240 \text{ km s}^{-1}$). There exists a decreasing trend in the velocity dispersion. The h_3 parameter shows complex variations (especially in the region where the velocity is negative). The h_4 parameter remains positive throughout the whole observed galaxy.

Galaxies from *Sample 4* will be modeled in next Chapter using the Schwarzschild technique.

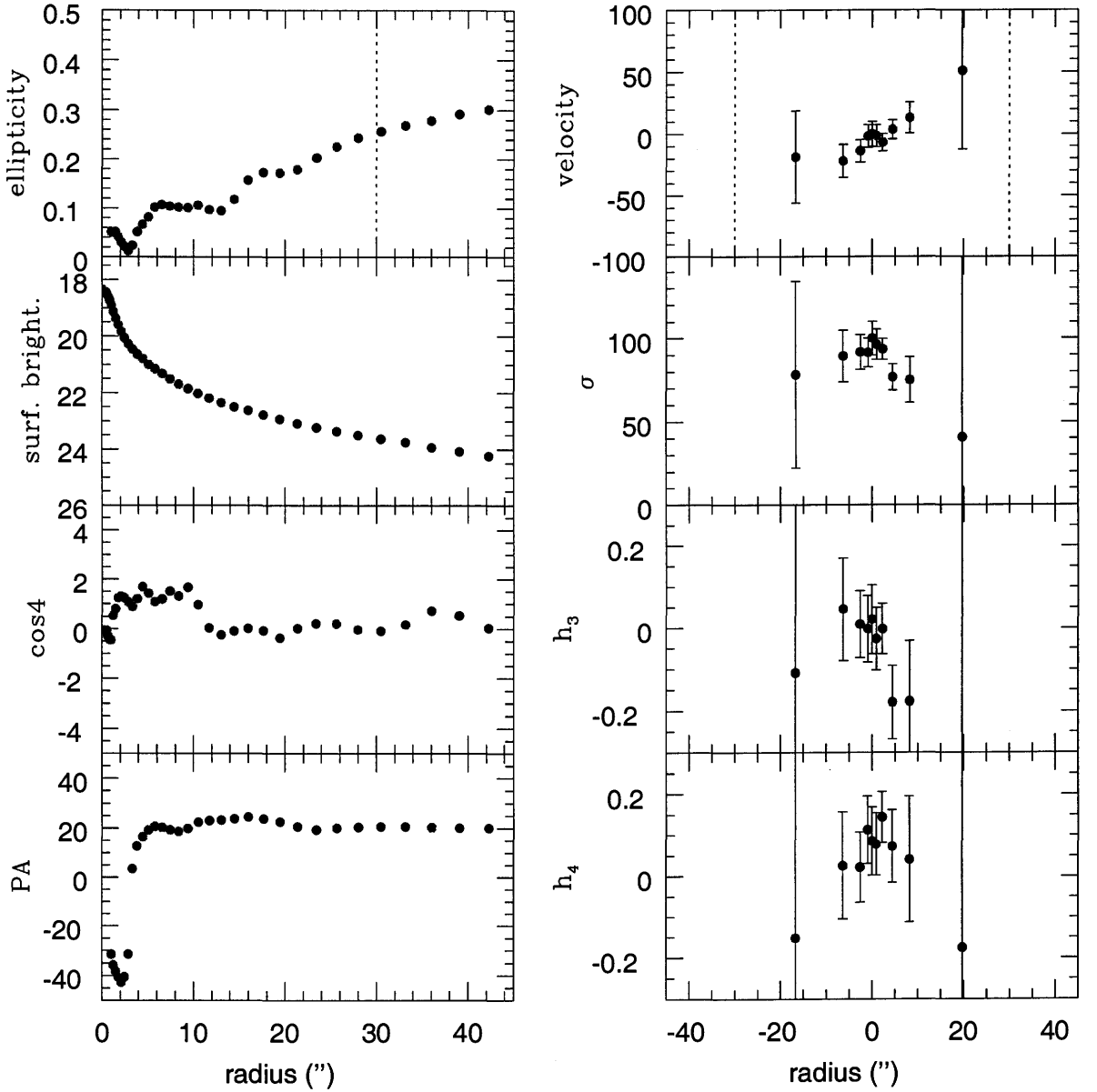


Figure 8: Left: Photometric profiles of NGC1336 in the B-band (taken from Caon et al. 1994). From top to bottom: ellipticity, surface brightness (in mag/sq.arcsec.), cos4 parameter, position angle. Right: stellar kinematics of NGC1336. From top to bottom: velocity, velocity dispersion, h_3 and h_4 parameters.

REFERENCES

- Bicknell, G.V., Carter, D., Killeen, N.E.B. & Bruce, T.E.G.: 1989, *ApJ*, 336, 639
- Binney, J.J. & Merrifield, M.R.: 1998, *Galactic Astronomy*, Princeton University Press (BM98)
- Bridges, T., Beasley, M., Faifer, F., Forbes, D., Forte, J., Gebhardt, K., Hanes, D., Sharples, R. & Zepf, S.: 2003, in press, in "Joint Discussion 6: Extragalactic Globular Clusters and their Host Galaxies", IAU General Assembly, July 2003. T. Bridges and D. Forbes (eds.), preprint

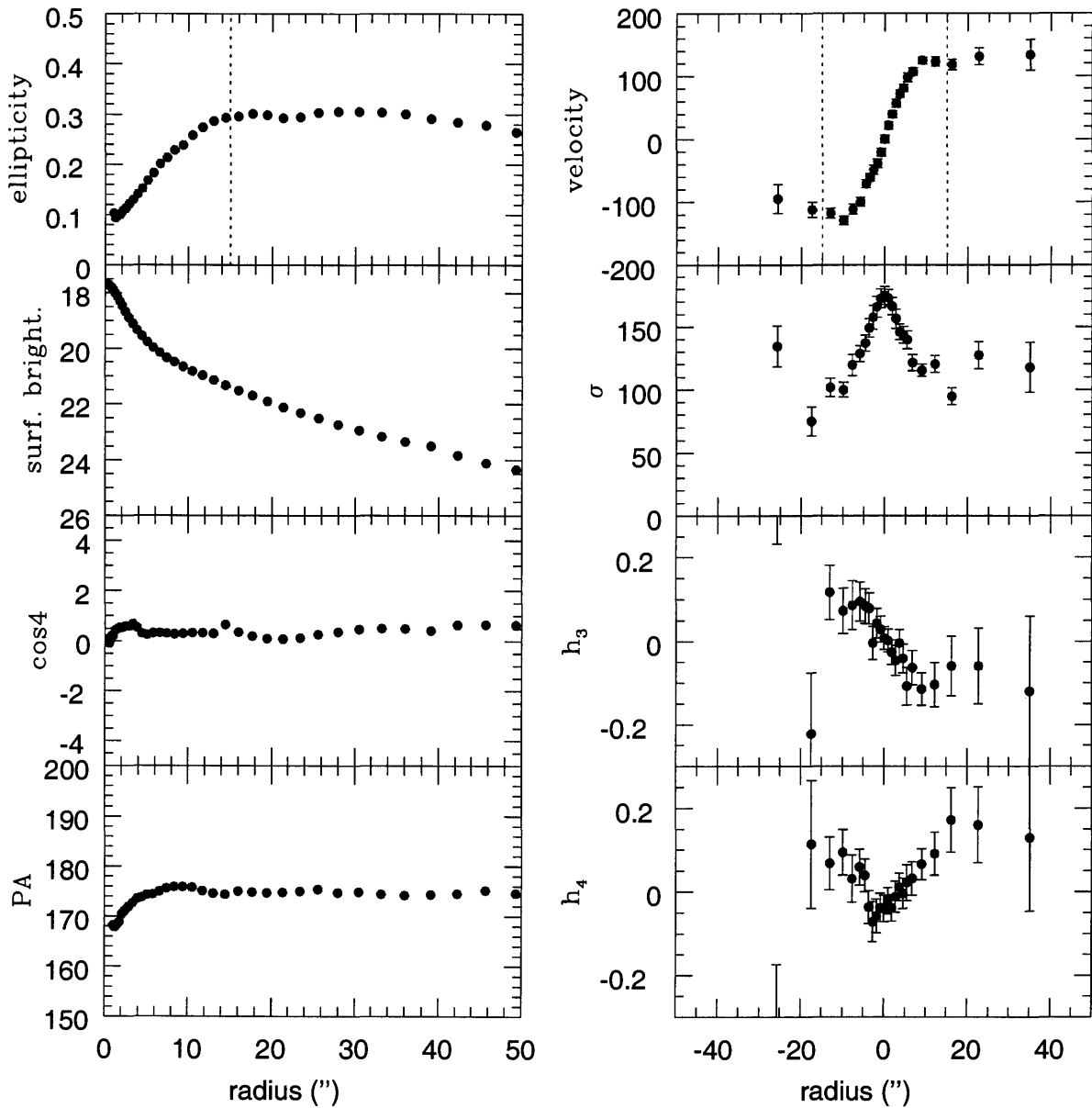


Figure 9: Left: Photometric profiles of NGC1339 in the B-band (taken from Caon et al. 1994). From top to bottom: ellipticity, surface brightness (in mag/sq.arcsec.), $\cos 4$ parameter, position angle. Right: stellar kinematics of NGC1339. From top to bottom: velocity, velocity dispersion, h_3 and h_4 parameters. Dashed line indicates one effective radius.

astro-ph/0310324

Caon, N., Capaccioli, M. & D'Onofrio, M.: 1994, A& ASS, 106, 199

Capaccioli, M., Held, E.V., Lorenz, H. & Vietri, M.: 1990, AJ, 99, 1813

Cappellari, M., Verolme, E.K., van der Marel, R.P., Verdoes Kleijn, G.A., Illingworth, G.D., Franx, M., Carollo, C.M. & de Zeeuw, P.T.: 2002, ApJ, 578, 787

Carollo, C.M., de Zeeuw, P.T., van der Marel, R.P., Danziger, I.J., & Qian, E.E.: 1995, ApJ, 441,

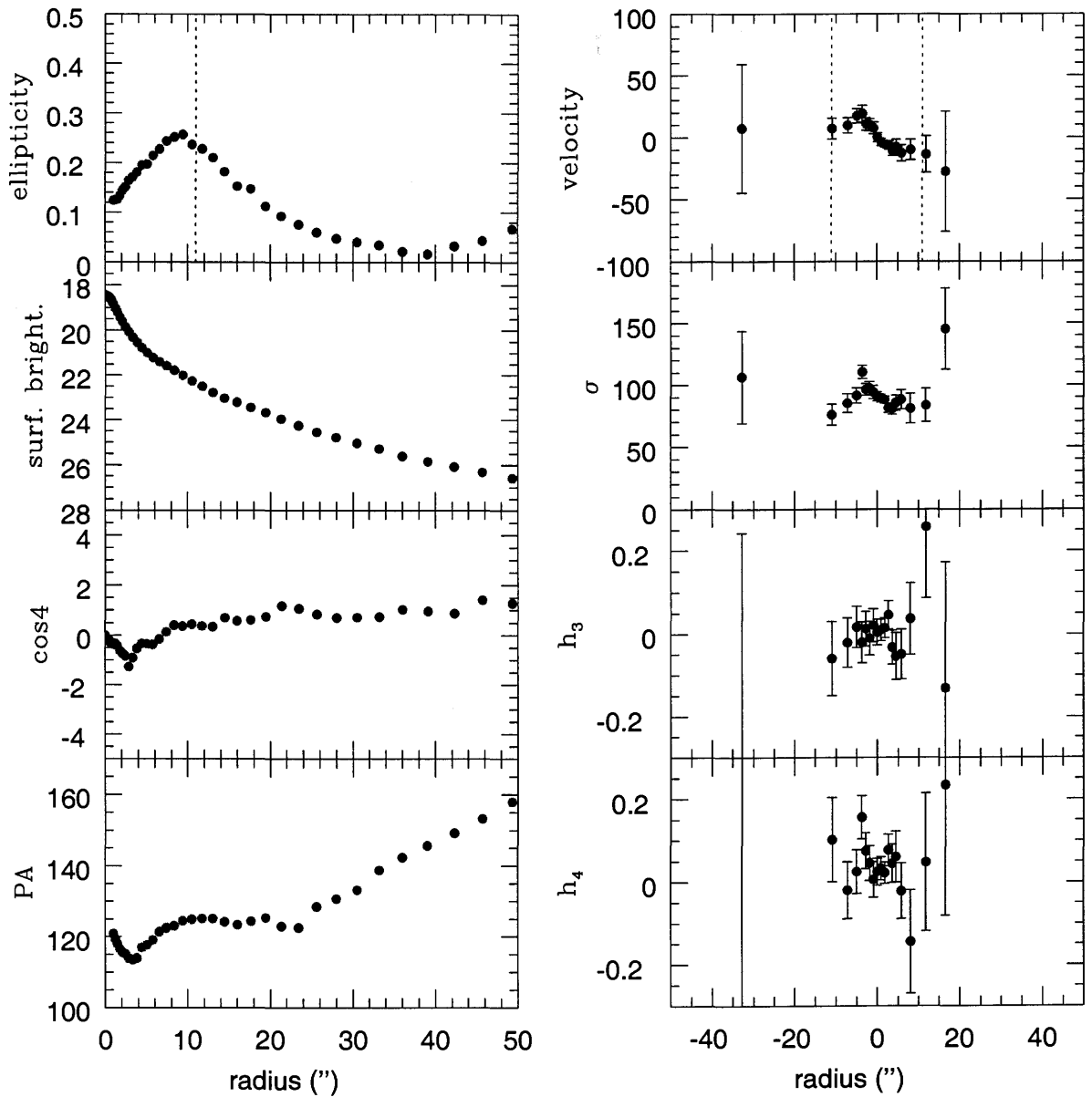


Figure 10: Left: Photometric profiles of NGC1373 in the B-band (taken from Caon et al. 1994). From top to bottom: ellipticity, surface brightness (in mag/sq.arcsec.), cos4 parameter, position angle. Right: stellar kinematics of NGC1373. From top to bottom: velocity, velocity dispersion, h_3 and h_4 parameters. Dashed line indicates one effective radius.

L25

Carollo, C.M., & Danziger, I.J.: 1994a, MNRAS, 270, 523

Carollo, C.M., & Danziger, I.J.: 1994b, MNRAS, 270, 743

Carollo, C.M., Danziger, I.J. & Buson, L.: 1993, MNRAS, 265, 553

Danziger I.J.: 1997, *Dark and Visible Matter in Galaxies*, ASP Conference Series, Vol. 117, Massimo Persic & Paolo Salucci (eds.), 28

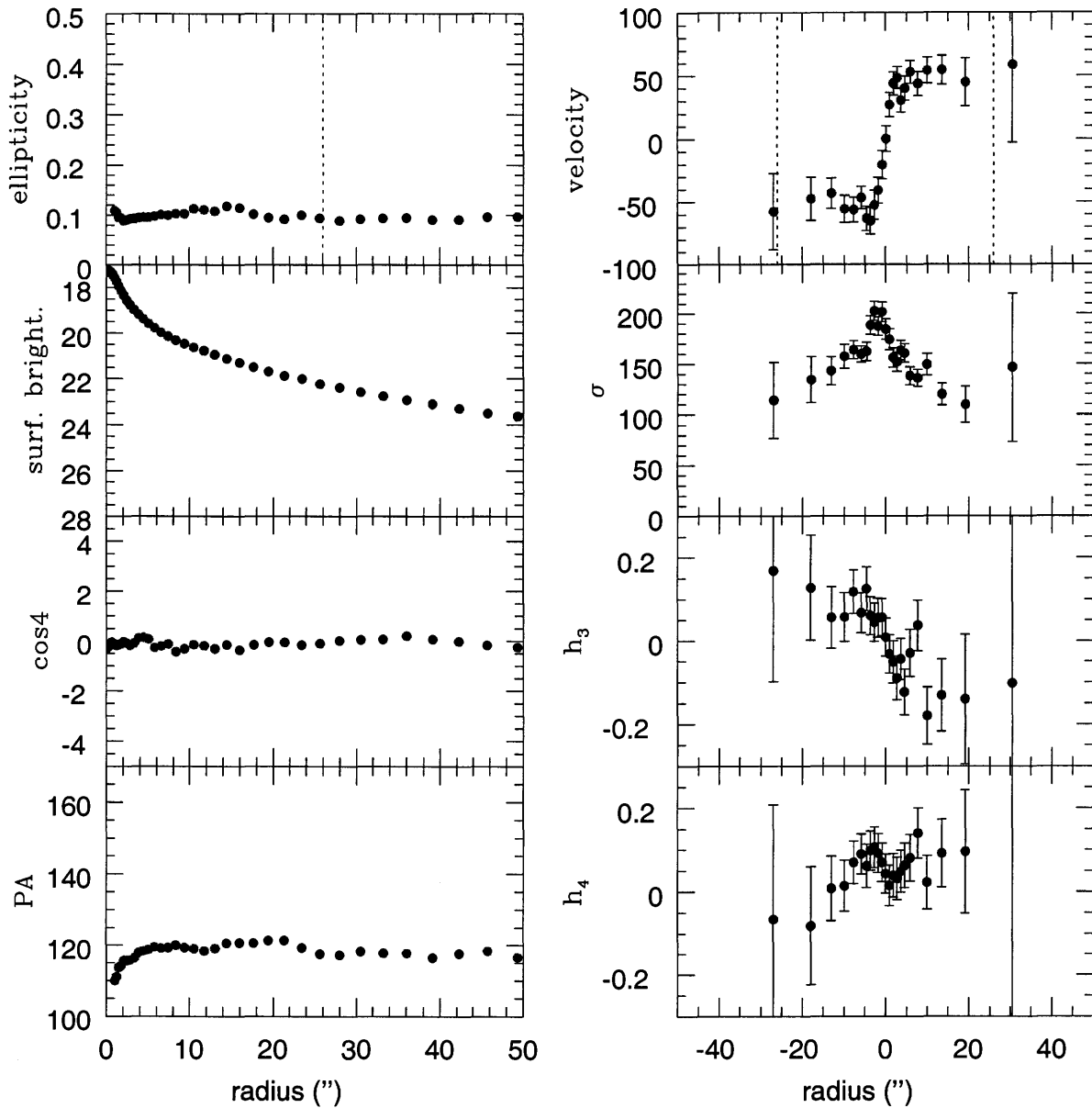


Figure 11: Left: Photometric profiles of NGC1374 in the B-band (taken from Caon et al. 1994). From top to bottom: ellipticity, surface brightness (in mag/sq.arcsec.), cos4 parameter, position angle. Right: stellar kinematics of NGC1374. From top to bottom: velocity, velocity dispersion, h_3 and h_4 parameters. Dashed line indicates one effective radius.

- Fabbiano, G., Elvis, M., Markoff, S., Siemiginowska, A., Pellegrini, S., Zezas, A., Nicastro, F., Trinchieri, G. & McDowell, J.: 2003, *ApJ*, 588, 175
- Fasano, G. & Bonoli, C. : 1989, *A&ASS*, 79, 291
- Fisher, D.: 1997, *AJ*, 113, 950
- Forbes, D.A., Reizel, D.B. & Williger, G.M.: 1995, *AJ*, 109, 1576
- Franx, M. & Illingworth, G.D.: 1988, *ApJ*, 324, L55

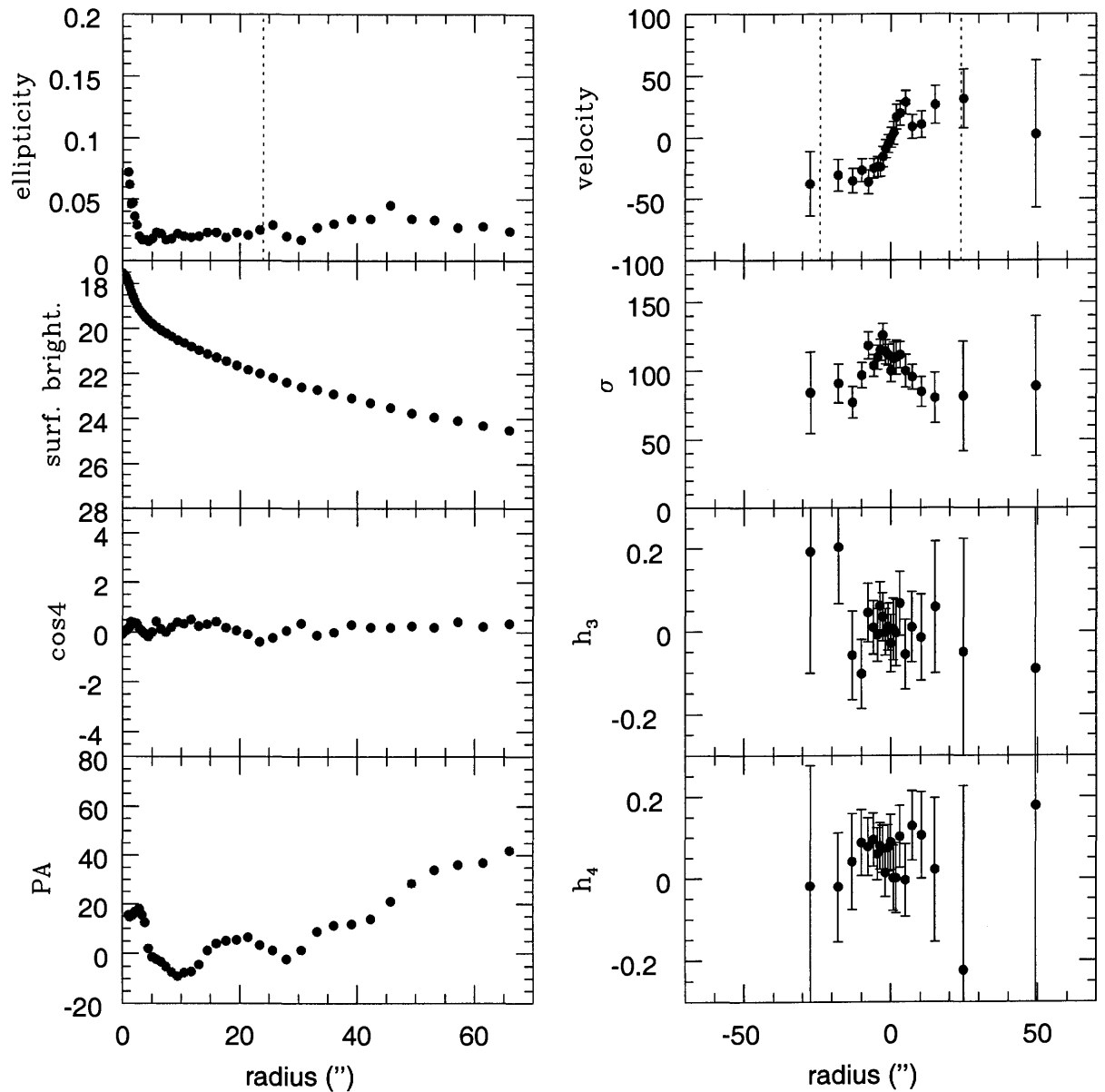


Figure 12: Left: Photometric profiles of NGC1379 in the B-band (taken from Caon et al. 1994). From top to bottom: ellipticity, surface brightness (in mag/sq.arcsec.), $\cos 4$ parameter, position angle. Right: stellar kinematics of NGC1379. From top to bottom: velocity, velocity dispersion, h_3 and h_4 parameters. Dashed line indicates one effective radius.

Gerhard, O.: 1993, MNRAS, 265, 213

Graham, A.W, Colless, M.M, Busarello, G., Zaggia, Z. & Longo, G.: 1998, A& ASS, 133, 325.

Gregg, M.D, Ferguson, H.C., Minniti, D., Tanvir, N. & Catchpole, R.: 2003, AJ, in press, preprint astro-ph/0312158

Jarvis, B.: 1987, AJ, 94, 30 (J87)

Kronawitter, A., Saglia, R.P., Gerhard, O. & a Bender, R.: 2000, A& ASS, 144, 53

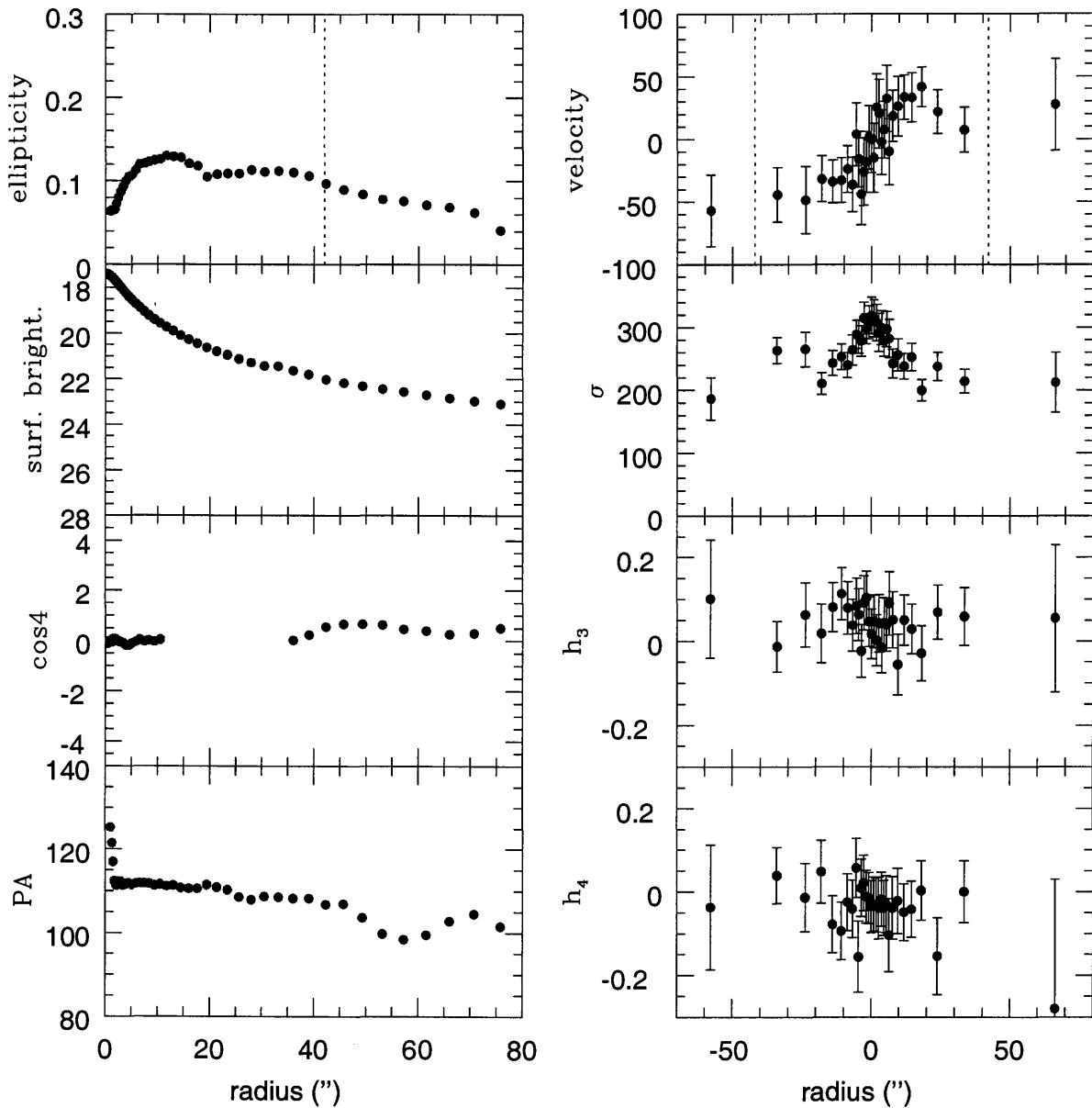


Figure 13: Left: Photometric profiles of NGC1399 in the B-band (taken from Caon et al. 1994). From top to bottom: ellipticity, surface brightness (in mag/sq.arcsec.), $\cos 4$ parameter (note lack of data between 10'' and 35''), position angle. Right: stellar kinematics of NGC1399. From top to bottom: velocity, velocity dispersion, h_3 and h_4 parameters. Dashed line indicates one effective radius.

- Rix, H.-W., de Zeeuw, P.T., Cretton, N., van der Marel, R.P. & Carollo, C.M.: 1997, *ApJ*, 488, 702
 Sargent, W.L.W., Schechter, P.L., Boksenberg, A. & Shortridge, K. : 1977, *AJ*, 212, 326
 Simkin, S.M.: 1974, *A&A*, 31, 129
 Slee, O. B., Sadler, E. M., Reynolds, J. E. & Ekers, R. D.: 1994, *MNRAS*, 269, 928
 Sparks, W. B., Hough, J. H., Axon, D. J., & Bailey, J.: 1986, *MNRAS*, 218, 429
 Statler, T.S.: 1995, *AJ*, 109, 1371

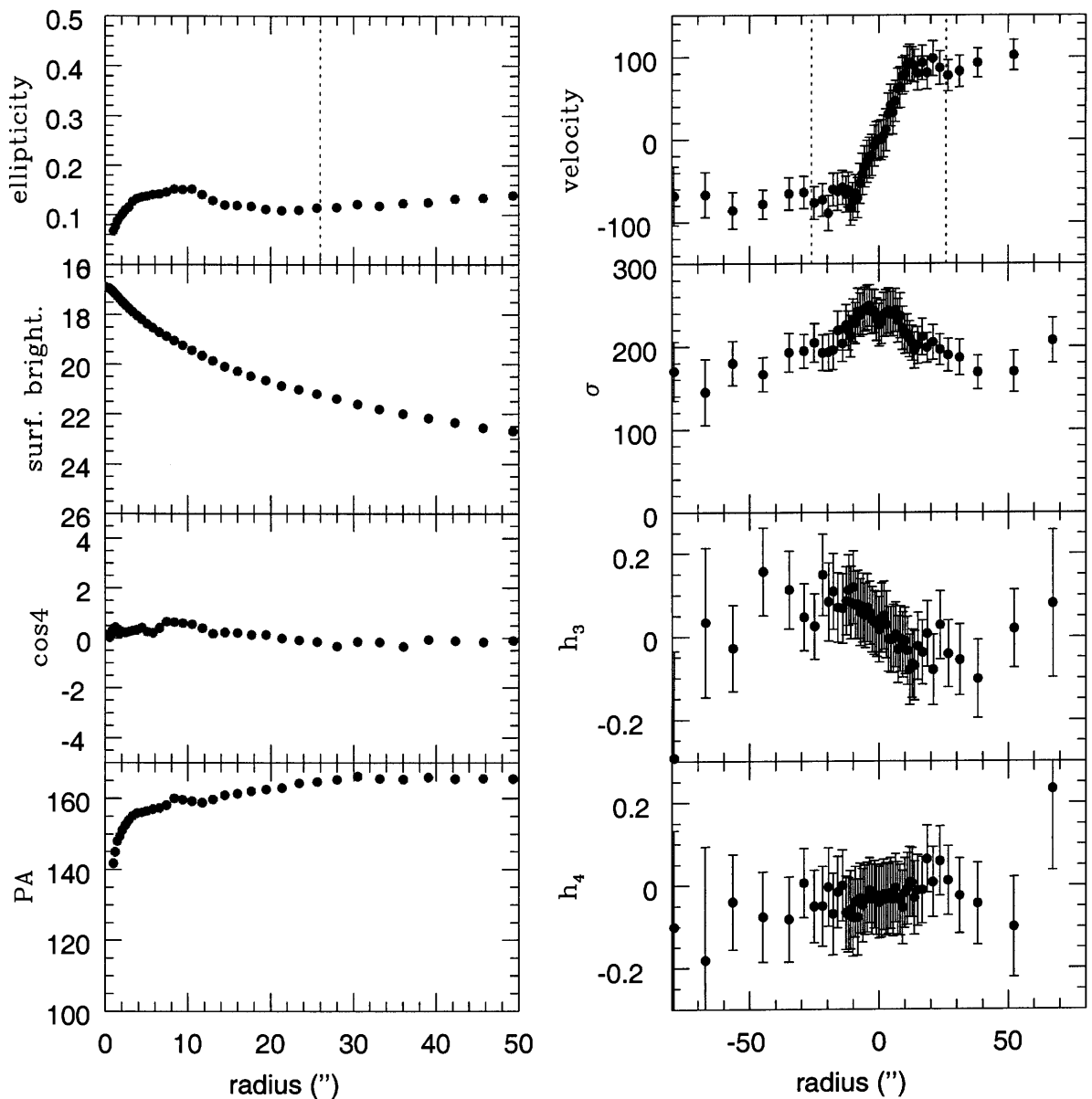


Figure 14: Left: Photometric profiles of NGC1404 in the B-band (taken from Caon et al. 1994). From top to bottom: ellipticity, surface brightness (in mag/sq.arcsec.), cos4 parameter, position angle. Right: stellar kinematics of NGC1404. From top to bottom: velocity, velocity dispersion, h_3 and h_4 parameters. Dashed line indicates one effective radius.

Statler, T., & Smecker-Hane, T.: 1999, ApJ, 117, 839

Tonry, J. & Davis, M. : 1979 : AJ, 84, 1511

van der Marel, R.P., & Franx, M.: 1993, ApJ, 407, 525

Verdoes Kleijn, G. A., van der Marel, R. P., Carollo, C. M., & de Zeeuw, P. T.: 2000, AJ, 120, 1221

Williams, T.B. & Schwarzschild, M.: 1979, ApJ, 227, 56

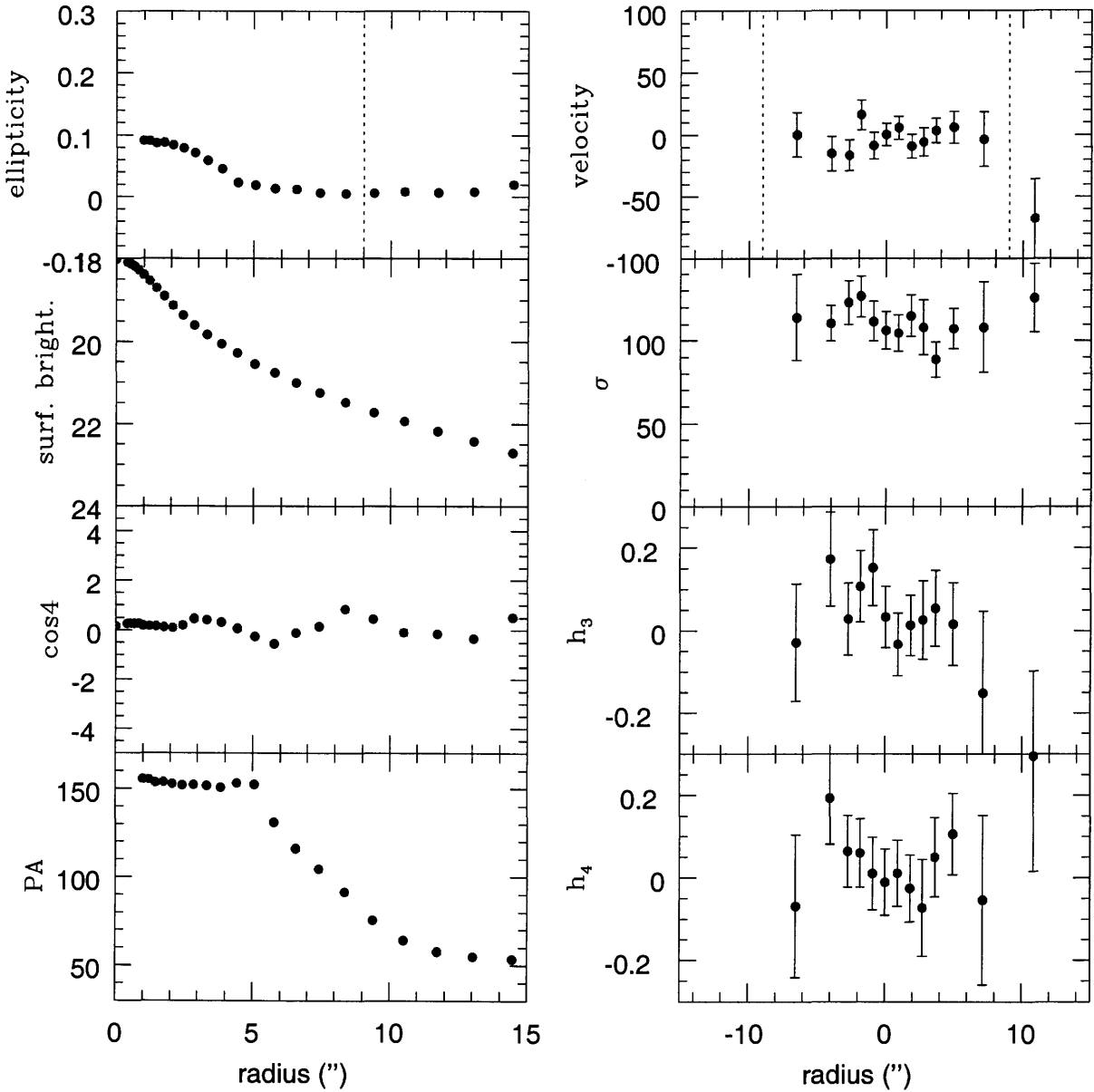


Figure 15: Left: Photometric profiles of NGC1419 in the B-band (taken from Caon et al. 1994). From top to bottom: ellipticity, surface brightness (in mag/sq.arcsec.), cos4 parameter, position angle. Right: stellar kinematics of NGC1419. From top to bottom: velocity, velocity dispersion, h_3 and h_4 parameters. Dashed line indicates one effective radius.

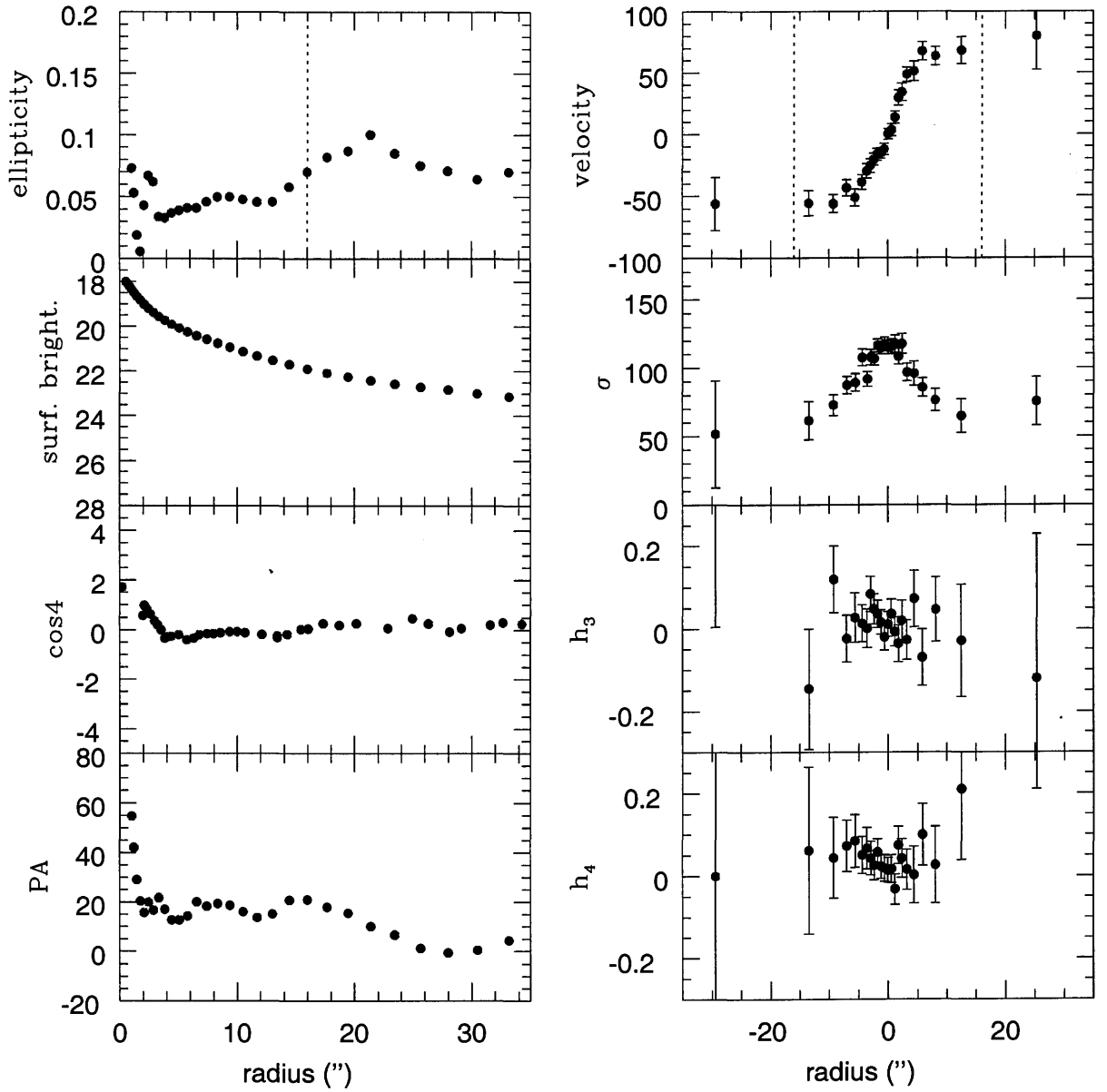


Figure 16: Left: Photometric profiles of NGC4339 in the B-band (taken from Caon et al. 1994). From top to bottom: ellipticity, surface brightness (in mag/sq.arcsec.), cos4 parameter, position angle. Right: stellar kinematics of NGC4339. From top to bottom: velocity, velocity dispersion, h_3 and h_4 parameters. Dashed line indicates one effective radius.

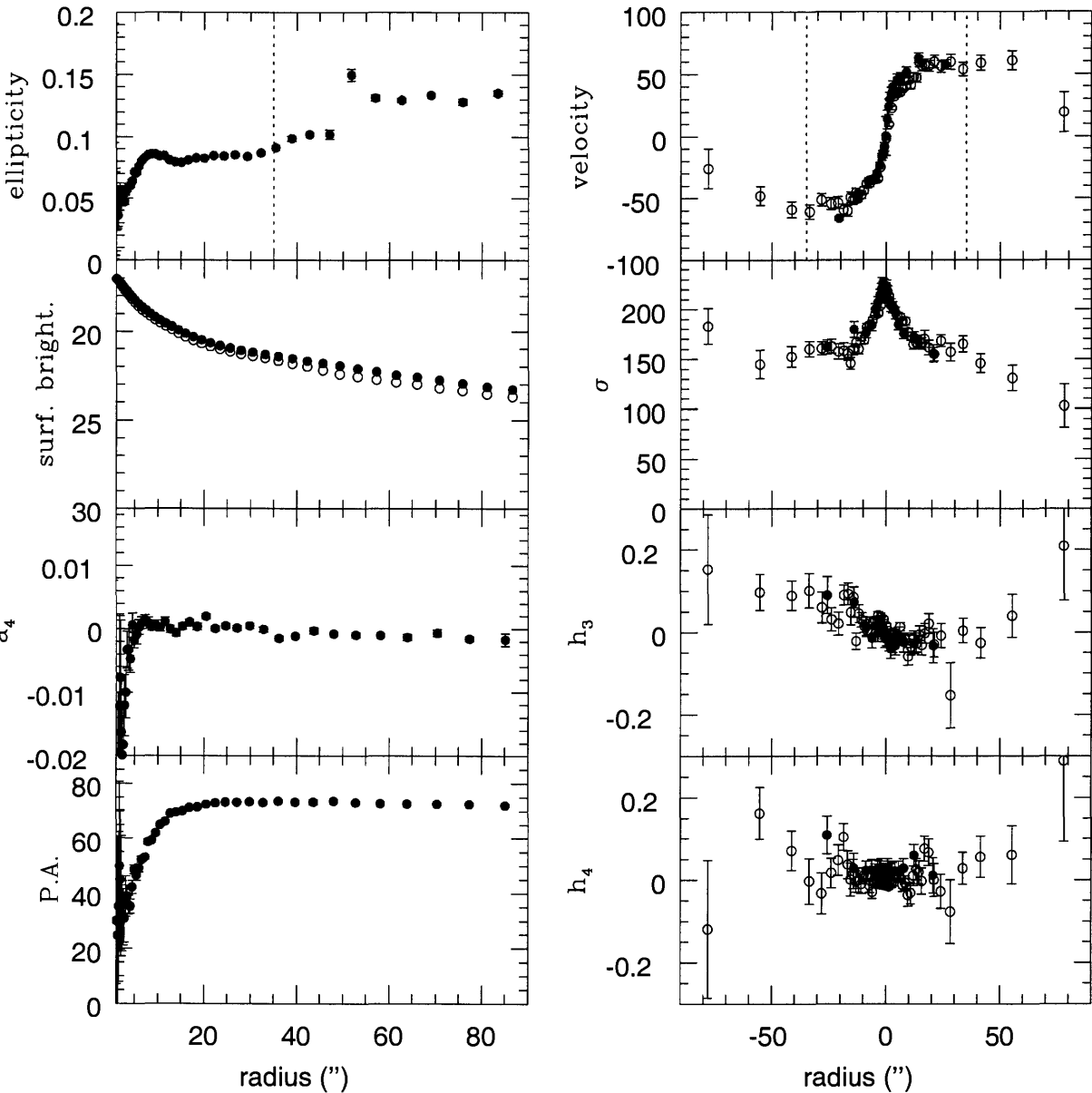


Figure 17: Left: Photometric profiles of NGC3379 in the B-band. From top to bottom: ellipticity, surface brightness from Capaccioli et al. (1990) (in mag/sq.arcsec.) for major (black circles) and minor (open circles) axis, $\cos 4$ parameter, position angle. Right: Comparison of stellar kinematics of my extraction (black circles) and Statler & Smecker-Hane (1999). From top to bottom: velocity, velocity dispersion, h_3 and h_4 parameters. Dashed line indicates one effective radius.

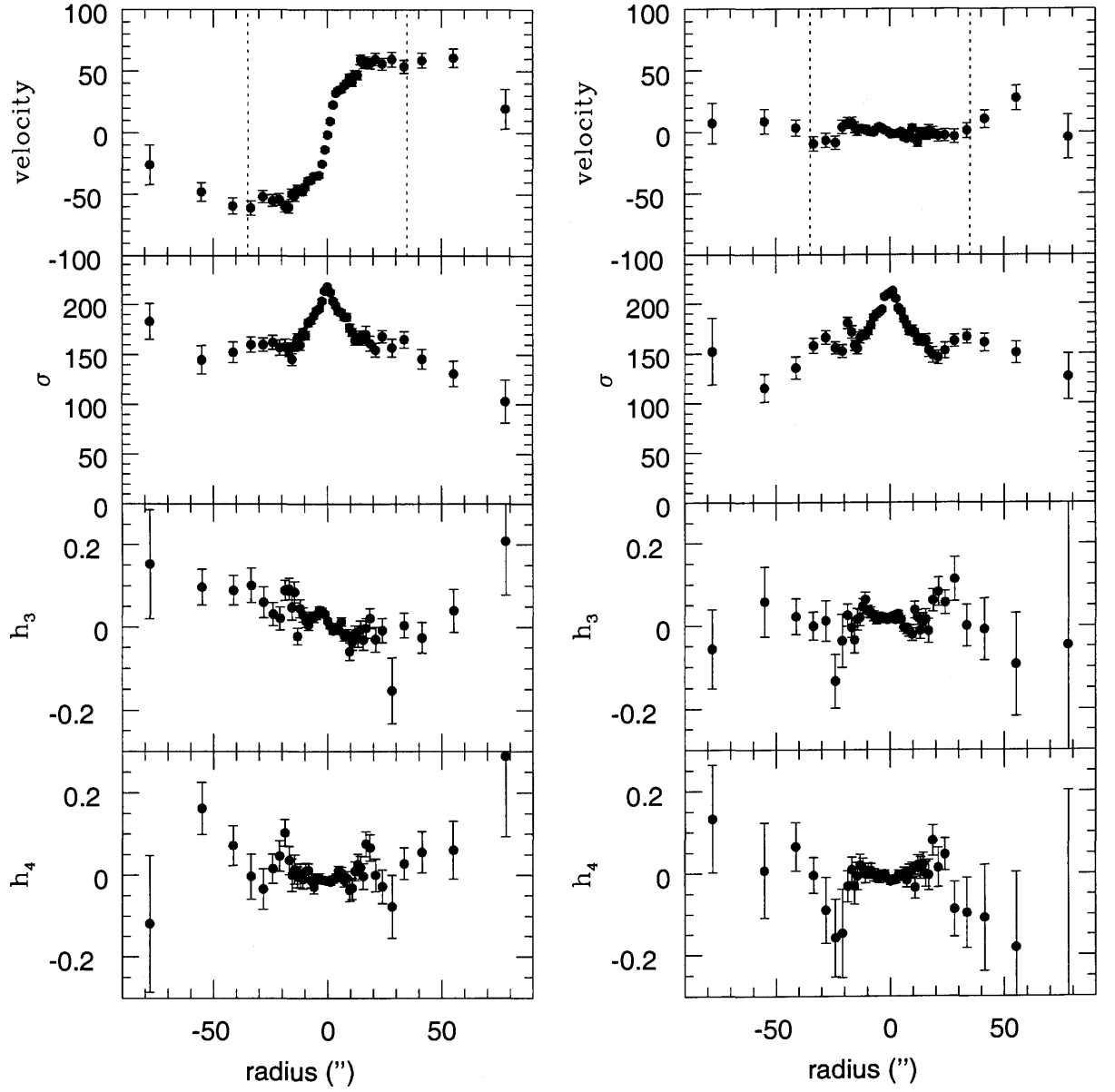


Figure 18: Stellar kinematics of NGC3379 (taken from Statler & Smecker-Hane (1999)) for major (left) and minor (right) axis. From top to bottom: velocity, velocity dispersion, h_3 and h_4 parameters. Dashed line indicates one effective radius.

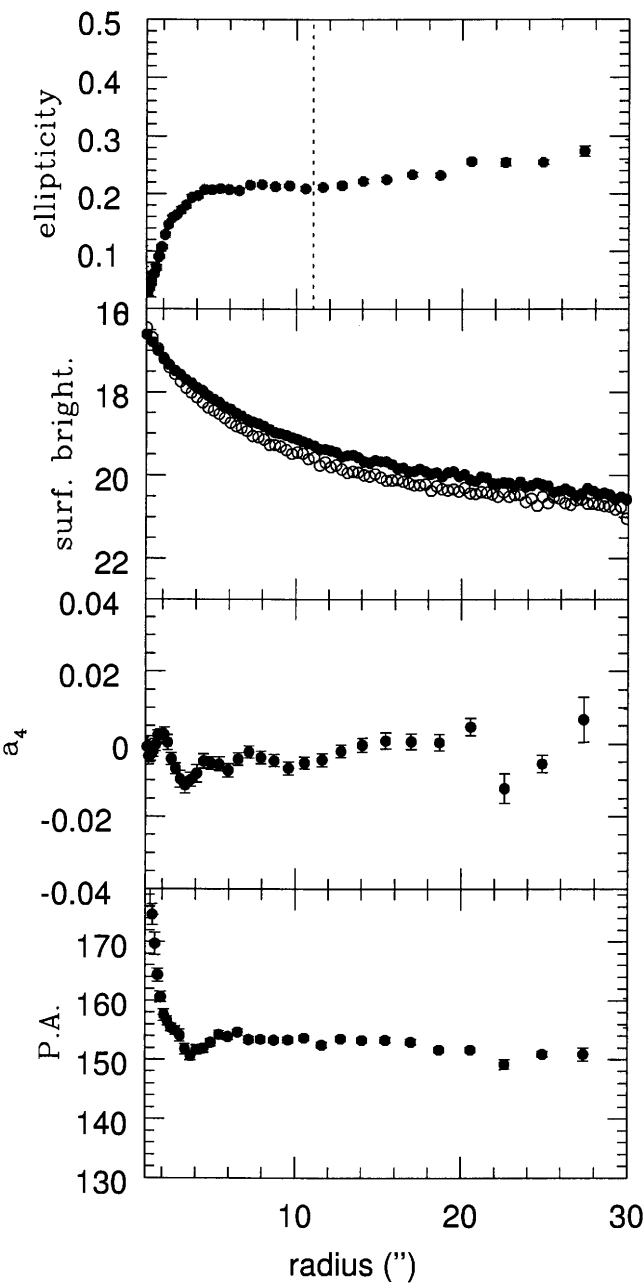


Figure 19: Photometric profiles of NGC4105 in the R-band. From top to bottom: ellipticity, surface brightness (in mag/sq.arcsec.), \cos^4 parameter, position angle.

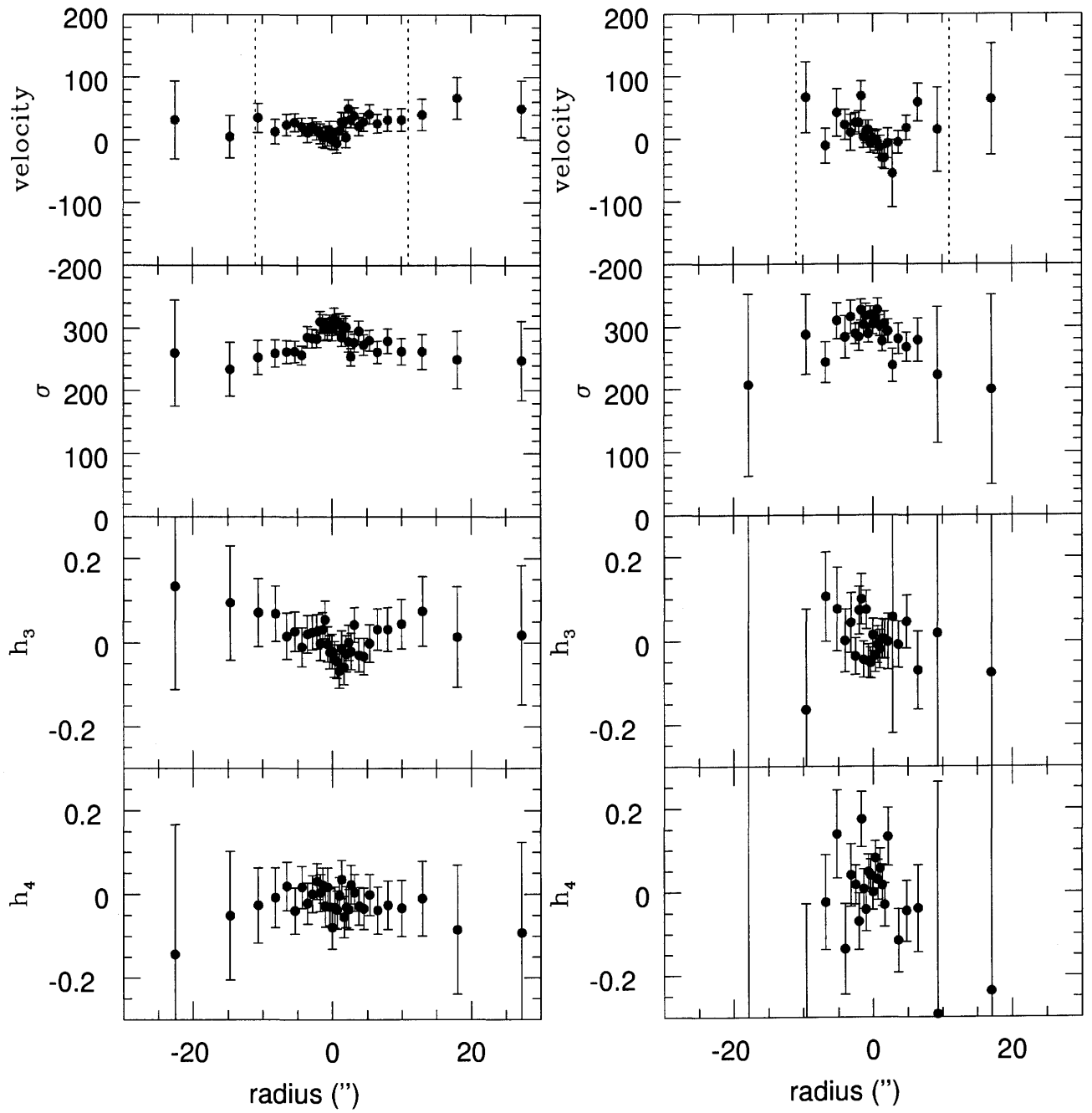


Figure 20: Stellar kinematics of NGC4105 for major (left) and minor (right) axis. From top to bottom: velocity, velocity dispersion, h_3 and h_4 parameters. Dashed line indicates one effective radius.

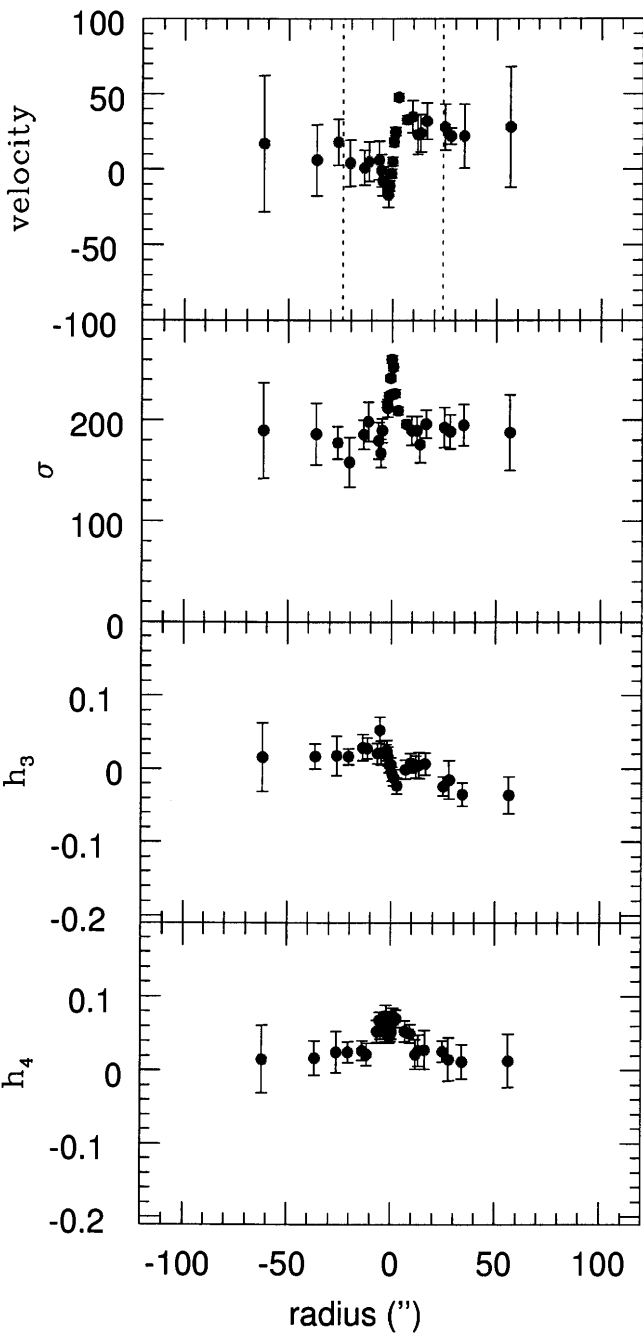


Figure 21: Stellar kinematics of NGC2434 for major axis. From top to bottom: velocity, velocity dispersion, h_3 and h_4 parameters. Dashed line indicates one effective radius. Data taken from Carollo et al. (1995).

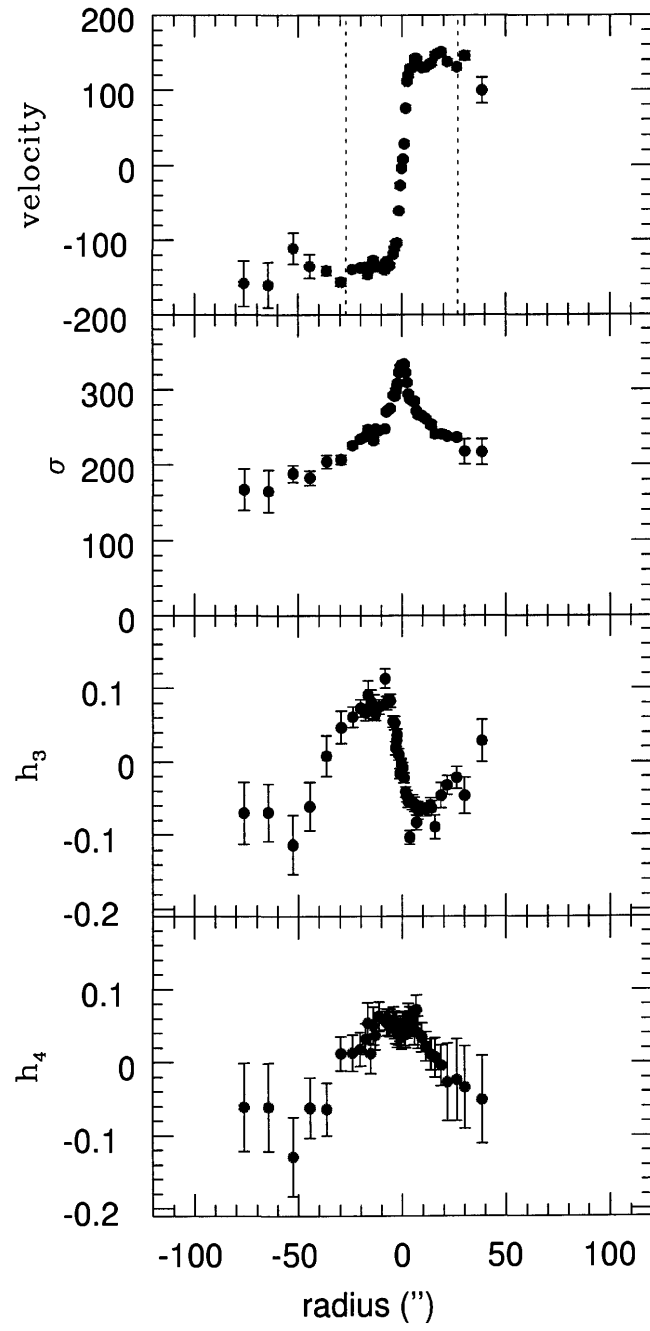


Figure 22: Stellar kinematics of NGC3706 for major axis. From top to bottom: velocity, velocity dispersion, h_3 and h_4 parameters. Dashed line indicates one effective radius. Data taken from Carollo et al. (1995).

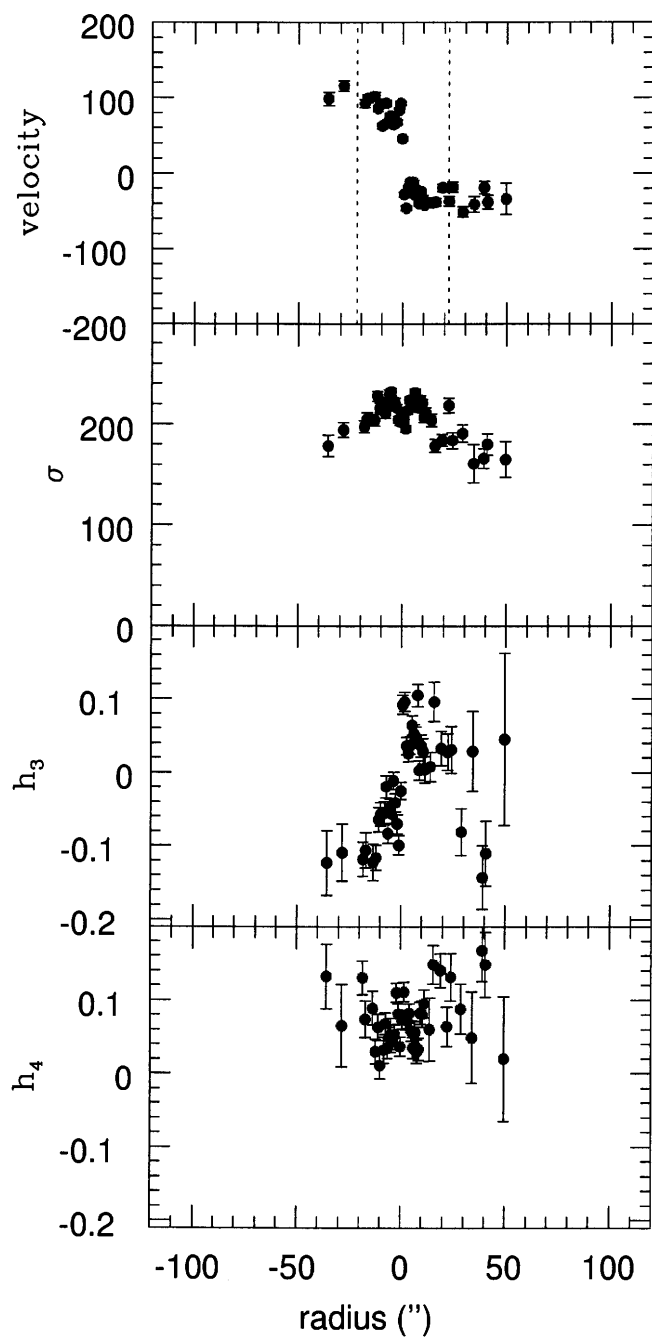


Figure 23: Stellar kinematics of NGC5018 for major axis. From top to bottom: velocity, velocity dispersion, h_3 and h_4 parameters. Dashed line indicates one effective radius. Data taken from Carollo et al. (1995).

2

DYNAMICAL MODELING OF EARLY-TYPE GALAXIES: TWO- AND THREE-INTEGRAL APPROACHES

2.1 TWO-INTEGRAL MODELING

2.1.1 THEORETICAL INTRODUCTION

For the two-integral (2I) modeling procedures I used the modeling technique developed by Binney, Davies & Illingworth (1990, hereafter BDI), and subsequently used by van der Marel, Binney & Davies (1990) and Cinzano & van der Marel (1994). Only in Cinzano & van der Marel (1994) does the modeling include h_3 and h_4 parameters. Statler, Dejonghe & Smecker-Hane (1999) used the modified version of this method to analyze mass distribution in NGC1700. Here I briefly present the assumptions and the modeling steps.

Two-integral modeling is the first step in understanding of the dynamics of the elliptical galaxies, because in cases of small departures from triaxiality (which is far more probable, and true in case of IC3370 as has been shown previously), comparison of real systems with the models can provide useful insights. The assumptions of axisymmetry and the fact that the velocity dispersion tensor is everywhere isotropic are the starting points for the procedure that includes the following three steps (cf. BDI): (i) inversion of the luminosity profiles and obtaining three-dimensional luminosity density that provides the mass density (under the assumption of constant mass-to-light ratio); (ii) evaluation of the potential and derivation of the velocity dispersion and azimuthal streaming (under the assumptions that the form of the distribution function is $f(E, L_z)$, where E is the energy and L_z is the angular momentum of the individual star about the symmetry axis of the galaxy and that the velocity dispersion is isotropic) and (iii) comparison of the projected kinematical quantities from the model with the observed kinematic parameters; optionally, a disk, and/or a dark halo can be included in the modeling procedure (see Fig. 1).

The first step in the modeling procedure involves making a least-squares fit for a flattened Jaffe model (Jaffe 1983, Eqs. (2) and (3)) or a flattened modified Hubble model. The brightness distribution in the case of the modified Hubble profile is given as (see Binney & Tremaine 1987, Eq. (2-39)):

$$I(R) = \frac{2j_0a}{1 + (R/a)^2},$$

(where j_0 is the central luminosity density and a is the core radius), and was used in the 2I modeling procedures of the galaxies for which I have sufficient data: photometry, and major and minor axis

long-slit spectra. Because I was mainly interested in the outer parts of galaxies I did not correct for the effects of seeing that are of importance near the centres of galaxies. Six Lucy iterations were used to get a fit of the surface brightness profile to the model. In cases when the disk was taken into account, the surface brightness of the disk was subtracted assuming that the disk is exponential.

For the evaluation of the dynamical quantities one assumes that the spheroid's mass density $\rho(R, z) = \Upsilon_s j(R, z)$ where Υ_s is some constant mass-to-light ratio, and $j(R, z)$ is a luminosity density along the line of sight. Here, it would be appropriate to present an estimate of the typical mass-to-light ratio in elliptical galaxies. van der Marel (1991) found in his sample of 37 bright ellipticals that the average mass-to-light ratio in the B-band is: $M/L_B = (5.95 \pm 0.25)h_{50}$. He also found that the mass-to-light ratio is correlated with the total luminosity: $M/L_B = 3.84h_{50}(L_B/L_{*,B})^{0.35}$, where $L_{*,B} \equiv 3.3 \times 10^{10}h_{50}^{-2}L_{\odot}$.

The gravitational potential Φ_s generated by the spheroid is :

$$\Phi_s(R, z) = \sum_{l=0}^5 \tilde{\Phi}_l(R) P_{2l} \left(\frac{z}{\sqrt{R^2 + z^2}} \right), \quad (1)$$

where P_k is the Legendre polynomial of order k . Six-point Gaussian evaluation is used to solve the integrals on a logarithmic grid of r values (r, z, θ are the usual cylindrical coordinates):

$$\tilde{\rho}_l(r) = \int_0^1 \rho(r \sin \theta, r \cos \theta) P_{2l}(\cos \theta) d(\cos \theta) \quad (2)$$

and direct evaluation of the integrals for these r values:

$$\tilde{\Phi}_l(r) = -4\pi G \left[\frac{1}{r^{2l+1}} \int_0^r \rho_l(s) s^{2l+2} ds + r^{2l} \int_0^\infty \rho_l(s) \frac{ds}{s^{2l-1}} \right] \quad (3)$$

and a linear interpolation of $\tilde{\Phi}_l$ versus $\log r$.

If one includes the disk, it is assumed that its mass-to-light ratio is Υ_d . The disk potential (cf. BDI and references therein) is given as:

$$\Phi_d = -\frac{2\pi G \Upsilon_d I_d(0)}{R_d} \int_0^\infty \frac{J_0(kR) e^{-kz}}{(R_d^{-2} + k^2)^{3/2}} dk. \quad (4)$$

For $z = 0$ this integral can be evaluated analytically. For $z \neq 0$, $R \neq 0$ this integral must be evaluated numerically.

When one has the potential $\Phi = \Phi_s + \Phi_d$ and the luminosity density j , the velocity dispersion σ in the meridional directions, under the assumptions of the distribution function of the form $f(E, L_z)$ is given by Satoh formula:

$$\sigma^2(R, z) = \frac{1}{j(R, z)} \int_z^\infty j d\Phi \quad (5)$$

where the integral is along a line of constant R . The mean-square azimuthal speed $\overline{v_\phi^2}$ is given as:

$$\overline{v_\phi^2} = \sigma^2 + R \frac{\partial \Phi}{\partial R} + \frac{R}{j} \frac{\partial (j \sigma^2)}{\partial R}. \quad (6)$$

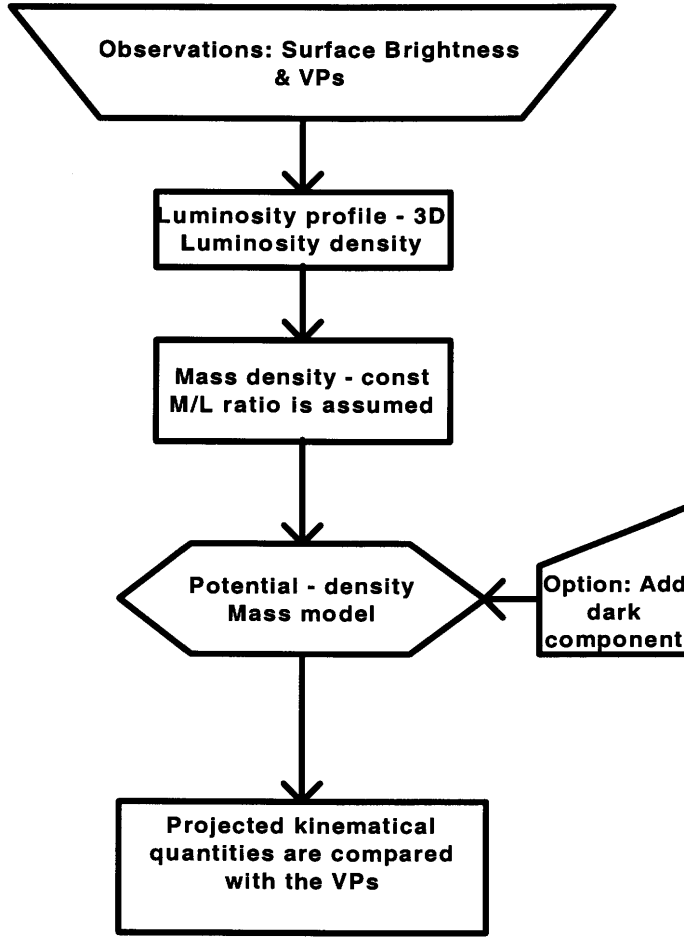


Figure 1: Flowchart of two-integral modeling procedure. VP stands for velocity profile.

Since I assume, for the moment, in this subsection, that the distribution function is of the form $f(E, L_z)$ the second radial velocity moment, $\overline{v_R^2} \equiv \sigma_R^2$, and the second vertical velocity moment, $\overline{v_z^2} \equiv \sigma_z^2$ are everywhere equal and $\overline{v_R v_z} = 0$. The Jeans equations are:

$$\frac{\partial \rho \overline{v_z^2}}{\partial z} + \rho \frac{\partial \Phi}{\partial z} = 0 \quad (7)$$

$$\frac{\partial \rho \overline{v_R^2}}{\partial R} + \rho \frac{\partial \Phi}{\partial R} + \frac{\rho}{R} [\overline{v_R^2} - \overline{v_\phi^2}] = 0. \quad (8)$$

I solve them searching for unknowns $\overline{v_\phi^2}$ and $\sigma_R^2 = \sigma_z^2$. Using a free parameter, k , one can, as usual, assign a part of the second azimuthal velocity moment $\overline{v_\phi^2}$ to streaming:

$$\overline{v_\phi} = k \sqrt{\overline{v_\phi^2} - \sigma_R^2}. \quad (9)$$

Then I project the dynamical quantities on to the sky to get predictions.

2.1.2 MODELING RESULTS

Using the two-integral axisymmetric modeling procedure I analyzed four galaxies for which I had sufficiently good major and minor axis stellar kinematics and photometry. I assume symmetry about the y-axis and therefore I folded all the observational data taking into account that velocity and h_3 are odd functions of the radius, and that velocity dispersion and h_4 are even functions of the radius. In all the following calculations a Hubble constant $H_0 = 70 \text{ km s}^{-1} \text{ Mpc}^{-1}$ has been assumed.

2.1.2.1 Sample 1

IC3370

As might be expected the axisymmetric modeling of IC3370 did not give a good fit to the observed data given the strong isophotal twisting present in this galaxy. I used the inclination angle of 50° that gave the best (but far from perfect) results. In Fig. 2 and Fig. 3 I present my modeling results for major, minor and intermediate axis.

Major axis (Fig. 2 (left)): For major axis $k = 0.6$ (dotted lines) can give a good fit in the inner regions ($\sim 25''$) for the velocity. A good fit is obtained in the outer regions ($> 50''$) for the velocity dispersion. On the contrary, $k = 1$ provides a good fit for the velocity in the outer region ($> 1R_e$); the velocity dispersion seems to be fitted well throughout the whole galaxy with $k = 1$. I experimented with the inclusion of the inner embedded disk of $6''$ (solid lines), but this does not change much the results – these lines overlap the dashed lines that are plotted for the case when the disk is not present. I made some tests with the inclusion of the dark matter halo. As in Carollo & Danziger (1994b) I added an isochrone Henon potential (with the core radius of 35 kpc): the results obtained with the dark matter are plotted as a dot-dashed line ($k = 1$ in this case). Note that up to $\sim 2R_e$ one cannot distinguish the velocity dispersion profile with the dark matter from the one without it. At $2R_e$ the model with the dark matter predicts a rapid increase of velocity dispersion, which is not observed in this galaxy. In fact, the decrease of the velocity dispersion follows almost perfectly the constant mass-to-light prediction (out to $\sim 3R_e$). Both h_3 and h_4 are fitted reasonably in all the given cases. The mass-to-light-ratio found in all the cases at $\sim 3R_e$ is ~ 5.4 .

Minor axis (Fig. 2 (right)): Because of the fact that the axisymmetric modeling predicts zero velocity for the minor axis, a successful fit could not be achieved (the same is true for the h_3 parameter). Modeling of the velocity dispersion therefore provided a possibility for several interesting tests. One can see that a $k = 0.6$ fit (dotted line, $M/L_B = 4.80$, no dark matter, no embedded disk) cannot produce a successful fit for the velocity dispersion. Therefore, in all other tests in the case of the minor axis I used $k = 1$. Two cases of $M/L_B = 6.59$, one with the embedded disk (solid line) and the other without (dashed line, but completely overlapped with the solid line) provided better, but a still unsatisfactory fit to the data. The same is valid when one adds the dark matter halo (in this case $M/L_B = 6.53$) (dot-dashed lines). Therefore, I increased the mass-to-light ratio to 9.68 (case without the dark matter and with the disk represented with the thick dashed line) to achieve a better agreement. Still better agreement is obtained when one increases further the mass-to-light ratio to 12.65: this is the case without the dark matter and the

included disk represented by the thick dot-dashed line. Note, however, the discrepancy in the inner parts of the galaxy.

Intermediate axis (Fig. 3): Several tests were done using lower values of the constant mass-to-light ratio. Successful fits are obtained for $k = 1$ (again the $k = 0.6$ case can be ruled out). All the models with $k = 1$ give a good fit in the inner parts of the galaxy ($\sim 20''$) and they all fail in the outer parts. In a similar manner they all reproduce well the velocity dispersion profile, except for the case when the dark matter halo is included (dot-dashed line) for which there is a non-existent peak (at $\sim 60''$). h_3 and h_4 parameters are fitted correctly throughout the whole galaxy (modeled h_3 shows departures in the outer region and h_4 shows small departures from the data in the inner part).

Strictly speaking IC3370 should not be modeled using the axisymmetric modeling technique. However, this technique permits the following tentative conclusion. In IC3370 up to $\sim 3R_e$ the dark matter halo is not needed for the successful modeling: the mass-to-light ratio varies between ~ 5 (based upon the major axis data) and ~ 13 (based upon the minor axis data). Note however, that $M/L_B \sim 13$ is the upper limit, because it must be stressed that this kind of modeling of the observed minor axis dispersions tends to *overestimate* the mass-to-light ratio (as given in BDI): this modeling, for a given M/L_B underestimates the minor axis dispersions since the model will be flattened by enhanced $\overline{v_\phi^2}$ which does not contribute to the minor axis profile. The real galaxy is flattened by enhanced $\overline{v_r^2}$ which contributes on the minor axis.

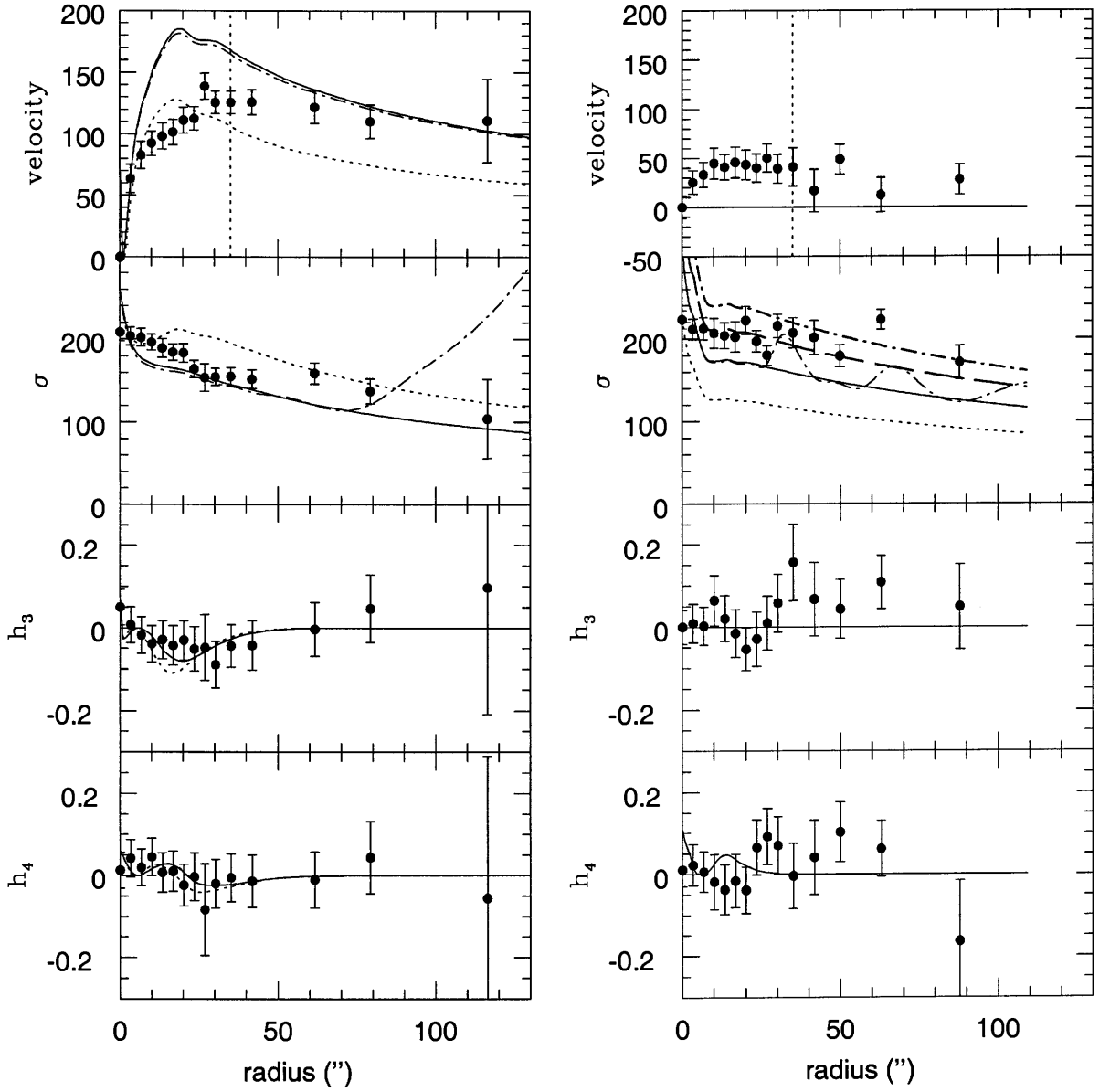


Figure 2: Predictions of the two-integral models for IC3370. Left: major axis predictions. Dotted lines: $k = 0.6$, $M/L_B = 5.42$, no dark matter included, no embedded disk. Dashed lines: $k = 1$, $M/L_B = 5.42$, no dark matter included, no embedded disk (overlapped with solid line). Solid lines: $k = 1$, $M/L_B = 5.28$, no dark matter included, embedded disk included. Dot-dashed lines: $k = 1$, $M/L_B = 5.42$, dark matter included, embedded disk included. Right: minor axis predictions. Dotted line: $k = 0.6$, $M/L_B = 4.80$, no dark matter included, no embedded disk. Dashed line: $k = 1$, $M/L_B = 6.59$, no dark matter included, no embedded disk (overlapped with the solid line). Solid line: $k = 1$, $M/L_B = 6.59$, no dark matter included, embedded disk included. Dot-dashed line: $k = 1$, $M/L_B = 6.53$, dark matter included, embedded disk included. Thick dashed line: $k = 1$, $M/L_B = 9.68$, no dark matter, embedded disk. Thick dot-dashed line: $k = 1$, $M/L_B = 12.64$, no dark matter, embedded disk. Vertical dotted line indicates one effective radius.

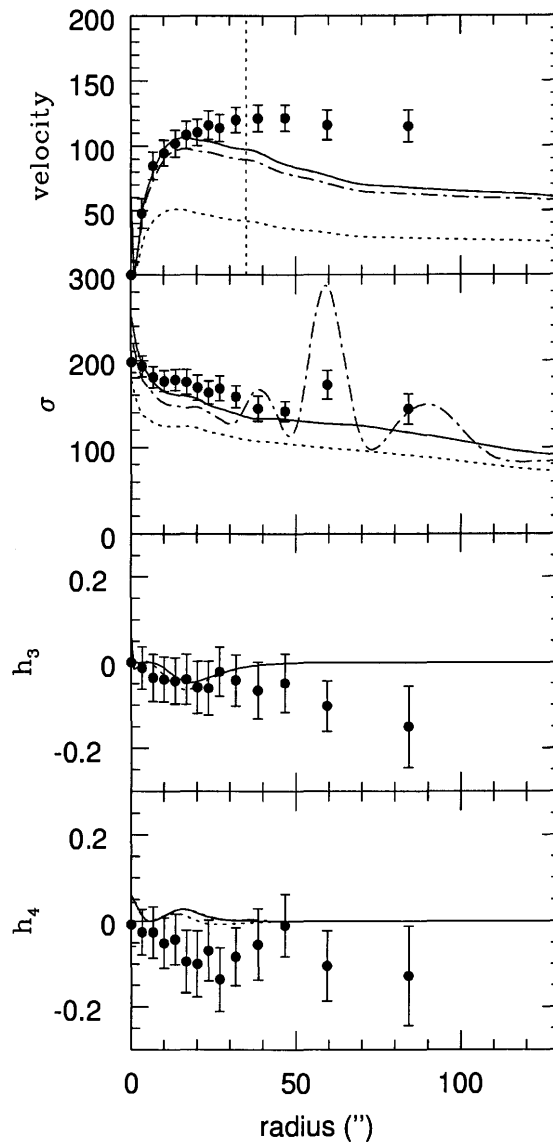


Figure 3: Predictions of the two-integral models for IC3370. Intermediate axis predictions. Dotted lines: $k = 0.6$, $M/L_B = 3.64$, no dark matter included, no embedded disk. Dashed lines: $k = 1$, $M/L_B = 5.19$, no dark matter included, no embedded disk (overlapped with solid line). Solid lines: $k = 1$, $M/L_B = 5.19$, no dark matter included, embedded disk included. Dot-dashed lines: $k = 1$, $M/L_B = 4.77$, dark matter included, embedded disk included. Vertical dotted line indicates one effective radius.

IC1459

This galaxy has a counterrotating core, and therefore, two-integral axisymmetric modeling based on the photometric profiles will necessarily fail in the inner regions. I used the inclination angle of 65° in all the cases because it provided the best fit to the data (although very far from perfect).

Major axis (Fig. 4 (left)): In the case of the major axis I tested $k = 0.6$ value: first, it gave marginally good fit for the velocity in the outer region of the galaxy ($M/L_B = 3.81$), and a marginally good fit in the region slightly beyond $1R_e$ for the velocity dispersion (dashed line), and, second, a case of larger $M/L_B = 6.83$ did not fit the velocity, nor the velocity dispersion

(solid line). In both of these cases no dark matter halo was included, and no embedded disk was assumed. Their inclusion does not alter the fit at all. If one takes $k = 1$, there are two cases that I decided to present: first, $M/L_B = 6.83$ (no dark halo, and no embedded disk) (dotted lines) the velocity is extremely large (it declines from $\sim 350 \text{ km s}^{-1}$ at $20''$ to $\sim 220 \text{ km s}^{-1}$ at $100''$); the velocity dispersion can be fitted, almost perfectly, throughout the whole observed galaxy, and second, the case when $M/L_B = 3.81$ (no dark halo, and no embedded disk) (dot-dashed lines) for which the fitted velocity has smaller values (although still much larger than the observed ones): in a region between $20''$ and $100''$ the velocity decreases from 260 km s^{-1} to 170 km s^{-1} ; the velocity dispersion is much lower, and the successful fit is attained only in the outer parts. The h_3 parameter, because of the fact that there is a counterrotating core, cannot be fitted. For the h_4 parameter this modeling did not give successful fit in the outer parts where there possibly exists a radial anisotropy (judging from the observed non-zero value of the h_4 parameter). The inclusion of dark matter and/or embedded disk does not alter the results. Therefore, one can state that only the test with $k = 1$ ($M/L_B = 6.83 \pm 0.13$) can provide a fit to the velocity dispersion. The fact that the predicted velocity is much larger is of a crucial importance and will be addressed below. I note that the inclusion of a dark halo (Henon potential, tested with different core radii) did not alter the fitting results in this case.

It was argued that the Gauss-Hermite estimates are not the best approximation of the mean line-of-sight velocity and velocity dispersion of the LOSVD (cf. Statler, Smecker-Hane & Cecil 1996, De Rijcke et al. 2003), because their real values depend on the h_3 and h_4 parameters. Only in the case of IC1459 (of all four galaxies analyzed using 2I technique only in this galaxy are there significant departures in the Gauss-Hermite parameters from zero for a major axis) I applied the correction for the velocity and velocity dispersion. I used De Rijcke et al. (2003) formulas to get the corrected values that are then compared with the modeling results. The corrected values are, for the velocity:

$$v_{\text{corr}} = v_{\text{GH}} + \sqrt{3}(h_3)_{\text{GH}}\sigma_{\text{GH}},$$

and for the velocity dispersion:

$$\sigma_{\text{corr}} = \sigma_{\text{GH}}(1 + \sqrt{6}(h_4)_{\text{GH}}),$$

where the index "GH" is related to the Gauss-Hermite estimates. This correction is done only in the case of the major axis, since in the case of minor axis the departures from zero in h_3 and h_4 are minimal. After the correction is done one can note two changes with respect to the uncorrected values (see Fig. 5): (i) the counterrotating core shows lower absolute velocity: about 40 km s^{-1} (the same effect is seen in NGC1700 by Statler, Smecker-Hane & Cecil 1996), (ii) the velocity dispersion values in the outer part have increased (h_4 is positive), but the general trend of decline remains. When one now examines the modeling results given in Fig. 5 one can see that better fit to the observations is obtained using $k = 0.6$, and the constant mass-to-light ratio $M/L_B = 5.31 \pm 0.10$ that is somewhat lower than the value estimated for the best fit in the uncorrected case. This however does not alter the main conclusion: IC1459 can be successfully fitted without invoking of dark matter. Note however, that the error bars for h_4 are rather large in the outer parts. New observations of IC1459 made (but still unpublished) by Bridges et al. (2003) should hopefully clarify the kinematics at $\sim 3R_e$.

Minor axis (Fig. 4 (right)): In Fig. 4 three $k = 0.6$ cases are plotted: one for $M/L_B = 3.05$ (dashed line) which does not provide a good fit for the velocity dispersion, and the other one for

which $M/L_B = 7.33$ that provides a better agreement (solid line). Finally, a thick short dashed line gives a prediction of the velocity dispersion for $M/L_B = 12.21$ and obviously does not provide a good fit (except marginally at $\sim 15''$). A better fit was obtained using $k = 1$: with the dotted lines I present a case with $M/L_B = 8.54$ (no dark matter, no embedded disk). However, a fit with $k = 1$, but with a lower value of mass-to-light ($M/L_B = 3.05$, dot-dashed line) predicts a velocity dispersion that is too low. Finally, if one increases mass-to-light ratio to $M/L_B = 14.23$ (thick long dashed line) one can get a prediction that seems valid at $\sim 25''$. Values of both velocity and h_3 parameter are consistent with zero for the minor axis, and h_4 is fitted properly for these cases. In this case, as well as in the case of the major axis, inclusion of the dark matter and the embedded disk did not alter the predictions.

I showed that in the case of the major axis the best fit for the velocity dispersion can be obtained using $k = 1$ and $M/L_B = 6.83 \pm 0.13$ (or 5.31 ± 0.10 obtained using corrected values of v and σ). However, with these assumptions the velocity is enormously high. This means that one is faced with the same situation that BDI described in the case of NGC720. Therefore, as in BDI, one can conclude that IC1459 *cannot have* a distribution function of the form $f(E, L_z)$, and that three-integral modeling is needed.

Because of the counterrotating core there is a strong hint that IC1459 is a result of the merger. That is why I compared the results of Bendo & Barnes (2000) who used an N-body code to study the LOSVD of simulated merger remnants with the stellar kinematics that I extracted. A reasonable agreement is seen in Fig. 9 by Bendo & Barnes (2003) which was reproduced here as Fig. 6 showing the dependence of the Gauss-Hermite parameters as functions of position along the major axis for a typical 3:1 merger (merger between disc galaxies with mass ratios of 3:1). Although in the central parts there is a small discrepancy between the observations and the simulation, in the outer parts there is an obvious trend for an increase in the h_4 parameter. Ostriker (1980) gave several arguments against the merging hypothesis. Here, I quote some which are of importance in the case of IC1459. The velocity dispersion obtained in the simulation is in almost excellent agreement with the observed values. Note, however, that the scaling in the simulation is arbitrary and that in the case of the simulation $(v/\sigma)_{\max} \approx 1$ whereas in the case of IC1459 this ratio is $(v/\sigma)_{\max} \approx 3.5$, i.e. the central velocity dispersion of IC1459 is very high ($\sim 350 \text{ km s}^{-1}$). This would mean that hypothetical gaseous tracers in a galaxy with $\sigma \approx 350 \text{ km s}^{-1}$ would show a circular velocity (cf. Binney & Tremaine 1987) of $v_{\text{circ}} = \sqrt{2}\sigma \approx 500 \text{ km s}^{-1}$ which is much more than is seen in any spiral. There is also a problem of metallicities in merging (not addressed in this simulation): the most metal-rich ellipticals seem to be far more metal rich than typical spirals.

2.1.2.3 Sample 3

NGC3379

It was already mentioned in the Introduction that NGC3379 is a galaxy for which the evidence for dark matter is scarce (Ciardullo et al. 1993, Romanowsky et al. 2003). I present my results for the two-integral axisymmetric modeling for the major and minor axis in Fig. 7. The inclination angle that I used in all the cases was 40° .

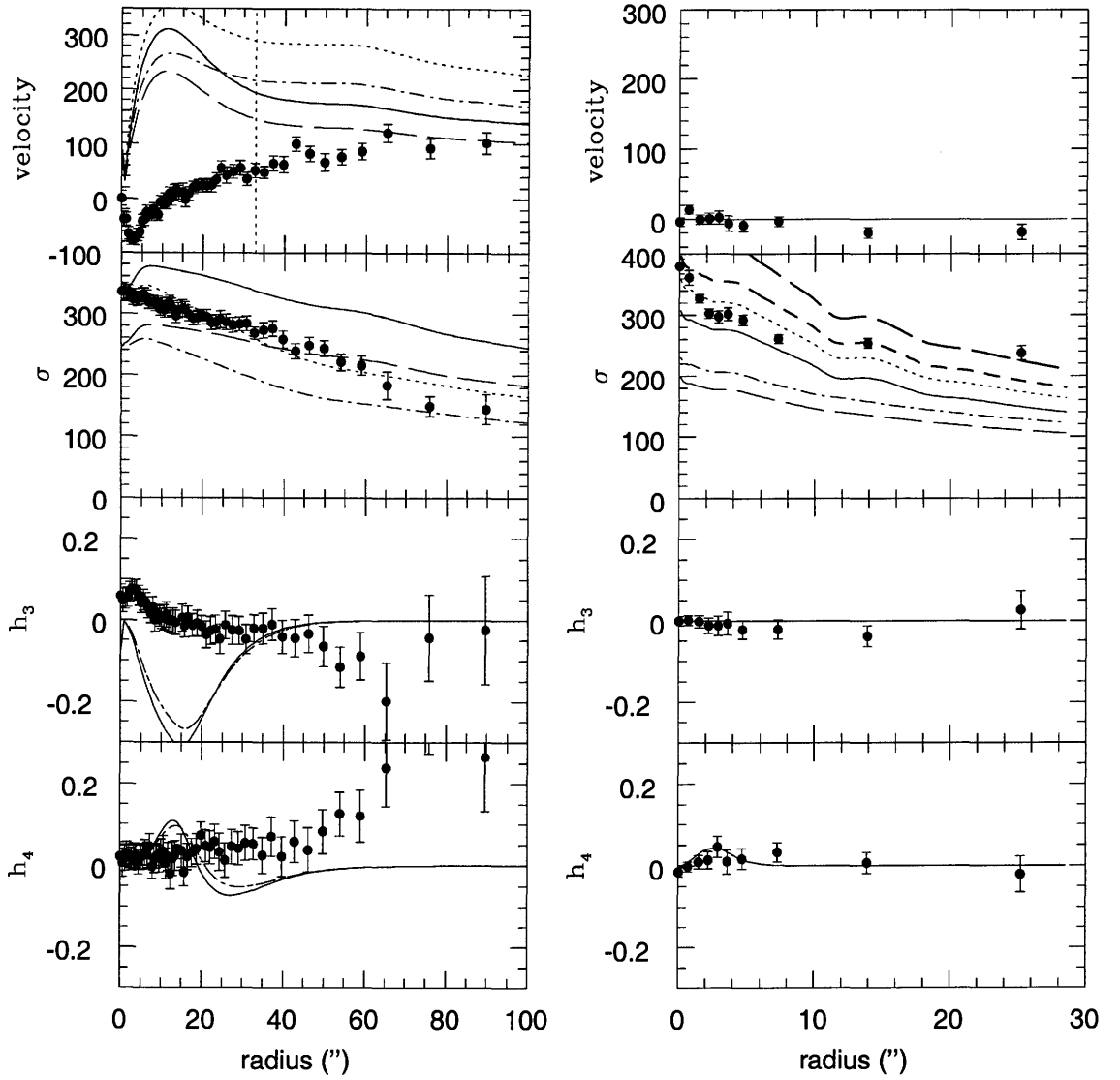


Figure 4: Predictions of the two-integral models for IC1459. Left: major axis predictions. Dotted lines: $k = 1$, $M/L_B = 6.83$, no dark matter included, no embedded disk. Dashed lines: $k = 0.6$, $M/L_B = 3.81$, no dark matter included, with embedded disk. Solid lines: $k = 0.6$, $M/L_B = 6.83$, no dark matter included, embedded disk included. Dot-dashed lines: $k = 1$, $M/L_B = 3.81$, no dark matter included, without embedded disk. Right: minor axis predictions. Dotted line: $k = 1$, $M/L_B = 8.54$, no dark matter included, with embedded disk. Dashed line: $k = 0.6$, $M/L_B = 3.05$, no dark matter included, with embedded disk. Solid line: $k = 0.6$, $M/L_B = 7.33$, no dark matter included, embedded disk included. Dot-dashed line: $k = 1$, $M/L_B = 3.05$, no dark matter included, without embedded disk. Thick long dashed line: $k = 1$, $M/L_B = 14.23$, no dark matter included, with embedded disk. Thick short dashed line: $k = 0.6$, $M/L_B = 12.21$, no dark matter included, with embedded disk. Vertical dotted line indicates one effective radius; in case of the minor axis it is out of scale.

Major axis (Fig. 7 (left)): When one takes $k = 1$ and does not include either a dark matter

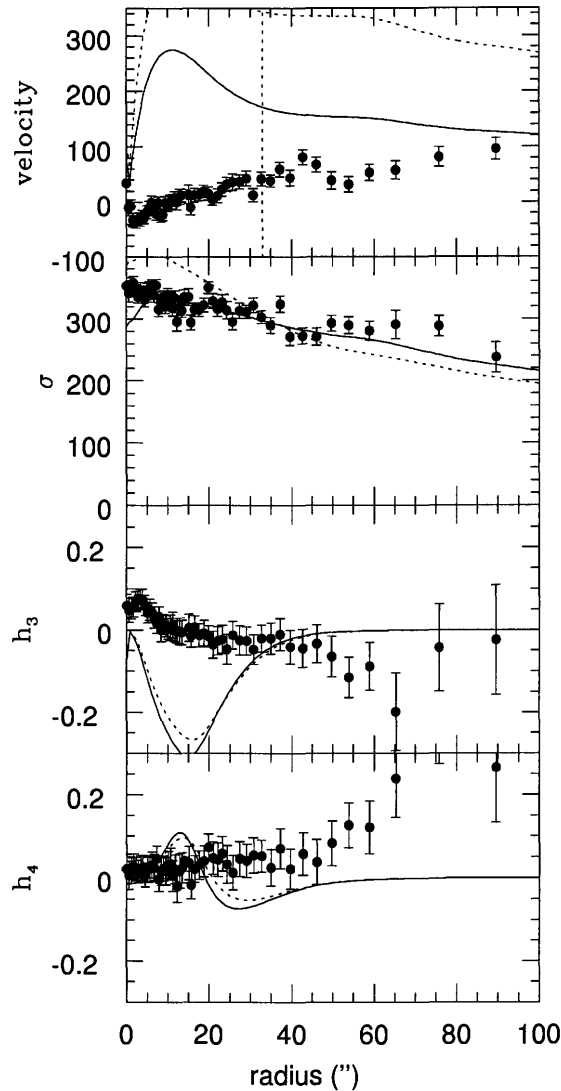


Figure 5: Predictions of the two-integral models for IC1459 for *corrected* values of the observed velocity and velocity dispersion (see text for details).. Dotted line: $k = 1$, $M/L_B = 9.56$, no dark matter included, no embedded disk. Solid line: $k = 0.6$, $M/L_B = 5.31$, no dark matter included, embedded disk included.

halo or an internal embedded disk, using $M/L_B = 5.44$ (dotted lines) one gets an exaggerated value of the velocity but a rather reasonable fit for the velocity dispersion (especially in the inner part). In all other cases for the major axis I will use $k = 0.5$ which provides a better fit to the data in the outer part of NGC3379. Again, inclusion of the dark matter halo (Henon potential, tested with different core radii) does not change the modeled values: for example, when one models a rotation curve, a result of a test used with an embedded disk and a dark halo (dot-dashed line) is overlapped with a solid line that represents a test made with the same mass-to-light ratio, $M/L_B = 4.75$, without an embedded disk and without a dark halo. This combination gives a good fit for the velocity dispersion in the outer regions. Also, a case with $M/L_B = 5.44$ (dashed line), without embedded disk and without a dark halo gives a good fit in the outer part of the galaxy. Note that the velocity cannot be fitted at all in the inner region ($< 20''$) where there is a strong isophotal

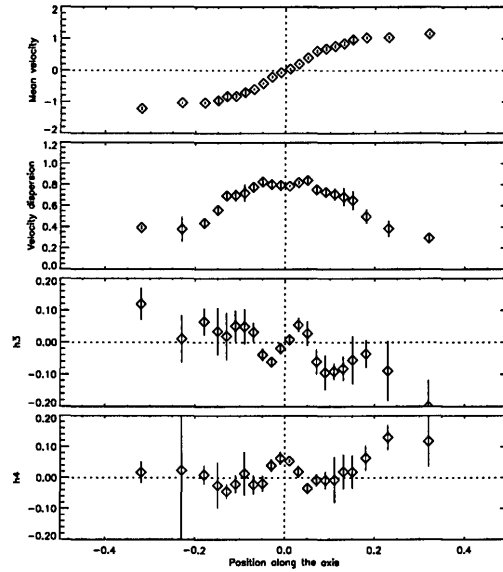


Figure 6: Taken from Bendo & Barnes (2000) (their Fig. 9). Parameters of the LOSVD along the major axis for a remnant, a typical 3:1 merger.

twist, as shown in the previous Chapter. Both h_3 and h_4 parameters are fitted similarly in all the models and the fit is very close to the observed values.

Minor axis (Fig. 7 (right)): Again, in the case of the minor axis I consider various tests related to the velocity dispersion. With a dotted line I present the $k = 1$ case with $M/L_B = 4.18$ without the dark matter, and without a disk: this does not provide a good fit. Neither can the case with $k = 0.5$ with a dark matter halo and a disk, with $M/L_B = 4.18$ (dot-dashed line overlapped with a solid line that belongs to the case with the same mass-to-light ratio, but without the dark matter). Thick dot-dashed line represents the test that used $M/L_B = 6.69$ ($k = 0.5$, without dark matter, and with embedded disk) and which provides a good fit in the inner region (out to $\sim 1R_e$), but fails in the outer regions. On the contrary, a test made with $M/L_B = 8.91$ and $k = 0.5$ (thick long dashed line) provides a good fit in the outer regions (beyond $\sim 1R_e$).

My conclusion based upon the two-integral modeling that I performed is that in NGC3379 there is no evidence for dark matter out to $\sim 2.3R_e$ and that this galaxy can be fitted with a constant mass-to-light ratio that is between ~ 5 and ~ 9 . From the minor axis modeling I infer that a small increase of the mass-to-light ratio cannot be ruled out. Here, parenthetically, the remark that was given previously in the case of IC3370 that minor axis modeling overestimates the mass-to-light ratio would be appropriate. These results are in agreement with the papers by other authors. Ciardullo et al. (1993) found that NGC3379 does not possess a dark halo, and that mass-to-light ratio is ~ 7 (their observations of PNe extend out to $3.5 R_e$). Also, Romanowsky et al. (2003) came to a similar conclusion that little if any dark matter is evident in the halo of this galaxy and they found that $M/L_B = 6.4 \pm 0.6$ (their observations extend to $\sim 5.5 R_e$).

NGC4105

Here I present my results for the two-integral axisymmetric modeling for the major and minor axis

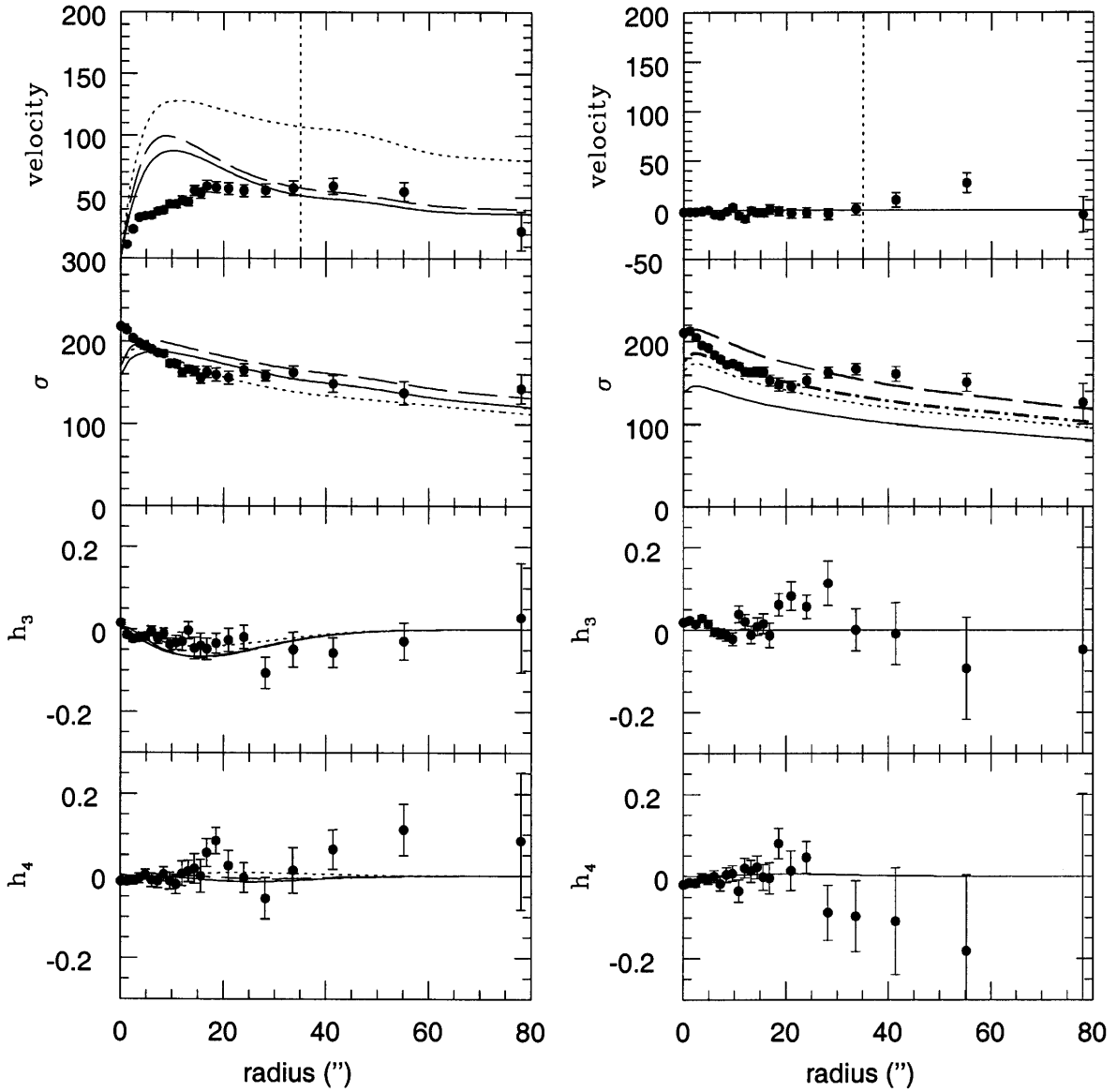


Figure 7: Predictions of the two-integral models for NGC3379. Left: major axis predictions. Dotted lines: $k = 1$, $M/L_B = 5.44$, no dark matter included, no embedded disk. Dashed lines: $k = 0.5$, $M/L_B = 5.44$, no dark matter included, without embedded disk. Solid lines: $k = 0.5$, $M/L_B = 4.75$, no dark matter included, embedded disk included. Dot-dashed lines: $k = 1$, $M/L_B = 4.75$, dark matter included, with embedded disk (overlapped with the solid line). Right: minor axis predictions. Dotted line: $k = 1$, $M/L_B = 4.18$, no dark matter included, without embedded disk. Dashed line: $k = 0.5$, $M/L_B = 4.18$, no dark matter included, with embedded disk. Solid line: $k = 0.5$, $M/L_B = 4.18$, no dark matter included, embedded disk included. Dot-dashed line: $k = 0.5$, $M/L_B = 4.18$, dark matter included, with embedded disk (overlapped with solid line). Thick long dashed line: $k = 0.5$, $M/L_B = 8.91$, no dark matter included, without embedded disk. Thick dot-dashed line: $k = 0.5$, $M/L_B = 6.69$, no dark matter included, with embedded disk. Vertical dotted line indicates one effective radius.

in Fig. 8. The inclination angle that I used in all the cases was 50° .

Major axis (Fig. 8 (left)): The case of $k = 0.5$ and $M/L_B = 4.50$ (no dark matter halo, no disk included) provided the best fit to the velocity dispersion for the distance $> 2''$ (dotted line). However, this case (as well as all the others mentioned below) predicts a grossly excessive velocity. The solid lines show the predictions of the case with $k = 1$, $M/L_B = 4.50$ (no dark matter halo, disk included), for which velocity is again exaggerated, and velocity dispersion is lower than observed (although beyond $\sim 2''$ within the error bars. Finally, with a dot-dashed line I present the case of $k = 1$, $M/L_B = 5.94$ (no dark matter halo, disk included), that predicts an even larger velocity, but a good fit to the velocity dispersion. The h_3 parameter predictions provide a rather good agreement with the observations (apart from the region between $10''$ and $20''$). The h_4 parameter is fitted properly in all the cases. Note that again inclusion of the embedded disk and/or the dark matter halo (Henon potential, tested with different core radii) does not change the predictions of the two-integral modeling.

Minor axis (Fig. 8 (right)): The case of $k = 0.5$ and $M/L_B = 5.86$ (no dark matter halo, no disk included) did not provide a successful fit to the velocity dispersion for a radius $< 10''$ (dotted line). The same conclusion is reached for the case of $k = 1$ and $M/L_B = 4.87$ (with a dark matter halo and a disk) presented as the dot-dashed line. The solid line is for the case of $k = 1$ and $M/L_B = 6.42$ (without dark matter, and with a disk) and this represents the best fit in all cases (note that it overlaps the cases with the same mass-to-light ratios, but (i) with the dark matter and a disk and (ii) without the dark matter and without the disk). Since h_3 and h_4 do not show large departures from zero, they are fitted properly.

My conclusion for NGC4105 is that this galaxy should be modeled using a three-integral approach (the modeling results are very similar to these obtained in the case of IC1459, and NGC720 from BDI). However, judging by axisymmetric modeling one can see that the dark matter is not needed (out to $\sim 2.5 R_e$) and that a successful fit (only for dispersion, for reasons given above) can be obtained for a constant mass to light ratio $M/L_B \sim 6$.

2.2 THREE-INTEGRAL MODELING

2.2.1 THEORETICAL INTRODUCTION

For axisymmetric potentials one can have orbits that have three integrals of motion: E , L_z and I_3 . There is no general expression for the third integral, I_3 . The assumption that the distribution has the form $f = f(E, L_z, I_3)$ broadens the range of possible axisymmetric motions (see Appendix 3 for details on orbits). Three-integral models are used for modeling of triaxial systems. Schwarzschild (1979) invented a very powerful method that can be used for the construction of axisymmetric and triaxial models of galaxies in equilibrium without explicit knowledge of the integrals of motion. The basic steps of this approach are the following: one specifies the mass model $\rho(r)$, finds its potential and then constructs a grid of cells in position space. Then initial conditions are chosen for a set of orbits and for every orbit one integrates the equations of motion for many orbital periods and measures how much time the orbit spends in each cell (that measures how much mass the orbit contributes to that cell). Finally, one needs to determine the non-negative weights for each orbit such that the summed mass in each cell is equal to the mass given by the original $\rho(r)$. For the last step one can use different methods; for example, Schwarzschild (1979) used linear programming.

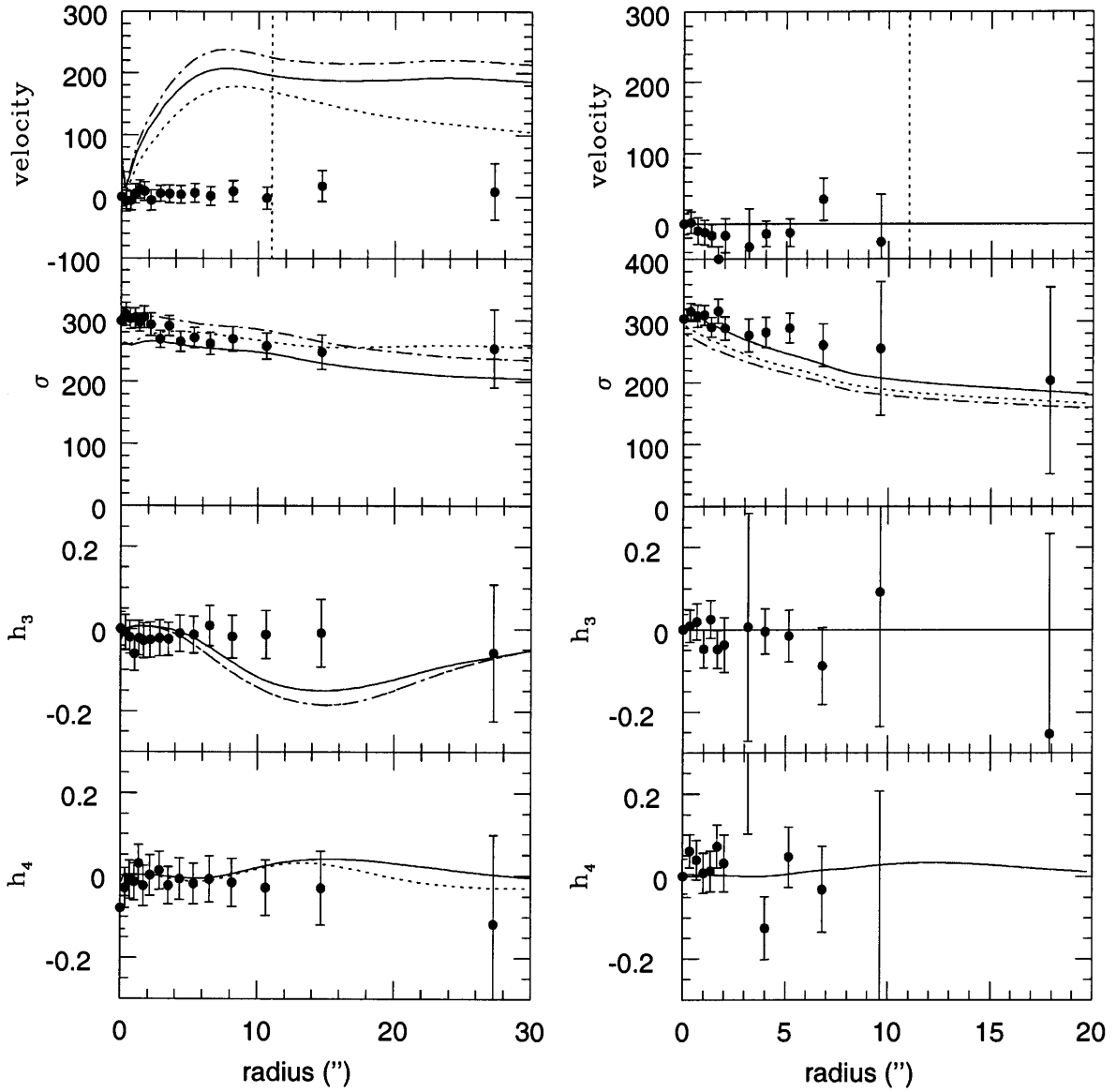


Figure 8: Predictions of the two-integral models for NGC4105. Left: major axis predictions. Dotted lines: $k = 0.5$, $M/L_B = 4.50$, no dark matter included, with embedded disk. Solid lines: $k = 1.0$, $M/L_B = 4.50$, no dark matter included, embedded disk included. Dot-dashed lines: $k = 1$, $M/L_B = 5.94$, without dark matter, with embedded disk. Right: minor axis predictions. Dotted line: $k = 0.5$, $M/L_B = 5.86$, no dark matter included, without embedded disk. Dashed line: $k = 1$, $M/L_B = 6.42$, no dark matter included, without embedded disk (overlapped by solid line). Solid line: $k = 1$, $M/L_B = 6.42$, no dark matter included, embedded disk included. Dot-dashed line: $k = 1$, $M/L_B = 4.87$, dark matter included, with embedded disk. Dashed line: $k = 1$, $M/L_B = 6.42$, with dark matter, with embedded disk (overlapped by solid line). Vertical dotted line indicates one effective radius.

A non-negative least squares (NNLS) method (Lawson & Hanson 1974) was used in this work (see Appendix 2 for details on NNLS).

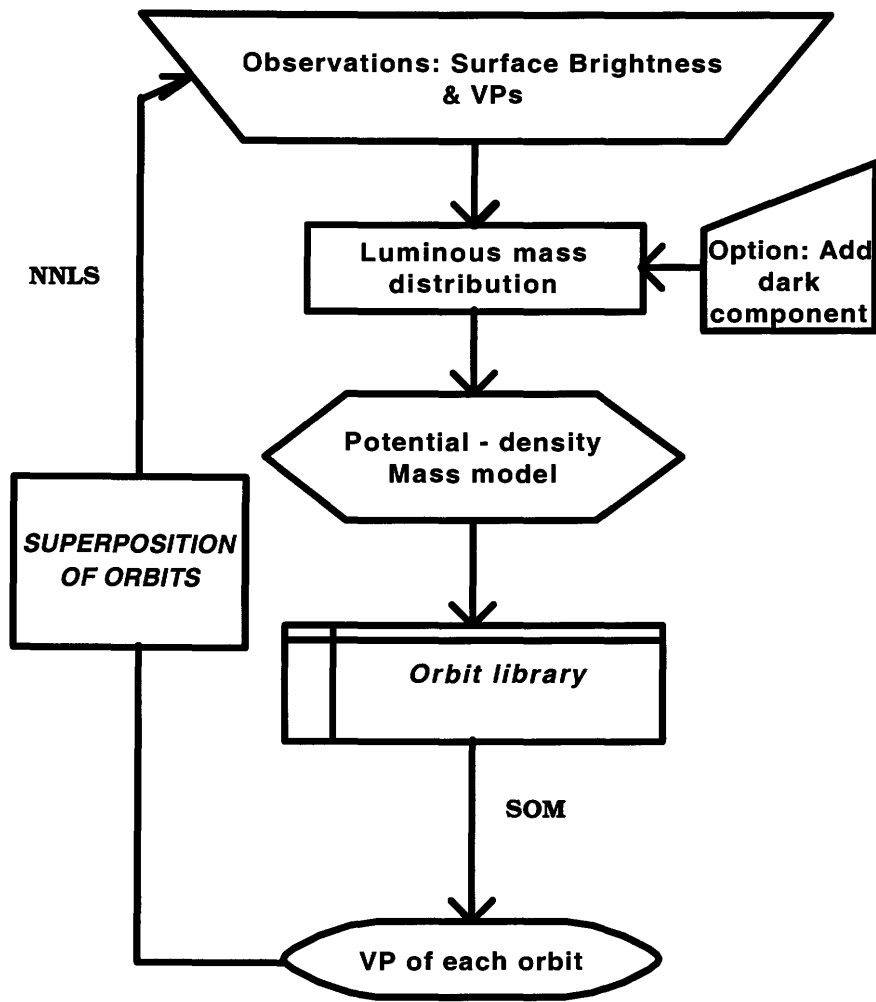


Figure 9: Flowchart of three-integral modeling procedure. (SOM stands for self-organizing maps; see Appendix 4 for details on SOMs, NNLS stands for non-negative least squares; see Appendix 2 for details on NNLS).

Schwarzschild's original idea has recently been further developed: namely, models are now made that match the bulk kinematics and LOSVD of observed galaxies. Rix et al. (1997) used such an approach to search for dark matter in elliptical galaxies. Cretton & van der Bosch (1999) used it to confirm the presence of nuclear black holes. Recently, Gebhardt et al. (2003) used the orbit superposition method for detection of central black holes in 12 galaxies. These works deal with axisymmetric modeling only. I have used the Rix et al. (1997) algorithm to build a new Schwarzschild modeling code that uses the so-called self-organizing maps (SOMs) (Kohonen 1997, Murtagh 1995) to extract velocity profiles from the large orbit library. The flowchart is presented in Fig. 9.

The details of the modeling procedure are given in Rix et al. (1997). I explain here several important steps. Note that in the paper of Rix et al. (1997) there are numerous unfortunate (uncorrected) typographical errors that are absent from the preprint version of this paper (available through LANL as astro-ph/9702126). Namely, in equations (4), (5), (7), (8), (9), (11) and (12) the sign ">" should be omitted. In equation (13) the comma sign (",") in the second term on the right hand side should be omitted and, finally, in equation (14) N_e in a matrix on the left hand side should read N_c , γN_0 in the vector on the left hand side should read γ_{N_0} and N_e in the vector on the right hand side should read N_c .

As already mentioned, details of orbit calculations are given in Appendix 3. Here I note that it is important to have the projected properties of orbits in order to compare them with the observations. As given in Cretton et al. (1999) only three coordinates in the phase space are available for comparison with the observations: the projected positions x' , y' (that are chosen to be aligned with the photometric major and minor axis), and the line-of-sight velocity, $v_{\text{los}} (\equiv v_{z'})$. If the inclination angle is i (for edge-on galaxy $i = 90^\circ$), these coordinates are related to the cylindrical coordinates (R, z, ϕ) as:

$$x' = R \sin \phi, \quad (10)$$

$$y' = -R \cos i \cos \phi + z \sin i, \quad (11)$$

and

$$v_{\text{los}} = (v_R \cos \phi - v_\phi \sin \phi) \sin i + v_z \cos i. \quad (12)$$

One can assign to each orbit in the library an index k , with $k = 1, \dots, N_0$, where N_0 is the total number of orbits (in this thesis $N_0 = 729$). The *occupation weight* of the orbit k in the storage cube cell that is centered on (x, y, v) is denoted as w_{xyv}^k . The occupation weights for each orbit are normalized to unit mass:

$$\sum_{xyv} w_{xyv}^k = 1, \quad \forall k. \quad (13)$$

After the calculation of the k -th orbit, one can proceed with the modeling with the direct comparison with the observational constraints. These constraints are taken at different constraint positions on the projected face of the galaxy. One can again use the photometric and kinematic data as in the case of the 2I modeling. The constraint positions are labeled by l , with $l = 1, \dots, N_c$. As in Rix et al. (1997) one can denote by $f_{xy,l}$ the fraction of the area of the storage cube cell centered on the grid point (x, y) that is contained within the constraint area l .

Let M_l^k be the fraction of the total mass in orbit k that contributes to constraint area l . This mass fraction is obtained by summing over the storage cube for the given orbit:

$$M_l^k = \sum_{xyv} f_{xy,l} w_{xyv}^k. \quad (14)$$

To calculate a dynamical model one needs to estimate its *orbital weights* γ_k , which measure the fraction of the total mass of the system that resides in each orbit k . The total mass fraction M_l of the model that contributes to constraint area l is then obtained as a sum over all orbits:

$$M_l = \sum_k \gamma_k M_l^k. \quad (15)$$

Under the assumption that the stellar population has the same mass-to-light ratio everywhere in the galaxy one can obtain the observed mass fractions M_l^{obs} at the constraint positions l from the observed surface brightnesses μ_l^{obs} as:

$$M_l^{\text{obs}} = \mu_l^{\text{obs}} A_l / L_{\text{tot}}, \quad (16)$$

A_l is the area of constraint position l , and L_{tot} is the total observed luminosity. When one wants to fit the predicted mass fractions M_l to the observed mass fractions M_l^{obs} one encounters a linear superposition problem for the γ_k .

For this kind of modeling one must be sure that the contributions of individual orbits to all kinematic constraints add up linearly. This can be achieved if one chooses the Gauss-Hermite coefficients h_m ($m = 1, \dots, M$) to describe the shape of the VP. The normalized VP contributed by orbit k to constraint position l is

$$\text{VP}_{l,v}^k = \frac{1}{M_l^k} \sum_{xy} f_{xy,l} w_{xyv}^k. \quad (17)$$

When one performs the sum over all orbits one obtains the total normalized VP at the constraint position l :

$$\text{VP}_{l,v} = \frac{1}{M_l} \sum_k \gamma_k M_l^k \text{VP}_{l,v}^k. \quad (18)$$

The Gauss-Hermite moment $h_{m,l}$ of order m at constraint position l is defined as an integral over $\text{VP}_l(v)$:

$$h_{m,l} = 2\sqrt{\pi} \int_{-\infty}^{\infty} \text{VP}_l(v) \alpha(w_l) H_m(w_l) dv. \quad (19)$$

The function α is a Gaussian weighting function:

$$\alpha(w_l) \equiv \frac{1}{\sqrt{2\pi}} \exp \left[-\frac{1}{2} w_l^2 \right]. \quad (20)$$

Here, w_l is defined as $w_l \equiv (v - V_l)/\sigma_l$, where the velocity V_l and dispersion σ_l are free parameters. The $H_m(w_l)$ are Hermite polynomials that were defined previously. In a similar manner one can define the Gauss-Hermite moment $h_{m,l}^k$ of orbit k and order m for constraint position l , as an integral over $\text{VP}_l^k(v)$ (of which $\text{VP}_{l,v}^k$ is the discrete representation). When one chooses the free parameters V_l and σ_l to be the same for each orbit k , it follows that

$$M_l h_{m,l} = \sum_k \gamma_k M_l^k h_{m,l}^k. \quad (21)$$

Therefore, fitting the observed Gauss-Hermite moments $h_{m,l}^{\text{obs}}$ through the combination $M_l^{\text{obs}} h_{m,l}^{\text{obs}}$ is also a linear superposition problem for the γ_k .

In practice one chooses V_l and σ_l equal to the parameters of the best-fitting Gaussian to the observed VP at constraint position l , which are the observationally determined quantities. This implies $h_{1,l}^{\text{obs}} = h_{2,l}^{\text{obs}} = 0$ for the first- and second-order observed Gauss-Hermite moments. When

one requires that the predicted moments $h_{1,l}$ and $h_{2,l}$ should reproduce this, the model VP automatically has the correct mean velocity and velocity dispersion (as determined through a Gaussian fit). So these latter quantities need not be fitted separately. As for the errors $\Delta h_{1,l}^{\text{obs}}$ and $\Delta h_{2,l}^{\text{obs}}$ that correspond to the observationally quoted errors ΔV in V_l and $\Delta\sigma$ in σ_l , one can obtain them using the following equations:

$$\Delta h_1 = -\frac{1}{2}\sqrt{2}\Delta V/\sigma, \quad \Delta h_2 = -\frac{1}{2}\sqrt{2}\Delta\sigma/\sigma. \quad (22)$$

The question of the zeroth-order moment h_0 is resolved by not including this quantity in the fit, because it is not accessible observationally. It determines the unknown difference in the line strength between the galaxy spectrum and the template spectrum. In practice one can safely use the assumption $h_0 = 1$.

After the calculation of the properties of all the orbits is finished for all constraint positions one proceeds with the evaluation of the non-negative superposition of orbital weights γ_k that best matches the observational constraints within the error bars. When the observational errors are normally distributed, the quality of the fit to the data is determined by the χ^2 statistic:

$$\chi^2 \equiv \sum_{l=1}^{N_p} \left(\frac{M_l^{\text{obs}} - \sum \gamma_k M_l^k}{\Delta M_l^{\text{obs}}} \right)^2 + \sum_{l=N_p+1}^{N_c} \sum_{m=1}^M \left(\frac{M_l^{\text{obs}} h_{m,l}^{\text{obs}} - \sum \gamma_k M_l^k h_{m,l}^k}{\Delta(M_l^{\text{obs}} h_{m,l}^{\text{obs}})} \right)^2. \quad (23)$$

Here, N_p are photometric constraints and $N_k = N_c - N_p$ are kinematic constraints (N_c is the number of constraint positions). I have chosen the number M of Gauss-Hermite moments that can be extracted from spectroscopic observations to be $M = 4$, since the kinematic parameters extracted from spectra are v , σ , h_3 and h_4 . Therefore when higher order moments can be routinely extracted from spectra it will be straightforward to include them in the fitting procedure also.

When one divides all quantities by their observational uncertainties, e.g., $M_1^{\text{obs}} \rightarrow M_1^{\text{obs}}/\Delta M_1^{\text{obs}}$, $M_1^1 h_{1,1}^1 \rightarrow M_1^1 h_{1,1}^1/\Delta(M_1^{\text{obs}} h_{1,1}^{\text{obs}})$, etc., the χ^2 minimization is converted into a least squares problem:

$$\begin{bmatrix} M_1^1 & \dots & \dots & M_1^{N_0} \\ M_2^1 & \dots & \dots & M_2^{N_0} \\ \vdots & \vdots & \vdots & \vdots \\ M_{N_p}^1 & \dots & \dots & M_{N_p}^{N_0} \\ M_{N_p+1}^1 h_{1,N_p+1}^1 & \dots & \dots & M_{N_p+1}^{N_0} h_{1,N_p+1}^{N_0} \\ \vdots & \vdots & \vdots & \vdots \\ M_{N_c}^1 h_{1,N_c}^1 & \dots & \dots & M_{N_c}^{N_0} h_{1,N_c}^{N_0} \\ \vdots & \vdots & \vdots & \vdots \\ \vdots & \vdots & \vdots & \vdots \\ M_{N_p+1}^1 h_{M,N_p+1}^1 & \dots & \dots & M_{N_p+1}^{N_0} h_{M,N_p+1}^{N_0} \\ \vdots & \vdots & \vdots & \vdots \\ M_{N_c}^1 h_{M,N_c}^1 & \dots & \dots & M_{N_c}^{N_0} h_{M,N_c}^{N_0} \end{bmatrix} \begin{bmatrix} \gamma_1 \\ \vdots \\ \vdots \\ \gamma_{N_0} \end{bmatrix} = \begin{bmatrix} M_1^{\text{obs}} \\ M_2^{\text{obs}} \\ \vdots \\ M_{N_p}^{\text{obs}} \\ M_{N_p+1}^{\text{obs}} h_{1,N_p+1}^{\text{obs}} \\ \vdots \\ M_{N_c}^{\text{obs}} h_{1,N_c}^{\text{obs}} \\ \vdots \\ \vdots \\ M_{N_p+1}^{\text{obs}} h_{M,N_p+1}^{\text{obs}} \\ \vdots \\ M_{N_c}^{\text{obs}} h_{M,N_c}^{\text{obs}} \end{bmatrix} \quad (24)$$

Here, M denotes mass fractions, "obs" is related to the observed quantities. The total number of orbits is N_0 (I used 729, and Rix et al. used 420 orbits). This least squares problem has to be solved for the occupation vector $(\gamma_1, \dots, \gamma_{N_0})$, with the constraints $\gamma_k \geq 0$, for $k = 1, \dots, N_0$ for $m = 1, 2, 3, 4$. I have used, as did Rix et al. (1997), a non-negative least-squares (NNLS) procedure described in Appendix 2. The dimension of the vector on the right hand side of the equation is 500. One hundred points belong to the photometric data and 400 points belong to kinematical data: 200 are zeros related to velocity and velocity dispersion, 100 points are related to h_3 parameter and 100 points are related to h_4 parameter. Since the extraction of the kinematical parameters provides smaller number of points (non equidistant), I made a fit to the observational data using Chebishev polynomials to get a hundred equidistant points that are then included in the vector on the right hand side (similar procedure is also applied on the photometric data). Obviously, the same grid used in this fitting is also used when obtaining data on the left hand side of the equation. Therefore, in the case of 729 orbits and 500 constraints, the dimension of the matrix on the left hand side is 729×500 , the dimension of the vector on the left hand side is 729, and the dimension of the vector on the right hand side is 500. Since this is an ill-posed problem, the regularization procedure has to be applied (in Appendix 1 I present the details of the procedure that I used).

The code that I have created was used for testing several astrophysically important potentials (details in Appendix 3) for the different samples of galaxies that I had. Results and discussions are given below.

The modeling of IC3370 deserves particular attention because of its strong isophotal twisting. Therefore, I present some details concerning the modeling of galaxies with an isophotal twist.

2.2.2 GALAXIES WITH ISOPHOTAL TWIST

Galaxies with some isophotal twist are very common: in fact, it is very difficult to find a galaxy with perfectly axisymmetric isophotes. This suggests the existence of triaxiality is frequent in the bulges of spiral galaxies and in elliptical galaxies. Although some departures from axisymmetry is present in all the galaxies from my samples, the case of IC3370 is particularly important, because this galaxy shows a large isophotal twist: position angle (PA) changes from $\sim 20^\circ$ in the internal parts of the galaxy to $\sim 80^\circ$ in the outer parts. The existence of an isophotal twist can be due to different dynamical processes: a differential rotation in the inner regions of the galaxies (cf. Carter 1978, Williams & Schwarzschild 1979), or some sort of tidal interaction of an oval (bar) distortion (Kormendy 1982), although as noted in Bertola, Vietri & Zeilinger (1988) this effect can be detected in non-barred galaxies. This second explanation is geometrical: if emitting ellipsoidal surfaces are concentric and coaxial but triaxial (without rotational symmetry) and non homologous (two different axial ratios vary with the distance from the center), their projections on the plane of the observer will be concentric ellipses, that are in general non-homologous (their ellipticity varies), and non-coaxial (isophote twist). Therefore, the twisting is purely an effect of the projection of non-homologous ellipsoids (Stark 1977). Simonneau, Varela & Muñoz-Tuñón (1998) (hereafter SVMT) gave a prescription on how to study the relation between the form and the position of the ellipsoidal structures and the form and the position of their elliptical projections: they analyzed the relative isophotal twisting as a function of the form of the ellipsoidal structures: variation of their axial ratios, position angles (ϕ, ψ) and the inclination angle, θ .

I here briefly present the SVMT procedure that I implemented by writing a FORTRAN code that provides an input for generating orbits in a triaxial potential when both p and q change along the radius (see Appendix 3, Eq. (23)).

First, let A , B and C be the semi-axes of an ellipsoid (elliptical galaxy in my case) and let $\{x, y, z\}$ be its own reference system, where the coordinate axes coincide with the symmetry axes of the ellipsoid. The axes x and y define its equatorial plane, $\{x, y\}$ and $\{z\}$ is the polar axis. In this frame the equation of this ellipsoid given by:

$$\frac{x^2}{A^2} + \frac{y^2}{B^2} + \frac{z^2}{C^2} = 1. \quad (25)$$

The object that is observed is aligned along the z_0 -direction, or line of sight of the observer (LSO). This direction allows one to define the observer's reference system $\{x_0, y_0, z_0\}$, where the observer plane $\{x_0, y_0\}$ is perpendicular to the LSO direction, the observer's polar axis, z_0 . The equatorial plane $\{x, y\}$ of the ellipsoid and the plane of the observer $\{x_0, y_0\}$ intersect in the so-called line of nodes (LN). The angle between both planes which is the angle subtended between z and z_0 , is defined as the inclination θ of the observed object. The position of the x and y axes (on their equatorial plane), and that of the x_0 and y_0 axes (in the observer's plane) with respect to the line of nodes (common to both planes), is also fundamental in analyzing the observations. The angle ψ is subtended between the x_0 -axis and the LN, on the $\{x_0, y_0\}$ -plane. The angle subtended between the x -axis and the LN on the equatorial plane $\{x, y\}$ is ϕ . One can choose the axis x between the two symmetry axes of the equatorial plane of the ellipsoid such that $\phi < \pi/2$ (see Fig. 10).

Three Euler angles (θ, ϕ, ψ) allow one to transform one reference system to another by means of three rotations: the first, $R_z(\phi)$, accounts for a rotation of angle ϕ around the z -axis, in order to align x with the LN; the second, $R_n(\theta)$, for a rotation of angle θ around axis n , to align z with z_0 ; and the third $R_{z_0}(\psi)$, for a rotation of angle ψ around the z_0 -axis, to align LN with x_0 . Then, for any point, the coordinates (x_0, y_0, z_0) in the observer's system are transformed into the coordinates (x, y, z) in the ellipsoidal system, according to the following equations:

$$\begin{pmatrix} x \\ y \\ z \end{pmatrix} = \begin{pmatrix} R_{xx} & R_{xy} & R_{xz} \\ R_{yx} & R_{yy} & R_{yz} \\ R_{zx} & R_{zy} & R_{zz} \end{pmatrix} \begin{pmatrix} x_0 \\ y_0 \\ z_0 \end{pmatrix}.$$

Here, R_{jk} are the matrix elements of the total rotation \mathcal{R} that correspond to the three partial rotations mentioned above:

$$\begin{aligned} R_{xx} &= \cos \phi \cos \psi + \cos \theta \sin \phi \sin \psi, \\ R_{xy} &= -\cos \phi \sin \psi + \cos \theta \sin \phi \cos \psi, \\ R_{xz} &= -\sin \theta \sin \phi, \\ R_{yx} &= -\sin \phi \cos \psi + \cos \theta \cos \phi \sin \psi, \\ R_{yy} &= \sin \phi \sin \psi + \cos \theta \cos \phi \cos \psi, \\ R_{yz} &= -\sin \theta \cos \phi, \\ R_{zx} &= \sin \theta \sin \psi, \\ R_{zy} &= \sin \theta \cos \psi, \end{aligned} \quad (R)$$

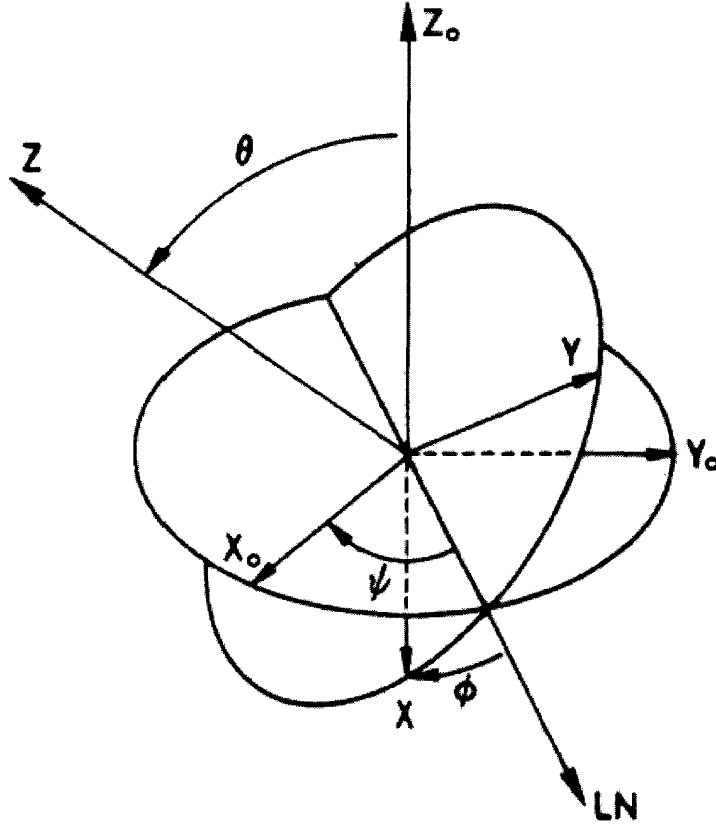


Figure 10: Taken from SVMT (their Figure 1). Reference systems of the ellipsoid is without subscripts. Observer's reference system is with a subscript "0". θ , ϕ , ψ are the Euler angles and LN stands for line of nodes.

$$R_{zz} = \cos \theta$$

where \mathcal{R} is a unitary matrix.

The ellipsoid from the Eq. (25) can now be written in the observer's reference system as:

$$(x_0, y_0, z_0) \mathcal{R}^{-1} \begin{pmatrix} 1/A^2 & 0 & 0 \\ 0 & 1/B^2 & 0 \\ 0 & 0 & 1/C^2 \end{pmatrix} \mathcal{R} \begin{pmatrix} x_0 \\ y_0 \\ z_0 \end{pmatrix} = 1.$$

For the z_0 component only, one gets:

$$P_0 + 2P_1 z_0 + P_2 z_0^2 = 1, \quad (26)$$

where

$$P_0 = Q_{xx}x_0^2 + Q_{yy}y_0^2 + 2Q_{xy}x_0y_0, \quad (27)$$

$$P_1 = Q_{xz}x_0 + Q_{yz}y_0, \quad (28)$$

$$P_2 = Q_{zz}, \quad (29)$$

where

$$Q_{jk} = \frac{R_{xj}R_{xk}}{A^2} + \frac{R_{yj}R_{yk}}{B^2} + \frac{R_{zj}R_{zk}}{C^2} \quad (j, k = x, y, z). \quad (30)$$

One can also write the expression for P_2 :

$$P_2 \equiv Q_{zz} = Q_{zz} = \frac{R_{xz}^2}{A^2} + \frac{R_{yz}^2}{B^2} + \frac{R_{zz}^2}{C^2} = \frac{\sin^2 \theta \sin^2 \phi}{A^2} + \frac{\sin^2 \theta \cos^2 \phi}{B^2} + \frac{\cos^2 \theta}{C^2} \quad (31)$$

Direct problem: ellipsoids vs. projected ellipses

Now one can proceed with establishing the relations that connect geometric properties of the emitting ellipsoids from their projections – isophotes. Eq. (26) for the ellipsoid given in Eq. (25), but referred in the observed plane, can be written as:

$$E(z_0) = 1$$

This ellipsoid projects an ellipse on to the plane of observer $\{\mathbf{x}_0, \mathbf{y}_0\}$ whose equation is obtained by removing z_0 in equations:

$$E(z_0) - 1 = 0$$

and

$$\frac{d}{dz_0}[E(z_0)] = 0.$$

Using Eq. (26) after differentiation one gets :

$$P_0 - \frac{P_1^2}{P_2} = 1,$$

which after using Eq. (27), Eq. (28), Eq. (29) and Eq. (30) becomes:

$$\frac{1}{Q_{zz}A^2B^2C^2}(q_{yy}x_0^2 + q_{xx}y_0^2 - 2q_{xy}x_0y_0), \quad (32)$$

where

$$q_{jk} \equiv A^2 R_{xj}R_{xk} + B^2 R_{yj}R_{yk} + C^2 R_{zj}R_{zk}. \quad (33)$$

Now one has the ellipse on which the ellipsoid is projected and one can continue with evaluating the semi-axis values and their positions with respect to the reference system $\{\mathbf{x}_0, \mathbf{y}_0\}$. Let $\{\mathbf{x}_e, \mathbf{y}_e\}$ be the proper axes of this ellipse for which one can measure the semi axes a and b , respectively.

The ellipse position is defined by the angle δ_e that is subtended between the axes \mathbf{x}_e and \mathbf{x}_0 of the observer plane ($\delta_e < \pi/2$, so the semi-axis a over \mathbf{x}_e can be greater or less than the semi-axis b over \mathbf{y}_e). From Eq. (32) it holds:

$$\tan 2\delta_e = \frac{2q_{xy}}{q_{xx} - q_{yy}}$$

and by taking into account the values of q_{jk} in Eq. (33) one has:

$$\tan 2(\delta_e + \psi) = \frac{(B^2 - A^2) \cos \theta \sin 2\phi}{A^2(\cos^2 \theta \sin^2 \phi - \cos^2 \phi) + B^2(\cos^2 \theta \cos^2 \phi - \sin^2 \phi) + C^2 \sin^2 \theta} \quad (34)$$

which allows one to place the axes of the projected ellipse on to the observer's plane, as a function of the ellipsoid dimensions (A, B, C) and of its orientation (θ, ϕ) .

Now from Eq. (32) of the projected ellipse on to the $\{\mathbf{x}_0, \mathbf{y}_0\}$ -plane, the a and b semi-axis values can be calculated from the following equations:

$$a^2 b^2 = A^2 B^2 C^2 Q_{zz},$$

and

$$a^2 + b^2 = q_{xx} + q_{yy}.$$

Using the set of equations for the R_{jk} elements from (R) as functions of the Euler's angles (θ, ϕ, ψ) , Eq. (31) and Eq. (33) for q_{xx} and q_{yy} , one obtains:

$$a^2 b^2 = A^2 C^2 \sin^2 \theta \cos^2 \phi + B^2 C^2 \sin^2 \theta \sin^2 \phi + A^2 B^2 \cos^2 \theta, \quad (35)$$

and

$$a^2 + b^2 = A^2(\cos^2 \phi + \cos^2 \theta \sin^2 \phi) + B^2(\sin^2 \phi + \cos^2 \theta \cos^2 \phi) + C^2 \sin^2 \theta. \quad (36)$$

Using these equations one can calculate the semi-axes a and b of the projected ellipse using the elements (A, B, C) of the ellipsoid and the corresponding Euler angles between the two reference systems. Eq. (34), Eq. (35) and Eq. (36) fully determine the projected ellipse on to the plane of the observer.

The inverse problem: ellipses vs. ellipsoids.

The inverse problem deals with the estimate of the parameters that characterize an ellipsoid using elements measured on to its projected ellipse. The ellipse is defined by its semi-axis values a and b , that are measured along its symmetry axes \mathbf{x}_e and \mathbf{y}_e , respectively. The relative position of the \mathbf{x}_e axis with respect to the line of nodes is defined by the angle δ (position angle) such as $0 \leq \delta \leq \pi/2$. The steps below describe the process of inverting Eq. (34), Eq. (35) and Eq. (36). The new auxiliary variable K is

$$K^2 = A^2 \cos^2 \phi + B^2 \sin^2 \phi = \frac{A^2 + B^2}{2} + \frac{A^2 - B^2}{2} \cos 2\phi. \quad (37)$$

Using Eq. (35) and Eq. (36) one has:

$$a^2 b^2 - K^2(a^2 + b^2) = [A^2 B^2 - K^2(A^2 - B^2)] \cos^2 \theta - K^2 \sin^2 \theta \quad (38)$$

and from equation Eq. (34) one has

$$\frac{\tan 2\delta[(a^2 + b^2) - 2K^2]}{2 \cos \theta} = -\frac{A^2 - B^2}{2} \sin^2 \phi \quad (39)$$

From Eq. (37) and Eq. (39) it is easy to establish the connection between the variable K (which includes three elements of the ellipsoid: A , B and PA ϕ) and the measured parameters of the projected ellipse: a , b and δ :

$$K^2 = \frac{a^2 + b^2}{2} + \frac{a^2 - b^2}{2} \cos 2\delta \equiv a^2 \cos^2 \delta + b^2 \sin^2 \delta. \quad (40)$$

From Eq. (39) follows the equation:

$$\frac{A^2 - B^2}{2} \sin^2 \phi = \frac{a^2 - b^2}{2} \frac{\sin 2\delta}{\cos \theta}. \quad (41)$$

From Eq. (37) and Eq. (41) it follows:

$$A^2 = \frac{a^2 + b^2}{2} \left[1 + E \left(\cos 2\delta + \sin 2\delta \frac{\sin \phi}{\cos \phi} \frac{1}{\cos \theta} \right) \right], \quad (42)$$

and

$$B^2 = \frac{a^2 + b^2}{2} \left[1 + E \left(\cos 2\delta - \sin 2\delta \frac{\cos \phi}{\sin \phi} \frac{1}{\cos \theta} \right) \right], \quad (43)$$

where E measures the ellipticity:

$$E \equiv \frac{a^2 - b^2}{a^2 + b^2} \quad (44)$$

Finally, from Eq. (36) it follows:

$$C^2 = \frac{a^2 + b^2}{2} \left[1 + E \left(2 \sin 2\delta \frac{\cos \theta}{\sin^2 \theta} \frac{\cos 2\phi}{\sin 2\phi} - \cos 2\delta \frac{1 + \cos \theta}{\sin^2 \theta} \right) \right]. \quad (45)$$

Thus the problem of finding ellipsoid quantities A , B and C has been solved: they are functions of the a , b and $\delta (= \delta_e + \psi)$ parameters that are associated with the projected ellipse and of the position angles (θ, ϕ) of the ellipsoid with respect to the observer. Briefly put:

$$A, B, C = f(a, b, \delta_e, \theta, \phi, \psi). \quad (46)$$

These calculations were implemented in a FORTRAN code that for a given galaxy calculates $p \equiv B/A$, and $q \equiv C/A$ parameters that are then used in generating of the orbit library in a triaxial potential of the form (see Eq. (23) of Appendix 3). The three Euler angles are free parameters: inclination θ is chosen from the two-integral (2I) modeling procedure (the angle that provides the best 2I fit is taken). The other two angles are then chosen by visual inspection of several combinations: the smoothest solutions that do not exceed a value of one for p and q are then taken. Since the Schwarzschild modeling is a CPU intensive procedure and a large disk storage is also required, it was only applied to IC3370 (but in future I plan to test it on several other galaxies from my sample).

2.2.3 MODELING RESULTS

Using the three-integral modeling procedure I analyzed all galaxies that were presented in Chapter 1. I again assume symmetry about the y -axis and therefore I folded all the observational data taking into account that velocity and h_3 are odd functions of the radius, and that velocity dispersion and h_4 are even functions of the radius. Symmetry assumption in the case of the galaxies that belong to the Fornax cluster (as shown in Chapter 1) is highly questionable so the results have to be taken with great caution.

2.2.3.1 Sample 1

IC3370

I performed numerous tests with this galaxy: different potentials, different inclinations, different values of the parameters that figure in the different potentials were tested. I present here only the best fits. An inclination of 50° was used everywhere. In Fig. 11 (left) I present two tests: one is for the $M/L_B = 7$ potential and is given as a thick solid line, and the other is a test made with an axisymmetric logarithmic potential ($q = 0.8$). As one might expect, given large isophotal twisting of IC3370, a test made with an axisymmetric potential does not provide a good fit to the data. A much better fit is obtained using a constant mass-to-light ratio potential. In Fig. 11 (right) I present results of modeling made in the triaxial logarithmic potential. The thin solid line is for the potential for which $p = q = 0.8$. Thick lines are for the particular modeling (as mentioned earlier applied only in case of IC3370) in a logarithmic triaxial potential in which p and q vary with a radius, as described above. Viewing angles that were chosen: $\theta = 80^\circ$, $\phi = 20^\circ$ and $\psi = 60^\circ$. The differences between them are not large and the general impression is that the triaxial potential provides a better fit for the h_4 parameter and the constant mass-to-light ratio provides a better fit for the h_3 parameter. If one assumes that adopting a logarithmic potential means that there is a dark matter within a given galaxy, the case of IC3370 is a difficult one: a conclusion based only on the Schwarzschild modeling implies that to $3R_e$ one cannot exclude constant mass-to-light ratio. The fact that logarithmic potential also fits this galaxy means that there is a hint of the existence of the dark matter. Therefore, some firm conclusion cannot be given as was possible in the case of the two-integral modeling, but the overall impression is that the constant mass-to-light ratio is more adequate at least interior to $\sim 2R_e$. In addition that I tested different values of mass-to-light ratios, but the predicted values of the Gauss-Hermite parameters all seem to be very similar.

IC1459

In Fig. 12 I present several examples of the modeling of IC1459. They are made with small variations in the inclination angle, but this does not affect the conclusions. On the left hand side I plotted two examples of modeling using a constant mass-to-light ratio: a case with $M/L_B = 10$ is plotted using a thick solid line, and a case with a larger $M/L_B = 20$ is plotted using a thin solid line. Note that in the case of the lower mass-to-light ratio a rather good fit for h_4 is attained up to $\sim 2R_e$. A larger mass-to-light potential produces a discrepancy with observed data in the inner region of IC1459. The h_3 parameter cannot be fitted properly in a region between $\sim 40''$

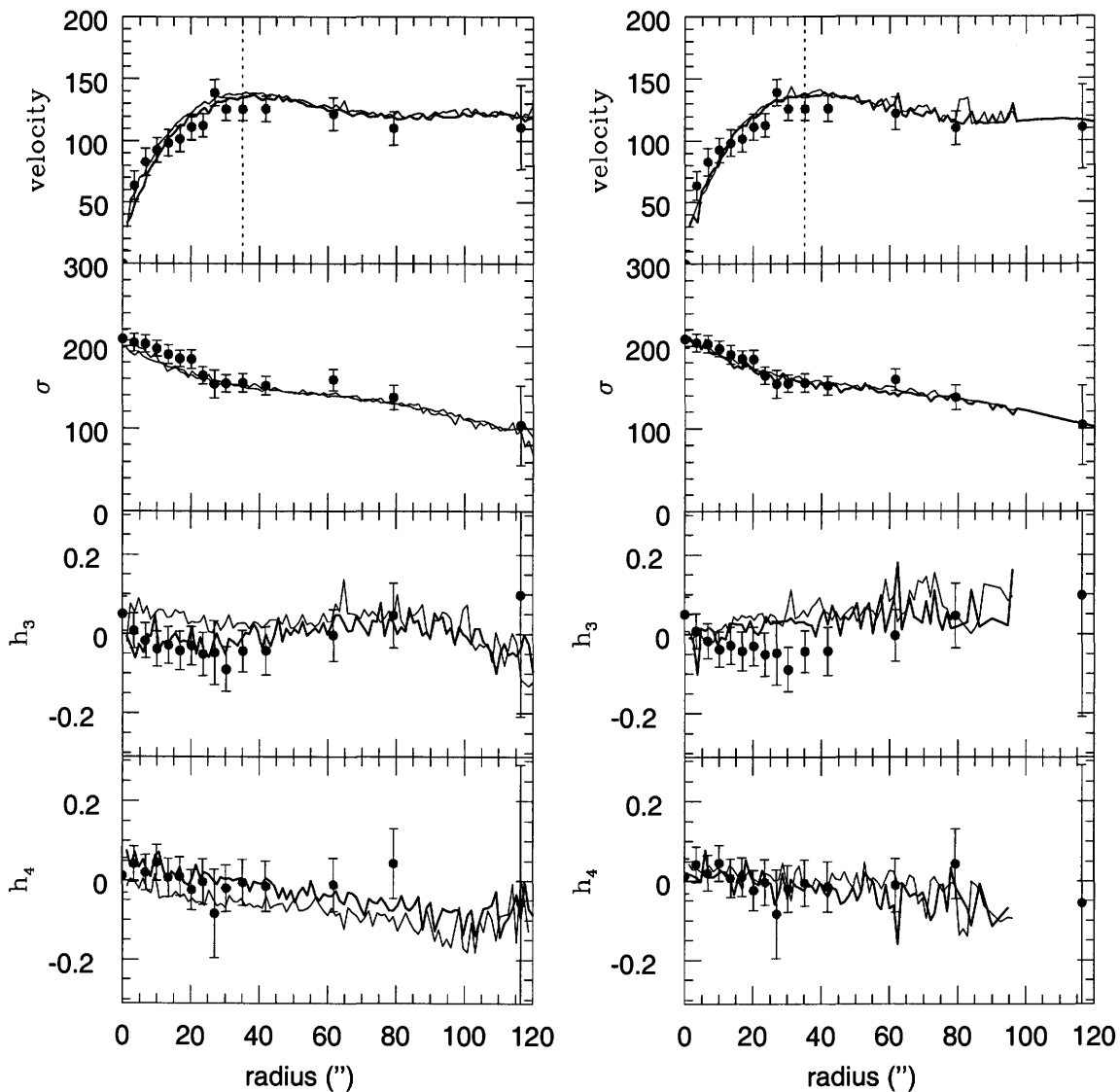


Figure 11: Predictions of the three-integral modeling for IC3370 for the major axis. Left: The thick solid line is for a constant mass-to-light potential with $M/L_B = 7$. The thin solid line is for the axisymmetric logarithmic potential with $q = 0.8$. Right: The thick solid line is for a triaxial logarithmic potential in which p and q vary along the radius. The thin solid line is for the triaxial logarithmic potential with fixed $p = q = 0.8$. Vertical dotted line indicates one effective radius.

and $\sim 70''$. On the right hand side of Fig. 12 I present two different tests made using logarithmic potentials: the thick solid line represents an axisymmetric logarithmic potential with $q = 0.8$, and the thin solid line is for the triaxial logarithmic potential with fixed $p = q = 0.8$. A constant mass-to-light ratio ($M/L_B = 10$) provides a better fit in the inner region. Again, in the case of IC1459 it is difficult to draw a conclusion concerning the existence of dark matter: the fact is that a constant mass-to-light ratio ($M/L_B \sim 10$) provides a successful fit up to $\sim 2R_e$, so a conservative statement would be that interior to $2R_e$ there is no need for the dark matter in this galaxy. Of

concern here is that $M/L_B \sim 10$ begins to be high for the stellar population expected in an E galaxy. For the outer regions, the situation is rather complex because none of the models tested (in addition to the tests shown here I performed numerous other tests with different combinations of parameters) could produce significant positive values of h_4 that may imply the existence of radial anisotropies. However, since the observed velocity dispersion steadily decreases one may conclude that the influence of the dark halo is very small (if any) interior to $3R_e$. One may wonder whether radial velocities could result from the process (coalition of two galaxies) that produced the counterrotating core (see the end of Section 2.1.2.1).

2.2.3.2 Sample 2

NGC1336

In Fig. 13 I present several examples of the modeling of NGC1336. The inclination angle was 50° in all the cases. On the left hand side I plotted two examples of modeling using a constant mass-to-light ratio: a case with $M/L_B = 7$ is plotted using the thick solid line, and a case with a smaller $M/L_B = 5$ is plotted using the thin solid line. While in both cases h_3 can be fitted, neither of these two tests provided a satisfactory fit to h_4 in the inner regions. On the right hand side of Fig. 13 I plotted two different tests made using logarithmic potentials: the thick solid line represents an axisymmetric logarithmic potential with $q = 0.8$, and the thin solid line is for the triaxial logarithmic potential with fixed $p = q = 0.8$. Both logarithmic potentials provide a better fit to the h_4 parameter; note, however, the larger noise in the case of the triaxial potential. Since the observations of NGC1336 extend out to $\sim 0.8 R_e$ one cannot say much about the dark matter in this galaxy. I only comment that the constant mass-to-light ratio potential is not adequate in the inner parts (interior to $\sim 5''$) and that in general logarithmic potentials provide a better fit. Note that this galaxy (Fig. 8 from Chapter 1) possesses an axisymmetric profile: the P.A. changes only in a very interior part ($\lesssim 2''$).

NGC1339

Fig. 14 shows four different examples of the modeling of NGC1336. The inclination angle was 50° in all the cases. On the left hand side I plotted two examples of modeling using a constant mass-to-light ratio: a case with $M/L_B = 7$ is plotted using the thick solid line, and a case with a smaller $M/L_B = 5$ is plotted using the thin solid line. In both cases h_3 can be fitted, except for the last observed point at $\sim 23''$. The modeled h_4 parameter shows departures from the observed one in the inner region; from $\sim 0''$ to $\sim 5''$ the fit is poor, and also beyond $15''$ it is not very good. On the right hand side of Fig. 14 I plotted two different tests made using logarithmic potentials: the thick solid line represents an axisymmetric logarithmic potential with $q = 0.8$, and the thin solid line is for the triaxial logarithmic potential with fixed $p = q = 0.8$. The triaxial potential provides a better fit to the h_3 parameter in the inner region. It is difficult to say which of the two provides a better agreement with the observed value of h_4 : in the inner region ($< 5''$) it is the axisymmetric potential, but between $\sim 5''$ and $\sim 10''$ it is the triaxial potential. Beyond $1R_e$ a successful fit could not be achieved. An axisymmetric potential provides a slightly better fit to h_3 (but in general the fit is not good). NGC1339 is an interesting example of a galaxy with a rather large h_4 parameter

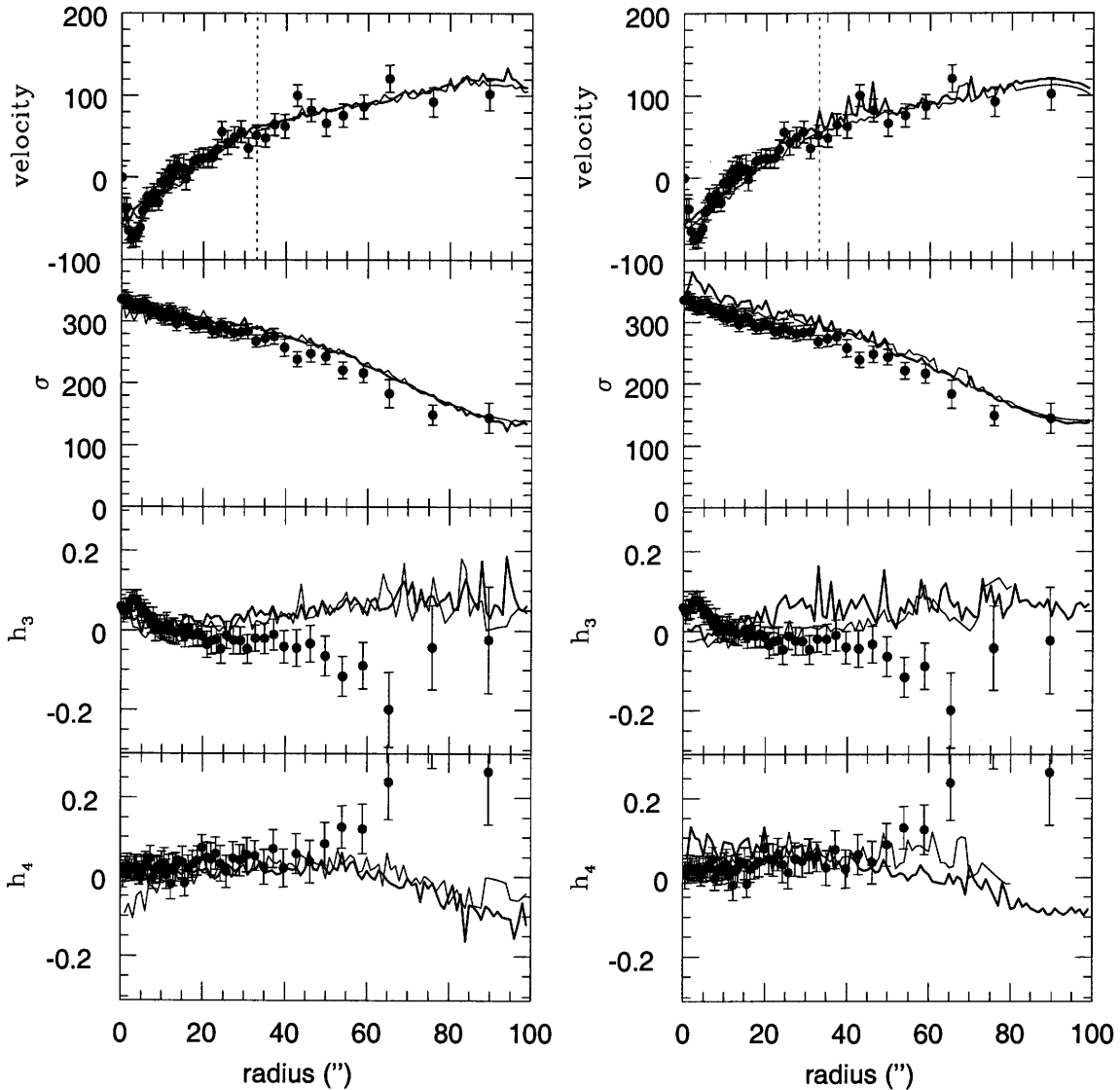


Figure 12: Predictions of the three-integral modeling for IC1459 for the major axis. Left: The thick solid line is for a constant mass-to-light potential with $M/L_B = 10$ (inclination angle is 50°). The thin solid line is for a constant mass-to-light potential with $M/L_B = 20$ (inclination angle is 70°). Right: The thick solid line is for an axisymmetric logarithmic potential ($q = 0.8$) (inclination angle is 50°). The thin solid line is for the triaxial logarithmic potential with fixed $p = q = 0.8$ (inclination angle is 50°). Vertical dotted line indicates one effective radius.

($h_4 \approx 0.15$ at $\sim 1.5R_e$) which shows an increase of the velocity dispersion. This could mean that there is dark matter in the outer parts of the galaxy. Certainly, this galaxy deserves deeper a spectroscopic study to better establish the behaviour of h_4 and the velocity dispersion in its outer parts.

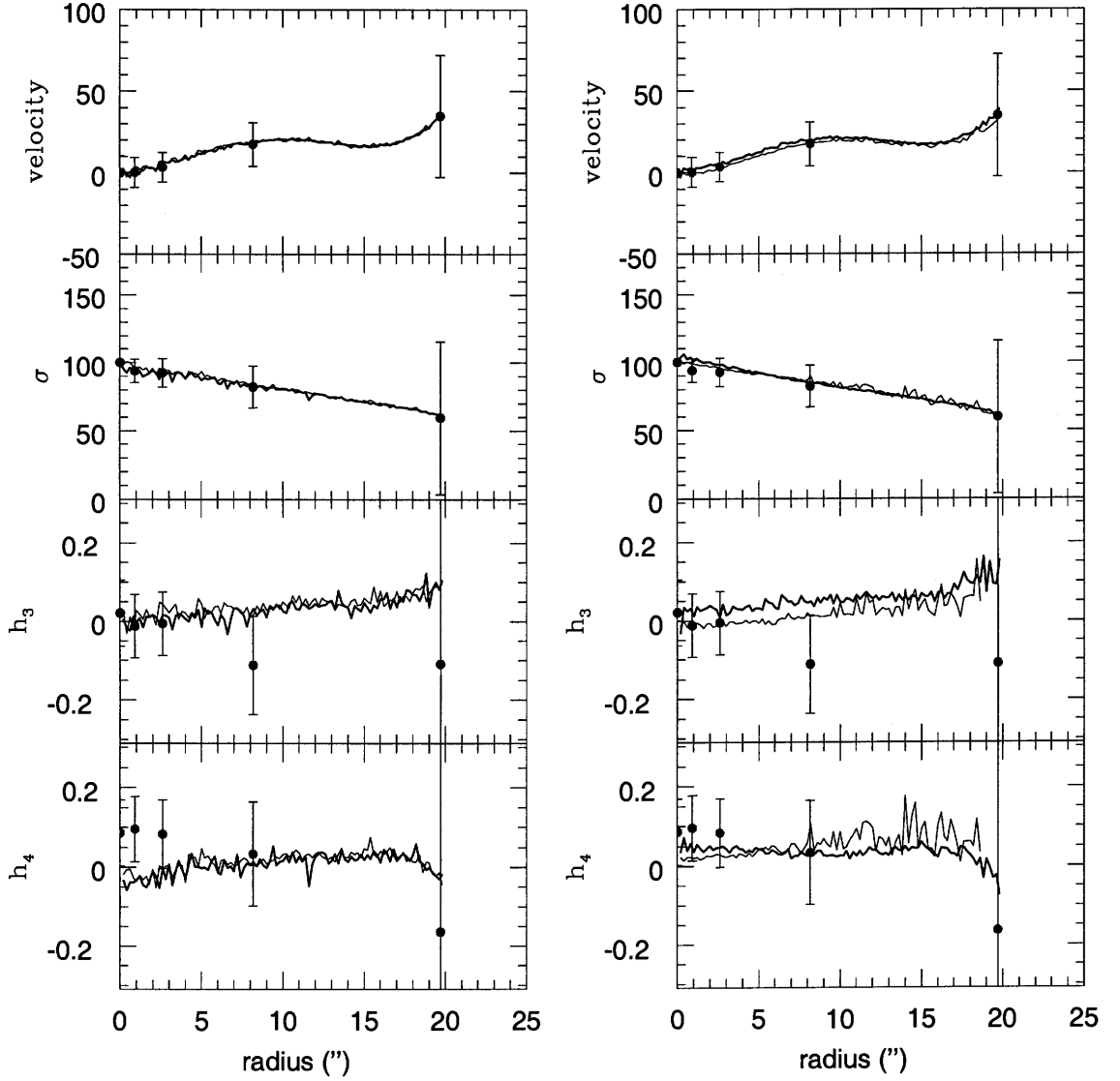


Figure 13: Predictions of the three-integral modeling for NGC1336 for the major axis. Left: The thick solid line is for a constant mass-to-light potential with $M/L_B = 7$ (inclination angle is 50°). The thin solid line is for the a constant mass-to-light potential with $M/L_B = 5$ (inclination angle is 50°). Right: The thick solid line is for a axisymmetric logarithmic potential ($q = 0.8$) (inclination angle is 50°). The thin solid line is for the triaxial logarithmic potential with fixed $p = q = 0.8$ (inclination angle is 50°).

NGC1373

In Fig. 15 I present several examples of the modeling of NGC1373. The inclination angle is 40° in the case of the constant mass-to-light ratio, and 50° in the case of the logarithmic potentials, but this does not affect the conclusions. On the left hand side I present two examples of modeling using a constant mass-to-light ratio: the case with $M/L_B = 6$ is plotted using thick solid line, and the case with a larger $M/L_B = 15$ is plotted using a thin solid line. On the right hand

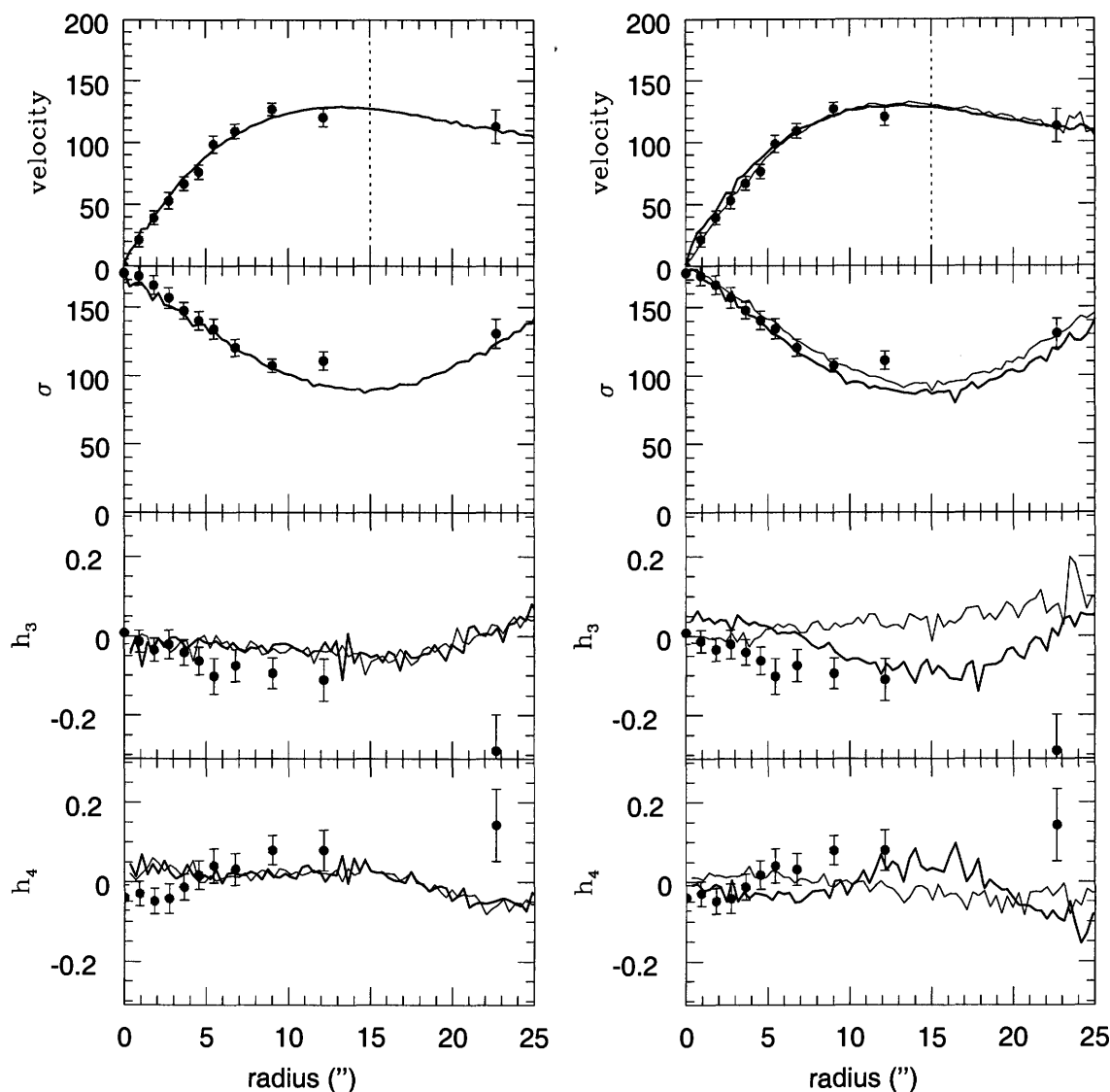


Figure 14: Predictions of the three-integral modeling for NGC1339 for the major axis. Left: The thick solid line is for a constant mass-to-light potential with $M/L_B = 7$ (inclination angle is 50°). The thin solid line is for the a constant mass-to-light potential with $M/L_B = 5$ (inclination angle is 50°). Right. The thick solid line is for a axisymmetric logarithmic potential ($q = 0.8$) (inclination angle is 50°). The thin solid line is for the triaxial logarithmic potential with fixed $p = q = 0.8$ (inclination angle is 50°).

side of Fig. 15 I plotted two different tests made using logarithmic potentials: the thick solid line represents an axisymmetric logarithmic potential with $q = 0.8$, and the thin solid line is for the triaxial logarithmic potential with fixed $p = q = 0.8$. It is very hard to draw any conclusions about the dark matter judging from this kind of modeling. All tests produced similar results and they all seem to fit the Gauss-Hermite parameters. However, there is a strong hint that there is dark matter in this galaxy, because from $1R_e$ the velocity dispersion has a strong increase. Because of the fact

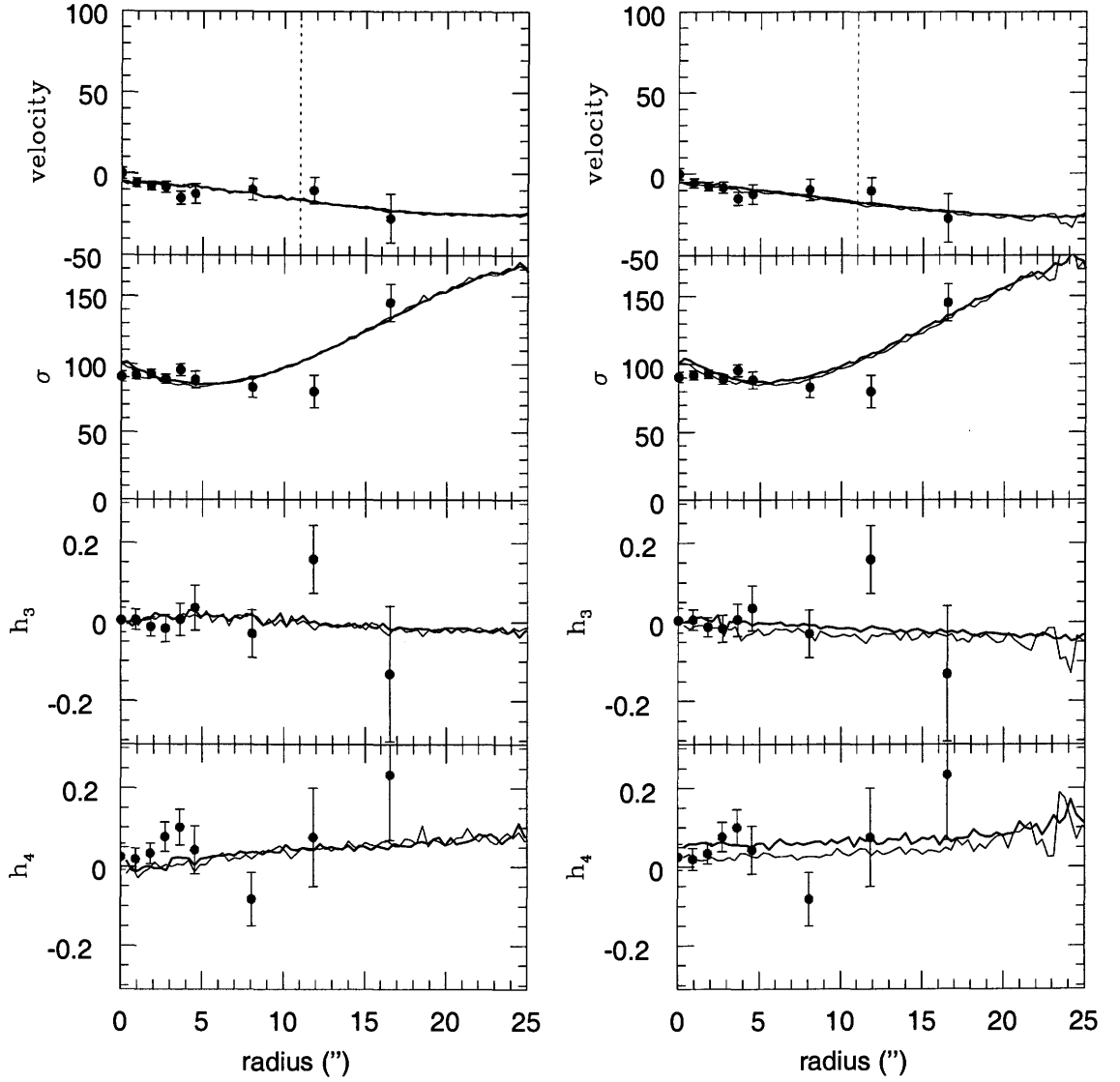


Figure 15: Predictions of the three-integral modeling for NGC1373 for the major axis. Left: The thick solid line is for a constant mass-to-light potential with $M/L_B = 6$. The thin solid line is for the a constant mass-to-light potential with $M/L_B = 15$. Right: The thick solid line is for a axisymmetric logarithmic potential ($q = 0.8$). The thin solid line is for the triaxial logarithmic potential with fixed $p = q = 0.8$. Inclination angle is 40° in the case of the constant mass-to-light ratio potentials and 50° in the case of the logarithmic ones. Vertical dotted line indicates one effective radius.

that there are asymmetries in the stellar kinematics and the Gauss-Hermite parameters have large error bars, this represents a case where firm conclusions cannot be given. This galaxy certainly deserves more attention, both observationally and theoretically.

NGC1374

Fig. 16 provides several examples of the modeling of NGC1374. The inclination angle is 40° in

all cases. On the left hand side I plotted two examples of modeling using a constant mass-to-light ratio: the case with $M/L_B = 6$ is plotted using a thick solid line, and a case with a larger $M/L_B = 15$ is plotted using a thin solid line. On the right hand side of Fig. 16 I plotted two different test made using logarithmic potentials: the thick solid line represents an axisymmetric logarithmic potential with $q = 0.9$, and the thin solid line is for the triaxial logarithmic potential with fixed $p = q = 0.9$. Also in this case it is very difficult to draw any conclusions about the dark matter judging from this kind of modeling. Both logarithmic potentials produced marginally better fits for h_4 in the inner regions of NGC1374. Beyond one effective radius all tests produced very similar results. This galaxy does not show a steeply declining velocity – note however that the data extend only to $\sim 1.2R_e$. This is another galaxy deserving more attention, both observationally and theoretically.

NGC1379

In Fig. 17 I present several examples of the modeling of NGC1379. The inclination angle was different for different cases (given in Fig. 17). On the left hand side I plotted two examples of modeling using a constant mass-to-light ratio: the case with $M/L_B = 7$ is plotted using a thick solid line, and the case with a larger $M/L_B = 15$ is plotted using thin solid line. On the right hand side of Fig. 17 I plotted two different test made using logarithmic potentials: thick solid line represents an axisymmetric logarithmic potential with $q = 0.9$, and the thin solid line is for the triaxial logarithmic potential with fixed $p = q = 0.8$. All tests produced rather similar results and they all seem to fit the Gauss-Hermite parameters (logarithmic potentials are insignificantly better). Therefore, it seems inappropriate to draw any conclusions about the dark matter judging from this kind of modeling for NGC1379: observational data extend out to $\sim 1R_e$, for which all tested models fit the observations. This is another good candidate for further observations: it would be especially interesting to see the behaviour of the velocity dispersion (and h_4) at larger radii.

NGC1399

Fig. 18 presents some examples of the modeling of NGC1399. The inclination angle was different for different cases (given in Fig. 18). On the left hand side I plotted two examples of modeling using a constant mass-to-light ratio: the case with $M/L_B = 7$ is plotted using a thick solid line, and the case with a larger $M/L_B = 15$ is plotted using thin solid line. On the right hand side of Fig. 18 I plotted two different test made using logarithmic potentials: the thick solid line represents an axisymmetric logarithmic potential with $q = 0.9$, and the thin solid line is for the triaxial logarithmic potential with fixed $p = q = 0.9$. All tests produced similar fits and they all seem to fit the Gauss-Hermite parameters. The axisymmetric logarithmic potential predicts a slightly larger velocity dispersion. It is interesting that constant mass-to-light ratio potentials predict h_3 and h_4 parameters that are in agreement with the observed values and the velocity dispersion does not show a tendency to decrease. NGC1399 has been the subject of numerous analyses (Saglia et al. 2000 and references therein). Saglia et al. (2000) found that the gravitational potential is dominated by the luminous component out to the last data point in their observations ($97''$), with a mass-to-light ratio $M/L_B = 10$. They found that the influence of the dark component

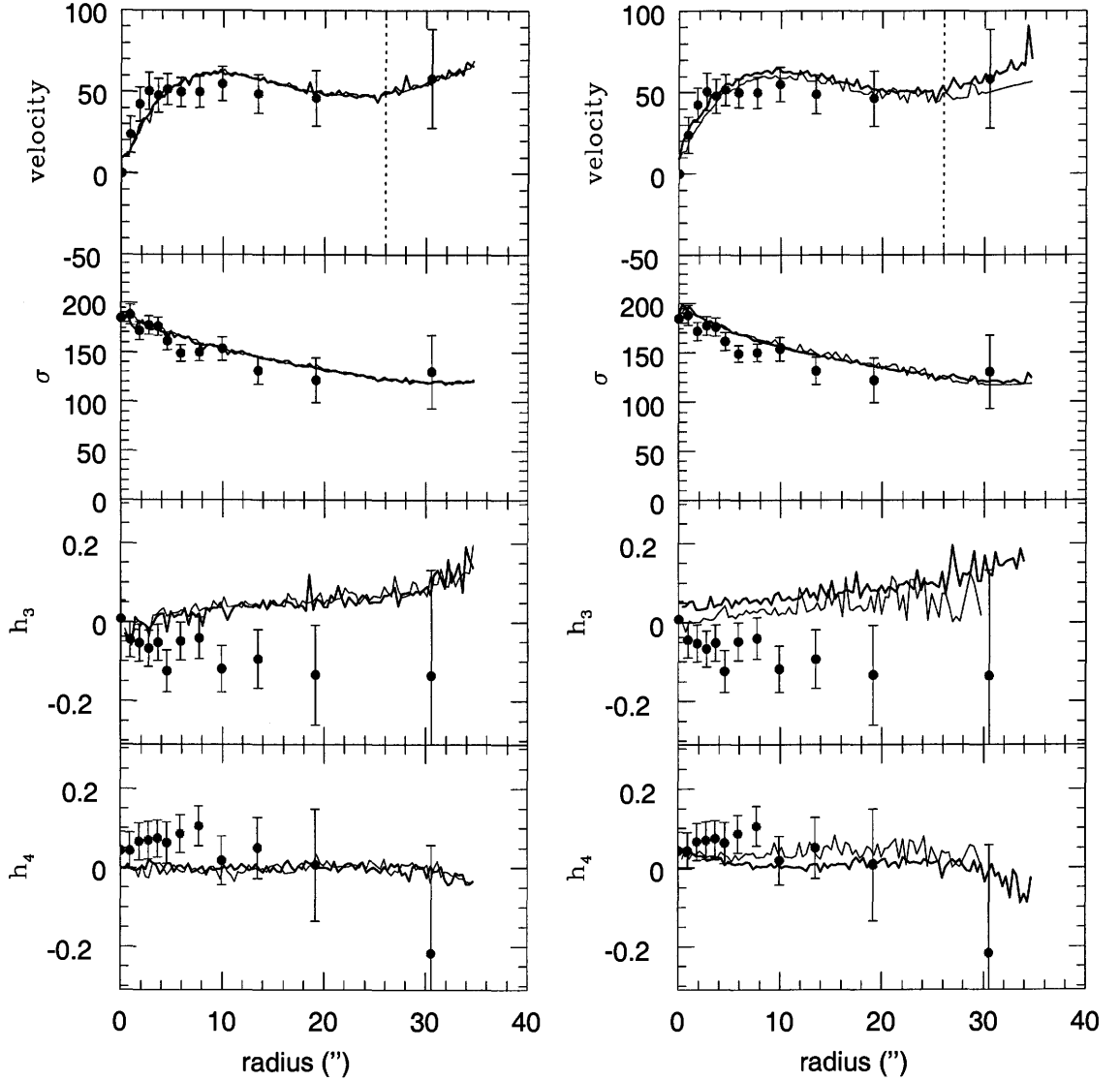


Figure 16: Predictions of the three-integral modeling for NGC1374 for the major axis. Left: The thick solid line is for a constant mass-to-light potential with $M/L_B = 6$. The thin solid line is for the a constant mass-to-light potential with $M/L_B = 15$. Right. The thick solid line is for a axisymmetric logarithmic potential ($q = 0.9$). The thin solid line is for the triaxial logarithmic potential with fixed $p = q = 0.9$. Inclination angle is 40° in all the cases. Vertical dotted line indicates one effective radius.

is marginally detected starting from $\sim 60''$. Recently, Napolitano et al. (2002) using isotropic axisymmetric Jeans equation found a mass-to-light ratio $M/L_B = 26$ within $400''$. Using the Schwarzschild modeling approach I found that both potentials give a good fit to the observed Gauss-Hermite parameters. I confirm that even in this simple modeling the discrepancy (for the in the velocity and in the velocity dispersion) emerges at $\sim 60''$: one can compare the fitted velocity dispersion in an axisymmetric case and in case of constant mass-to-light ratio. Both agree within

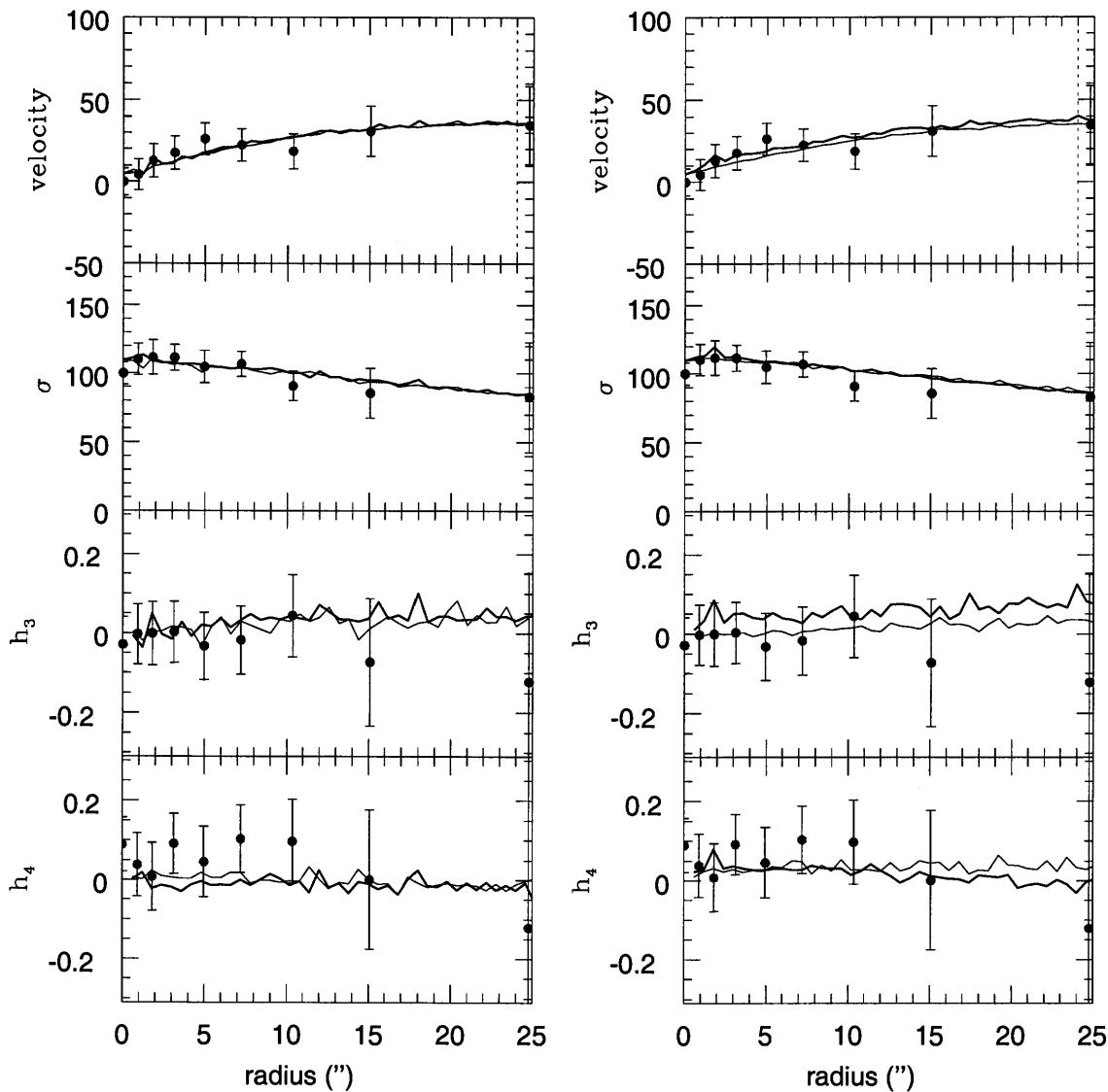


Figure 17: Predictions of the three-integral modeling for NGC1379 for the major axis. Left: The thick solid line is for a constant mass-to-light potential with $M/L_B = 7$ (inclination angle is 40°). The thin solid line is for a constant mass-to-light potential with $M/L_B = 15$ (inclination angle is 30°). Right: The thick solid line is for an axisymmetric logarithmic potential ($q = 0.9$) (inclination angle is 30°). The thin solid line is for a triaxial logarithmic potential with fixed $p = q = 0.8$ (inclination angle is 50°). Vertical dotted line indicates one effective radius.

the error bars, but the axisymmetric modeling predicts larger velocity dispersion.

I stress that there exists uncertainty related to NGC1399: the problem of establishing its effective radius. As noted in TABLE 1-1 I used the effective radius of $42''$ given by Bicknell et al. (1989), but Caon et al.(1994) calculated a value of $127''$ by fitting their extended photometry. As suggested in Saglia et al. (2000) the value of the effective radius of NGC1399 is highly uncertain, because its light profile is very shallow in the outer regions. Note, however, that this value did

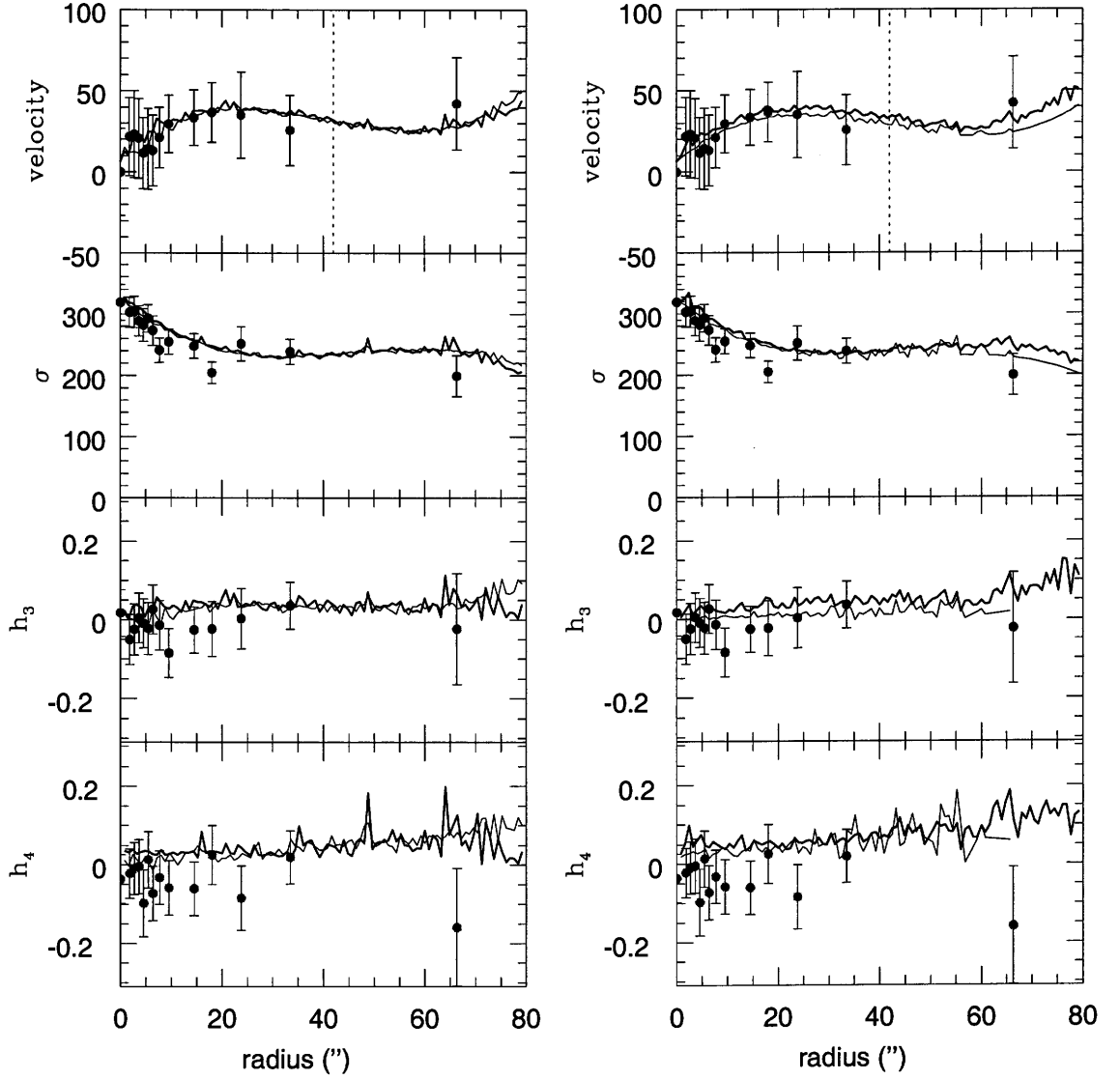


Figure 18: Predictions of the three-integral modeling for NGC1399 for the major axis. Left: The thick solid line is for a constant mass-to-light potential with $M/L_B = 7$ (inclination angle is 40°). The thin solid line is for the a constant mass-to-light potential with $M/L_B = 15$ (inclination angle is 30°). Right: The thick solid line is for a axisymmetric logarithmic potential ($q = 0.9$) (inclination angle is 30°). The thin solid line is for the triaxial logarithmic potential with fixed $p = q = 0.8$ (inclination angle is 50°). Vertical dotted line indicates one effective radius.

not influence the modeling procedure and the final results — it is given in the plot merely as an orientation for the reader.

NGC1404

In Fig. 19 I present several examples of the modeling of NGC1404. The inclination angle was

different for different cases (given in Fig. 19). On the left hand side I plotted two examples of modeling using a constant mass-to-light ratio: the case with $M/L_B = 6$ is plotted using a thick solid line, and the case with a larger $M/L_B = 15$ is plotted using a thin solid line (in both cases the inclination was 40°). On the right hand side of Fig. 19 I plotted the results of two different tests made using logarithmic potentials: the thick solid line represents an axisymmetric logarithmic potential with $q = 0.8$ (inclination was 50°), and the thin solid line is for the triaxial logarithmic potential with fixed $p = q = 0.8$ (inclination was 60°). All tests produced similar results and they all seem to fit the Gauss-Hermite parameters. The best fit of the Gauss-Hermite parameters is obtained using constant mass-to-light potential ($M/L_B = 6$), and this is especially true in the outer parts of the galaxy where all other potentials seem to fail. Note also that this potential produced the lowest amount of noise in the fit; in the case of the logarithmic potentials there is much noise in the fit of the velocity and velocity dispersion. Therefore, judging from the Schwarzschild modeling, one can say that NGC1404 can be fitted out to $\sim 3R_e$ with the constant mass-to-light ratio potential for which $M/L_B = 6$, and that there is no need for dark matter. It may be that the flat dispersion profile from $\sim 1.6R_e$ to $\sim 3R_e$ is flat owing to strong tangential anisotropies (note the large error bars for h_4). However, this conclusion is not firm, because as can be seen from the right hand side of Fig. 19 axisymmetric potentials provide a rather good fit to h_4 . This is another galaxy from the Fornax cluster that deserves further spectroscopic observations at several slit positions, so that two-integral modeling can be performed and its results compared with the Schwarzschild modeling.

NGC1419

In Fig. 20 I show several examples of the modeling of NGC1419. The inclination angle was 40° in all cases. On the left hand side I plotted two examples of modeling using a constant mass-to-light ratio: the case with $M/L_B = 6$ is plotted using a thick solid line, and the case with a larger $M/L_B = 15$ is plotted using a thin solid line. On the right hand side of Fig. 20 I plotted two different tests made using logarithmic potentials: the thick solid line represents an axisymmetric logarithmic potential with $q = 0.9$, and the thin solid line is for the triaxial logarithmic potential with fixed $p = q = 0.9$. All tests produced nearly the same result and they all seem to fit the Gauss-Hermite parameters (partly because of the large error bars). Because of this and the fact that the observations extend only out to $\sim 1R_e$ I refrain from drawing a conclusion about the existence of dark matter in NGC1419.

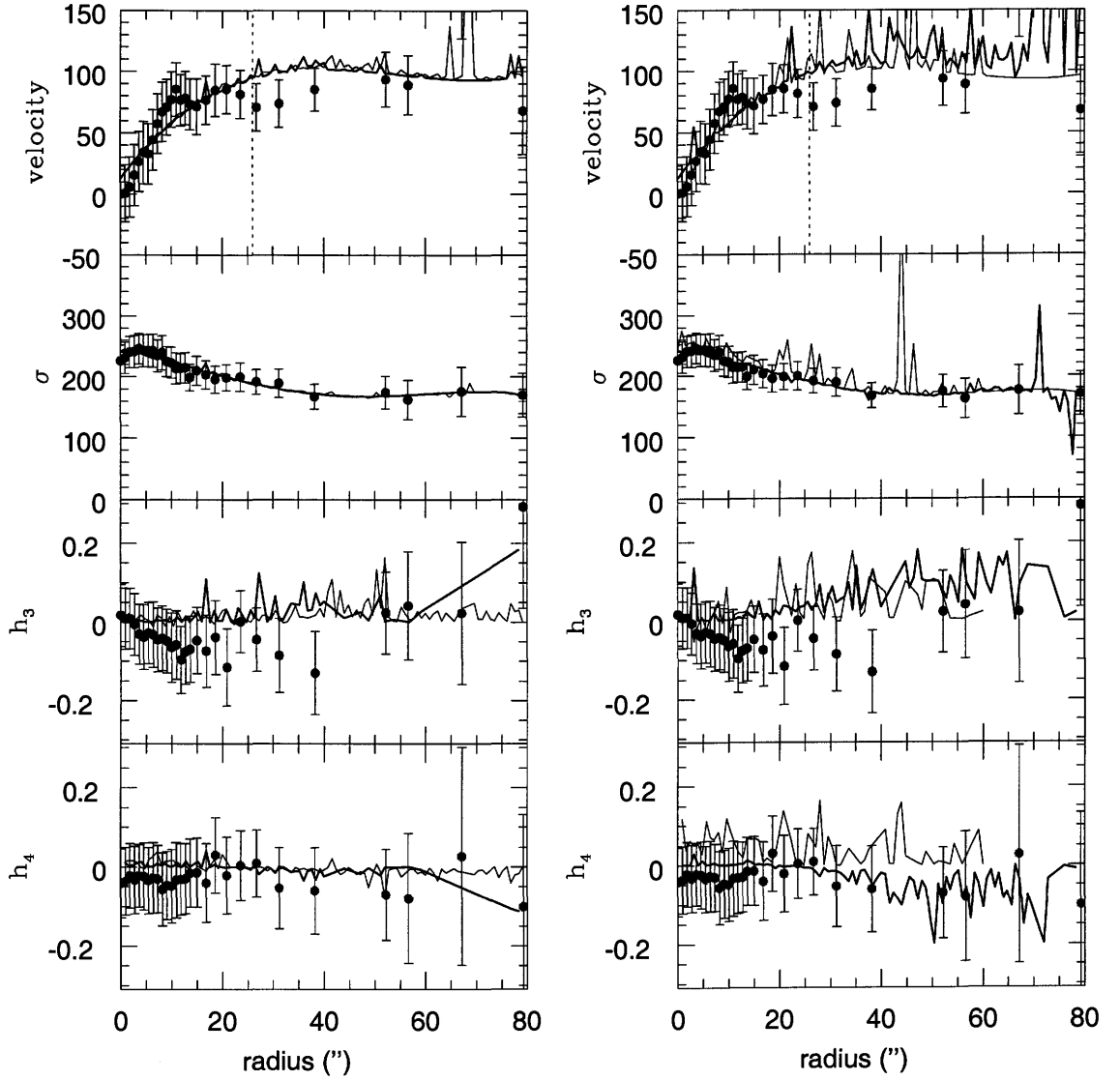


Figure 19: Predictions of the three-integral modeling for NGC1404 for the major axis. Left: The thick solid line is for a constant mass-to-light potential with $M/L_B = 7$ (inclination angle is 40°). The thin solid line is for the a constant mass-to-light potential with $M/L_B = 15$ (inclination angle is 30°). Right. The thick solid line is for a axisymmetric logarithmic potential ($q = 0.9$) (inclination angle is 30°). The thin solid line is for the triaxial logarithmic potential with fixed $p = q = 0.8$ (inclination angle is 50°). Vertical dotted line indicates one effective radius.

2.2.3.3 Sample 3

NGC4339

In Fig. 21 I show several examples of the modeling of NGC4339. The inclination angle was 40° in all cases. On the left hand side I plotted two examples of modeling using a constant mass-to-

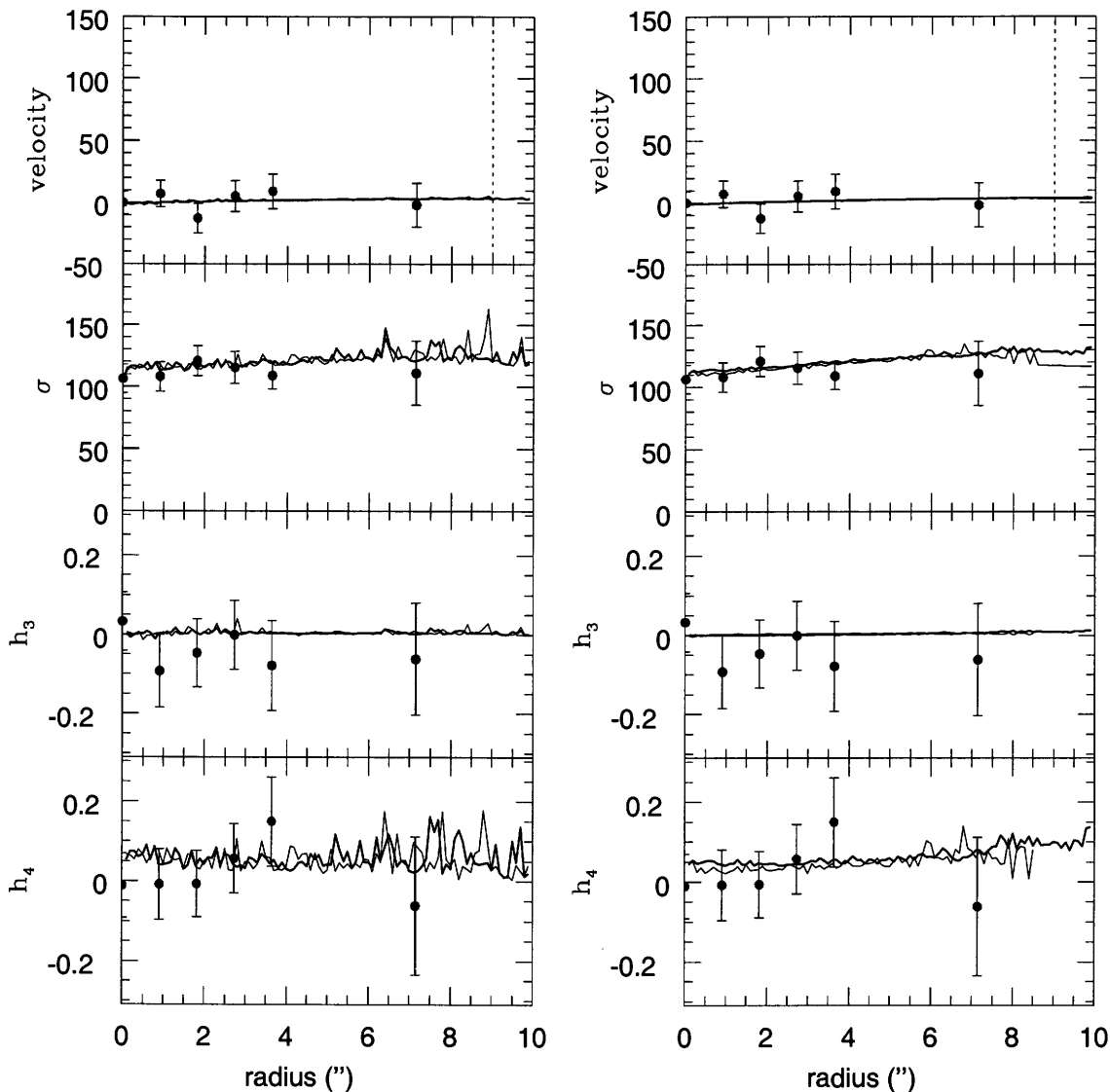


Figure 20: Predictions of the three-integral modeling for NGC1419 for the major axis. Left: The thick solid line is for a constant mass-to-light potential with $M/L_B = 6$. The thin solid line is for the a constant mass-to-light potential with $M/L_B = 15$. Right. The thick solid line is for a axisymmetric logarithmic potential ($q = 0.9$). The thin solid line is for the triaxial logarithmic potential with fixed $p = q = 0.8$. Inclination angle is 40° in all the cases. Vertical dotted line indicates one effective radius.

light ratio: the case with $M/L_B = 6$ is plotted using a thick solid line, and the case with a larger $M/L_B = 15$ is plotted using a thin solid line. On the right hand side of Fig. 21 I plotted two different tests made using logarithmic potentials: the thick solid line represents an axisymmetric logarithmic potential with $q = 0.9$, and the thin solid line is for the triaxial logarithmic potential with fixed $p = q = 0.9$. Note that I have omitted the outer two points outer point in h_3 and the outer point in h_4 because of their large uncertainty. Constant mass-to-light ratio potentials

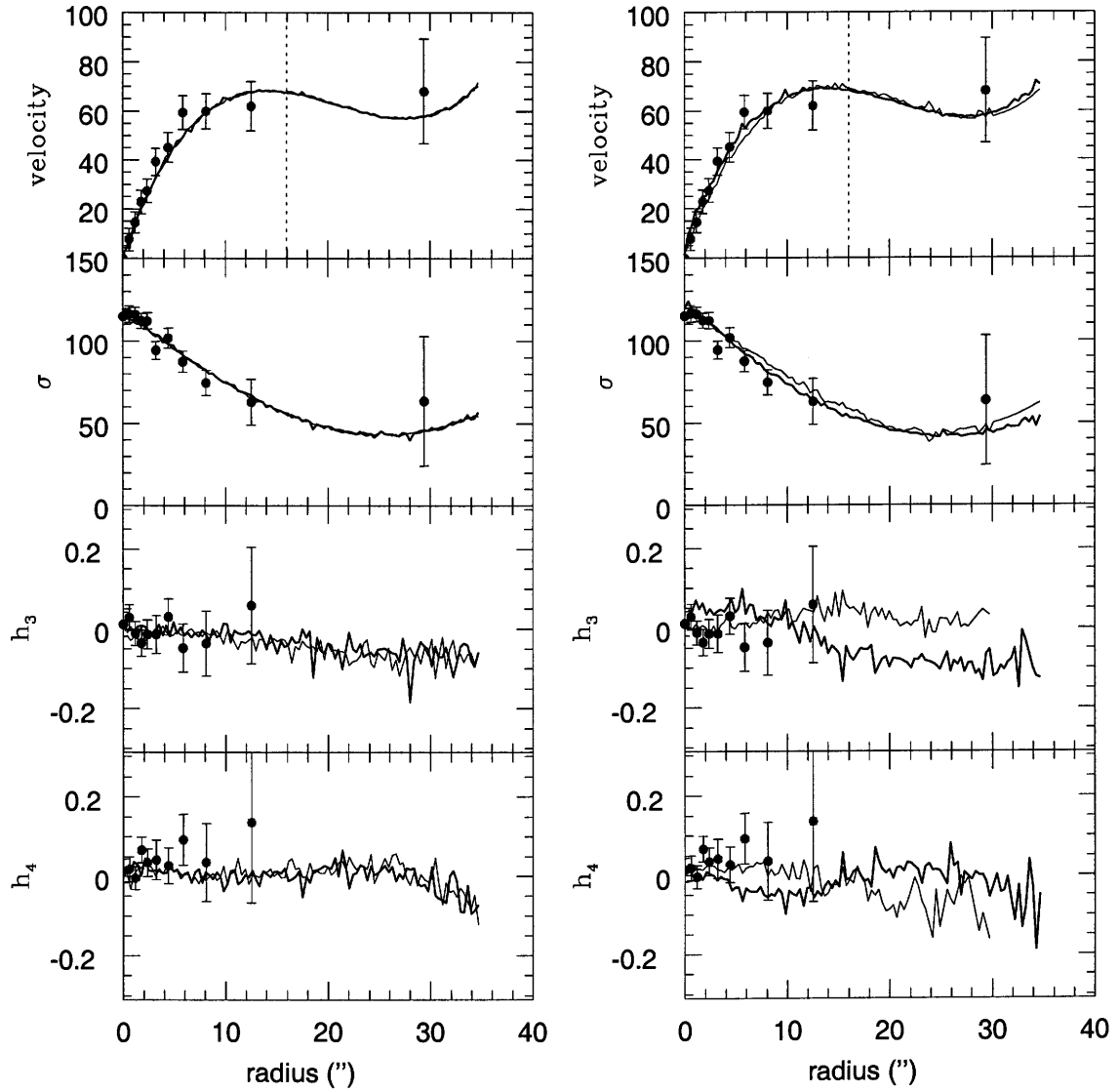


Figure 21: Predictions of the three-integral modeling for NGC4339 for the major axis. Left: The thick solid line is for a constant mass-to-light potential with $M/L_B = 6$. The thin solid line is for the a constant mass-to-light potential with $M/L_B = 15$. Right. The thick solid line is for a axisymmetric logarithmic potential ($q = 0.9$). The thin solid line is for the triaxial logarithmic potential with fixed $p = q = 0.8$. Inclination angle is 40° in all the cases. Vertical dotted line indicates one effective radius.

provided better fit interior to $1R_e$. In the outer parts both axisymmetric and constant mass-to-light ratio potentials give similar results. Therefore, in this case also I refrain from drawing a conclusion about the existence of dark matter in NGC4339.

NGC3379

In Fig. 22 I present several examples of the modeling of NGC3379. Again there is a small variation

in the inclination angle (indicated in caption of Fig. 22), but this does not affect the conclusions. On the left hand side I plotted two examples of modeling using a constant mass-to-light ratio: the case with $M/L_B = 7$ is plotted using a thick solid line, and the case with a larger $M/L_B = 10$ is plotted using thin solid line. In both cases a good fit for h_4 is obtained up to the last observed point ($\sim 2.3R_e$). The h_3 parameter cannot be fitted properly. Note the larger noise in the case of a slightly larger mass-to-light ratio. On the right hand side of Fig. 22 I plotted two different tests made using logarithmic potentials: the thick solid line represents an axisymmetric logarithmic potential with $q = 0.9$, and the thin solid line is for the triaxial logarithmic potential with fixed $p = q = 0.9$. From these plots one can conclude that the constant mass-to-light ratio between 7 and 9 can provide a good fit for h_4 . Note, however, that the h_3 parameter cannot be fitted in any of the cases that I present. Both logarithmic and triaxial potentials fail to produce a satisfactory fit in the inner region of the galaxy. In the outer parts the results of modeling that used such a potential do not show large discrepancies with respect to the observed points and look very similar to the results obtained in the case when constant mass-to-light ratio potentials were used in calculating orbits. Overall conclusion is that, as in the two-integral modeling, the constant mass-to-light ratio potential for $7 \lesssim M/L_B \lesssim 10$ can provide a good description of the observed stellar kinematics in NGC3379 and that there is no need for a dark matter halo interior to $\sim 2.3R_e$. However, there is a problem of fitting the h_3 parameter which cannot be fitted using available potentials.

NGC4105

In Fig. 23 I present several examples of the modeling of NGC4105. Again there is a small variation in the inclination angle (indicated in caption of Fig. 23), but this does not affect the conclusions. On the left hand side I plotted two examples of modeling using a constant mass-to-light ratio: the case with $M/L_B = 7$ is plotted using a thick solid line, and the case with a larger $M/L_B = 10$ is plotted using thin solid line. All tests provided a similar result, and one can only note that the triaxial logarithmic potential provided a marginally better fit to the h_4 profile, although, it must also be noted that the noise is larger in the outer region of NGC4105. In both cases a good fit for h_4 is obtained up to the last observed point ($\sim 2.3R_e$).

2.2.3.4 Sample 4

The photometric and kinematic data for three galaxies, NGC2434, NGC3706 and NGC5018, were taken from the literature (kinematics from Carollo et 1995, and photometry from Carollo & Danziger 1994a,b) in order to compare the modeling results. The results from Carollo et al. (1995) are given in Fig. 24.

NGC2434

In Fig. 25 I present several examples of the modeling of NGC2434. The inclination angle is taken to be 50° in the case of the constant mass-to-light ratio potentials and 40° in case of logarithmic potentials. On the left hand side I plotted two examples of modeling using a constant mass-to-light ratio: the case with $M/L_B = 5$ is plotted using a thick solid line, and the case with a larger

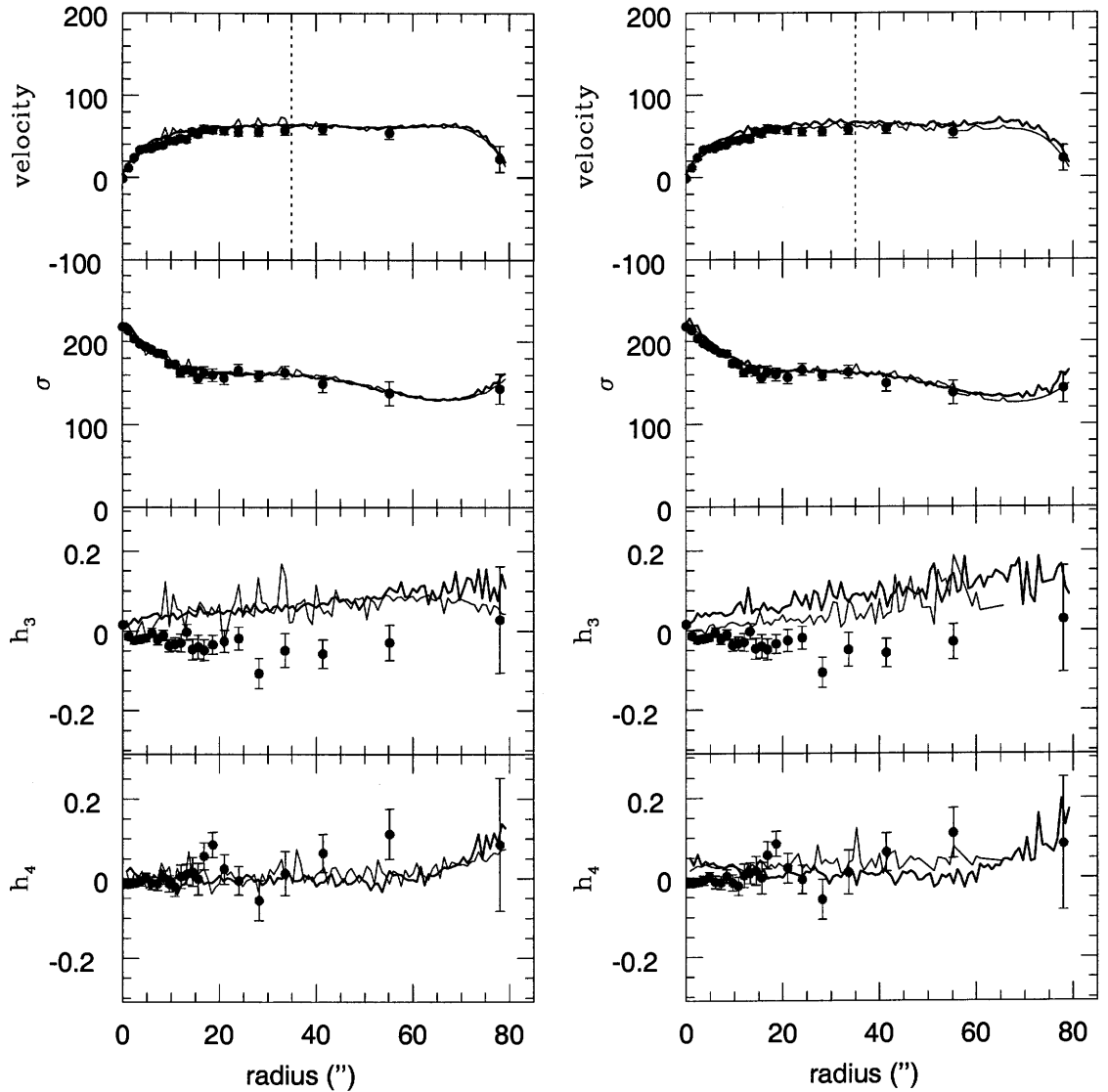


Figure 22: Predictions of the three-integral modeling for NGC3379 for the major axis. Left: The thick solid line is for a constant mass-to-light potential with $M/L_B = 7$ (inclination angle is 40°). The thin solid line is for the a constant mass-to-light potential with $M/L_B = 10$ (inclination angle is 50°). Right: The thick solid line is for a axisymmetric logarithmic potential ($q = 0.9$) (inclination angle is 40°). The thin solid line is for the triaxial logarithmic potential with fixed $p = q = 0.9$ (inclination angle is 40°). Vertical dotted line indicates one effective radius.

$M/L_B = 10$ is plotted using a thin solid line. On the right hand side of Fig. 25 I plotted two different test made using logarithmic potentials: the thin solid line represents an axisymmetric logarithmic potential with $q = 0.9$, and the thick solid line is for the triaxial logarithmic potential with fixed $p = q = 0.9$. It is difficult to draw conclusions about the dark matter judging from this kind of modeling. All tests produced similar results and they all seem to fit the Gauss-Hermite parameters. Carollo et al. (1995) and Rix et al. (1997) found evidence for the existence of dark

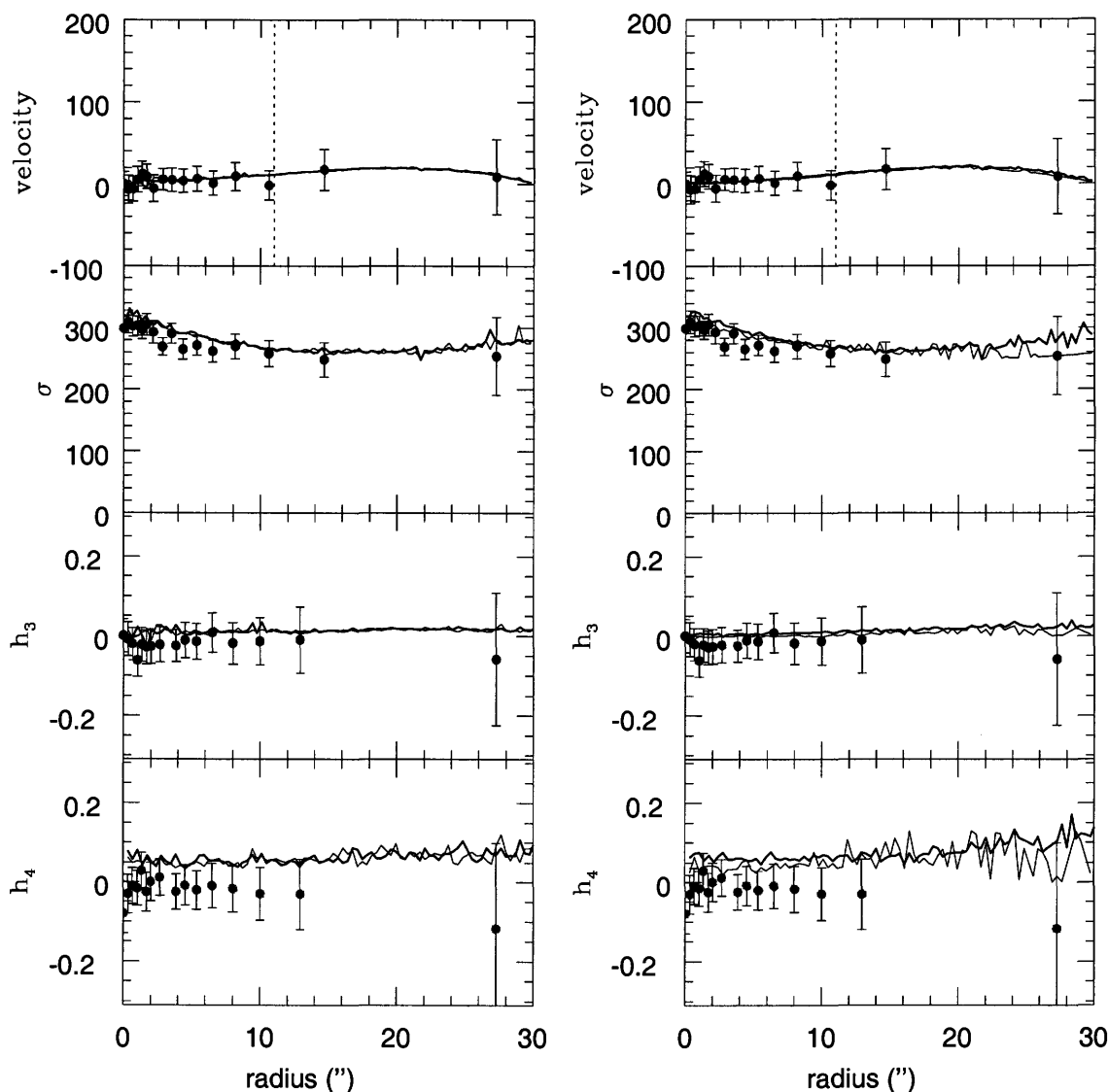


Figure 23: Predictions of the three-integral modeling for NGC4105 for the major axis. Left: The thick solid line is for a constant mass-to-light potential with $M/L_B = 7$ (inclination angle is 50°). The thin solid line is for a constant mass-to-light potential with $M/L_B = 10$ (inclination angle is 50°). Right: The thick solid line is for an axisymmetric logarithmic potential ($q = 0.9$) (inclination angle is 50°). The thin solid line is for the triaxial logarithmic potential with fixed $p = q = 0.9$ (inclination angle is 40°). Vertical dotted line indicates one effective radius.

matter in NGC2434. My simple modeling shows that out to $\sim 2.4R_e$, although the logarithmic potential is not excluded (especially, the triaxial variant represented with the thin line in Fig. 25 on the right-hand side), constant mass-to-light ratio potentials provides a similar fit. It is important to add that in case of the triaxial potential the NNLS fit gave solutions for h_4 out to $\sim 50''$.

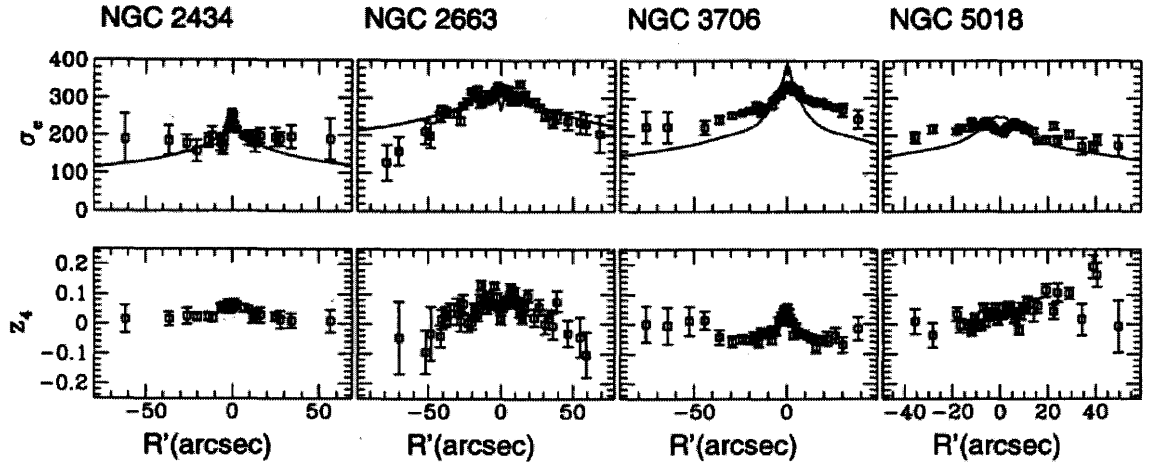


Figure 24: Fig. 2. from Carollo et al. (1995). Modeling results for the sample of Carollo et al. (1995). Note that galaxy NGC2663 is not included in my analysis. Velocity dispersion σ_e of the best-fitting Gaussian to the even part of the velocity profile VP_e and the Gauss-Hermite moment z_4 of VP_e , as function of projected radius R' . Solid lines are predictions of σ_{rms} , the rms projected line-of-sight velocity, for edge-on models with distribution function $f(E, L_z)$, and no dark halo. The greater are the discrepancies between the observed points and the modeling curve, the larger is certainty that there is a dark halo in a given galaxy. See details in Carollo et al. (1995).

NGC3706

In Fig. 26 I present several examples of the modeling of NGC3706. The inclination angle is taken to be 50° in the case of the constant mass-to-light ratio potentials and 40° in the case of logarithmic potentials. On the left hand side I plotted two examples of modeling using a constant mass-to-light ratio: the case with $M/L_B = 5$ is plotted using a thick solid line, and the case with a larger $M/L_B = 10$ is plotted using a thin solid line. On the right hand side of Fig. 26 I plotted two different tests made using logarithmic potentials: the thin solid line represents an axisymmetric logarithmic potential with $q = 0.9$, and the thick solid line is for the triaxial logarithmic potential with fixed $p = q = 0.9$. In this case the best fit is obtained using a triaxial logarithmic potential, and so I can confirm the conclusion of Carollo et al. (1995) that most probably there is a dark matter in this galaxy. This is the case for which the discrepancy between the two-integral models (without dark matter) made by Carollo et al. (1995) and the observations is the largest (see Fig. 24). Note, however, that the h_3 parameter cannot be fitted (especially in the internal region of the galaxy). It is important to add that in the case of the triaxial potential the NNLS fit gave solutions for h_4 out to $\sim 65''$.

NGC5018

In Fig. 27 I present several examples of the modeling of NGC5018. The inclination angle is taken to be 80° in all the cases. On the left hand side I plotted two examples of modeling using a constant

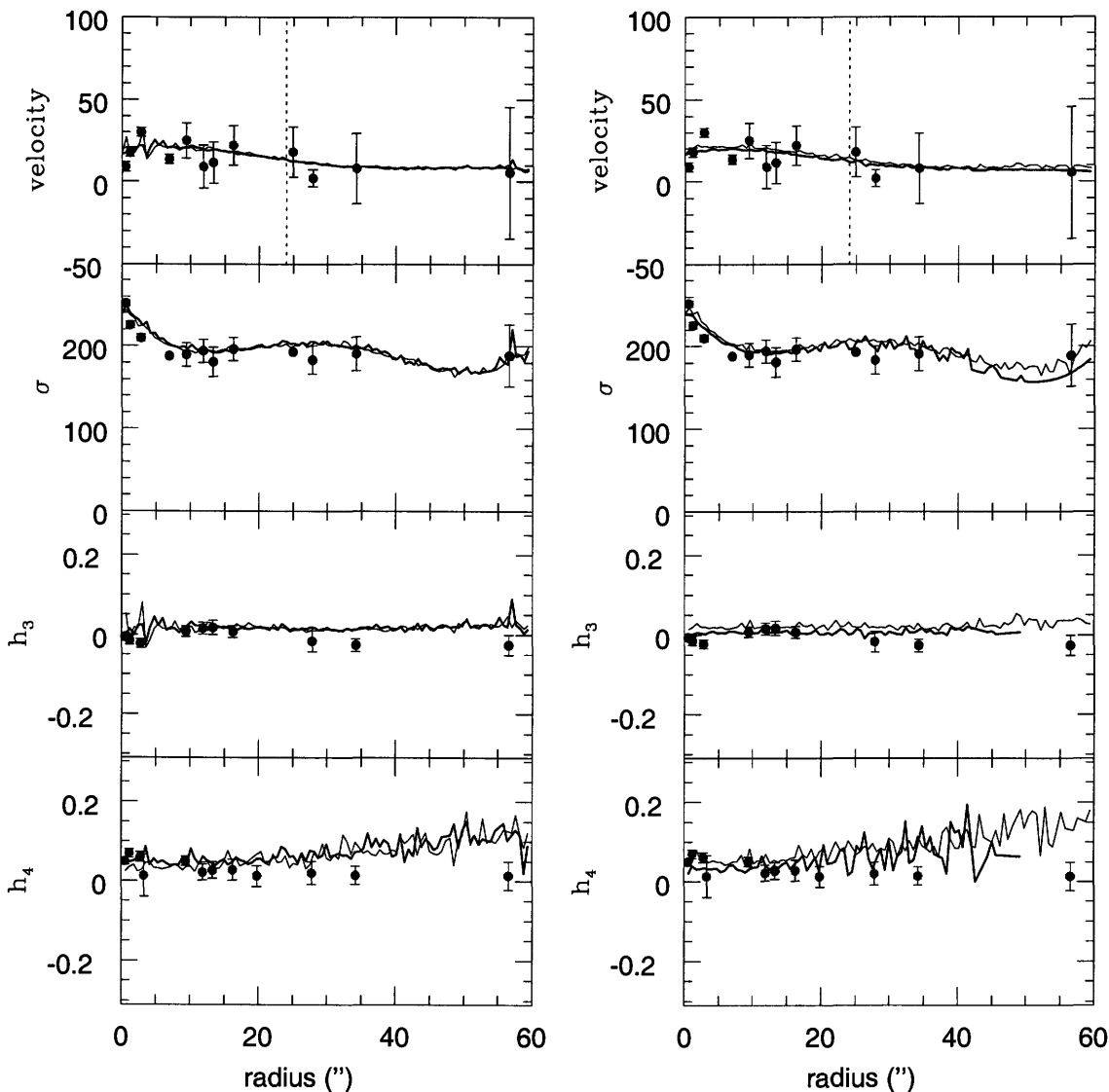


Figure 25: Predictions of the three-integral modeling for NGC2434 for the major axis. Left: The thick solid line is for a constant mass-to-light potential with $M/L_B = 5$. The thin solid line is for the a constant mass-to-light potential with $M/L_B = 10$. Right. The thin solid line is for a axisymmetric logarithmic potential ($q = 0.9$). The thick solid line is for the triaxial logarithmic potential with fixed $p = q = 0.9$. Inclination angle is taken to be 50° in case of the constant mass-to-light ratio potentials and 40° in case of logarithmic potentials. Vertical dotted line indicates one effective radius.

mass-to-light ratio: the case with $M/L_B = 5$ is plotted using a thick solid line, and the case with a larger $M/L_B = 10$ is plotted using a thin solid line. On the right hand side of Fig. 27 I plotted two different test made using logarithmic potentials: the thin solid line represents an axisymmetric logarithmic potential with $q = 0.9$, and the thick solid line is for the triaxial logarithmic potential with fixed $p = q = 0.9$. In this case the best fit is again obtained using triaxial logarithmic potential, so I again confirm the conclusion of Carollo et al. (1995) that most probably there is

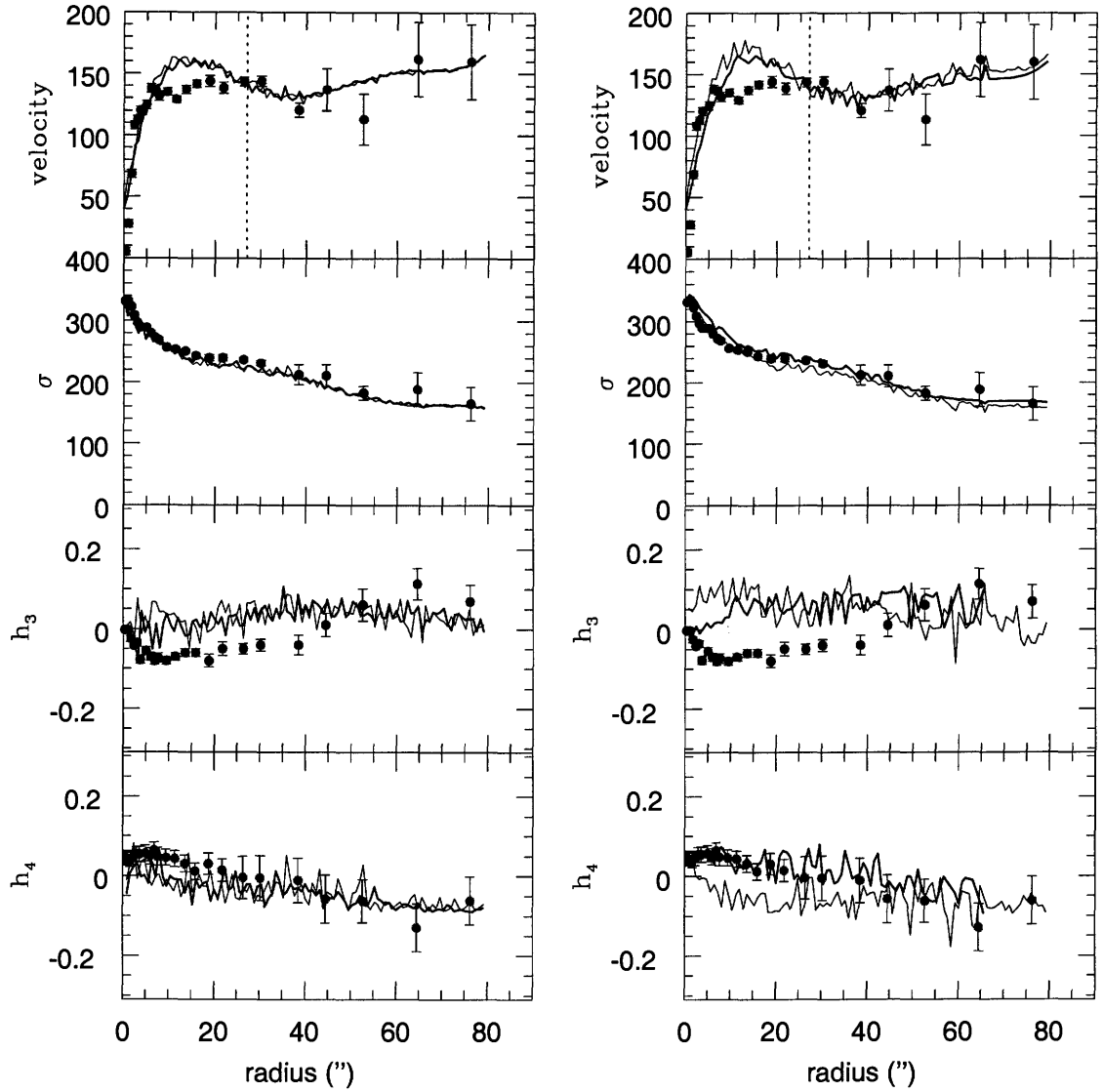


Figure 26: Predictions of the three-integral modeling for NGC3706 for the major axis. Left: The thick solid line is for a constant mass-to-light potential with $M/L_B = 5$. The thin solid line is for the a constant mass-to-light potential with $M/L_B = 10$. Right: The thin solid line is for a axisymmetric logarithmic potential ($q = 0.9$). The thick solid line is for the triaxial logarithmic potential with fixed $p = q = 0.9$. Inclination angle is 40° in all the cases. Vertical dotted line indicates one effective radius.

dark matter in this galaxy. It is again important to add that for the triaxial potential the NNLS fit gave solutions for h_4 out to $\sim 40''$. The case is not so strong as it is for NGC3706 where the effect is visible also when one compares the two-intergal modeling result with the observations in Fig. 24.

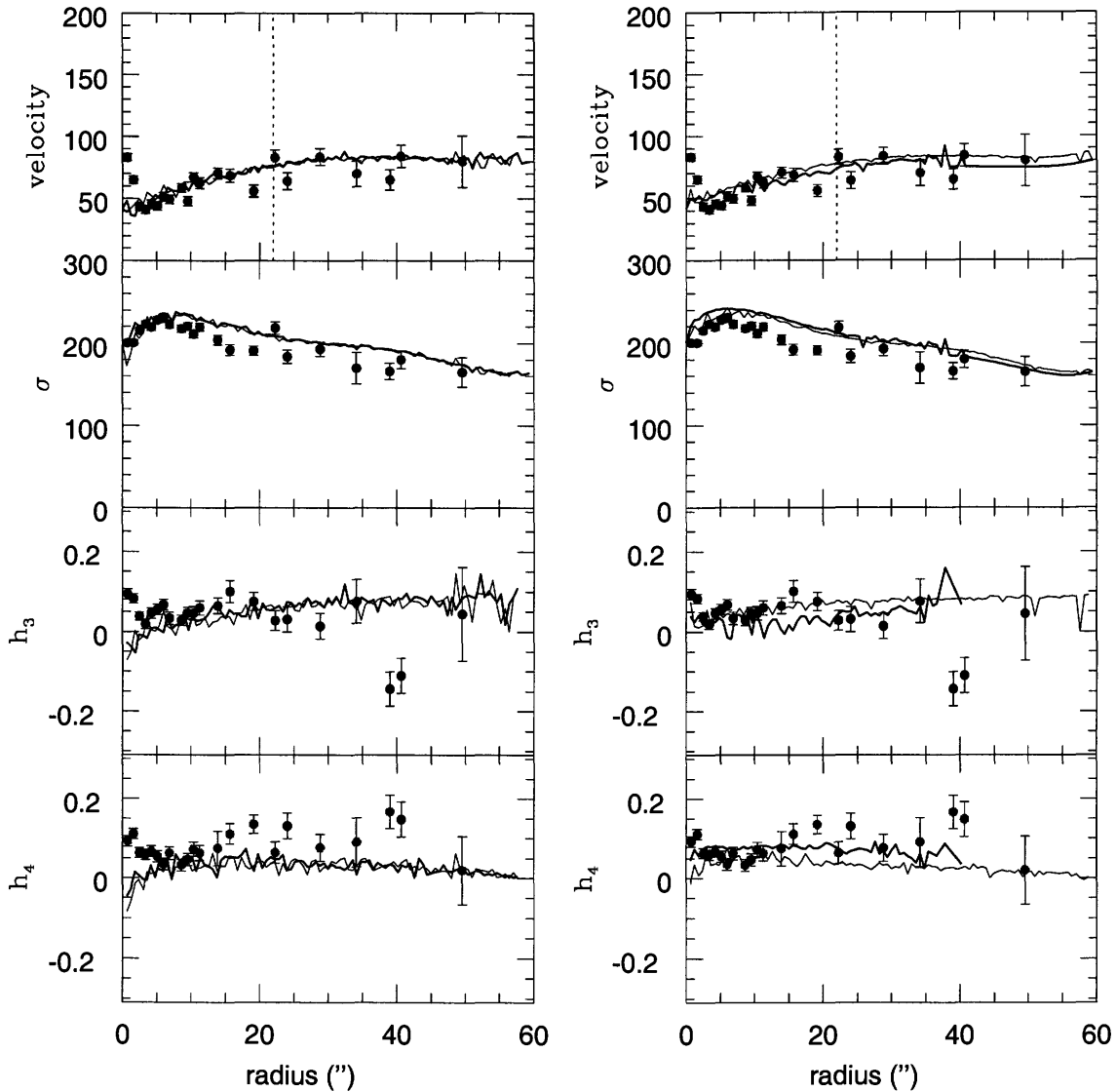


Figure 27: Predictions of the three-integral modeling for NGC5018 for the major axis. Left: The thick solid line is for a constant mass-to-light potential with $M/L_B = 5$. The thin solid line is for the a constant mass-to-light potential with $M/L_B = 10$. Right: The thin solid line is for a axisymmetric logarithmic potential ($q = 0.9$). The thick solid line is for the triaxial logarithmic potential with fixed $p = q = 0.9$. Inclination angle is 80° in all the cases. Vertical dotted line indicates one effective radius.

REFERENCES

- Bertola, F., Vietri, M. & Zeilinger, W. W.: 1988, *Messenger*, 52, 24.
 Bendo, G.J. & Barnes, J.E.: 2000, *MNRAS*, 316, 315
 Bicknell, G.V., Carter, D., Killeen, N.E.B. & Bruce, T.E.G.: 1989, *ApJ*, 336, 639
 Binney, J.J., Davies, R.D., & Illingworth, G.D.: 1990, *ApJ*, 361, 78 (BDI)
 Binney, J.J. & Tremaine, S.: 1987, *Galactic Dynamics*, Princeton University Press

- Bridges, T., Beasley, M., Faifer, F., Forbes, D., Forte, J., Gebhardt, K., Hanes, D., Sharples, R. & Zepf, S.: 2003, in press, in "Joint Discussion 6: Extragalactic Globular Clusters and their Host Galaxies", IAU General Assembly, July 2003. T. Bridges and D. Forbes (eds.), preprint astro-ph/0310324
- Caon, N., Capaccioli, M. & D'Onofrio, M.: 1994, A& ASS, 106, 199
- Carollo, C.M., de Zeeuw, P.T., van der Marel, R.P., Danziger, I.J., & Qian, E.E.: 1995, ApJ, 441, L25
- Carollo, C.M., & Danziger, I.J.: 1994a, MNRAS, 270, 523
- Carollo, C.M., & Danziger, I.J.: 1994b, MNRAS, 270, 743
- Ciardullo, R., Jakoby, G.H. & Dejonghe, H.G.: 1993, ApJ, 414, 454
- Cinzano, P., & van der Marel, R.P.: 1994, MNRAS, 270, 325
- Carter, D.: 1978, MNRAS, 182, 797
- De Rijcke, S., Dejonghe, H., Zeilinger, W.W. & Hau, G.K.T.: 2003, A& A, 400, 119
- Cretton, N. & van der Bosch, F.C: 1999, ApJ, 514, 704.
- Cretton, N., Rix, H.-W. & de Zeeuw, P.T.: 1999, ApJ, 536, 319.
- Gebhardt, K., Richstone, D., Tremaine, S. Lauer, T.R., Bender, R., Bower, G., Dressler, A. Faber, S.M., Filippenko, A.V., Green, R., Grillmair, C., Ho, L.C., Kormendy, J., Magorrian, J. & Pinkney, J.: 2003, ApJ, 583, 92
- Jaffe, W.: 1983, MNRAS, 202, 995.
- Kohonen, T.: 1997, *Self-Organizing Maps*, Springer-Verlag.
- Kormendy, J.: 1982, in *Morphology and dynamics of galaxies; Proceedings of the Twelfth Advanced Course*, Saas-Fee, Switzerland, March 29-April 3, 1982, Sauverny, Switzerland, Observatoire de Geneve, 1983, 113.
- Lawson, C.L. & Hanson, R.J.:1974, *Solving Least Squares Problems*, Englewood Cliffs, New Jersey: Prentice-Hall
- Murtagh, F.: 1995, Pattern Recognition Letters, 16, 399.
- Napolitano, N.R., Arnaboldi, M. & Capaccioli, M.: 2002, A& A, 383, 791
- Ostriker, J.P.: 1980, Comments on Astrophysics, Vol. 8, No. 6, 177
- Rix, H.-W., de Zeeuw, P.T., Cretton, N., van der Marel, R.P. & Carollo, C.M.: 1997, ApJ, 488, 702
- Romanowsky, A.J., Douglas, N.G., Arnaboldi, M., Kuijken, K., Merrifield, M.R., Napolitano, N.R., Capaccioli, M. & Freeman, K.C.: 2003, Science, 5640, 1696
- Saglia, R.P., Kronawitter, A., Gerhard, O. & Bender, R.: 2000, AJ, 119, 153
- Schwarzschild, M.: 1979, ApJ, 232, 236
- Simonneau, E., Varela, A.M. & Muñoz-Tuñón, C.: 1998, Nuovo Cimento, 113, 927 (SVMT)
- Stark, A.A.: 1977, ApJ, 213, 368
- Statler, T., Smecker-Hane, T. & Cecil, G.N: 1996, AJ, 111, 1512
- Statler, T., Dejonghe, H., & Smecker-Hane, T.: 1999, AJ, 117, 126
- van der Marel, R.P.: 1991, MNRAS, 253, 710
- van der Marel, R.P., Binney, J. & Davies, R.L.: 1990, MNRAS, 245, 582
- van der Marel, R.P., & Franx, M.: 1993, ApJ, 407, 525
- Williams, T.B. & Schwarzschild, M.: 1979, ApJ, 227, 56

3

GALAXIES WITH X-RAY HALOES

In the sample of galaxies that I analyzed several galaxies are catalogued as X-ray sources: IC1459, NGC1399, NGC1404, NGC4105 and NGC3379. X-rays are important for the early-type galaxies because they can provide independent constraints on the masses and mass-to-light ratios out to large radii (for a review see Danziger 1997, Mathews & Brighenti 2003, hereafter MB03).

The Einstein Observatory detected X-ray haloes around these galaxies, and the mass of the hot gas was estimated to be equal $\sim 10^{10} M_{\odot}$. Originally, Fabricant, Lecar & Gorenstein (1980) found that the mass of the dark halo of M87 lies between $1.7 \times 10^{13} M_{\odot}$ and $4.0 \times 10^{13} M_{\odot}$, and that the dark halo extends out to $50'$ (or 230 kpc). Therefore, an M/L ratio of 180 can be estimated from these data. The basics for the mass calculations inferred from X-rays were given in this paper, and I here only briefly present basic assumptions and formulas. One assumes that spherical symmetry holds, and that the condition of hydrostatic equilibrium is valid:

$$\frac{dP_{\text{gas}}}{dr} = -\frac{GM(r)\rho_{\text{gas}}}{r^2}, \quad (1)$$

where $M(r)$ is the mass interior to the radius r , and the gas obeys the perfect gas law:

$$P_{\text{gas}} = \frac{\rho_{\text{gas}} k T_{\text{gas}}}{\mu m_H}, \quad (2)$$

where μ is the mean molecular weight for full ionization (taken to be 0.61), and m_H is the mass of the hydrogen atom. From these two equations one can give the expression for the gravitating mass interior to radius r (e.g. Danziger 1997):

$$M(r) = -\frac{kT_{\text{gas}}r}{G\mu m_p} \left(\frac{d\ln\rho}{d\ln r} + \frac{d\ln T_{\text{gas}}}{d\ln r} \right). \quad (3)$$

In the parenthesis on the right-hand-side one can add a term related to an additional nonthermal turbulent, magnetic, or cosmic ray pressure P_{nt} (e.g. MB03), so that the previous formula would read:

$$M(r) = -\frac{kT_{\text{gas}}r}{G\mu m_p} \left(\frac{d\ln\rho}{d\ln r} + \frac{d\ln T_{\text{gas}}}{d\ln r} + \frac{P_{\text{nt}}}{P_{\text{gas}}} \frac{d\ln P_{\text{nt}}}{d\ln r} \right). \quad (4)$$

Although in early-type galaxies that contain strong radio sources one can estimate the pressure P_{nt} (MB03) this pressure is usually ignored in mass determinations of these galaxies, so I will neglect it in this thesis.

Hot gas in early-type galaxies derives from two sources: internal and external. *Internal sources* are evolving stars that continuously eject gas at a rate of $\sim 1.3[L_B/(10^{11}L_{B,\odot})] M_\odot \text{ yr}^{-1}$, where L_B is luminosity in B-band. As noted by MB03 it is generally assumed that gas ejected by orbiting red giant stars passes through shocks and is raised to the stellar kinematic temperature:

$$T_* \approx T_{vir} \approx \mu m_p \sigma^2 / k \sim 10^7 \text{ K} \sim 1 \text{ keV}, \quad (5)$$

where σ is the stellar velocity dispersion. Also, type Ia supernovae can provide some additional heating. For some massive galaxies in my sample large X-ray luminosities of $L_x \sim 10^{40} - 10^{43} \text{ ergs s}^{-1}$ for $L_B > 3 \times 10^{10} L_{B,\odot}$, are detected (see TABLE 3-1). This indicates that most of the internally produced gas is currently trapped in the galactic or group potential. At times when most of the galactic stars were forming, type II supernovae were driving winds of metal-enriched gas into the inter-galactic environment. The gas that was expelled in this way enriched the hot gas in the outer regions of the early-type galaxies. Later, some of this local gas fell back into the central galaxy, thus providing an *external source* of gas. An additional source of external gas was provided by a continued accretion from the ambient cosmological flow that was gravitationally bound to the group or cluster (MB03). The diffuse external gas that arrived after having fallen through the deeper potential well of the surrounding group (cluster), was shock-heated to the virial temperature of the galaxy group (cluster). This more distant accreted and shocked gas is hotter than gas virialized to T_* deeper in the stellar potential of the early-type galaxy. These two together an outwardly increasing gas temperature that is observed (see Fig. 1, right). Fig. 1 was taken from MB03 and it shows the dependence $\rho_* \propto n_e^2$ that was found in the early-type galaxies. It is obvious that relation $n_e \propto \rho_*^{1/2}$ holds over a wide range in galactic radius. Here, n_e is the electron density of the hot gas. In giant elliptical galaxies it is typically $n(0) \sim 0.1 \text{ cm}^{-3}$ at the center and declines with radius as $n \propto r^{-1.25 \pm 0.25}$.

The total mass of hot gas in massive elliptical galaxies is roughly several times $10^{10} M_\odot$ (about $\lesssim 1$ percent of the total stellar mass). This number depends on the extent of the given galaxy.

If one wants to calculate the mass and mass-to-light ratio of elliptical galaxy based upon X-ray observations one can use the following approach (which was used in Kim & Fabbiano (1995), hereafter KF95, for NGC507 & NGC499): one assumes circular symmetry and derives a radial profile of the X-ray surface brightness measured in concentric rings centered on the X-ray centroid. In a given range one then fits the analytic King approximation model:

$$\Sigma_X \sim \left[1 + \left(\frac{r}{a} \right)^2 \right]^{-3\beta+0.5} \quad (6)$$

(for details see KF95). Here a is the core radius (the radius where the surface brightness falls to half of its central value), and slope β . If the temperature of the X-ray emitting gas does not change much as a function of radius one can assume isothermality – in all cases in this thesis this assumption is valid because I have dealt mostly with the internal parts of galaxies (inside at most 3 effective radii). Now using this assumption together with the formula for $n_e \propto r^{-3\beta}$ (KF95) (see above) one can estimate the total gravitational mass at a given radius r (assuming hydrostatic equilibrium) in a convenient form (Kim & Fabbiano (1995)):

$$M_T = 1.8 \times 10^{12} (3\beta + \alpha) \left(\frac{T}{1 \text{ keV}} \right) \left(\frac{r}{10^3 \text{ arcsec}} \right) \left(\frac{d}{10 \text{ Mpc}} \right) M_\odot, \quad (7)$$

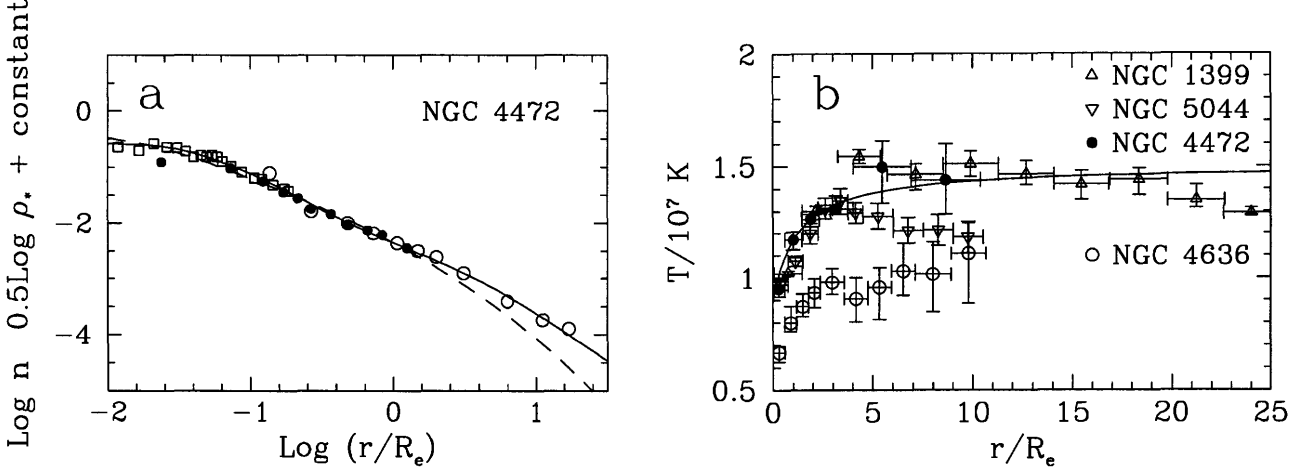


Figure 1: Taken from MB03 (their Figure 2). (Left panel:) The observed and azimuthally averaged electron density profile $n(r)$ in NGC 4472 is shown as a function of radius normalized to the effective radius $R_e = 8.57$ kpc at distance $d = 17$ Mpc. The observations are from *Einstein* (Trinchieri, Fabbiano, & Canizares 1986) (filled circles) and ROSAT (Irwin & Sarazin 1996) (open circles); for the inner region MB03 have Abel-inverted Chandra surface brightness data from Loewenstein et al. (2001) (open squares) and normalized them to previous observations. The solid line is an analytic fit to the observations. The dashed line is the square root of the stellar density $\rho_*^{1/2}(r)$ normalized to n at $r = R_e$. (Right panel:) Typical temperature profiles for several bright E galaxies, taken from Brighenti & Mathews (1997), based on the following sources: NGC 1399: ROSAT PSPC from Jones et al. (1997); NGC 5044: ROSAT PSPC from David et al. (1994); NGC 4636: ROSAT PSPC from Trinchieri et al. (1994); NGC 4472: ROSAT HRI AND PSPC from Irwin & Sarazin (1996). The solid line is an approximate analytic fit to $T(r)$ for NGC 4472. Note that galaxy NGC 1399 is present in my sample and will be analyzed later.

here the exponent α is related to the temperature ($T \sim r^{-\alpha}$) and is taken to be zero in all cases below. This formula is valid outside the core region.

The mass-to-light ratio (in the B-band) can be expressed as a function of radius r :

$$\frac{M_T}{L_B} = 1.16 \times 10^{-2} 10^{\frac{B}{2.5}} (3\beta + \alpha) \left(\frac{T}{1\text{keV}} \right) \left(\frac{r}{10^3 \text{arcsec}} \right) \left(\frac{d}{10 \text{Mpc}} \right)^{-1}, \quad (8)$$

where B is the B magnitude of galaxy inside radius r (Kim & Fabbiano 1995).

I present the results for my sample of galaxies with X-ray haloes below, taking $\beta = 0.5$, except for the faint X-ray galaxy NGC3379 where $\beta = 0.64$ (result taken from Brown & Bregman 2001). In TABLE 3-1 I present estimated masses and mass-to-light ratios for the galaxies within the radius for which I had the long-slit spectra. The data sources are given at the bottom of TABLE 3-1.

Using Eq. (3) one can estimate the total integrated mass $M(r)$ within a given radius. Loewenstein & White (1999) using the relationship between the X-ray temperatures and stellar velocity dispersions (the $T - \sigma$ relation: $\langle T \rangle \propto \langle \sigma \rangle^{1.45}$, where $\langle \dots \rangle$ denotes mean value) found that minimum values of dark matter core radii scale as $r_{\text{DM}} > 4(L_V/3L_*)^{3/4} h_{80}^{-1}$ kpc and that the minimum dark matter mass fraction is $\gtrsim 20\%$ within one optical effective radius r_{eff} and is $\gtrsim 39\%$ - 85% within $6 r_{\text{eff}}$, depending on the stellar density profile and observed value of β_{spec} . Here,

$$\beta_{\text{spec}} \equiv \frac{\mu m_p \langle \sigma \rangle^2}{k \langle T \rangle} \quad (9)$$

When dark matter dominates the gravitational potential on large scales, then $\langle T \rangle$ is a measure of the dark matter content within the extraction radii (in this case $6 r_{\text{eff}}$ (Loewenstein & White (1999)). The Fundamental plane (FP) ¹ provides a link between the velocity dispersion and the global luminosity and therefore β_{spec} is a good quantity for establishing the dark-to-luminous matter ratio within the optical radius. One can also use temperature profiles as an additional constraint on dark matter; unfortunately, these profiles are available only for galaxies that are very bright in X-rays.

TABLE 3-1
X-RAY AND MASS PROPERTIES OF GALAXIES WITH X-RAY HALOES

Name	r ($''$)	r (kpc)	r/r_{eff}	B	$\log L_X$ (erg s^{-1})	T (keV)	D (Mpc)	M ($10^{11} M_{\odot}$)	$(\frac{M}{L})_B$
IC1459	100	11.7	2.86	11.13	41.19 ¹	0.60 ^{2,3}	24.16	3.91	15.53
NGC1399	70	6.91	1.67	10.25	41.44 ¹	1.08 ³	20.36	4.16	8.13
NGC1404	80	10.79	3.08	10.82	41.27 ¹	0.62 ³	27.81	3.72	6.60
NGC4105	30	4.02	2.73	11.26	41.94 ⁵	0.76 ³	27.66	1.70	4.58
NGC3379	80	5.04	1.60	10.10	39.78 ¹	0.26 ⁴	13.01	9.24	3.86

NOTE: References: (1) Brown & Bregman (1998), (2) Fabbiano et al. (2003), (3) Davis & White (1996), (4) Brown & Bregman (2001), (5) Fabbiano, Kim & Trinchieri (1992)

In TABLE 3-1 I give a list of galaxies from different samples that posses X-ray haloes. The second and third columns give the radius for each galaxy out to which long-slit spectra extend to (in arcsecs and kiloparsecs, respectively). The fourth column expresses this in units of effective radii. Total B-magnitudes in the fifth column were taken from the LEDA catalog. In the sixth column are the data for X-ray luminosities that were collected from the literature (see the notes to TABLE 3-1). Temperatures in the seventh column were collected from the paper by Davis & White (1996), except in the case of NGC3379 for which the temperature is taken from the Brown & Bregman (2001) paper that deals with emission mechanisms in X-ray faint galaxies. In the case of IC1459 there is also a recent estimate by Fabbiano et al. (2003) that agrees well with Davis & White (1996). Distances in the eighth column are calculated using $H_0 = 70 \text{ km s}^{-1} \text{ Mpc}^{-1}$ (using heliocentric radial velocities from the NED archive). In the ninth column the mass of each galaxy in units of $10^{11} M_{\odot}$ is estimated using Eq. (7) for a radius given in the second column, and finally, in the tenth column the estimate of the mass-to-light ratio for each galaxy is given using Eq. (8) again for the radius in the second column. It is important to repeat that in the approximation which I have made in all cases the temperature is taken to be constant in the given region so α parameter from Eq. (7) and Eq. (8) is taken to be zero.

¹ Elliptical galaxies populate a two-dimensional manifold in the space of their observable quantities: effective radius, r_{eff} , effective surface brightness (mean surface brightness within r_{eff}), and central velocity dispersion σ . This manifold was named fundamental plane (FP), cf. Djorgovski & Davis (1987), Dressler (1987), see also Binney & Merrifield (1998).

In Fig. 2 and Fig. 3 are presented graphical estimates of the mass-to-light ratios (in the B-band) for the galaxies from my samples. Shaded regions with indicated lower and upper limits provide estimates obtained using the value of T_σ for the lower limit and $T_X = 1.5T_\sigma$ for the upper limit, because Brown & Bregman (1998) for objects with few counts assumed this latter limit (for example in the cases of NGC1399 and NGC1404). For several galaxies they found that $T_X \approx 2T_\sigma$: this relation was used only in the case of NGC3379 (for which they do not provide the estimate of T_X) thus giving a corresponding upper limit. The case for which $T_X = 1.5T_\sigma$ is also plotted as a thick dotted line in Fig. 3. T_σ is calculated using Eq. (5) which after insertion of appropriate values becomes:

$$kT_{\sigma[\text{keV}]} = 6.367 \times 10^{-6} \sigma_{[\text{km/s}]}^2 \quad (10)$$

where σ is expressed in km s^{-1} . Estimates from two-integral (2I) (where available) and three-integral (3I) modeling are also included. In the case of NGC3379 I also included available results on the mass-to-light ratio that were obtained using PNe (Ciardullo et al. 1993 (C93), and Romanowsky et al. 2003 (R03)) and globular clusters (GCs) (preliminary results by Bridges et al. 2003 originally presented in the V-band were transformed into the B-band using $B-V=0.97$, taken from the LEDA database). It should be noted however that the methodology of the PNe and GCs does not provide measures of h_3 and h_4 as tests of the models.

A detailed stellar dynamical modeling of these galaxies was given in Chapter 2 of this thesis. Here, I only briefly note that Figures 2 and 3 show in graphical form how X-rays can be used as an independent tracer of the mass of the early-type galaxy: they show an overlapping (in some cases good, in other cases poor) of X-ray data with the estimates obtained using stellar dynamical models. A careful inspection of Figs. 2 and 3 shows that there is an overlapping of the mass-to-light ratio predictions based on the X-rays calculations and those based using other methods (2I and/or 3I modeling, PNe, GCs). If one leaves out, for the moment, the cases of NGC1399 and NGC1404 for which only 3I estimates are available, and use 2I estimates, one can see that agreement between 2I modeling and X-ray estimates is: (i) poor (IC1459), (ii) very good (NGC4105) and (iii) excellent (NGC3379). The conclusion that can be drawn from this small sample is that a good agreement between the stellar dynamics estimate and the X-ray halo estimate can be attained in the region between ~ 1 and $\sim 2 - 3R_e$ in two cases. The results for other two galaxies analyzed using 3I technique only (NGC1399, NGC1404) also seem to support this conclusion. The case of IC1459 (the galaxy with the counterrotating core) is the only one for which there is a strong discrepancy between the X-ray and stellar dynamics estimate. Note, however, that for NGC4105 there is a hint of the counterrotating core and yet there is agreement between the two methods. The reason for a poor agreement in the case of IC1459 may lie in the temperature determination in the inner parts of the galaxy (inside $3 R_e$): lower temperature ($T \sim 0.6 \text{ keV}$, taken from Davis & White 1996) does provide at least a marginal concordance with the 2I modeling; the estimate based on T_σ (Eq. (10)) is large which is a consequence of the large central velocity dispersion of this galaxy.

What is, however, intriguing is the obvious rising trend in the mass-to-light ratios based on the X-ray estimates: if one again leaves out NGC1399 and NGC1404, where only 3I estimates exist, one can see from Figs. 2 and 3, that the mass-to-light ratio obtained from X-rays beyond $2R_e$ is either too large (IC1459, NGC4105), or consistent with 2I estimates (NGC3379). Using the PNe observations that provide mass-to-light ratio estimates out to much larger radii, one can see that the conclusions based on the X-rays for NGC3379 are inconsistent with the observations (see Fig. 3) beyond $3R_e$. (Unexpected behaviour of the mass-to-light ratio in this galaxy based on the GCs is in

agreement with the X-ray estimates.) Using these findings, together with the recent result of Peng et al. (2003) who have recently found that for NGC5128 at $15 R_e$ the mass-to-light ratio is only 13 (in the B-band) (much lower than the value expected from the X-rays analysis: $M/L_B \sim 112 \pm 28$, cf. Bahcall, Lubin & Dorman 1995), one can infer that there is a discrepancy between the mass-to-light ratios calculated using X-rays and PNe techniques at the large radii (beyond $3R_e$) from the center. One possible reason could be that the initial assumptions about the hot gas are not correct. In a very recent review Bosma (2003) writes: "Yet the new Chandra and XMM data show a wealth of detail in the images of the X-ray gas of individual galaxies, so much that one can question the validity of the hydrostatic equilibrium equation used to evaluate masses". Bosma (2003) also notes that another complication related to the mass determinations based on the X-rays is the contribution to the X-ray flux of low mass X-ray binaries, which presumably occur in globular clusters and in the field. Of course, it could be that the estimates based on the PNe are erroneous, but one should bear in mind that (for example for NGC5128, out to $\sim 1.2R_e$) some estimates for the mass-to-light ratio based on the HI synthesis observations are much lower than those expected from the X-ray approach (see Introduction, cf. van Gorkom et al. 1990). However, it should be noted that Sarazin, Irwin & Bregman (2001) studied the X-ray faint elliptical galaxy NGC4697 using high spatial resolution *Chandra* observations which resolved most of the X-ray counts (61% within one effective radius) into point sources. Recently, Paolillo et al. (2003) have analyzed the X-ray halo of the elliptical galaxy NGC507 in the Pisces cluster, and found that 20% of the sources detected in the NGC507 halo are due to point sources, while the nature of the remaining population is not clear (they could be either accreting binaries hosting a massive black hole or density clumps of the X-ray halo). It is also possible that the extended X-ray emission traces in fact the group or cluster potential rather than the potential of the elliptical galaxy itself (Bosma 2003). It is worthwhile noting that all five galaxies given in TABLE 3-1 belong either to some group (IC1459, NGC3379, NGC4105) or to the Fornax cluster (NGC1399, NGC1404). The reason for the large discrepancy between the X-ray based estimates and PNe estimates at large radii is unclear and remains to be solved.

REFERENCES

- Bahcall, N.A., Lubin, L.M. & Dorman, V.: 1995, *ApJ*, 447, L81
 Binney, J.J. & Merrifield, M.R.: 1998, *Galactic Astronomy*, Princeton University Press
 Bosma, A: 2003, to appear in the proceedings of IAU Symposium 220 "Dark matter in galaxies", S. Ryder, D.J. Pisano, M. Walker, and K. Freeman (eds.), preprint astro-ph/0312154
 Bridges, T., Beasley, M., Faifer, F., Forbes, D., Forte, J., Gebhardt, K., Hanes, D., Sharples, R. & Zepf, S.: 2003, in press, in "Joint Discussion 6: Extragalactic Globular Clusters and their Host Galaxies", IAU General Assembly, July 2003. T. Bridges and D. Forbes (eds.), preprint astro-ph/0310324
 Brighenti, F., Mathews, W.G.: 1997, *ApJ*, 486, L83.
 Brown, B.A. & Bregman, J.N: 1998, *ApJ*, 495, L75
 Brown, B.A. & Bregman, J.N: 2000, *ApJ*, 539, 592
 Brown, B.A. & Bregman, J.N: 2001, *ApJ*, 547, 154
 Ciardullo, R., Jacoby, G.H. & Dejonghe, H.G.: 1993, *ApJ*, 414, 454
 Danziger, I.J.: 1997, in *Dark and Visible Matter in Galaxies*, ASP Conference Series, Vol. 117, M. Persic & P. Salucci (eds.), 28

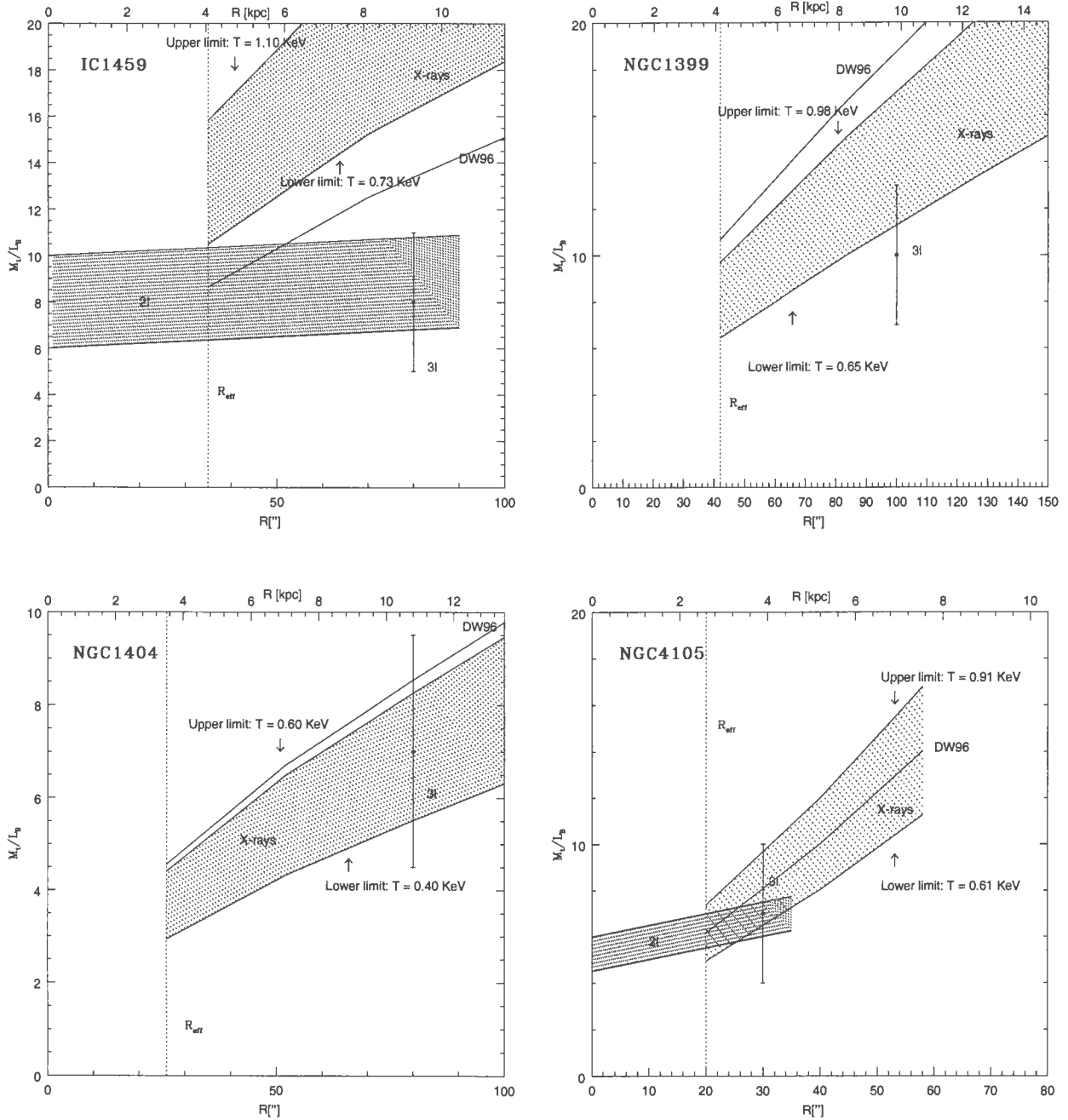


Figure 2: Mass-to-light ratios of four galaxies with X-ray haloes from my sample (part I): IC1459, NGC1399, NGC4105 and NGC1404 (clockwise). Mass-to-light ratios are given in the B-band. The scale of the lower x-axis is given in arcseconds and the upper x-axis is in kiloparsecs. For the problem of the determination of the effective radius of NGC1399 see Chapter 2. For each galaxy, the effective radius is plotted as a dashed vertical line. Limits on the mass are given using lower and upper limits obtained using T_σ (see text for details). Mass dependence on the temperatures from the paper by Davis & White (1996) is denoted as "DW96". Where available I included results from the dynamical modeling: "2I" refers to two-integral modeling and "3I" refers to three-integral modeling. Stripes in the 2I case provide the limits within which the kinematics can be fitted (see text for details). 3I modeling points with error bars should be understood as the range within which the 3I modeling procedure provides a reasonable fit to the observed kinematical data.

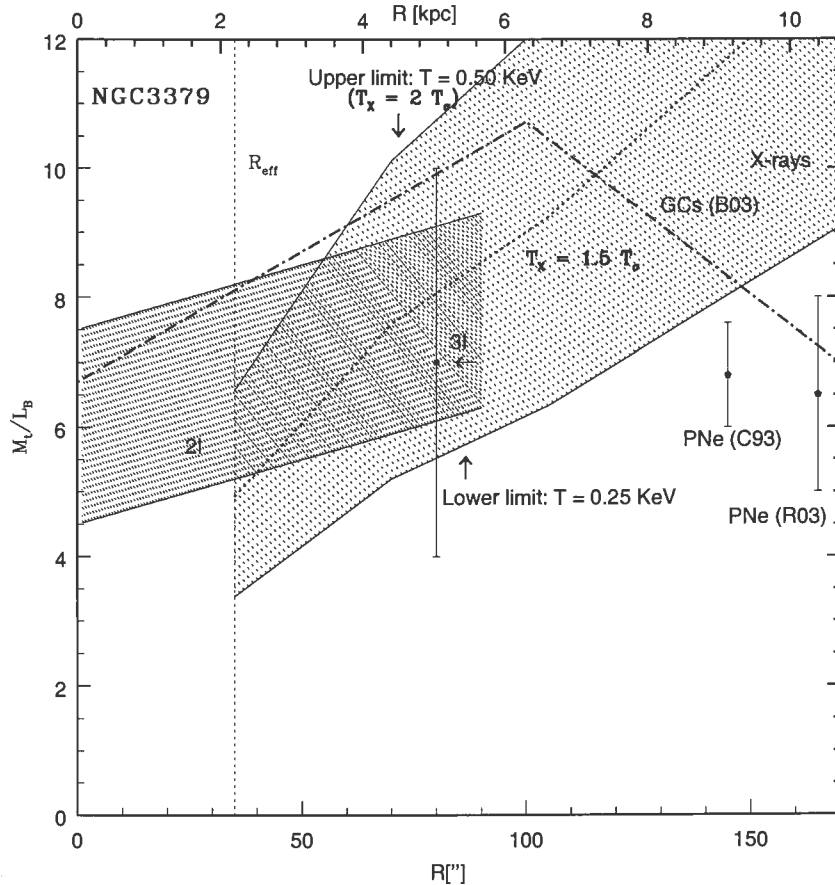


Figure 3: Mass-to-light ratios of a galaxy with X-ray halo from my sample (part II): NGC3379. See caption of Fig. 2 for explanation. Note that in this case three additional points are given in the plot: R03 refers to Romanowsky et al. (2003), C93 to Ciardullo, Jacoby & Dejonghe (1993). B03 refers to Bridges et al. (2003) preliminary result based on the globular clusters (GCs) (see Introduction and this Chapter for details) and is represented by a thick dot-dashed line. Note also that for NGC3379 Davis & White (1996) do not provide an estimate of temperature. In this case two upper limits are given: one for $T_X = 1.5T_\sigma$ represented by a thick dotted line, and one for which $T_X = 2T_\sigma$ as a solid line.

- David, L.P., Jones, C., Forman, W., Daines, S.: 1994, *ApJ*, 428, 544
 Davis, D.S. & White, R.E.: 1996, *ApJ*, 470, L35
 Djorgovski, G. & Davis, M.: 1987, *ApJ*, 313, 59
 Dressler, A.: 1987, *ApJ*, 317, 1
 Fabbiano, G., Elvis, M., Markoff, S., Siemiginowska, A., Pellegrini, S., Zezas, A., Nicastro, F., Trinchieri, G. & McDowell, J.: 2003, *ApJ*, 588, 175
 Fabbiano, G., Kim, D.-W. & Trinchieri, G.: 1992, *ApJSS*, 80, 531
 Fabricant, D. & Gorenstein, P.: 1980, *ApJ*, 241, 560
 Fabricant, D. & Gorenstein, P.: 1983, *ApJ*, 267, 535
 Fabricant, D., Lecar, M. & Gorenstein, P.: 1980, 241, 552
 Irwin, J.A. & Sarazin, C.L.: 1996, *ApJ*, 471, 683
 Jones, C., Stern, C., Forman, W., Breen, J., David, L., Tucker, W. & Franx, M.: 1997, *ApJ*, 482,

- Kim, D.-W. & Fabbiano, G.: 1995, *ApJ*, 441, 182 (KF95)
- Loewenstein, M., Mushotzky, R.F., Angelini, L., Arnaud K.A., Quataert E.: 2001, *ApJ*, 555, L21
- Loewenstein, M. & White, R.E.: 1999, *ApJ*, 518, 50
- Mathews, W.G. & Brighenti, F.: 2003a, *Annu. Rev. Astron. Astrophys.*, 41, 191 (MB03)
- Mathews, W.G. & Brighenti, F.: 2003b, preprint astro-ph/0309367
- Paolillo, M., Fabbiano, G., Peres, G. & Kim, D.-W., 2003, *ApJ*, 586, 850
- Peng, E.W., Ford, H.C. & Freeman, K.C.: 2003, *ApJ*, in press, preprint astro-ph/0311236
- Romanowsky, A.J., Douglas, N.G., Arnaboldi, M., Kuijken, K., Merrifield, M.R., Napolitano, N.R., Capaccioli, M. & Freeman, K.C.: 2003, *Science*, 5640, 1696
- Sarazin, C.L., Irwin, J.A. & Bregman, J. N.: 2001, *ApJ*, 556, 533
- Shigeyama, T.: 1998, *ApJ*, 497, 587
- Trinchieri, G., Fabbiano, G., Canizares, C.R.: 1986, *ApJ*, 310, 637
- Trinchieri, G., Kim, D.-W., Fabbiano, G. & Canizares, C.R.C.: 1994, *ApJ*, 428, 555
- van Gorkom, J. H., van der Hulst, J. M., Haschick, A. D. & Tubbs, A. D.: 1990, *AJ*, 99, 1781

4

LINE STRENGTH INDICES

4.1 MEASUREMENTS

S. Faber initiated in 1972 a long-term spectroscopic project that was aimed at the study of the stellar populations in globular clusters and early-type galaxies. For this purpose the Image Dissector Scanner IDS on the Shane 3m telescope of Lick Observatory was used. Faber and her collaborators observed a large number of galaxies, and stars of all types, field and cluster giants, subgiants and dwarfs in the spectral range from $\sim 4000 \text{ \AA}$ to $\sim 6200 \text{ \AA}$ with a $\sim 8.6 \text{ \AA}$ FWHM resolution. The Lick group defined and measured 21 indices to monitor the strength of spectral features in stars and galaxies (see Gonzalez 1993).

Spectral indices were defined in Faber et al. (1985) and reprinted in Binney & Merrifield (1998)¹. Note, however, that since the early papers of the Lick group the wavelength accuracy has improved and new definitions are now valid. All of my calculations were based on the updated version of the indices table taken from the WWW site of G. Worthey².

In order to define an index one should define a central band of width Δ_0 and two side bands. The "side-band level" I_s is defined to be the mean intensity over the two side bands, and the intensity of the central feature I_c is the mean intensity in the central band. There are two groups of indices: one is measured as an equivalent width (for example iron indices):

$$w = (1 - \frac{I_c}{I_s})\Delta_0$$

and the other is measured in magnitudes (for example Mg_2):

$$w = -2.5\log(1 - \frac{I_c}{I_s}).$$

The spectra that I had were centered to be near the Mg_2 feature ($\sim 5150 \text{ \AA}$). For the comparison with the models I will use Mg_2 and iron indices and their definitions are given in TABLE 4-1 (for a full list of definitions see WWW site of G. Worthey).

¹ Note the misprint in the book of Binney & Merrifield, for the Mg_2 index the central band should read: 515.600–519.725 nm instead of 515.600–519.750 nm, cf. Faber et al. (1985).

² <http://astro.wsu.edu/worthey/html/index.table.html>

TABLE 4-1
DEFINITIONS OF INDICES USED IN THIS THESIS

Name	Index band		blue continuum		red continuum		Units
Mg ₂	5154.125	5196.625	4895.125	4957.625	5301.125	5366.125	mag
Fe5270	5245.650	5285.650	5233.150	5248.150	5285.650	5318.150	ang
Fe5335	5312.125	5352.125	5304.625	5315.875	5353.375	5363.375	ang

NOTE: Units: "mag" refers to the index measured in magnitudes, and "ang" refers to the index measure in Angstroms.

For the purpose of measuring of the line strength indices I have written a set of routines in FORTRAN that I embedded in the MIDAS scripts in order to extract indices from the long-slit spectra. I relied on the AVINT routine by Davis & Rabinowitz (1984) that was included in the SLATEC library of programs³. This routine, based on overlapping parabolas, calculates the integral

$$\int_a^b f(x)dx$$

when $f(x)$ is tabulated in nonequally spaced abscissas – this is the most general case: in my calculations abscissas were equally spaced. I tested the routine using some elementary functions and also some standard spectra obtained from the site of G. Worthey and the agreement was excellent with the elementary functions and very good in the case of the Worthey's spectra.

I performed two tests to verify the accuracy of my spectral indices calculations. The first test is an example (p. 61) from Chapter 2.3 of Davis & Rabinowitz (1984): integrals of four functions given in TABLE 4-2 over [0,1] are calculated using the AVINT algorithm. The functions are calculated at $x = 0.00, 0.10, 0.15, 0.20, 0.23, 0.25, 0.30, 0.40, 0.45, 0.48, 0.53, 0.62, 0.78, 0.82, 0.89, 0.92$ and 1.00 . The agreement with both theoretical and values calculated by Davis & Rabinowitz is extremely good. In the second test I calculated the aforementioned three indices for all seven IDS stars whose spectra and indices are given on the WWW site of G. Worthey (see TABLE 4-3). The agreement, is typically very good, although I note that in case of a very low Mg₂ (HYA VB 95) and a very low Fe5335 (HYA VB 103_R) there are some discrepancies. I also note the discrepancy with the Worthey's calculations in the case of HR 6770 (in iron indices). As an additional test I will compare my results with the results of other authors when such data exist for the internal parts of early-type galaxies.

³ <http://www.netlib.org/slatec/src>.

TABLE 4-2

COMPARISON OF CALCULATIONS OF INTEGRALS OF ANALYTIC FUNCTIONS

function	exact	this thesis	Davis & Rabinowitz
$x^{1/2}$	0.6666 6667	0.6634 2467	0.6634 2607
$x^{1/4}$	0.8000 0000	0.7883 1637	0.7883 1842
$x^{1/8}$	0.8888 8889	0.8676 3126	0.8676 3089
$x^{1/16}$	0.9411 7647	0.9126 5356	0.9126 5294

TABLE 4-3

COMPARISON WITH THE WORTHEY'S CALCULATIONS

Name	calc.	Mg ₂	Fe5270	Fe5335
HYA VB 111	(W)	0.0294	1.2326	0.5729
HYA VB 111	(S)	0.0296	1.2866	0.6132
HYA VB 112	(W)	0.0368	0.9764	0.7577
HYA VB 112	(S)	0.0367	0.9562	0.7827
HYA VB 103 _R	(W)	0.0264	2.3431	-0.1757
HYA VB 103 _R	(S)	0.0267	2.2108	-0.0804
HYA VB 103 _{R+L}	(W)	0.0298	1.3770	0.3774
HYA VB 103 _{R+L}	(S)	0.0300	1.3709	0.4655
HYA VB 95	(W)	0.0181	0.3502	0.2472
HYA VB 95	(S)	-0.0082	0.3585	0.5283
HR 6770	(W)	0.1490	3.4392	2.5624
HR 6770	(S)	0.1371	2.4596	0.8761
HR 7429	(W)	0.3599	3.6879	3.5034
HR 7429	(S)	0.3613	3.8625	3.5029

NOTE: Letter "W" refers to the calculations of Worthey, and letter "S" refers to the results obtained using AVINT routine in this thesis. Note that in the case of HYA VB 103 two different spectra were given.

The routines that I have written were used on the deredshifted spectra, and measurements were standardized to a Lick system. Two steps were necessary to transform the spectra into the Lick system (see for example Halliday 1998):

1. correction to zero velocity dispersion, and
2. correction to the Lick IDS spectral resolution ($\sim 8.2\text{\AA}$ at $\sim 5200\text{\AA}$).

The correction for the effects of the velocity dispersion included the following steps: different stellar spectra were smoothed by Gaussians of various widths that correspond to measurements of $\sigma = 0 - 400\text{ km s}^{-1}$ in the intervals of 35 km s^{-1} . The smoothing was done using IRAF task gauss. Then a correction factor is calculated by a comparison of the each smoothed spectrum with a measurement for the original unsmoothed stellar spectrum. In the case of the molecular index Mg_2 the correction factor is defined as a difference between the measurement of the original unbrodened stellar spectrum and that of the spectrum broadened to a particular velocity dispersion:

$$C(\sigma) = I_{\text{orig}} - I_{\sigma}.$$

For the atomic indices ($\text{Fe}5270(=\text{Fe}1)$, $\text{Fe}5335(=\text{Fe}2)$) ⁴ correction factor is defined as the ratio between the original and the smoothed line indices:

$$C(\sigma) = I_{\text{orig}}/I_{\sigma}.$$

Because the bands are wide, the corrections for Mg_2 are very small, so I do not apply them. On the contrary, the corrections for the iron indices can be significant, and I present in Fig. 1 the calculated values of the corrections for the iron indices in the case of IC3370.

The second correction is related to the different spectral resolution of my observations and those of the Lick IDS. The spectra of the calibration lamps (for example Helium-Argon) were inspected to measure the instrumental resolution and then the galaxy frames were broadened so as to match the Lick spectral resolution ($\sim 8.2\text{\AA}$ at $\sim 5200\text{\AA}$).

Following the paper of Carollo, Danziger & Buson (1993) the estimate of the errors for the indices was calculated using:

$$\epsilon_i = \frac{\sqrt{\text{OBJ} + 2 \times \text{DK} + \left(1 + \frac{1}{N_{\text{rows}}}\right) \times \text{SKY} + \text{ron}^2}}{\text{OBJ}},$$

where OBJ is the total count in the object, SKY is the total count in the sky, DK is the total count in dark, and ron is the read-out noise of the CCD. The term $\frac{1}{N_{\text{rows}}}$ comes from a subtraction of a sky averaged on $N_{\text{rows}}(=30)$ rows from the galactic spectra. One can now define the error on the line-strength index:

$$\epsilon = \text{coeff} \times \sqrt{\sum_{i=c1, c2, b} \epsilon_i^2},$$

where $c1$, $c2$ and b indicate respectively the two continua and the index band. The coefficient is equal to $1.08(= -2.5\log e)$ for the Mg_2 index (and is mentioned here only for the sake of

⁴ As usual, one defines $\langle \text{Fe} \rangle = \frac{\text{Fe}5270 + \text{Fe}5335}{2}$.

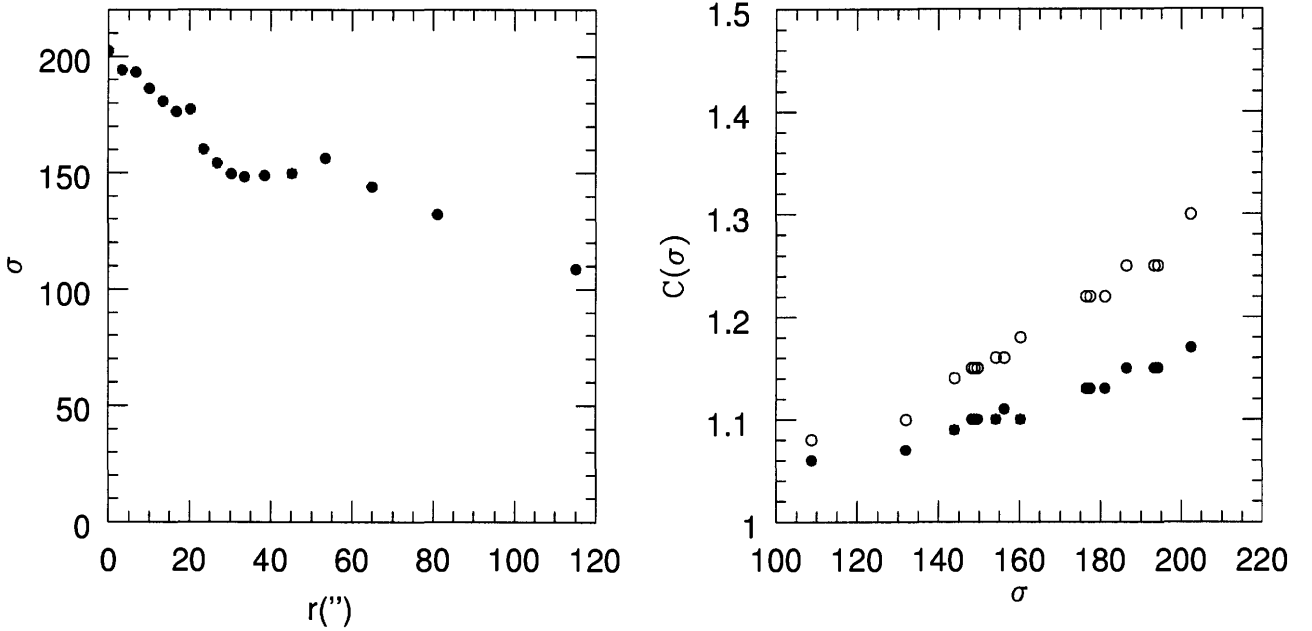


Figure 1: The corrections for the iron indices for IC3370. Left: Dependence of the velocity dispersion on the radius. Right: Values of the corrections of the iron indices: black circles denote Fe5270 and open circles denote Fe5335.

completeness, because the Mg_2 correction was not applied), and to $\frac{(C_{\text{feat}} \times W_{\text{pix}})}{C_{\text{cont}}}$ for the iron indices (C_{feat} is the total count in the feature, W_{pix} is the pixel width in \AA , and C_{cont} is the average continuum).

In the case of Sample 2 (Fornax galaxies) I had spectra of three template stars: HD4188, HD26846 and HD4128. Since for HD4188 the calculated Mg_2 index was negative, for HD26846 Fe5335 was negative and for HD4128 both Mg_2 and Fe5335 were negative, no reliable corrections could have been obtained and therefore for this Sample I do not present result of calculations of indices. The stellar populations of early-type galaxies in the Fornax cluster are given in detail in Kuntschner (2000).

The results which I obtained are in a good agreement with these of Carollo, Danziger & Buson (1993) for IC1459 (Mg_2 is in an excellent agreement, Fe5270 that I obtained is somewhat higher ~ 3.8 in the center whereas they obtained ~ 3.4) and IC3370 (Mg_2 in an excellent agreement, iron indices for IC3370 are not given in Carollo, Danziger & Buson 1993). For NGC3379 both Mg_2 and iron indices that I obtained are in a very good agreement with these obtained by Kuntschner et al. (2001). For NGC4339 I obtained a lower value of Mg_2 (~ 0.20) than that found in Davis et al. (1987) that is 0.26. Finally, for NGC4105 the central value for Mg_2 that I obtained (~ 0.26) is a bit lower than that given by Davis et al. (1987) (~ 0.3). Iron indices were not compared for NGC4339 and NGC4105 because they are not given in Davis et al. (1987).

4.2 MODELING

The modeling of the indices in this thesis was based on the Pipino & Matteucci (2003) paper and the models were calculated by A. Pipino. Here, I briefly present the basics of the model.

This is a multi-zone photo-chemical evolution model for elliptical galaxies that takes into account detailed nucleosynthetic yields, feedback from supernovae and an initial infall episode. Its

basic prediction is that for galaxies with higher mass the infall and the star formation timescales are shorter: the most massive objects are older than the less massive ones (the larger galaxies stop forming stars at earlier times). According to this scenario, the galaxies are created outside-in: the outermost regions accrete gas, form stars and develop a galactic wind very quickly, whereas in the central core the star formation can last up to ~ 1.3 Gyr.

This monolithic collapse model in which ellipticals formed relatively quickly and at high redshifts is opposed to the hierarchical clustering model according to which ellipticals form over a large redshift interval. An evidence in favour of the monolithic collapse (for a full list see e.g. Calura 2003) is the increase in the strength of the metal metal absorption lines (Mass-Metallicity relation) with the velocity dispersion (see Fig. 10). The sample of five galaxies (especially galaxies with different peculiarities, such as counterrotating core, isophotal twisting, possible lack of dark matter) is of course too small to draw statistically significant conclusions, but the trend of increasing strength with the velocity dispersion is obvious.

Several different models were run with a calibration derived in the Pipino & Matteucci (2003) paper that uses calibration relations of Worthey (1994). This calibration is derived for a 12 Gyr old simple stellar population (SSP) with solar abundance ratios and $[\text{Fe}/\text{H}] > -0.5$ and the relations are:

$$\text{Mg}_2 = 0.187 \cdot [\text{Fe}/\text{H}] + 0.263,$$

$$\langle \text{Fe} \rangle = 1.74 \cdot [\text{Fe}/\text{H}] + 2.97,$$

where notation $[\text{Fe}/\text{H}]$ is defined to be:

$$[\text{Fe}/\text{H}] \equiv \log_{10} \left(\frac{n(\text{Fe})}{n(\text{H})} \right)_{\text{galaxy}} - \log_{10} \left(\frac{n(\text{Fe})}{n(\text{H})} \right)_{\odot},$$

where $n(\text{Fe})/n(\text{H})$ is the abundance (by number) of iron relative to hydrogen.

There exists a significantly different calibration based on the synthetic indices by Tantalo et al. (1998). At present the quality of fit with this calibration is not good, especially for the Mg_2 index where unphysical results occur. One suspects that this calibration needs to be revised.

Results of different runs are given in Fig. 11-Fig. 15. In several runs a dark matter halo was included for which the profile was taken from Bertin et al. (1992). The assumption that was made in this case is that the total mass of the dark component is ten times larger than that of the luminous one. Dark halo has a scale radius of $10 R_e$. Because of the fact that no significant amount of dark matter was found in this thesis from the dynamical modeling, several runs were made without the dark matter component. Physically, the lack of the dark matter means that the galactic wind in a given galaxy starts earlier at a given radial distance from the center but does not affect the chemical evolution. These runs seem to provide a better agreement with the observed data (see below).

An important conclusion from the paper of Pipino & Matteucci (2003) is that the variations of Mg_2 depend on the radial gradients in $[\text{Fe}/\text{H}]$ and $[\text{Mg}/\text{Fe}]$ (see Fig. 7 in their paper), while the predicted $\langle \text{Fe} \rangle$ gradient reflects instead the variation of the real abundance, $[\text{Fe}/\text{H}]$, as a function of galactic radius (see their Fig. 8). Therefore, one can conclude that the modeling of the iron indices is more reliable in establishing the real variation of the metallicity with the radius.

The results of the modeling are as follows. Two cases for which I had the spectra that extend out to large radial distances are especially difficult ones: IC1459 (with a counterrotating core) and IC3370 (with the large isophotal twisting). The calibration based on Worthey (1994) provided

various degrees of fit to the observed data. Several tests were done for each galaxy, and only the best fits to the observed values were plotted. The masses that were used are given in captions of Fig. 11-Fig. 15. Different input parameters are given in Pipino & Matteucci (2003): the best model "IIb" was used. For IC3370 (see Fig. 11) the model with dark matter can provide a good fit for the iron index, but fails for Mg_2 , whereas the test done without the dark matter provides better agreement for Mg_2 throughout the whole galaxy. None of the computed models could provide a good fit for Mg_2 index of IC1459 (see Fig. 12). The model which is devoid of dark matter provides better agreement in the outer parts of IC1459 (beyond $1R_e$). The observational results for NGC3379 (see Fig. 13) unfortunately do not extend out to a large radial distance and firm conclusions cannot be drawn. In the case of NGC4339 (see Fig. 14) the model without dark matter provide a good fit beyond $\sim 10''$ for both indices (the fit for Mg_2 is better). Finally, in the case of NGC4105 (see Fig. 15) the models provide an excellent fit to the Mg_2 index (again for the test done without the dark matter); none of the models run could fit the iron index.

As I have shown, the approach of Pipino & Matteucci can provide satisfactory fits in several difficult cases with the assumption of the absence of the dark halo in the given galaxy. One may argue that the changes of different input parameters to the model could improve the fit for a given galaxy without depriving it of its dark matter content. Several such tests were run: (i) the efficiency of star formation (ν) was varied but without a significant improvement of the fit (in the case of IC3370, for example), (ii) the infall timescale (τ) was varied but again without a significant improvement of the fit (again for IC3370). Only the exclusion of the dark matter halo could improve the fit to the data. It is probably premature to draw a conclusion about the dark matter content in early-type galaxies based on this kind of modeling (certainly, more tests are needed on a larger sample), but this approach in combination with the dynamical analyses could provide some insights into the chemo-dynamical properties and history of these galaxies.

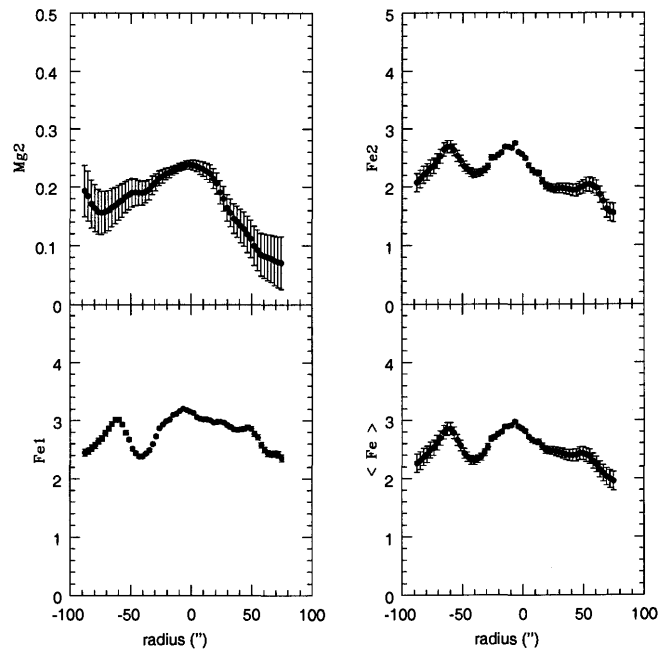


Figure 2: Mg_2 and iron indices (Fe_{5270} , Fe_{5335} , and $\langle Fe \rangle$) for the major axis of IC3370.

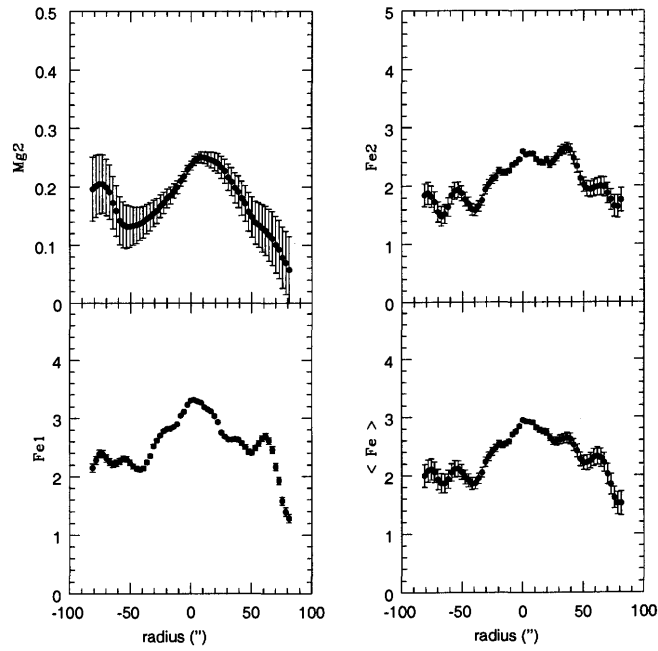


Figure 3: Mg_2 and iron indices (Fe_{5270} , Fe_{5335} , and $\langle Fe \rangle$) for the minor axis of IC3370.

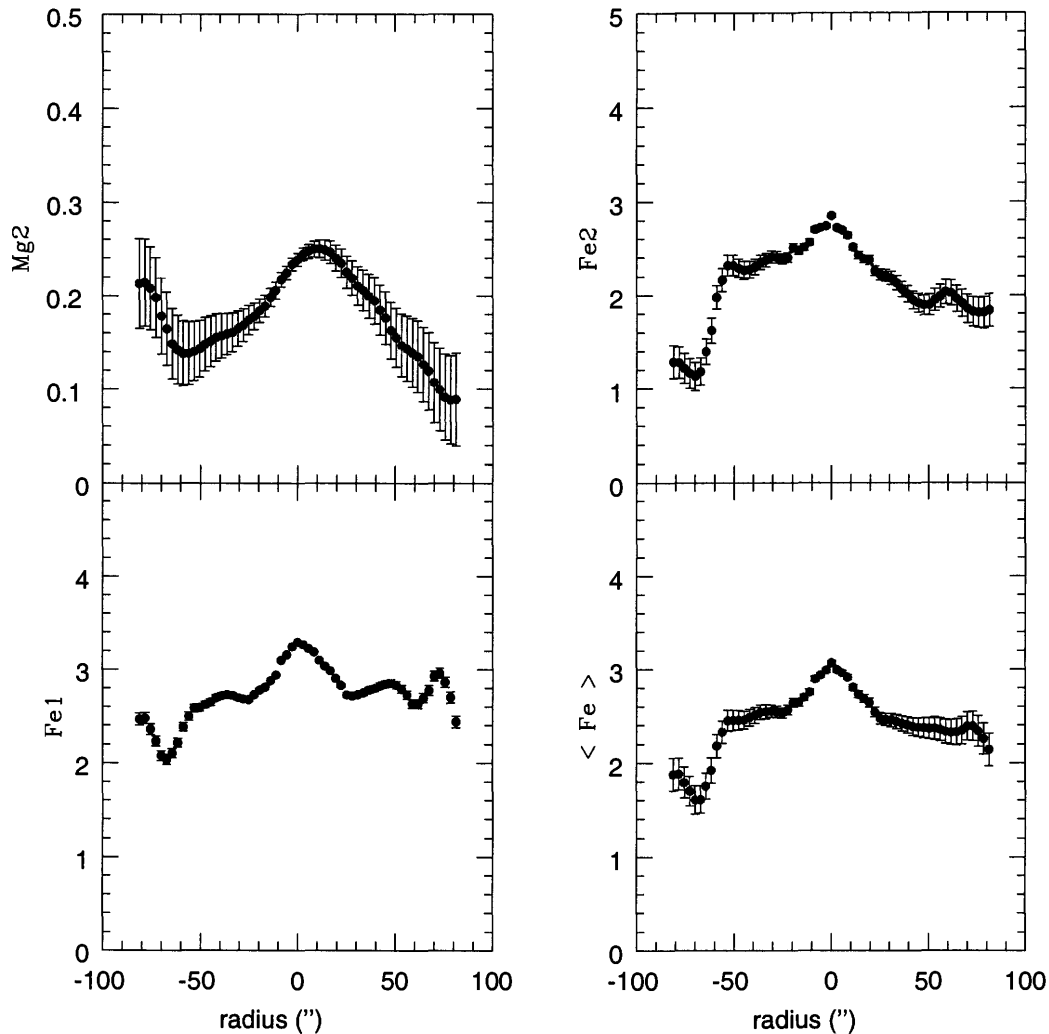


Figure 4: Mg₂ and iron indices (Fe5270, Fe5335, and <Fe>) for the intermediate axis of IC3370.

REFERENCES

- Bertin, G., Saglia, R.P. & Stiavelli, M.: 1992, *ApJ*, 384, 423
 Binney, J.J. & Merrifield, M.R.: 1998, *Galactic Astronomy*, Princeton University Press
 Calura, F.: 2003, PhD thesis, Univ. of Trieste
 Carollo, C.M., Danziger, I.J. & Buson, L.: 1993, *MNRAS*, 265, 553
 Davis, P.J. & Rabinowitz, P.: 1984, *Methods of Numerical Integration*, second edition, Academic Press, Inc., Harcourt Brace Jovanovich, Publishers
 Davies, R.L., Burstein, D., Dressler, A., Faber, S.M., Lynden-Bell, D., Terlevich, R.J. & Wegner, G.: 1987, *ApJS*, 64, 581
 Faber, S.M., Friel, E.D., Burstein, D. & Gaskell, C.M.: 1985, *ApJSS*, 57, 711
 Gonzales, J.J.: 1993, Ph.D. Thesis, Univ. of California, Santa Cruz

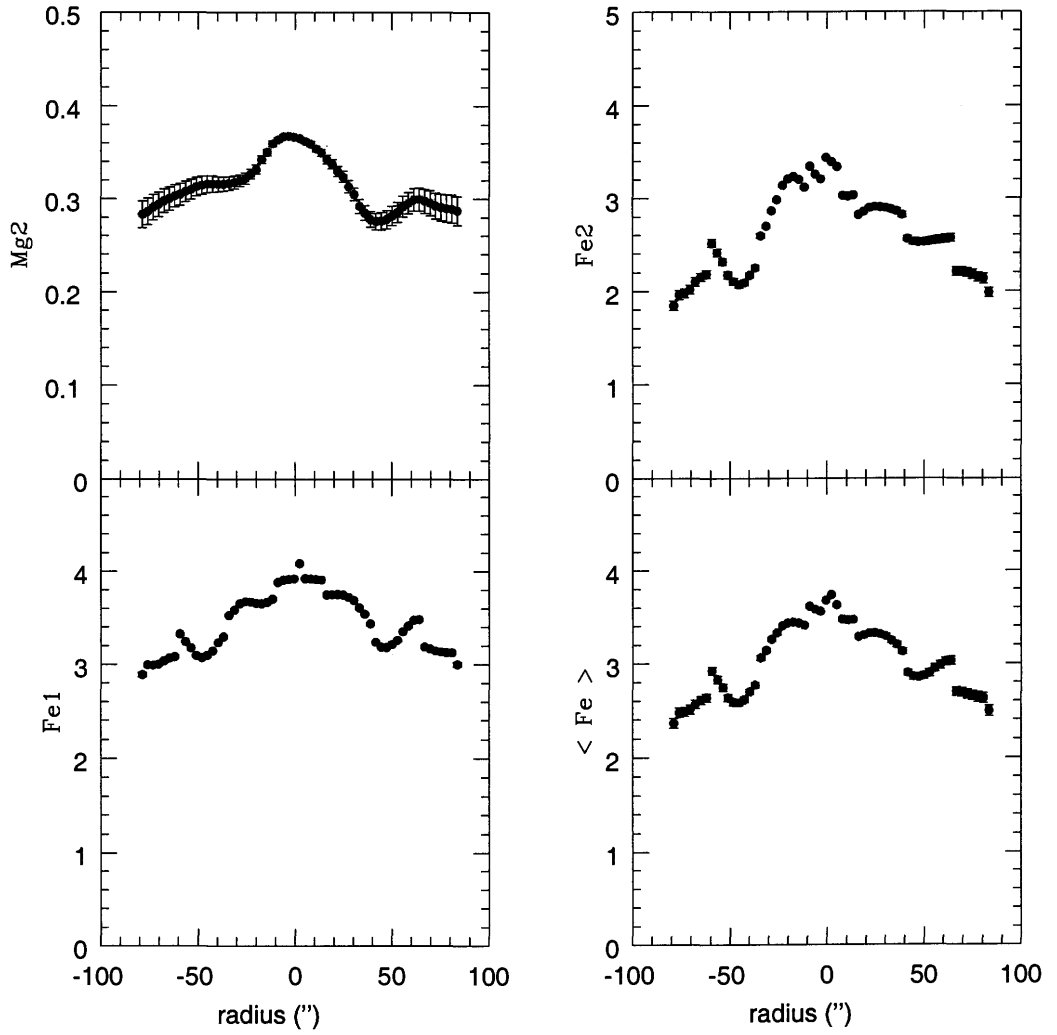


Figure 5: Mg2 and iron indices (Fe5270, Fe5335, and $\langle \text{Fe} \rangle$) for the major axis of IC1459.

Halliday, C.: 1998, Ph.D. Thesis, Univ. of Durham

Kuntschner, H.: 2000, MNRAS, 315, 184

Kuntschner, H., Lucey, J.R., Smith, R.J., Hudson, M.J., Davies, R.L. 2001, MNRAS, 323, 615

Pipino, A. & Matteucci, F.: 2003, MNRAS, in press, preprint astro-ph/0310251

Tantalo, R., Bressan, A. & Chiosi, C.: 1998, A&A, 333, 419.

Worthey, G.: 1994, ApJS, 95, 107

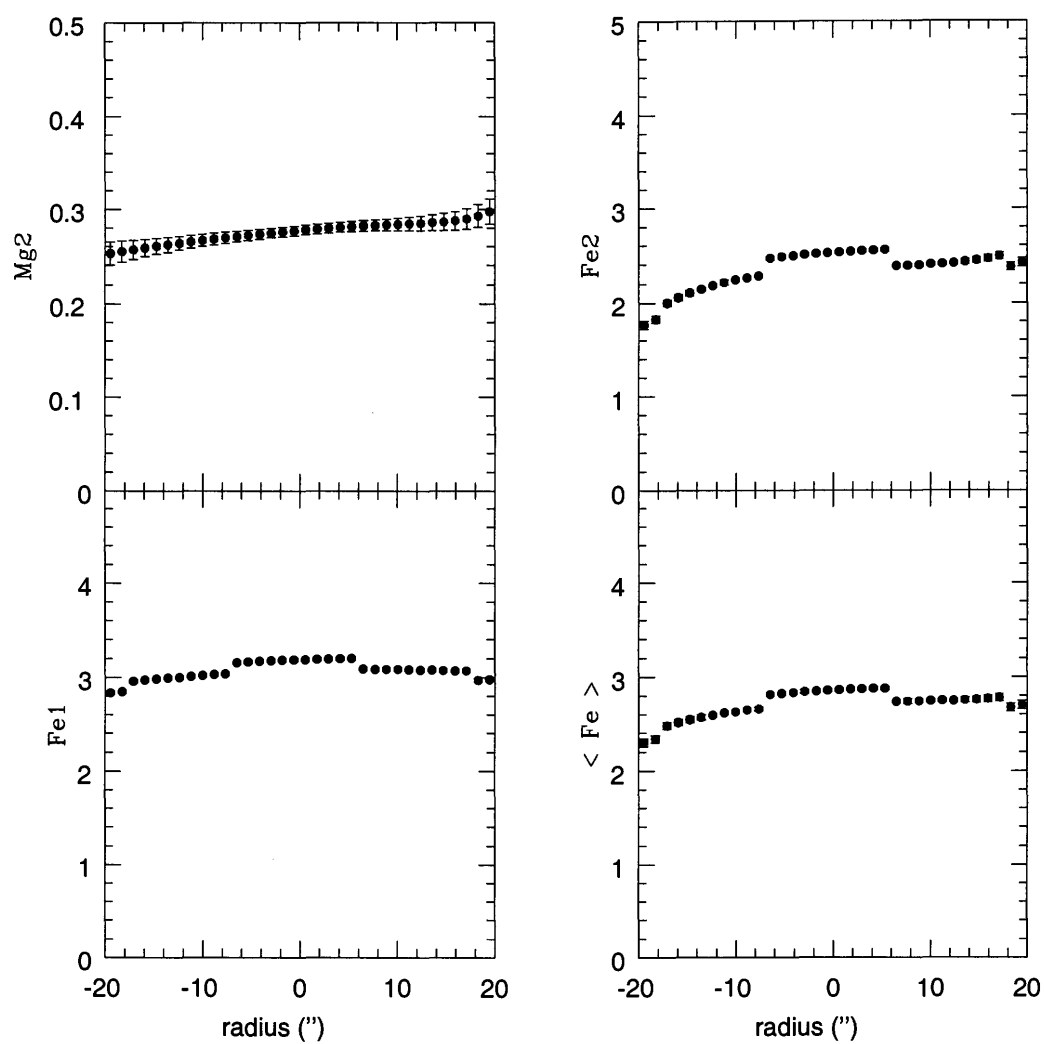


Figure 6: $Mg2$ and iron indices ($Fe5270$, $Fe5335$, and $\langle Fe \rangle$) for the major axis of NGC3379.

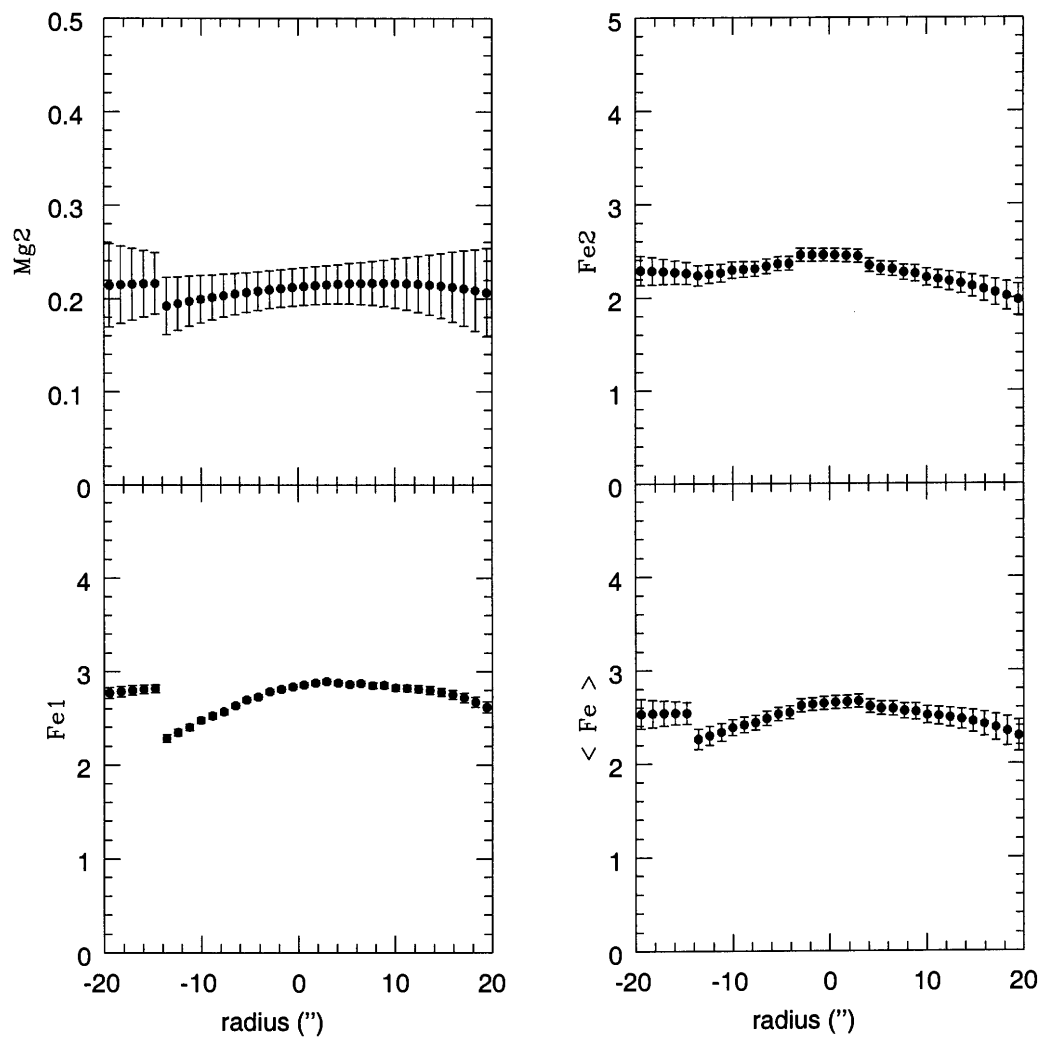


Figure 7: Mg_2 and iron indices (Fe_{5270} , Fe_{5335} , and $\langle Fe \rangle$) for the major axis of NGC4339.

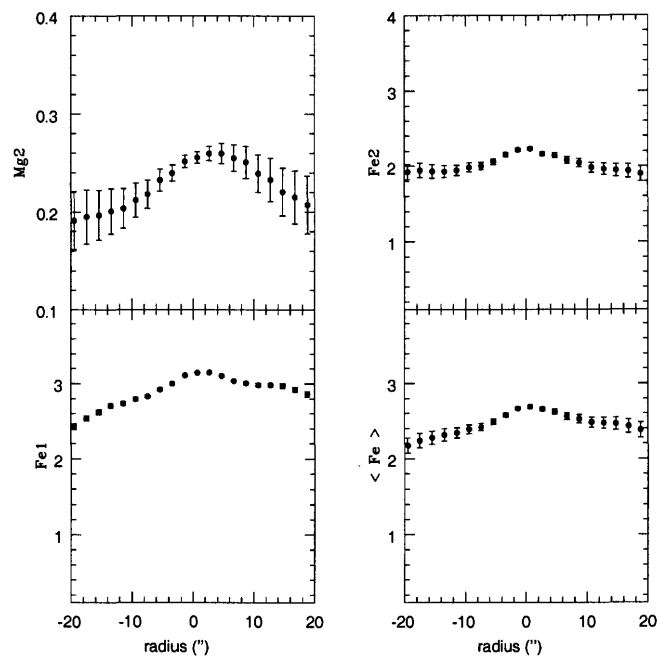


Figure 8: Mg_2 and iron indices (Fe_{5270} , Fe_{5335} , and $\langle Fe \rangle$) for the major axis of NGC4105.

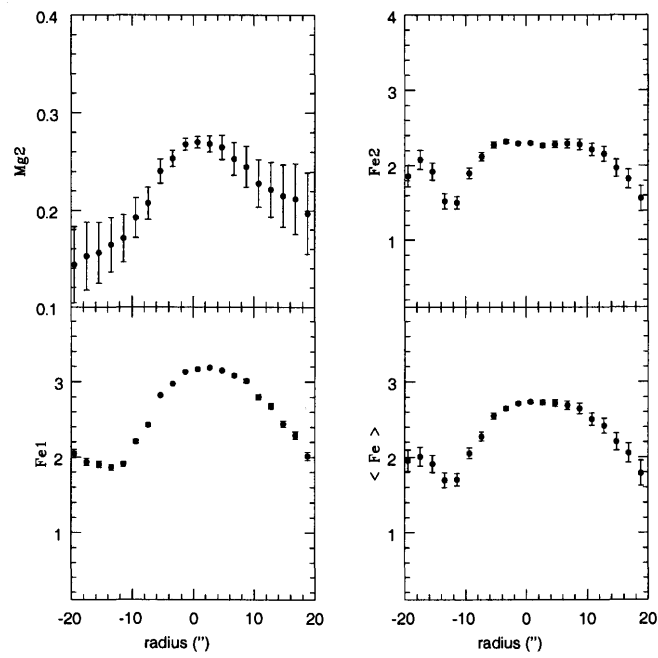


Figure 9: Mg_2 and iron indices (Fe_{5270} , Fe_{5335} , and $\langle Fe \rangle$) for the minor axis of NGC4105.

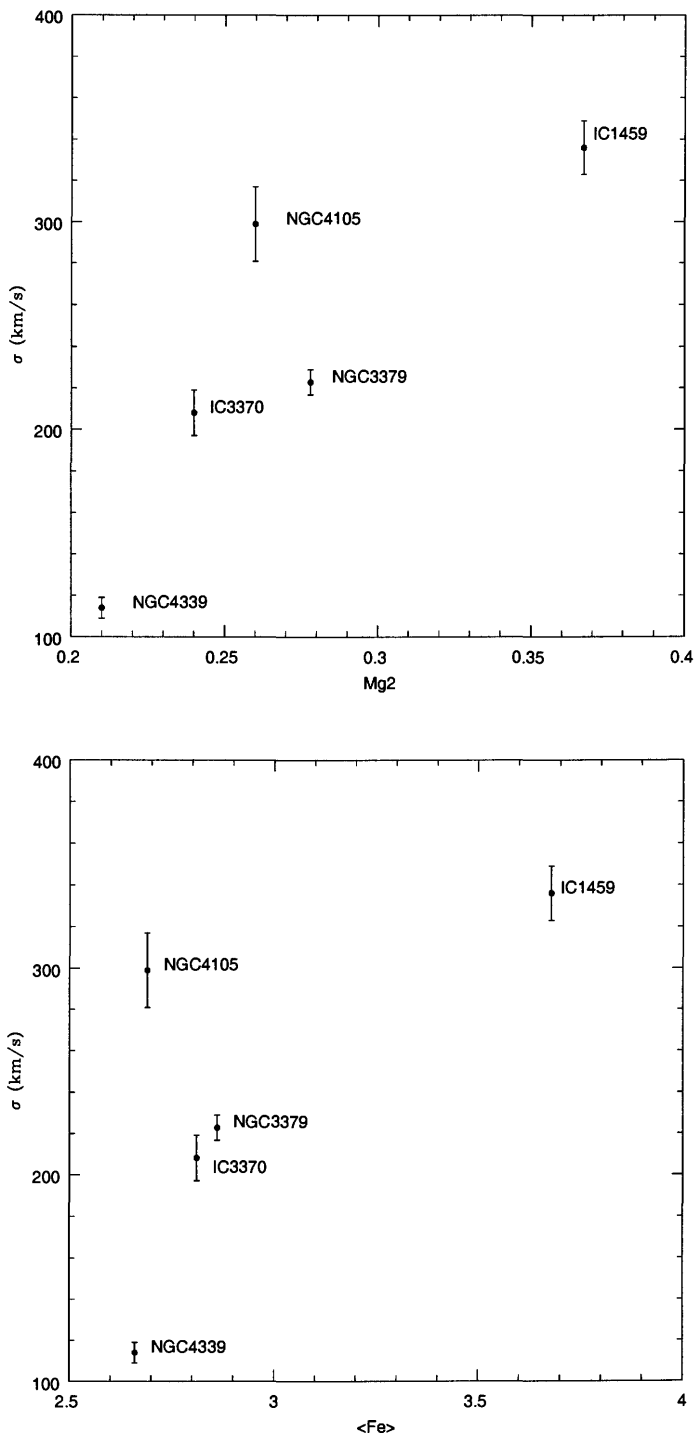


Figure 10: Mass-Metallicity relation for the galaxies in my samples. Left: Mg_2 index (in magnitudes) vs. velocity dispersion (in km/s). Right: $\langle Fe \rangle$ index (in Angstroms) vs. velocity dispersion (in km/s).

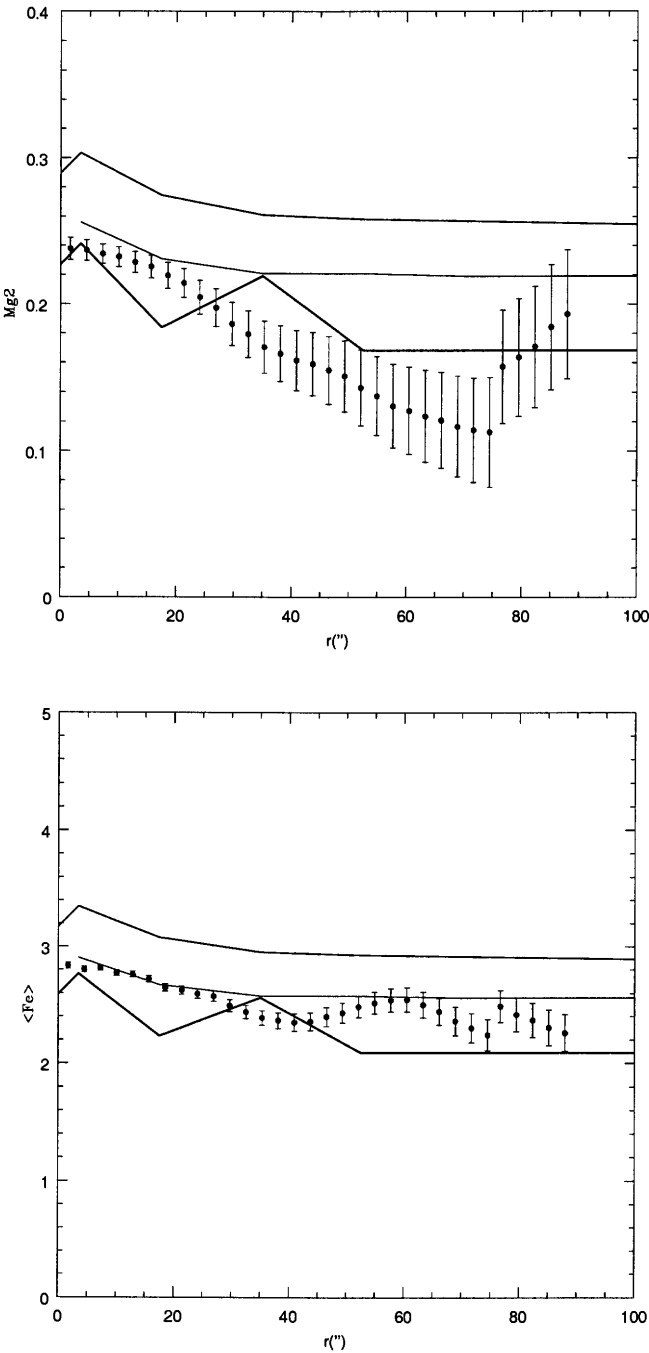


Figure 11: Modeling of Mg_2 index (above) and $\langle Fe \rangle$ (below) for IC3370 using model of Pipino & Matteucci (2003). Thin solid lines are for the case for which the total mass is $1.15 \times 10^{11} M_{\odot}$, with dark matter, thicker solid lines are for the case for which the total mass is $4.00 \times 10^{11} M_{\odot}$, with dark matter, and finally, the thickest solid lines are for the case for which the total mass is $1.15 \times 10^{11} M_{\odot}$ and *without* dark matter.

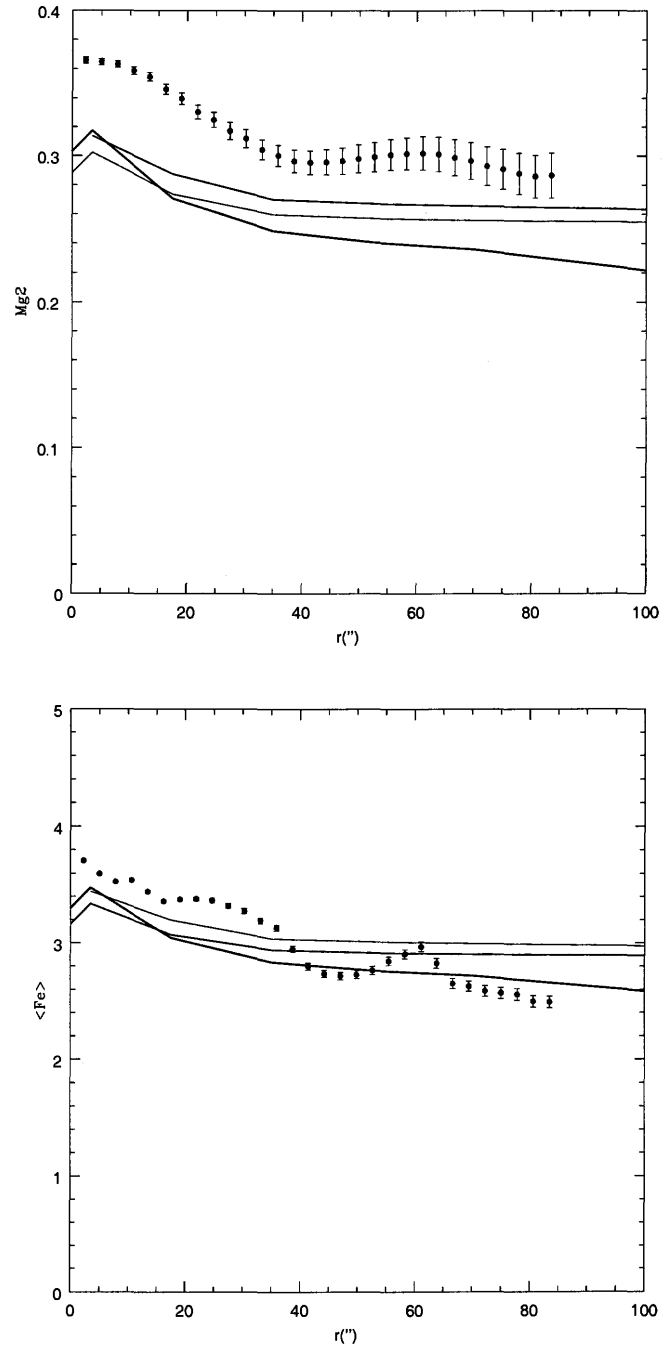


Figure 12: Modeling of Mg_2 index (above) and $\langle Fe \rangle$ (below) for IC1459 using model of Pipino & Matteucci (2003). Thin solid lines are for the case for which the total mass is $6.00 \times 10^{11} M_{\odot}$, with dark matter, thicker solid lines are for the case for which the total mass is $2.38 \times 10^{11} M_{\odot}$, with dark matter, and finally, the thickest solid lines are for the case for which the total mass is $6.00 \times 10^{11} M_{\odot}$ and *without* dark matter.

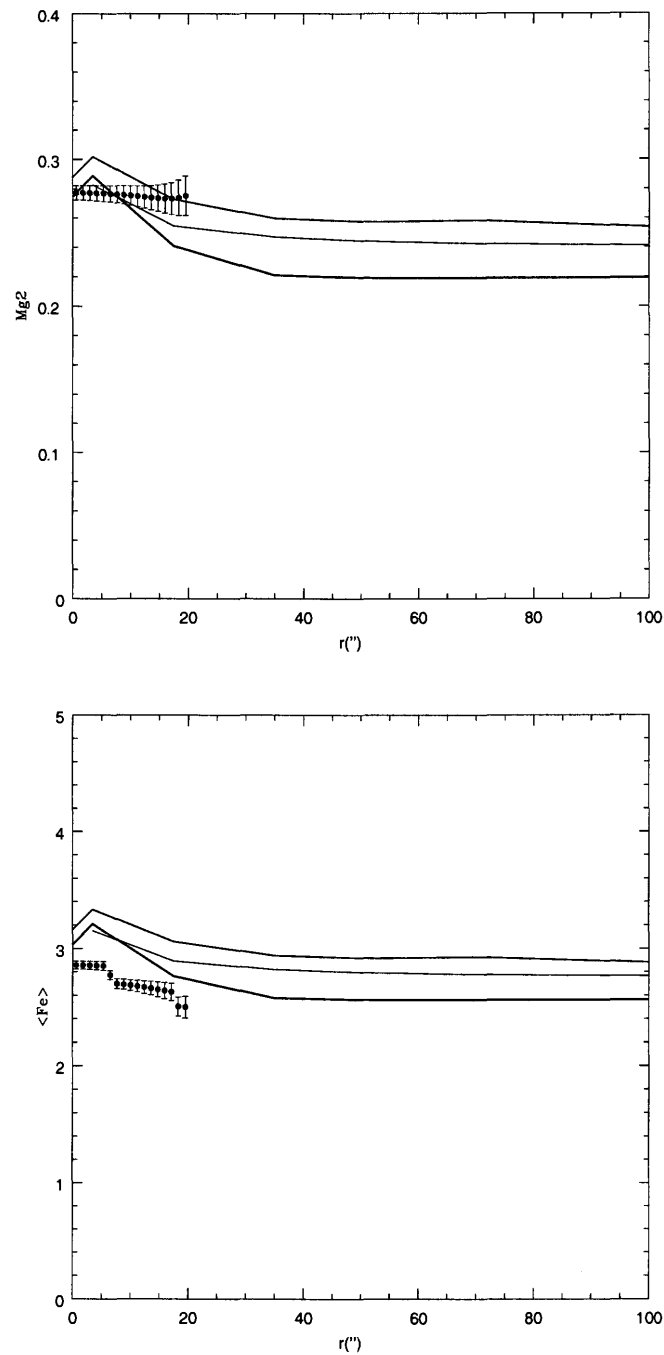


Figure 13: Modeling of Mg_2 index (above) and $\langle Fe \rangle$ (below) for NGC3379 using model of Pipino & Matteucci (2003). Thin solid lines are for the case for which the total mass is $1.00 \times 10^{11} M_{\odot}$, with dark matter, thicker solid lines are for the case for which the total mass is $1.82 \times 10^{11} M_{\odot}$, with dark matter, and finally, the thickest solid lines are for the case for which the total mass is $1.00 \times 10^{11} M_{\odot}$ and *without* dark matter.

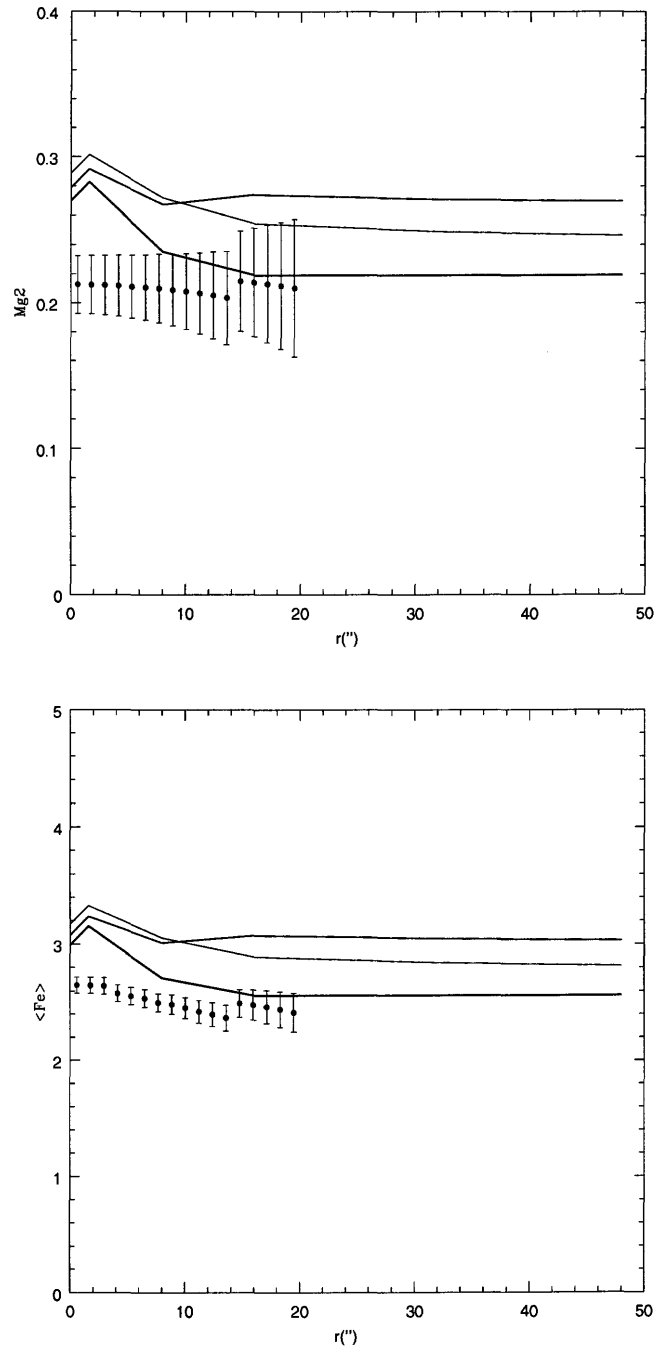


Figure 14: Modeling of Mg_2 index (above) and $\langle Fe \rangle$ (below) for NGC4339 using model of Pipino & Matteucci (2003). Thin solid lines are for the case for which the total mass is $7.00 \times 10^{10} M_{\odot}$, with dark matter, thicker solid lines are for the case for which the total mass is $5.5 \times 10^{10} M_{\odot}$, with dark matter, and finally, the thickest solid lines are for the case for which the total mass is $7.00 \times 10^{10} M_{\odot}$ and *without* dark matter.

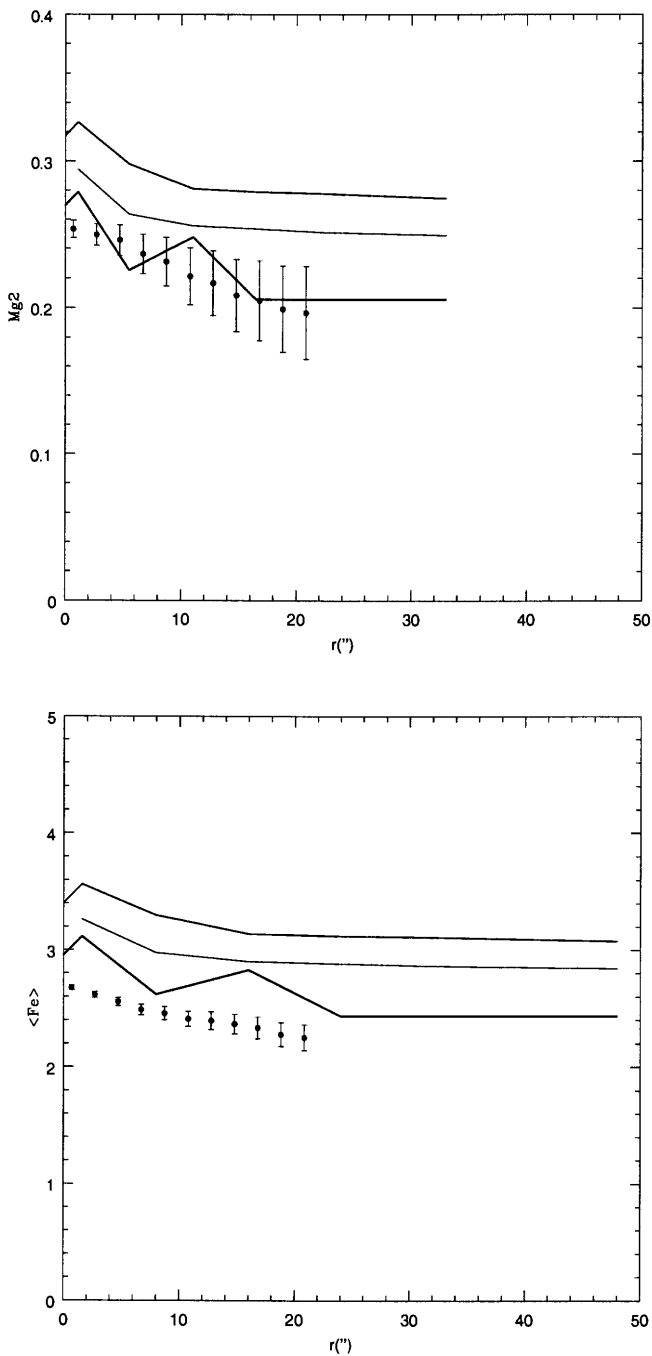


Figure 15: Modeling of Mg_2 index (above) and $\langle Fe \rangle$ (below) for NGC4105 using model of Pipino & Matteucci (2003). Thin solid lines are for the case for which the total mass is $5.00 \times 10^{10} M_\odot$, with dark matter, thicker solid lines are for the case for which the total mass is $2.00 \times 10^{11} M_\odot$, with dark matter, and finally, the thickest solid lines are for the case for which the total mass is $5.00 \times 10^{10} M_\odot$ and *without* dark matter.

5

CONCLUSIONS

It has been shown that the problem of dark matter in the early-type galaxies is not completely resolved, although analyses of the observational data and the modeling presented in this thesis in combination with other methodologies found in the literature can provide some important conclusions.

The *first conclusion* is that the former point of view (cf. Binney & Merrifield 1998, hereafter BM98) is still valid: it remains very difficult to establish unambiguously the existence of dark haloes in early-type galaxies based on observations alone. Small values of the $|h_4|$ parameter at large radial distances from the center of a given galaxy can mean that there is no significant orbital anisotropy and that a slow decline (or even increase) of the velocity dispersion is due to the existence of a dark halo. However, as I have shown in the case of the two galaxies, for which the spectra extend to $\sim 3R_e$ (IC1459, IC3370), and at least for two other cases which are well studied in literature (NGC5128 out to $\sim 15R_e$ and NGC3379 out to $\sim 6R_e$) the velocity dispersion does not show such a slow decline (even if the h_4 parameter does show a non-zero value at $\sim 3R_e$ in the case of IC1459). In principle, it is incorrect to draw conclusions about dark matter in a given galaxy judging only from the behaviour of the velocity dispersion, if the h_4 parameter is not known. Therefore, all statements in literature when there is claim about the existence of dark matter in a given galaxy, but without providing the information about h_4 should be taken with caution, and the data should be, if possible, reanalyzed. A question that one naturally poses is: "how can one establish whether the decline is 'slow'?", or, more precisely, "what is the criterion for the behaviour of the velocity dispersion in the absence of a dark halo?".

These coupled questions lead to the *second conclusion*, also recognized earlier (cf. BM98): for a confirmation of the existence of dark matter in early-type galaxies detailed modeling is needed. As shown in the previous Chapters, one can use two- and three-integral modeling techniques. Each one has its own merits and shortcomings. Two-integral modeling (Binney, Davies, & Illingworth 1990) gives a prediction of the velocity dispersion behaviour and sometimes it might be enough to perform only this analysis: this would be an ideal case of an axisymmetric galaxy in which there are only two integrals of motion. It is not an easy task to find a priori a galaxy which simultaneously possesses these two features: of the four galaxies studied in this thesis using a two-integral approach (IC1459, IC3370, NGC3379, NGC4105), none of them fulfilled both of these two requirements. It is however interesting to see how they differ with respect to these given requirements: the best fit to the whole observed velocity profile was found in the case of NGC3379; beyond $\sim 20''$ (the region where this galaxy is axisymmetric) the whole velocity profile can be fitted for both major and minor axis, thus leading to the conclusion that the dark halo is not necessary. This result is in agreement with the recent study of Romanowsky et al. (2003)

who studied this galaxy using planetary nebulae (PNe). For IC1459 and NGC4105 the velocity dispersion declines again in an agreement with the no dark matter hypothesis, but since the two-integral modeling cannot provide a simultaneous fit to velocity and velocity dispersion one can conclude that the motion in these two galaxies depends on three integrals of motion. Note also that since IC1459 possesses a stellar counter-rotating core, two-integral modeling based on photometry, fails in the inner regions of this galaxy. The case of IC3370 was particularly difficult to model because this galaxy shows a large isophotal twist, indicating triaxiality. Still, using the two-integral approach, the fit to the velocity dispersion was obtained without the introduction of a dark halo. Regardless of the fact that the two-integral modeling is not suitable when there are strong departures from axisymmetry and when the motion depends on the third integral, this method is very convenient for establishing the possible range of the mass-to-light ratio of a given galaxy. Its application gave results that are in agreement with the results obtained using other methods: for example, for IC1459 the estimated mass-to-light ratio ($6 \lesssim M/L_B \lesssim 10$) is in agreement with the value found using X-ray data, while for NGC3379 the obtained mass-to-light ratio ($5 \lesssim M/L_B \lesssim 9$) is in agreement with the values found using X-ray data, PNe, and globular clusters. It is important to note that a constant mass-to-light ratio does not exclude the presence of a dark halo: if the dark matter has the same profile as the stars, the derived mass-to-light ratio will be constant with radius, but of course, it will be higher than that produced by the stars alone (cf. Ashman 1992). But if the mass-to-light ratio of a given galaxy is not significantly different from the result obtained by van der Marel (1991): $M/L_B = (5.95 \pm 0.25)h_{50}$, one can claim that no significant amount of the dark matter is present. An additional clue related to the two-integral modeling is that there is a tendency for a slight increase of the mass-to-light ratio in the outer parts of the early-type galaxies which I studied.

The existence of the triaxiality and the existence of the third integral of motion in the early-type galaxies initiated the development of the three-integral techniques based on the Schwarzschild's (1979) orbit superposition method. The *third conclusion* is related to the three-integral modeling in general: using the three-integral modeling technique one can obtain better fits to the observed galaxy kinematics but the price that one has to pay is rather high. This method is very CPU intensive and requires large disk storage and therefore its application is rather difficult which is the reason why so far only a fairly small number of galaxies has been analyzed in such a way: to date (in fact, until June 2003, see Gebhardt (2003) review) only 17 galaxies were analyzed using three different codes¹ for the orbit superpositions (none of them is freely available), and the analyses mainly dealt with the inner parts, i.e. central massive black holes. Gebhard (2003) however warns: "With so few groups using orbit-based codes, we must be certain that the immense freedom allowed by these codes does not bias the results due to some feature of an individual code." Therefore, one may conclude that the interpretation of the results obtained using the orbit superposition method must be taken with the greatest caution and used (wherever possible) in combination with the results obtained using other methods. The "immense freedom" inherent in these models (choice of orbits, choice of potential, features of the potential, number of orbits, etc) still permits some conclusions related to the "features of an individual code" and the properties of galaxies to be drawn. In my implementation (which makes the second code to be added to the Gebhard's list) orbit superposition method provided hints about the applicability of a given potential. It also gave a possibility to test different features of a given potential (flattening, different

¹ Here, I add the code of Romanowsky & Kochanek 2001 that was applied in the Romanowsky et al. 2003 paper.

mass-to-light ratios, for example). Since this method (Rix et al. 1997 implementation) forces the fit of the velocity and the velocity dispersion, one has to study carefully the modeling of the Gauss-Hermite parameters. I found that in the very difficult case of IC3370 the constant mass-to-light ratio potential provides a better fit to h_3 and h_4 interior to $2R_e$ (see Fig. 11 in Chapter 2) and that inside this region dark matter is not required. Between 2 and 3 effective radii the triaxial logarithmic potential provides a marginally better fit for h_4 indicating that there is a hint of the presence of a dark halo in the outer regions. Also, as can be seen from the same Figure, an axisymmetric potential is clearly ruled out, which is in agreement with the fact that this galaxy shows a strong isophotal twisting. Another example, IC1459 (see Fig. 12 from Chapter 2), shows how difficult it is to discriminate between different potentials using orbit superposition techniques. Clearly, one can easily rule out unrealistically large mass-to-light ratios (~ 20 in the B-band) in the inner parts of the galaxy. Beyond $\sim 1R_e$ both mass-to-light ratio potentials (for $M/L_B \sim 10$ and ~ 20) seem to provide similar fits. None of the potentials used managed to fit satisfactorily the h_4 parameter in the outer parts, therefore making it difficult to draw conclusions about the dark matter in IC1459. This method provides similar fits for different potentials when one is constrained to the galaxy's inner parts: in the Fornax sample, for example, it is very difficult to see differences in the modeling curves which were plotted using different potentials. Also, in the case of the Carollo et al. (1995) sample, of all four galaxies, my implementation only in the case of NGC3706, the galaxy for which the modeling curve shows the largest departure from the observed data, provides a hint of the dark matter halo (see Figs. 24 and 26 from Chapter 2); all other galaxies can be reasonably fitted with a constant mass-to-light ratio potential. The overall conclusion is that the three-integral modeling, in my implementation, can only provide a useful hint about applicability of a given potential for a given set of orbits. Given the "immense freedom" of this kind of modeling, this method should (or better, must) be used in combination with other approaches to infer the existence of dark haloes.

The problems that arose in the three-integral method which show that different approaches have to be applied to a given galaxy in order to determine the existence of the dark halo lead to a *fourth conclusion*: discrepancies between the results of different methodologies have to be studied very carefully because they may indicate that some of the fundamental physical assumptions are not valid and need to be revised and/or some new assumptions should be taken into account. To illustrate the present doubts I compiled the TABLE 5-1 which shows state of art results in dark matter research. In the first column I put the method of research: in some cases I included two different sets of data because they show small differences. For example, Romanowsky et al. (2003) claim that there is no dark matter in the outer parts of their sample, whereas Peng et al. (2003) infer that for NGC5128 the dark halo exists although the estimated mass-to-light ratio is much smaller than expected. In both of these the information about h_3 and h_4 is missing. Note, however, that Romanowsky et al. (2003) took into account in their analysis possible orbital anisotropies, while Peng et al. (2003) assumed orbital isotropy for which they found confirmation in the recent mass estimates of NGC5128 obtained with Chandra and XMM and presented in the paper by Kraft et al. (2003). Since the major part of this thesis is dedicated to the study of the integrated stellar spectra I dedicated one row of TABLE 5-1 to my results, and put together the estimates from the literature in a separate one. The second column is my personal estimate of the "strength" of different methods to predict the existence of dark matter haloes. It is given in asterisks using the following scale: one means that the method provides no evidence of the dark matter, and five

asterisks means that a given method very strongly suggests existence of dark haloes (intermediate cases are in between). The third column is the radius out to which a given method is being applied (it is given in units of effective radius), the fourth column presents the mass-to-light ratio obtained with a given method at the radius given in the third column (note that it is given in the B-band; I converted the data originally given in other bands to the B-band for the sake of comparison). Finally, in the fifth column are the references. One can see that methods based on gas (hot gas from X-ray observations) and cold gas (from neutral hydrogen observations) give large mass-to-light ratios. It is of interest to note that especially X-ray analyses strongly suggest very large mass-to-light ratios in the outer parts of early-type galaxies, which has not been confirmed recently using other methods (such as PNe or globular clusters (GCs)). Of course, one should be cautious about these two new techniques when drawing conclusions, because the number of analyzed galaxies is still very small. However, some of the two basic postulates of this method: (i) the fact that the gas obeys the perfect gas law and (ii) the fact that the condition of hydrostatic equilibrium obtains, may not be valid (see the discussion in Chapter 3). In the case of the mass-to-light ratio estimate based on the cold gas the basic assumptions are (cf. Oosterloo et al. 2002): (i) spherical mass distribution and (ii) circular orbits of the gas, which may not be true. Also, since the cold gas is not frequent in the early-type galaxies this method is unsuitable for larger surveys in the future. One may notice that in this thesis strong evidence for dark haloes in the early-type galaxies was not found thereby reducing the "strength" of the integrated spectra method (here I assume both observations and two- and three-integral modeling) from four (found in literature) to two (I put two, and not one, because of the slight trend of increase of the mass-to-light ratio for galaxies studied using two-integral technique and because in some cases the Schwarzschild modeling suggested the applicability of the logarithmic potential). The reasons for this could be (i): my results are biased because my sample included only galaxies that do not have much dark matter, (ii) the modeling that I used was not suitable for the detection of the dark matter. The first of these statements could be true, but one should bear in mind that I analyzed galaxies that are isolated (field), that belong to some group and that belong to a Fornax cluster. The samples of galaxies included both bright and intermediate luminosity galaxies². A bigger sample would, of course, be useful, but even the present one should be large enough to provide some conclusions that might be indicative of the existence of dark matter in the early-type galaxies. The second statement could also be true, but again, one should take into account that given the "immense liberty" (at least in the three-integral modeling case) such an outcome was one of the possible ones. Therefore, in order to see the convergence of results for a given galaxy (observations plus modeling for every given method), a combination of different methodologies is necessary. The lensing technique, another promising new method, can provide useful insights about the dark matter in distant early-type galaxies ($z \sim 1$), especially about the evolution of the stellar mass-to-light ratio with redshift. Results obtained so far strongly suggest the existence of large amounts of dark matter ($> 50\%$ of the mass inside the Einstein radius) in the early-type galaxies. Probably, the best way to study the dark haloes in the near future would be by using PNe and GCs in combination with the integrated spectra data: stellar spectra should provide reliable estimates of the velocity profiles out to $\sim 3R_e$ and PNe and/or GCs in the outer parts. For example, Bridges et al. (2003) obtained (but has not published) results for GCs of, among other galaxies, IC1459 — it will be of great interest to compare their findings with the results obtained in this thesis.

² About a possible bias, see also the fifth conclusion below.

TABLE 5-1

RESULTS OF DARK MATTER RESEARCH IN EARLY-TYPE GALAXIES
USING DIFFERENT METHODOLOGIES

Method	DM evidence	Radius	M/L_B	Reference
Hot gas	*****	$6 R_e$	33.5	Loewenstein & White (1999)
Warm gas	*	$1 R_e$	5	Pizzella et al. (1997)
Cold gas	****	$6 R_e$	18	Oosterloo et al. (2002)
PNe (1)	*	$6 R_e$	6.4	Romanowsky et al. (2003)
PNe (2)	**	$15 R_e$	13	Peng et al. (2003)
GCs	*	$6 R_e$	8	Bridges et al. (2003)
Integrated spectra (1)	**	$3 R_e$	5-10	this thesis
Integrated spectra (2)	****	$1-3 R_e$	5-20	see Introduction
Lensing	*****	$5 R_e$	8	Treu & Koopmans (2002)

As a *fifth conclusion* I confirm using my samples of galaxies that in galaxies with larger values of the effective radius in physical units there is a hint of dark matter: Bertin et al. (1994) found that for galaxies that have $R_e > 8$ kpc one can argue in favor of dark matter. Note that this value was calculated for $h_0 = 0.5$, whereas throughout this thesis I have used $h_0 = 0.7$, which after rescaling gives the boundary value of the effective radius ≈ 5.7 kpc. I found that indeed, for galaxies which have $R_e > 5.7$ kpc there is evidence for the existence of a dark halo. Such cases are: IC3370 ($R_e \approx 7.1$ kpc) and NGC3706 ($R_e \approx 6.01$ kpc). The case of NGC1399 for which there is a strong hint of dark matter, is a difficult one because of the problem of the determination of its effective radius: if one adopts Caon et al. (1994) value of $127'' (=12.72$ kpc) this would put this galaxy in the group of galaxies with large effective radius in kpc. For galaxies which have $R_e < 5.7$ kpc the modeling did not provide much evidence for the existence of dark haloes (except for NGC1339 and NGC1373 for which there is a hint based on the rising velocity dispersion and large h_4 at $\sim 1.5 R_e$). As suggested by Bertin et al. (1994): "this might be taken as an indication that dark haloes come roughly as objects of the same physical size, so that they would emerge preferentially from the stellar dynamical data only when the luminous galaxy is sufficiently extended". This is an interesting fact which certainly deserves a deeper study (possibly with PNe, and/or GCs) in the future.

A *sixth conclusion* should be related to the relationship between the X-ray haloes and dark haloes: unfortunately, some firm statement cannot be given at this point. Of the five galaxies which have X-ray haloes (IC1459, NGC1399, NGC1404, NGC4105 and NGC3379) using the stellar dynamics models, only in the case of NGC1399 is there a hint of a dark halo. The results from the observations using the X-ray technique suggest much larger mass-to-light ratios at the large radial distance from the center than that obtained using PNe technique. For example, for NGC5128 Peng et al. (2003) obtained $M/L_B \sim 13$ which much lower than the value expected from the X-rays analysis: $M/L_B \sim 112 \pm 28$, (Bahcall, Lubin & Dorman 1995). The reason for such a large discrepancy between these two estimates at large radii is unclear and remains to be solved.

Given the problems in establishing the very existence of the dark matter haloes in the early-type galaxies the *seventh conclusion* comes as no surprise: one cannot say much about the nature of the dark matter content of these galaxies, for example, whether it is baryonic or non-baryonic.

The final, *eighth conclusion* is related to the modeling of the line strength indices: it was shown that in several cases (most notably of IC1459 and IC3370) a better fit to the observed values is obtained without dark matter.

PROSPECTS FOR THE FUTURE

If we want to establish unambiguously the existence of dark haloes in early-type galaxies we need to perform more accurate studies involving different interconnected branches of astrophysics. To date, different important aspects (for example, stellar dynamics, X-ray haloes and other mass tracers, chemical evolution) have been studied in detail, but much is left to be done, especially observationally, always bearing in mind the theoretical assumptions which have to be constantly questioned. First of all, it is absolutely necessary to enlarge the sample of integrated stellar spectra of early-type galaxies observed out to at least three effective radii. For all the existing observations a critical reanalysis that takes into account the full line-of-sight velocity distribution is needed (when such data exist). On the basis of the results from this thesis, a good way to proceed would be to choose several early-type galaxies which should be isolated, which should exhibit axisymmetry and are devoid of peculiarities (such as counterrotating core), which should possess an X-ray halo, and preferably have other possible mass tracers (for example, PNe and/or GCs) in order to perform a detailed stellar kinematic modeling (inside $\sim 3R_e$) and an X-ray study (beyond $1R_e$). This is, of course, an ambitious undertaking – a search for such candidates is already a demanding task. Other mass tracers will have to be studied and the results should be confronted with the previous two analyses. Detailed chemical evolution modeling should also be performed. Only in this way can we expect that the dark matter problem in early-type galaxies will be solved.

REFERENCES

- Ashman, K.M.: 1992, PASP, 104, 1109
 Bahcall, N.A., Lubin, L.M. & Dorman, V.: 1995, ApJ, 447, L81
 Bertin, G., Bertola, F., Buson, L. M., Danzinger, I. J., Dejonghe, H., Sadler, E. M., Saglia, R. P., de Zeeuw, P. T. & Zeilinger, W. W.: 1994, A&A, 292, 381
 Binney, J.J., Davies, R.D. & Illingworth, G.D.: 1990, ApJ, 361, 78
 Binney, J.J. & Merrifield, M.R.: 1998, *Galactic Astronomy*, Princeton University Press (BM98)
 Bridges, T., Beasley, M., Faifer, F., Forbes, D., Forte, J., Gebhardt, K., Hanes, D., Sharples, R. & Zepf, S.: 2003, in press, in "Joint Discussion 6: Extragalactic Globular Clusters and their Host Galaxies", IAU General Assembly, July 2003. T. Bridges and D. Forbes (eds.), preprint astro-ph/0310324
 Caon, N., Capaccioli, M. & D'Onofrio, M.: 1994, A&ASS, 106, 199
 Carollo, C.M., de Zeeuw, P.T., van der Marel, R.P., Danziger, I.J. & Qian, E.E.: 1995, ApJ, 441, L25
 Gebhardt, K.: 2003, to appear in "Carnegie Observatories Astrophysics Series, Vol. 1: Coevolution of Black Holes and Galaxies," ed. L. C. Ho, preprint astro-ph/0306090

- Kraft, R. P., Forman, W. R., Jones, C., Murray, S. S., Hardcastle, M. J. & Worrall, D. M.: 2003, *ApJ*, 592, 129
- Loewenstein, M. & White, R.E.: 1999, *ApJ*, 518, 50
- Oosterloo, T. A., Morganti, R. Sadler, E. M., Vergani, D. & Caldwell, N.: 2002, *AJ*, 123, 729
- Peng, E.W., Ford, H.C. & Freeman, K.C.: 2003, *ApJ*, in press, preprint astro-ph/0311236
- Pizzella, A. Amico, P., Bertola, F., Buson, L.M., Danziger, I.J., Dejonghe, H., Sadler, E.M., Saglia, R.P., de Zeeuw, P.T. & Zeilinger, W.W.: 1997, *A & A*, 323, 349
- Rix, H.-W., de Zeeuw, P.T., Cretton, N., van der Marel, R.P. & Carollo, C.M.: 1997, *ApJ*, 488, 702
- Romanowsky, A.J. & Kochanek, C.S.: 2001, *ApJ*, 553, 722
- Romanowsky, A.J., Douglas, N.G., Arnaboldi, M., Kuijken, K., Merrifield, M.R., Napolitano, N.R., Capaccioli, M. & Freeman, K.C.: 2003, *Science*, 5640, 1696
- Schwarzschild, M.: 1979, *ApJ*, 232, 236
- Treu, T. & Koopmans, L.V.E.: 2002, *ApJ*, 575, 87
- van der Marel, R.P.: 1991, *MNRAS*, 253, 710

APPENDIX 1

ILL-POSED PROBLEMS AND REGULARIZATION

A1.1 Introduction

The solution of the system of equations given in eq. (14) of Rix et al. (1997) gives the orbital weights γ_k . Non-negative least square (NNLS) fit always gives a formally unique solution (more about NNLS in a separate appendix). However, this solution will in principle be very irregular in phase space which is physically implausible. Non-negativity is the only physical constraint on the distribution function (DF).

The study of the extremely simple worked example (from Hansen (2001)) provides a description of the problems that one faces when encountered with an ill-posed problem such as the one mentioned above. One can consider the following least-squares problem:

$$\min_x \|Ax - b\|_2. \quad (1)$$

Here, coefficient matrix A and right-hand side (RHS) vector b are given by:

$$A = \begin{pmatrix} 0.16 & 0.10 \\ 0.17 & 0.11 \\ 2.02 & 1.29 \end{pmatrix} \quad (2)$$

and

$$b = \begin{pmatrix} 0.27 \\ 0.25 \\ 3.33 \end{pmatrix}. \quad (3)$$

In this case the RHS vector b is generated by simply adding a small perturbation to an exact RHS that corresponds to the exact solution

$$x = \begin{pmatrix} 1.00 \\ 1.00 \end{pmatrix} :$$

$$b = \begin{pmatrix} 0.16 & 0.10 \\ 0.17 & 0.11 \\ 2.02 & 1.29 \end{pmatrix} \times \begin{pmatrix} 1.00 \\ 1.00 \end{pmatrix} + \begin{pmatrix} 0.01 \\ -0.03 \\ 0.02 \end{pmatrix}. \quad (4)$$

The problem with this least-squares problem is that the matrix A is ill-conditioned. Namely, since its condition number¹ is equal to 1.0975×10^3 (using MATLAB cond routine), this means

¹ The condition number of a matrix A is a measure of the sensitivity of the solution of a system of linear equations to errors in the data. It also gives an indication of the accuracy of the results from matrix inversion and the linear equation solution. If the condition number of A is large, A is said to be ill-conditioned. A value near 1 indicates a well-conditioned matrix. The condition number is the ratio of the largest singular value of A to the smallest.

that the computed solution will be very sensitive to perturbations of the data. If now one calculates the ordinary least-squares (LSQ) solution by means of QR factorization (using, for example, NAG routine F08AEF) one obtains the solution:

$$x_{\text{LSQ}} = \begin{pmatrix} 7.01 \\ -8.40 \end{pmatrix} . \quad (5)$$

It is quite obvious that this solution is worthless. One therefore must try to apply some procedure in order to get a better approximation to the exact solution: $\bar{x}^T = (1 \ 1)$.

The very large condition number implies that the columns of the matrix A are nearly linearly dependent. Therefore one could try to replace the ill-conditioned matrix $A = (a_1 \ a_2)$ with either $(a_1 \ 0)$ or $(0 \ a_2)$, both of each are well conditioned. Thus one gets two so-called basic solutions:

$$x_B^1 = \begin{pmatrix} 1.65 \\ 0.00 \end{pmatrix} , \quad x_B^2 = \begin{pmatrix} 0.00 \\ 2.58 \end{pmatrix} . \quad (6)$$

The corresponding residual norms are both small:

$$\| Ax_B^{(1)} - b \|_2 = 0.031, \quad \| Ax_B^{(2)} - b \|_2 = 0.036, \quad (7)$$

and these solutions are much less sensitive to perturbations of the data. However, as can be seen these solutions are again not good and they have nothing in common with the exact solution: $\bar{x}^T = (1 \ 1)$.

When one tries to find the ordinary least-squares solution, x_{LSQ} one can encounter a major difficulty that its norm is much greater than the norm of the exact solution. Therefore, one can try to add some side constraint that the solution norm must not exceed a certain value α :

$$\min_x \| Ax - b \|_2 \quad \text{subject to} \quad \| x \| \leq \alpha. \quad (8)$$

For a set of different α 's ($\alpha = 0.1, 1.0, 1.385, 10$) one obtains:

$$x_{0.1} = \begin{pmatrix} 0.08 \\ 0.05 \end{pmatrix} , \quad x_{1.0} = \begin{pmatrix} 0.84 \\ 0.54 \end{pmatrix} , \quad x_{1.385} = \begin{pmatrix} 1.17 \\ 0.74 \end{pmatrix} , \quad x_{1.385} = \begin{pmatrix} 6.51 \\ -7.60 \end{pmatrix} . \quad (9)$$

It is obvious that if one sets the value of α properly (for example, in this case, $\alpha = 1.385$), one can obtain the solution that is rather close to the exact one: $\bar{x}^T = (1 \ 1)$. However, one must take care when choosing α , and the proper choice is not obvious.

The example given above is the a very small one but it provides an idea of problems that one encounters when dealing with large matrices and vectors: in this thesis when I solve the NNLS problems I use 729 orbits and 500 constraints that leads to matrices whose dimensions are 729×500 . The problems are the following:

- The condition number of the matrix A is large.
- Replacement of A by a well-conditioned matrix derived from A does not necessarily lead to a useful solution.
- One must take care when imposing additional constraints.

To overcome these problems numerical regularization theory is used in order to provide efficient and numerically stable methods for inclusion of proper side constraints that lead to useful stabilized solutions. These methods also provide robust ways for choosing the optimal weight given to the side constraints such that the regularized solution is a good approximation to the desired unknown solution.

A good introduction to the regularization can be found in the book *Numerical Recipes in Fortran* (Press et al. 1994). In my implementation of the regularization I have relied on the functions written in MATLAB by P.C. Hansen (descriptions are given in a manual *Regularization Tools. A Matlab Package for Analysis and Solution of Discrete Ill-Posed Problems* (Hansen 2001)).

A1.2 Discrete Ill-Posed Problems

The definition of the ill-posed problem due to J. Hadamard states that the problem is ill-posed if the solution is not unique or if it is not a continuous function of the data –i.e., if an arbitrarily small perturbation of the data can cause an arbitrarily large perturbation of the solution. As a side note, Hadamard believed (beginning of the 20th century) that ill-posed problems were “artificial” in that they would not describe physical systems (for applications in astronomy see Craig & Brown 1986).

Certain finite-dimensional discrete problems have properties that are very similar to those of ill-posed problems² (for example, being highly sensitive to high-frequency perturbations), so it is common to associate the term *discrete ill-posed problems* with these problems. For linear systems of equations:

$$Ax = b, \quad A \in \mathbb{R}^{m \times n} \quad (10)$$

and linear least-squares problems

$$\min_x \|Ax - b\|_2, \quad A \in \mathbb{R}^{m \times n}, \quad m > n, \quad (11)$$

one can say that these are discrete ill-posed problems if both of these two criteria are met: (i) the singular values of A decay gradually to zero and (ii) the ratio between the largest and the smallest nonzero singular values is large. The first criterion implies that there is no “nearby” problem with a well-conditioned coefficient matrix and with well-determined numerical rank (see below). The routines used in MATLAB environment require singular value decomposition (SVD) so this will be discussed in more detail later. The second criterion implies that the matrix A is ill-conditioned.

A1.3 Tikhonov regularization

The most common and most widely used form of regularization is the so-called Tikhonov regularization. The basic idea is to define a regularized solution x_λ as the minimizer of the following weighted combination of the residual norm and the side constraint:

$$x_\lambda = \operatorname{argmin} \{ \|Ax - b\|_2^2 + \lambda^2 \|L(x - x^*)\|_2^2 \}, \quad (12)$$

where the regularization parameter λ controls the weight given to minimization of the side constraint relative to minimization of the residual norm. Here, x^* is an initial estimate of the solution,

² Ill-posed problems must be infinite dimensional (see Hansen 2001).

and L is typically either the identity matrix I_n or a $p \times n$ discrete approximation of the $(n - p)$ -th derivative operator. It is obvious that a large value of λ (large amount of regularization) favors a small solution seminorm at the cost of a large residual norm, while a small value of λ (small amount of regularization) has the opposite effect. The regularization parameter λ thus controls the properties of the regularized solution and should be chosen with care.

One should stress that there are many other regularization methods apart from Tikhonov regularization: (i) direct regularization methods are: least-squares with a quadratic constraint, damped SVD/GSVD (generalized SVD), truncated SVD (TSVD), truncated GSVD (TGSVD), maximum entropy regularization, and (ii) iterative regularization methods are: conjugate gradients and LSQR, bidiagonalization with regularization, ν method.

A1.4 SVD and Generalized SVD

Some useful tools in analyses of ill-posed problems are the singular value decomposition (SVD) and its generalization to two matrices, the generalized singular value decomposition (GSVD) of the matrix pair (A, L) . Let $A \in \mathbb{R}^{m \times n}$ be a rectangular matrix with $m \geq n$. Then the SVD of the matrix A is a decomposition of the form:

$$A = U \Sigma V^T = \sum_{i=1}^n u_i \sigma_i v_i^T, \quad (13)$$

where $U = (u_1, \dots, u_n)$ and $V = (v_1, \dots, v_n)$ are the matrices with orthonormal columns, $U^T U = V^T V = I_n$, and $\Sigma = \text{diag}(\sigma_1, \dots, \sigma_n)$ has non-negative diagonal elements appearing in non-increasing order such that:

$$\sigma_1 \geq \sigma_2 \geq \dots \geq \sigma_n \geq 0. \quad (14)$$

The numbers σ_i are the singular values of the matrix A (see the definition of the condition number above). The vectors u_i and v_i are the left and right singular vectors of A , respectively. According to the definition, the condition number of A is equal to:

$$\text{cond}(A) = \frac{\sigma_1}{\sigma_n}. \quad (15)$$

The GSVD of the matrix pair (A, L) is a generalization of the SVD of A in the sense that the generalized singular values of (A, L) are the square roots of the generalized eigenvalues of the matrix pair $(A^T A, L^T L)$. The dimension of $A \in \mathbb{R}^{m \times n}$ and $L \in \mathbb{R}^{p \times n}$ satisfy $m \geq n \geq p$ (this is always fulfilled in the case of the ill-posed problems). The GSVD is the decomposition of A and L in the form:

$$A = \begin{pmatrix} \Sigma & 0 \\ 0 & I_{n-p} \end{pmatrix} X^{-1}, \quad L = V(M, 0)X^{-1}, \quad (16)$$

where the columns of $U \in \mathbb{R}^{m \times n}$ and $V \in \mathbb{R}^{p \times p}$ are orthonormal, $X \in \mathbb{R}^{n \times n}$ is nonsingular, and Σ and M are $p \times p$ matrices: $\Sigma = \text{diag}(\sigma_1, \dots, \sigma_p)$, $M = \text{diag}(\mu_1, \dots, \mu_p)$. The diagonal values of Σ and M are non-negative and ordered in the following manner:

$$0 \leq \sigma_1 \leq \dots \leq \sigma_p \leq 1, \quad 1 \geq \mu_1 \geq \dots \geq \mu_p > 0, \quad (17)$$

and are normalized such that:

$$\sigma_i^2 + \mu_i^2 = 1, \quad i = 1, \dots, p. \quad (18)$$

Now one can define the generalized singular values γ_i of (A, L) as the ratios:

$$\gamma_i = \frac{\sigma_i}{\mu_i}, \quad i = 1, \dots, p. \quad (19)$$

A1.5 The L-Curve

The so-called L-curve is a very convenient graphical tool for analysis of discrete ill-posed problems. It is a plot for all valid regularization parameters of the (semi)norm $\|Lx_{\text{reg}}\|_2$ of the regularized solution versus the corresponding residual norm $\|Ax_{\text{reg}} - b\|_2$ (see Fig. 1). Thus, the L-curve displays the compromise between the minimization of these quantities (see also Fig. 18.4.1. from Press et al. (1994)). Its name came from the fact that for discrete ill-posed problems the L-curve (when plotted in log-log scale), almost always has a characteristic L-shaped form (more or less deformed). There is a distinct corner that separates vertical and horizontal parts of the curve.

For a general-form regularization ($L \neq I_n$) the following equation holds that gives the expression for error in x_{reg} :

$$x_{\text{reg}} - \bar{x} = \left(\sum_{i=1}^p f_i \frac{u^T e}{\sigma_i} x_i + \sum_{i=p+1}^n (u^T e) x_i \right) + \sum_{i=p+1}^n (f_i - 1) \frac{u^T \bar{b}}{\sigma_i} x_i. \quad (20)$$

Here, x_{reg} is a regularized solution, the term in parenthesis denotes the perturbation error due to the perturbation e , and the second term is the regularization error that is caused by regularization of the unperturbed component \bar{x} . Filter factors for the Tikhonov regularization are given as:

$$f_i = \frac{\sigma_i^2}{(\sigma_i^2 + \lambda^2)} \quad \text{for } L = I_n \quad (21)$$

and

$$f_i = \frac{\gamma_i^2}{(\gamma_i^2 + \lambda^2)} \quad \text{for } L \neq I_n \quad (22)$$

When one introduces only little regularization, most of the filter factors f_i are approximately one and the error $x_{\text{reg}} - \bar{x}$ is dominated by the perturbation error. On the contrary, if one introduces plenty of regularization, most filter factors are small ($f_i \ll 1$, and $x_{\text{reg}} - \bar{x}$ is dominated by the regularization errors.

In the case of the Tikhonov regularization the L-curve divides the first quadrant into two regions: any regularized solution must lie on or above this curve (see Fig. 1). Thus the solution obtained using the Tikhonov regularization is optimal in the sense that for a given residual norm there does not exist a solution with smaller seminorm than the Tikhonov solution (the same also

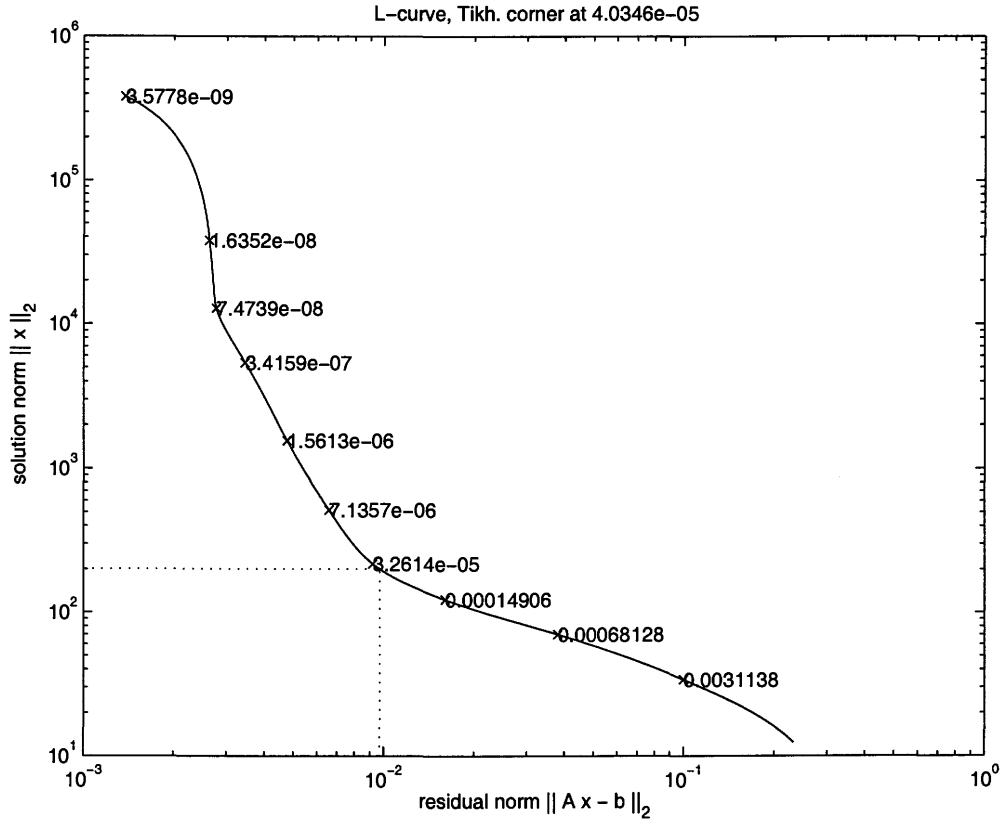


Figure 1: L-curve in case of orbits in triaxial logarithmic potential for which $p = q = 0.9$. Inclination is 40° and box orbits are used.

holds when one interchanges the roles of the norms). When one locates the corner of the L-curve one can compute an approximation to the optimal regularization parameter that leads to a computation of regularized solution with a good balance between two error types. The definition of the L-curve's corner is the point with the maximum curvature in log-log scale.

A1.6 Tikhonov Regularization

Tikhonov regularization is a direct method because the regularized solution x_λ (defined in eq. (Eq. (12))) is the solution to the following least-squares problem:

$$b = \min \left\| \begin{pmatrix} A \\ \lambda L \end{pmatrix} x - \begin{pmatrix} b \\ \lambda Lx^* \end{pmatrix} \right\|_2 \quad (23)$$

This problem is then solved taking into account the non-negativity of the orbital weights (see Appendix 2 for more details about NNLS).

A1.7 Choice of the Regularization Parameter

The appropriate choice of the regularization parameter means a good balance between the perturbation error and the regularization error in the regularized solution. There are two approaches:

(1) methods based on knowledge, or a good estimate of $\|e\|_2$ (the norm of the perturbation of the RHS) and (2) methods that do not require the knowledge of $\|e\|_2$, but extract the necessary information from the given RHS. I have used the L-curve criterion that belongs to the second class using Hansen (2001) routines written in MATLAB. For a continuous regularization parameter λ , I compute the curvature of the curve $(\log \|Ax_\lambda - b\|_2, \log \|Lx_\lambda\|_2)$, where λ is curve's parameter and then search for a point with maximum curvature: this point then can be defined as the L-curve corner. In a similar manner, when the regularization parameter is discrete one can approximate the discrete L-curve in log-log scale by a two-dimensional spline curve, compute the point on the spline curve with maximum curvature and define the corner of the discrete L-curve as the point which is closest to the corner of the spline curve.

REFERENCES

- Craig, I.J.D & Brown, J.C.: 1986, *Inverse Problems in Astronomy*, Adam Hilger, Bristol.
- Hansen, P.C.: 2001, *Regularization Tools. A Matlab Package for Analysis and Solution of Discrete Ill-Posed Problems*. Software described in this report is published in Numerical Algorithms, 1994, **6**, 1.
- Press, W.H., Teukolsky, S.A., Vetterling, W.T. & Flannery, B.P.: 1994, *Numerical Recipes in Fortran*, Cambridge University Pres.
- Rix, H.-W., de Zeeuw, P.T., Cretton, N., van der Marel, R.P. & Carollo, C.M.: 1997, ApJ, 488, 702

APPENDIX 2

NNLS (NON-NEGATIVE LEAST SQUARES)

As it is shown in Chapter 2 and in Appendix 1, in solving the least-squares problem (Rix et al. 1997, eq. (14)) there is a constraint that for the occupation vector $(\gamma_1, \dots, \gamma_{N_0})$, the following relation holds: $\gamma_k \geq 0$, for $k = 1, \dots, N_0$ (N_0 is the number of orbits. This is the non-negative least squares (NNLS) problem to be solved after the regularization procedure has been performed:

$$\text{Minimize } \|Ex - f\| \text{ subject to } x \geq 0.$$

The standard algorithm for this is given by Lawson & Hanson (1974) and the following discussion relies on this book.

Initially one takes the matrix E (matrix on the left hand side of eq. (14) from Rix et al). Its dimension is $m_2 \times n$ (in my case, $m_2 = 500$ and $n = 729$)¹ so the dimension is 500×729 , because I used 500 observational constraints and 729 orbits). The vector that consists of observational points on the right hand side of this equation has the dimension $m_2 = 500$. Finally, the unknown vector x has the dimension $n = 729$. Auxiliary n -vectors w and z provide a working space. Index sets \mathcal{P} and \mathcal{Z} are defined and modified in the course of execution of the algorithm. Variables indexed in the set \mathcal{Z} are held at the value zero. Variables indexed in the set \mathcal{P} will be free to take values different from zero. If such a variable takes a non-positive value, the algorithm will either move the variable to a positive value or else set the variable to zero and move its index from from set \mathcal{P} to set \mathcal{Z} . The solution vector x is given as an output.

The following steps are contained in the NNLS algorithm:

- Step 1 Set $\mathcal{P} := \text{NULL}$, $\mathcal{Z} := \{1, 2, \dots, n\}$, and $x := 0$.
- Step 2 Compute the n -vector $w := E^T(f - Ex)$
- Step 3 If the set \mathcal{Z} is empty or if $w_j \leq 0$ for all $j \in \mathcal{Z}$, go to Step 12.
- Step 4 Find an index $t \in \mathcal{Z}$ such that $w_t = \max\{w_j : j \in \mathcal{Z}\}$.
- Step 5 Move the index t from set \mathcal{Z} to set \mathcal{P} .
- Step 6 Let $E_{\mathcal{P}}$ denote the $m_2 \times n$ matrix defined by:

$$\text{Column } j \text{ of } E_{\mathcal{P}} := \begin{cases} \text{column } j \text{ of } E & \text{if } j \in \mathcal{P} \\ 0 & \text{if } j \in \mathcal{Z} \end{cases}$$

Compute the n -vector z as a solution of the least-squares problem $E_{\mathcal{P}}z \cong f$. Only the components $z_j, j \in \mathcal{P}$ are determined by this problem. Define: $z_j := 0$ for $j \in \mathcal{Z}$.

- Step 7 If $z_j > 0$ for all $j \in \mathcal{P}$, set $x := z$ and go to Step 2.

¹ In the batch procedure that I have written these two numbers are free parameters and can have whatever positive value, but for the sake of comparison between different potentials and orbits I use one fixed combination: 500×729 .

- Step 8 Find an index $q \in \mathcal{P}$ such that
 $x_q/(x_q - z_q) = \min\{x_j/(x_j - z_j) : z_j \leq 0, j \in \mathcal{P}\}.$
 Step 9 Set $\alpha := x_q/(x_q - z_q).$
 Step 10 Set $x := x + \alpha(z - x).$
 Step 11 Move from set \mathcal{P} to set \mathcal{Z} all indices
 $j \in \mathcal{P}$ for which $x_j = 0$. Go to Step 6.
 Step 12 The end of computation.

The solution vector x as a final result of this algorithm satisfies:

$$x_j > 0, \quad j \in \mathcal{P}$$

and

$$x_j = 0, \quad j \in \mathcal{Z}.$$

REFERENCES

- Lawson, C.L. & Hanson, R.J.:1974, *Solving Least Squares Problems*, Englewood Cliffs, New Jersey: Prentice-Hall
 Rix, H.-W., de Zeeuw, P.T., Cretton, N., van der Marel, R.P. & Carollo, C.M.: 1997, ApJ, 488, 702

APPENDIX 3

ORBITS

In this Appendix I will present some necessary details connected with the orbits of individual stars in a given potential. The fundamental approximation is valid: forces from individual stars are neglected and only large-scale forces from the overall mass distribution (made up of billions of stars) is considered (cf. Binney & Tremaine 1997, hereafter BT87). Small-scale irregularities due to individual stars or objects like globular clusters and molecular clouds are ignored.

A3.1 GRAVITATIONAL POTENTIALS

A3.1.1 Orbits in Spherical Potentials

The gravitational potential, $\Phi(x)$ for an arbitrary mass density $\rho(x)$ is given as (see, for example, Barnes (2003)):

$$\Phi(x) = -G \int d^3x' \frac{\rho(x')}{|x - x'|} \quad (1)$$

where G is the gravitational constant and the integral is taken over all space.

The potential energy of a test mass m is given as:

$$U = m\Phi(x). \quad (2)$$

Using Poisson's equation one can establish the relationship between density and potential:

$$\nabla^2\Phi = 4\pi G\rho, \quad (3)$$

from which it is obvious that linearity holds: if ρ_1 generates potential Φ_1 and ρ_2 generates Φ_2 then the sum $\rho_1 + \rho_2$ generates the sum $\Phi_1 + \Phi_2$.

If one considers a spherical shell of mass m , Newton's first and second theorems state:

1. the gravitational force inside a spherical shell of matter vanishes and
2. the gravitational force on a body that lies outside a closed spherical shell of matter is the same as it would be if all the shell's matter were concentrated into a point at its center.

The potential of an arbitrary spherical mass distribution is:

$$\Phi(r) = - \int_{r_0}^r dx \, a(x) = G \int_{r_0}^r dx \frac{M(x)}{x^2}, \quad (4)$$

the mass that is enclosed is given as:

$$M(r) = 4\pi \int_0^r dx \, x^2 \rho(x). \quad (5)$$

A3.1.2 Examples

For a point of mass M a Keplerian potential is given as:

$$\Phi(r) = -G \frac{M}{r}. \quad (6)$$

Orbits in this potential obey the three Kepler's laws. A circular orbit at radius r has velocity: $v_c(r) = \sqrt{GM/r}$. A circular velocity that declines with increasing radius like $r^{\frac{1}{2}}$ is therefore called Keplerian. Kepler was the first to understand that in the Solar system $v_c \propto r^{\frac{1}{2}}$.

For a uniform sphere of mass M and radius a the potential is:

$$\Phi(r) = \begin{cases} -2\pi G\rho(a^2 - r^2/3), & r < a \\ -Gm/r, & r > a \end{cases} \quad (7)$$

where ρ is the mass density.

For a singular isothermal sphere that has a density profile: $\rho(r) = \rho_0(r/r_0)^{-2}$ the potential is:

$$\Phi(r) = 4\pi G\rho_0 r_0^2 \ln(r/r_0). \quad (8)$$

The circular velocity is constant with radius: $v_c = \sqrt{4\pi G\rho_0 r_0^2}$. In case of galaxies with flat rotation curves this potential can be used as a valid approximation, but some outer cut-off must be imposed to obtain a finite total mass.

A3.1.3 Potential-Density Pairs

Using Poisson's equation one can obtain pairs of functions (potentials and density) characterized by a total mass M and a length scale a . A very short list is given in TABLE A3-1 (for a detailed list, see Ciotti 2001):

TABLE A3-1
POTENTIAL DENSITY PAIRS FOR SPHERICAL POTENTIALS

Name	$\Phi(r)$	$\rho(r)$
Plummer	$-G \frac{M}{\sqrt{r^2 + a^2}}$	$\frac{3M}{4\pi a^3} (1 + (r^2/a^2))^{-5/2}$
Hernquist	$-G \frac{M}{r+a}$	$\frac{M}{2\pi} \frac{a}{r(r+a)^3}$
Jaffe	$-G \frac{M}{a} \ln \left(\frac{a}{r+a} \right)$	$\frac{M}{4\pi} \frac{a}{r^2(r+a)^2}$

A3.1.4 Example

An example of an orbit generated in the Hernquist spherical potential (initial conditions were: $x_0 = 0.3$, $y_0 = 0.0$, $z_0 = 0.4$, $v_x = 0.0$, $v_y = 0.4$, and $v_z = 0.0$) is given in Fig. 1. Radial length scale was 0.1. The number of time steps in this case, as well as in all other cases that follow, was 16384. Here, $L_z = 0.08$. From the z - x plot it is obvious that the motion is confined to two dimensions.

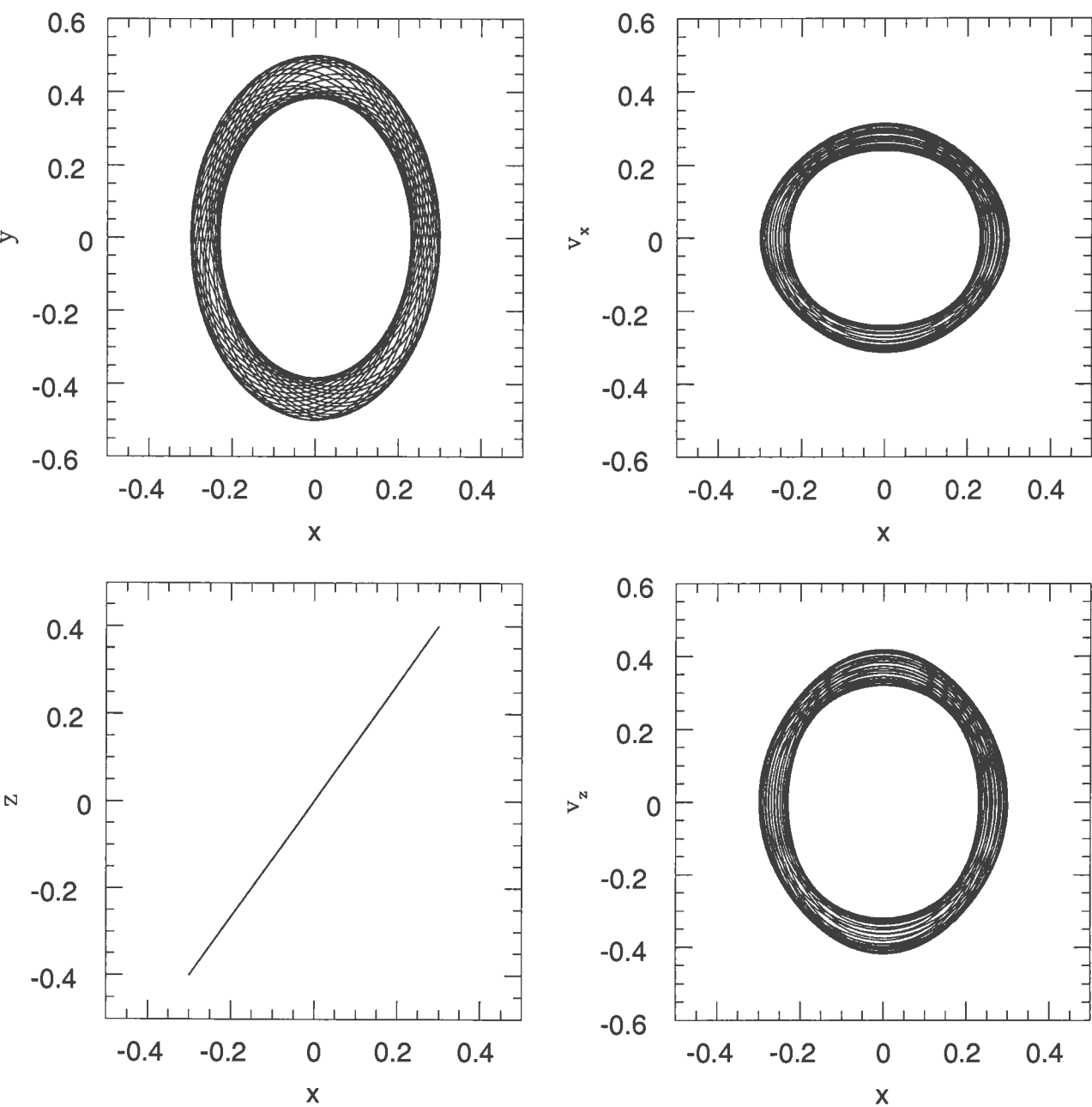


Figure 1: Example of an orbit in the Hernquist potential. Clockwise from the top left corner: dependence of y coordinate on x coordinate, dependence of v_x component of the velocity \mathbf{v} on x coordinate, dependence of v_z component of the velocity \mathbf{v} on x coordinate and dependence of z coordinate on x coordinate. See text for details.

A3.1.5 Constants and integrals of motion

The constants of motion are functions of phase-space coordinates and time which are constant along orbits:

$$C(r(t), v(t), t) = \text{const.} \quad (9)$$

Here, $r(t)$ and $v(t) = dr/dt$ are a solution to the equations of motion. The function $C(r, v, t)$ must be constant along every orbit (its value depends on the orbit). If the phase-space has $2n$ dimensions, there are always $2n$ independent constants of motion.

Integrals of motion are functions of phase-space coordinates alone which are constant along orbits:

$$I(r(t), v(t)) = \text{const.} \quad (10)$$

It can be seen that that an integral of motion cannot depend on time, so all integrals are constants of motion but the opposite is not valid, not all constants are integrals of motion. There are two kinds of integrals (cf. classic paper of Henon & Heiles 1964): non-isolating and isolating. For a non-isolating integral the corresponding hypersurface consists of an infinity of sheets that fill the phase space densely, so that the equation

$$I_j = C_j \quad (j = 1, \dots, 5) \quad (11)$$

does not give any information and is equivalent to no condition at all. Therefore, physically, nonisolating integrals do not have significance (integrals I_4 and I_5 are generally nonisolating). Isolating integrals (usually called simply "integrals") are important and they constrain the shapes of orbits. In a phase-space of $2n$ dimensions, an isolating integral defines a hypersurface of $2n - 1$ dimensions. Regular orbits are those that have $N = n$ isolating integrals. In such cases each orbit is confined to a hypersurface of $2n - N$ dimensions.

A3.1.6 Axisymmetric potentials

In the case of the axisymmetric potentials one works in a cylindrical coordinate system (R, ϕ, z) that is centered on the galactic nucleus. The galaxy's symmetry axis is aligned with the z -axis. In this case the mass distribution is a function of two variables: cylindrical radius, R , and height z . I will not include potentials related to axisymmetric disks (see Ciotti 2001) because they are important in the context of spiral galaxies. For a flattened system I list two potential-density pairs:

TABLE A3-2

POTENTIAL DENSITY PAIRS FOR FLATTENED POTENTIALS

Name	$\Phi(r)$	$\rho(R, z)$
Miyamoto-Nagai (MN)	$-\frac{GM}{\sqrt{R^2+(a+\sqrt{b^2+z^2})^2}}$	$\left(\frac{b^2 M}{4\pi}\right) \frac{aR^2+(a+3\sqrt{z^2+b^2})(a+\sqrt{z^2+b^2})^2}{[R^2+(a+\sqrt{z^2+b^2})]^{5/2}(z^2+b^2)^{3/2}}$
Logarithmic	$\frac{1}{2}v_0^2\ln(R_c^2 + R^2 + z^2/q)$	$\left(\frac{v_0^2}{4\pi Gq^2}\right) \frac{(2q^2+1)R_c^2+R^2+(2-q^{-2})z^2}{(R_c^2+R^2+z^2q^{-2})^2}$

The logarithmic potential is used in this thesis in several of its variants. Its importance comes from the fact that it can describe galaxies with approximately flat rotation curves: for the $z = 0$ plane the circular velocity $v_c = v_0 R / \sqrt{R_c^2 + R^2}$ rises linearly for $R \ll R_c$ and is approximately constant for large R . As one can see from the potential-density pairs from TABLE A3-2 (density is obtained using Poisson’s equation), the density in the case of the logarithmic potential is "dimpled" at the poles (see Fig. 2.8 of Binney & Tremaine 1987). Namely, for $q^2 < \frac{1}{2}$ the density along the z -axis is negative, which is obviously unphysical.

The stars which have motion in the equatorial plane in the axisymmetric potential can be reduced to a two-dimensional problem using the conservation of the z -component of angular momentum of any star. If the symmetric potential (symmetric about the plane $z = 0$) is $\Phi(R, z)$ the general equation of motion of the star is:

$$\frac{d^2r}{dt^2} = -\nabla\Phi(R, z).$$

(12)

In the cylindrical coordinates the following relations hold:

$$r = Re_R + ze_z$$

(13)

(where e_R and e_z are unit vectors, as well as e_ϕ). Now one can write the acceleration in the cylindrical coordinates (cf. BT87, p. 114, and their equation 1B-24):

$$\ddot{R} - R\dot{\phi}^2 = -\frac{\partial\Phi}{\partial R}$$

(14)

$$\frac{d}{dt}\left(R^2\dot{\phi}\right) = 0$$

(15)

$$\ddot{z} = -\frac{\partial\Phi}{\partial z}$$

(16)

The second of these equations (Eq. (15)) describes the conservation of the component of angular momentum about the z -axis, $L_z = R^2\dot{\phi}$, and the remaining two describe the coupled oscillations of the star in the R and z -directions. From Eq. (14) one can eliminate $\dot{\phi}$ to obtain equations for the evolution of R and z :

$$\ddot{R} = -\frac{\partial\Phi_{\text{eff}}}{\partial R} \quad ; \quad \ddot{z} = -\frac{\partial\Phi_{\text{eff}}}{\partial z} \quad ;$$

(17)

where the effective potential has been introduced:

$$\Phi_{\text{eff}} \equiv \Phi(R, z) + \frac{L_z^2}{2R^2}. \quad (18)$$

Therefore the three-dimensional motion of a star in an axisymmetric potential $\Phi(R, z)$ can be reduced to the motion of the star in the plane (see Fig. 2). This non-uniformly rotating plane with coordinates (R, z) is often called the meridional plane. Effective potential governs the star's motion in the meridional plane, which rotates about the z -axis with angular velocity L_z/R^2 . On the meridional plane the effective potential has a minimum at $R > 0$ and $z = 0$ and a steep angular momentum barrier as $R \rightarrow 0$ (BT87, Figure 3-2). If the motion of a star in this plane is constrained only by the energy E (see the formula below) a star should travel everywhere inside within a closed contour of constant Φ_{eff} . This is, however, not always observed: it can happen that stars launched from rest at different points along a contour of constant Φ_{eff} follow distinct trajectories. This is a consequence of the existence of a third integral, for which, however, general expression does not exist (as in the case of two classic integrals given in equations for energy E , and a z -component of the angular momentum ($L_z = Rv_\phi$)). The existence of the third integral implies that a star's orbit is a combination of three period motions: radial, azimuthal, and vertical. The orbit can thus be represented as a path on an invariant 3-torus. In the case of some axisymmetric potentials orbits can go everywhere energetically permitted on the meridional plane. These orbits do not permit the description in terms of motion on an invariant 3-torus. These are irregular, or stochastic orbits in an axisymmetric potential that respect only two classical integrals: E and J_z .

The energy E of a star that is moving in an arbitrary axisymmetric potential Φ is given as:

$$E = \frac{1}{2} [\dot{R}^2 + (R\dot{\phi})^2 + \dot{z}^2] + \Phi = \frac{1}{2} (\dot{R}^2 + \dot{z}^2) + \left(\Phi + \frac{L_z^2}{2R^2} \right) \quad (19)$$

that is

$$E = \frac{1}{2} (\dot{R}^2 + \dot{z}^2) + \Phi_{\text{eff}}. \quad (20)$$

One can see that the effective potential Φ_{eff} is the sum of the gravitational potential energy of the orbiting star and the kinetic energy associated with its motion in the ϕ -direction. The difference between Φ_{eff} and E is the kinetic energy of the motion in the (R, z) plane. Kinetic energy is non-negative, and therefore the orbit is restricted to the area of the meridional plane that satisfies the relation: $E \geq \Phi_{\text{eff}}$. The curve that bounds this area is called the zero-velocity curve, because the orbit can only reach this curve if its velocity is instantaneously zero.

As noted in BT87 (p. 117) eq. (14) cannot be solved analytically, unless the gravitational potential Φ is of some special form. However, one can follow the evolution of $R(t)$ and $z(t)$ by integrating the equations of motion numerically, starting with some initial conditions.

The motion of the representative point is in the four-dimensional phase space (R, z, \dot{R}, \dot{z}) . This is complicated to visualize, so one can study orbits in (R, z) plane using a simple technique of the surface of section (see Richstone 1982). Because the energy $E(R, z, \dot{R}, \dot{z})$ is conserved, one can plot the motion of the representative point in a three-dimensional space (for example, (R, z, \dot{R}) and then determine \dot{z} to within a sign by the known value of E). Further on, one can decide to plot the points by choosing the moment when the representative point of the star

crosses some plane (say $z = 0$ plane) in the phase space. Therefore, one can plot (R, \dot{R}) only when $\dot{z} > 0$ to remove the ambiguity due to the sign of \dot{z} : one can plot the values of R and \dot{R} every time that the star crosses the equator going upward. These plots are called surfaces of section and were first used by Poincaré (see Fig. 3).

If one now supposes that the star's motion in (R, z) plane respects an additional isolating integral, I , the trajectory of its phase point in the three-dimensional space with coordinates (R, z, \dot{R}) is restricted by the condition $I = \text{const.}$ to a two-dimensional region, which must cut the plane $z = 0$ through (R, z, \dot{R}) space in a curve, called the orbit's invariant curve. Therefore, if I exists for any orbit, the points that are generated by that orbit in the surface of section must lie on a curve. If, however, the only isolating integral admitted by motion in the (R, \dot{R}) plane is E , the points generated by each orbit will fill one or more areas in the surface of section (see Fig. 3). In Fig. 5 one can see the example that the points lie on the smooth curve in the (R, \dot{R}) surface of section, so it seems that some isolating integral, I is respected by this orbit. This is the example of the third integral.

A3.1.7 Example

An example of an orbit generated in the axisymmetric logarithmic potential (initial conditions were: $x_0 = 0.3$, $y_0 = 0.0$, $z_0 = 0.4$, $v_x = 0.0$, $v_y = 0.4$, and $v_z = 0.0$ is given in Fig. 2 and Fig. 3. Here, $L_z = 0.08$. Potential velocity scale was 1.0, the value of the core radius was $R_c = 0.2$, and the flattening of the potential was $q = 0.8$. From the z - x plot it is again obvious that the motion is confined to two dimensions.

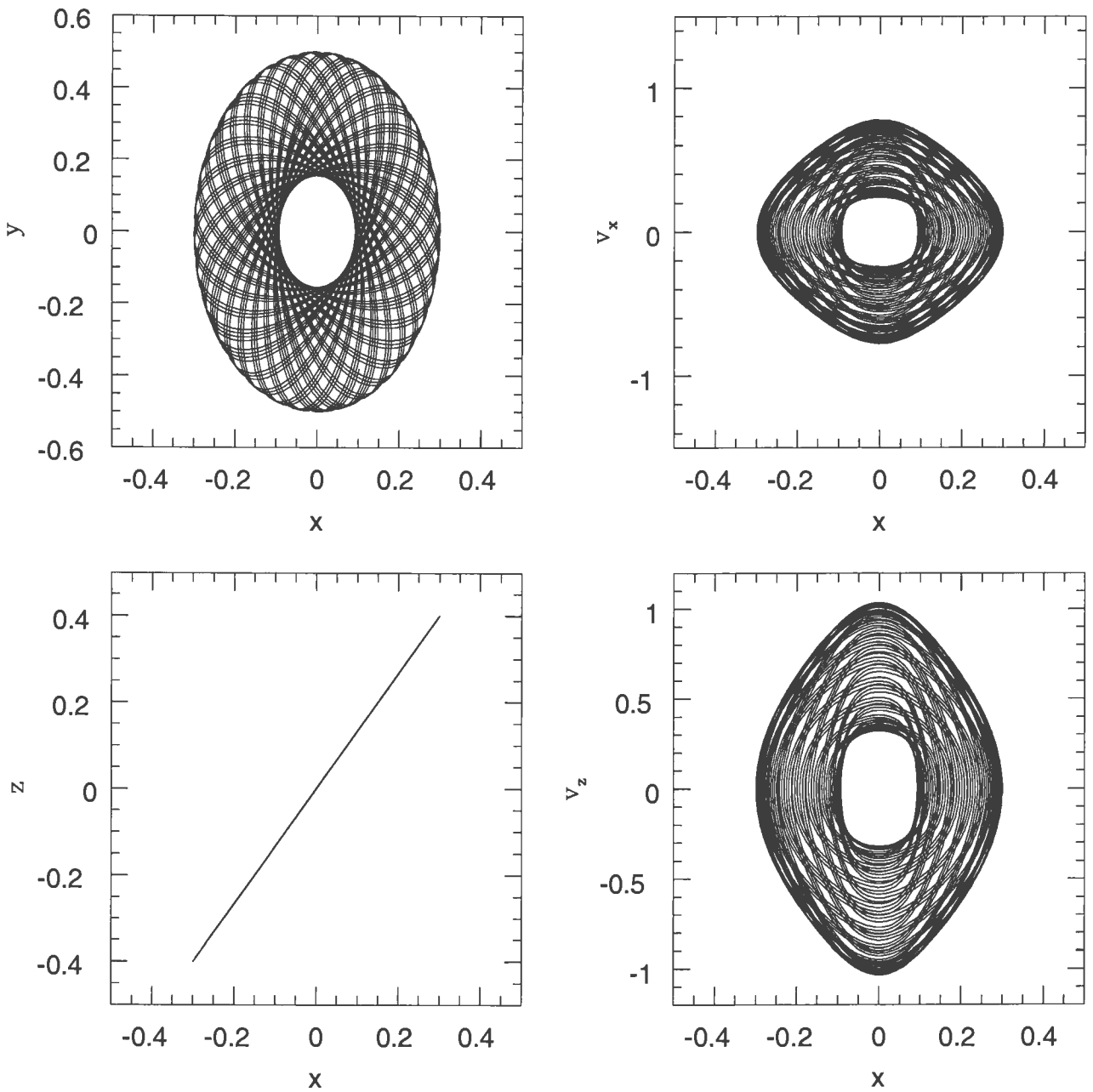


Figure 2: Example of an orbit in the logarithmic axisymmetric potential. Clockwise from the top left corner: dependence of y coordinate on x coordinate, dependence of v_x component of the velocity \mathbf{v} on x coordinate, dependence of v_z component of the velocity \mathbf{v} on x coordinate and dependence of z coordinate on x coordinate. See text for details.

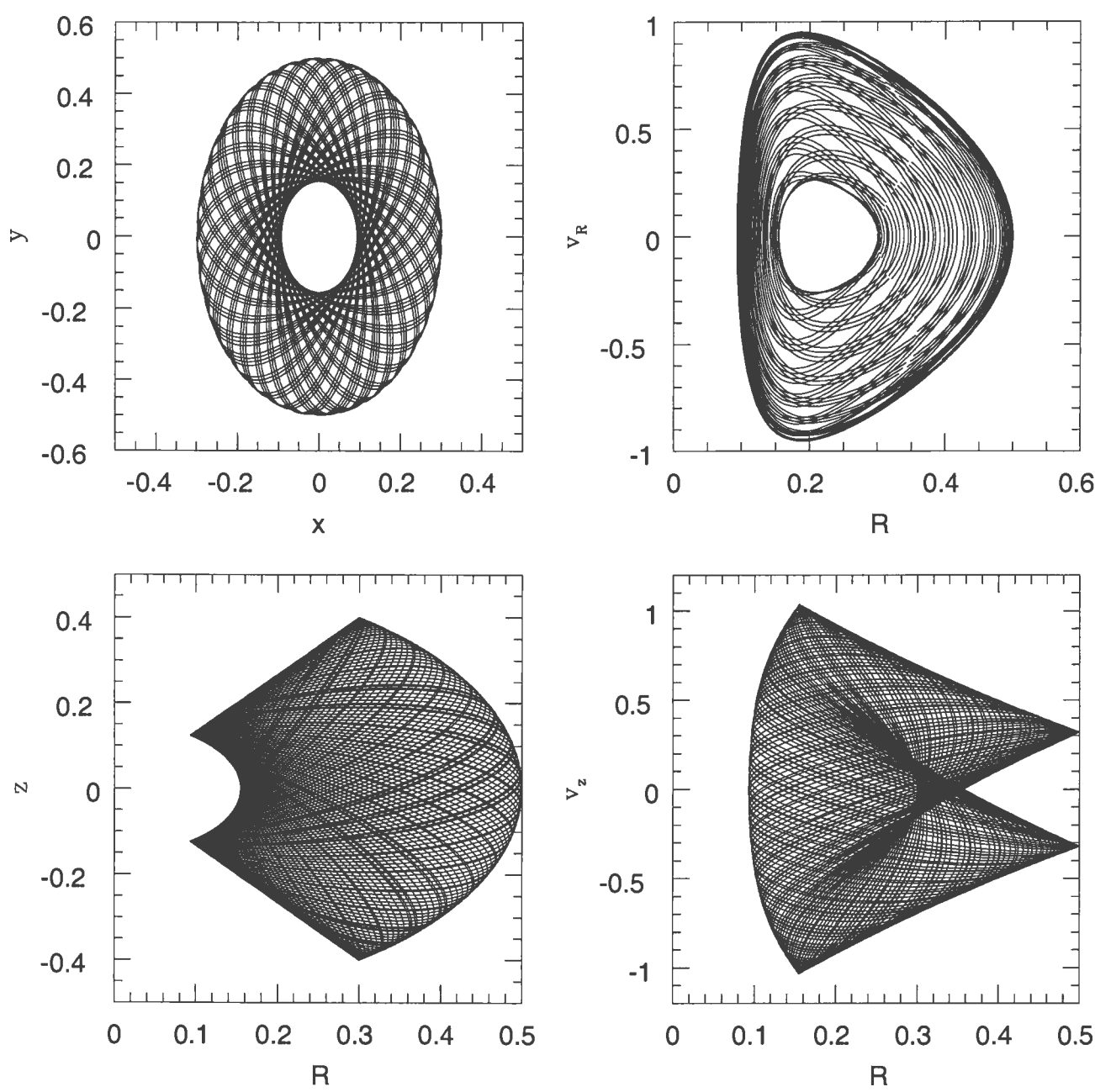


Figure 3: Example of an orbit in the logarithmic axisymmetric potential (same orbit as in Fig. 2 but using cylindrical coordinates). Clockwise from the top left corner: dependence of y coordinate on x coordinate (same plot as in Fig. 2), dependence of v_R component of the velocity \mathbf{v} on R coordinate, dependence of v_z component of the velocity \mathbf{v} on R coordinate and dependence of z coordinate on R coordinate.

A3.1.8 Triaxial potentials

In the construction of the triaxial potentials, the first step is to generalize an infinitely thin spherical shell into an infinitely thin homeoid (a shell bounded by two similar ellipsoids having a constant

ratio of axes) which has constant density between surfaces m^2 and $m^2 + dm^2$, where:

$$m^2 = x^2 + \frac{y^2}{b^2} + \frac{z^2}{c^2}. \quad (21)$$

The acceleration inside the shell vanishes (in a similar way like in the spherical case). Therefore one can write $\Phi = \text{const.}$ inside the shell and on its surface. Outside the shell, the potential is stratified on ellipsoidal surfaces that are defined by:

$$m^2 = \frac{x^2}{1+\tau} + \frac{y^2}{1+\tau} + \frac{z^2}{1+\tau}, \quad (22)$$

where parameter $\tau > 0$ labels the surface. In two extreme cases: (i) $\tau = 0$ the isopotential surface coincides with the homeoid, and (ii) when $\tau \rightarrow \infty$ the isopotential surfaces become spherical.

Making a superposition of a series of thin homeoids one can obtain a triaxial mass distribution with $\rho = \rho(m^2)$. The acceleration at a given point (x_0, y_0, z_0) is generated by the mass within $m^2 < m_0^2 = x_0^2 + y_0^2/b^2 + z_0^2/c^2$. This is again similar to the situation that one encounters in the case of a spherical system where the acceleration at distance r is only due to the mass within that radius, r .

Finally, one can write the expression for the logarithmic potential in the triaxial case:

$$\Phi(x, y, z) = \frac{1}{2}v_0^2 \ln \left(R_c^2 + x^2 + \frac{y^2}{b^2} + \frac{z^2}{c^2} \right). \quad (23)$$

Again, as is in the aforementioned two-dimensional case it is not guaranteed that the corresponding density will be positive if the potential is too strongly flattened.

A3.1.8.1 Orbits in Non-Axisymmetric Potentials

Non-axisymmetric potentials with $\Phi = \Phi(x, y)$ or $\Phi = \Phi(x, y, z)$ admit a richer variety of orbits. In this case, the only classical integral of motion in such a potential is the energy given as:

$$E = \frac{1}{2}|v|^2 + \Phi(r). \quad (24)$$

Some potentials permit other integrals of motion; in such potentials regular orbits may be mapped onto invariant tori. However, not all regular orbits can be continuously deformed into one another. Therefore, orbits can be grouped into topologically distinct orbit families. Each orbit family requires in principle a different invariant torus.

A3.1.8.2 Separable Potentials

In case of separable potentials all orbits are regular and the mapping to the invariant tori can be constructed analytically and all integrals of motion are known. This is a special case, and real galaxies do not have such a potential, but it has been shown in numerical experiments that non-axisymmetric galaxy models with finite cores or shallow cusps usually generate potentials that resemble separable potentials.

The orbits in a separable potential can be classified into different families. In two-dimensions there are two types of closed, stable orbits: (1) loop orbits that loop around the center, and (2) box orbits that oscillate back and forth along the major axis (cf. BT87, Chapter 3.3.1). In three dimensions, a separable potential permits four orbit families: (1) box orbits, (2) short-axis tube orbits (loop around the short (minor) axis), (3) inner long-axis tube orbits and (4) outer long-axis tube orbits. Two families of long axis-tube orbits that orbit around the long (major) axis come from different closed stable orbits and explore different regions of space (BT87, Figure 3-20, also Statler (1987)). Schwarzschild (1979) in his seminal paper defined box orbits as orbits for which one may choose a starting point in space but a definite velocity, namely zero. X-tube orbits are defined as orbits for which one may choose as starting conditions arbitrary x and z coordinates and arbitrary y velocity component; other three phase-space coordinates are set to zero. There is no intermediate-axis tube because closed orbits that loop around the intermediate axis are unstable.

A3.1.9 Example

An example of an orbit generated in the triaxial logarithmic potential (initial conditions were: $x_0 = 0.5$, $y_0 = 0.3$, $z_0 = 0.7$, $v_x = 0.0$, $v_y = 0.0$, and $v_z = 0.0$) is given in Fig. 4 and Fig. 5. Here $L_z = 0$, flattening of the potential $p = q = 0.9$ and the core radius $R_c = 0.3$. Note the difference in the z - x plot with respect to Fig. 1 and Fig. 2. Also, note the difference in $R - v_R$ plot with respect to Fig. 3. Because the initial velocity $v = 0$, the motion is again in two dimensions.

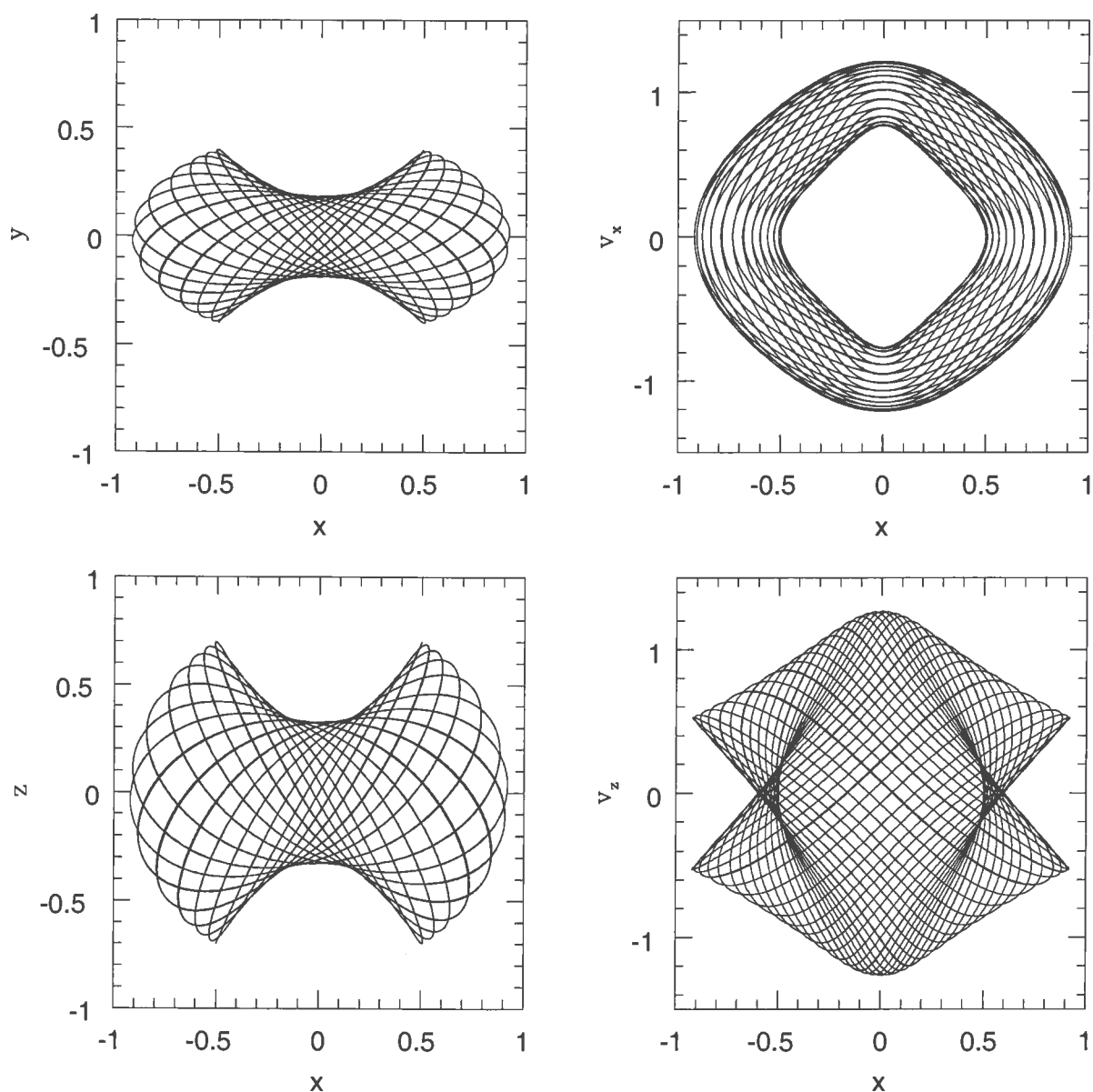


Figure 4: Example of an orbit in the logarithmic triaxial potential ($p = q = 0.9$). Clockwise from the top left corner: dependence of y coordinate on x coordinate, dependence of v_x component of the velocity \mathbf{v} on x coordinate, dependence of v_z component of the velocity \mathbf{v} on x coordinate and dependence of z coordinate on x coordinate. See text for details.

A3.2. LEAPFROG INTEGRATOR

In this thesis I generated orbits using a leapfrog integrator. This scheme is useful when one deals

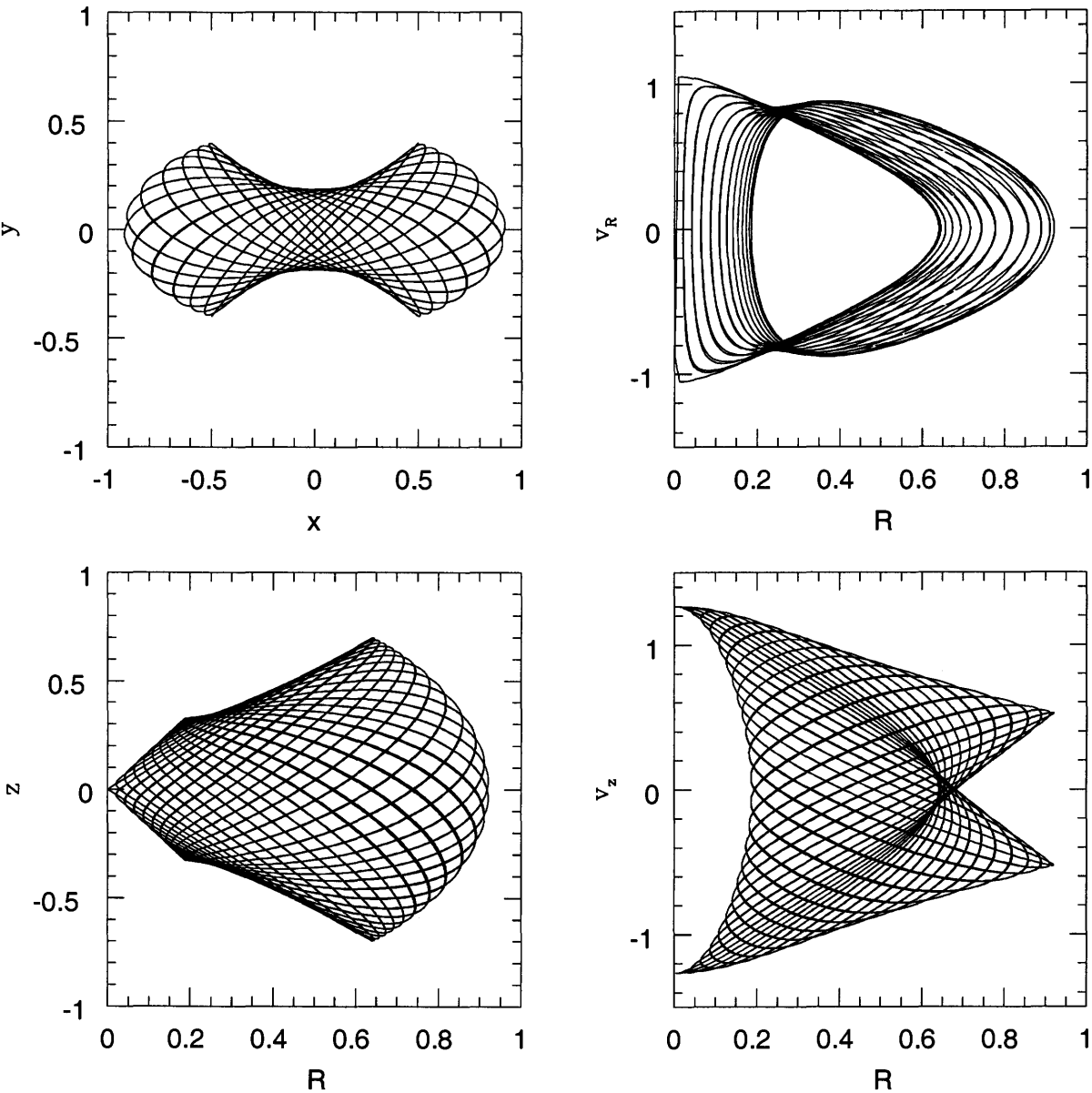


Figure 5: Example of an orbit in the logarithmic triaxial potential (same orbit as in Fig. 4 but using cylindrical coordinates). Clockwise from the top left corner: dependence of y coordinate on x coordinate (same plot as in Fig. 2), dependence of v_R component of the velocity \mathbf{v} on R coordinate, dependence of v_z component of the velocity \mathbf{v} on R coordinate and dependence of z coordinate on R coordinate.

with the second-order problems and Newtonian equations of motion are second-order in time (see for example, Barnes 2003). Both positions and velocities are needed to specify the dynamical state of the system.

From classical mechanics it is known that one can obtain the equations of motion in an arbitrary coordinate system using a function called Lagrangian that depends on the generalized coordi-

nates, generalized velocities and possibly the time. The equations of motion can be obtained using the principle of least action. The Lagrangian is:

$$L(x, \dot{x}, t) = T - U = \frac{1}{2}m\dot{x}^2 - U(x, t) \quad (25)$$

where x is the generalized coordinate, and \dot{x} is the generalized velocity. Using the Euler-Lagrange equation one can find the trajectory $x(t)$:

$$\frac{d}{dt} \frac{\partial L}{\partial \dot{x}} - \frac{\partial L}{\partial x} = 0. \quad (26)$$

From these two equations it follows:

$$\frac{d}{dt}(m\dot{x}) + \frac{dU}{dx} = 0 \quad (27)$$

which is in fact the Newton's law of motion usually expressed as:

$$m \frac{d^2 x}{dt^2} = f(x). \quad (28)$$

In a similar manner, one can use the generalized momentum

$$p = \frac{dL}{d\dot{x}} = m\dot{x} \quad (29)$$

define the Hamiltonian function as:

$$H(x, p) = p\dot{x} - L(x, \dot{x}, t) = \frac{1}{2}m\dot{x}^2 + U(x, t) = \frac{1}{2m}p^2 + U(x, t), \quad (30)$$

which is numerically equal to the total energy.

Now one can write the equations of motion:

$$\frac{dp}{dt} = -\frac{\partial H}{\partial x}, \quad \frac{dx}{dt} = \frac{\partial H}{\partial p} \quad (31)$$

which after using the definition of the Hamiltonian becomes:

$$\frac{dp}{dt} = -\frac{dU}{dx}, \quad \frac{dx}{dt} = \frac{p}{m} \quad (32)$$

that are identical to the familiar form:

$$\frac{dx}{dt} = v, \quad m \frac{dv}{dt} = f(x). \quad (33)$$

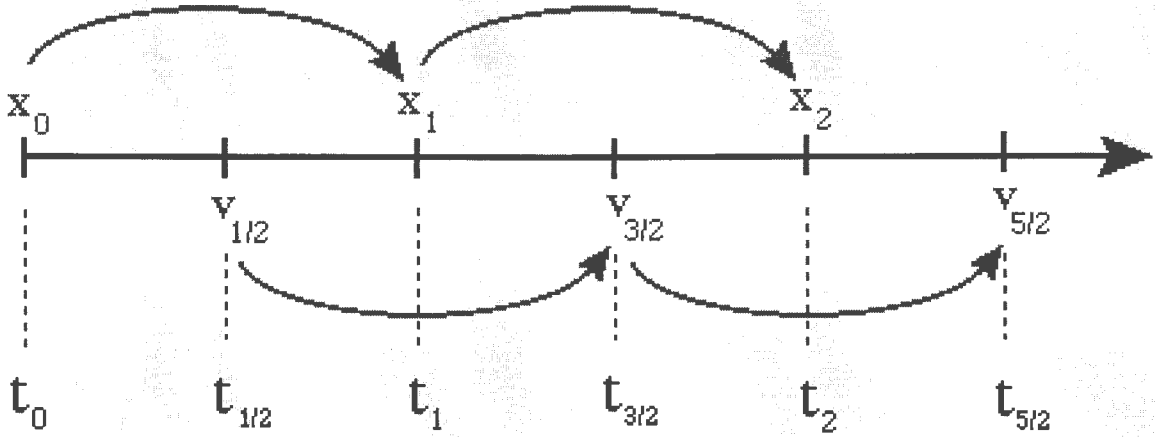


Figure 6: Scheme of leapfrog integration

There are different numerical integrators for solving a system of coupled ordinary differential equations but not all respect the symmetric structure in Eq. (25). The time-centered leapfrog integrator does respect this structure. In second-order systems it is useful to define the velocities at the mid-points of the intervals – it is said that the velocities are staggered with respect to the positions x . If $x[k] = x(kh)$ is the position at time $t = kh$, where k is the step number and h is the time-step. Velocity $v[k + 1/2] = v([k + 1/2]h)$ is the velocity a half-step later (see Fig. 6). The leapfrog step is:

$$x[k + 1] = x[k] + hv[k + 1/2] \quad (34)$$

$$v[k + 3/2] = v[k + 1/2] + ha(x[k + 1]), \quad (35)$$

where $a(x) = -(1/m)\partial U/\partial x$ is the acceleration. In this scheme both x and v are treated symmetrically: they are both reversible. The leapfrog scheme is time reversible and that is important because it guarantees conservation of energy, angular momentum and any other conserved quantity. The problem of the leapfrog integrator is the need to offset the position and velocity variables by half a timestep. One can do the split of the velocity step:

$$v[k + 1/2] = v[k] + (h/2)a(x[k]), \quad (36)$$

$$x[k + 1] = x[k] + hv[k + 1/2] \quad (37)$$

$$v[k + 1] = v[k + 1/2] + (h/2)a(x[k + 1]), \quad (38)$$

This is equivalent to Eq. (34) and (35). When used as a mapping from time kh to time $(k + 1)h$ eqs. Eqs. (37) and (38) are equivalent to starting Eqs. (36) through (38) with the linear approximation:

$$v[1/2] = v[0] + (h/2)a(x[0]) + \mathcal{O}(h^2). \quad (39)$$

The solution jump-starts from a phase-space point offset in velocity by $\mathcal{O}(h^2)$ from specified $v[0]$ and similar errors are made in extracting $v[k]$ at later times. The leapfrog method is only second-order accurate, but it is very stable.

REFERENCES

- Barnes, J.E.: 2003, home page <http://www.ifa.hawaii.edu/~barnes/>
Binney, J. & Tremaine, S.: 1987, *Galactic Dynamics*, Princeton University Press (BT87).
Ciotti, L.: 2001, *Lecture Notes on Stellar Dynamics*, Scuola Normale di Pisa editore.
Henon, M. & Heiles, C.: 1964, AJ, 69, 73.
Richstone, D.O.: 1982, ApJ, 252, 496
Schwarzschild, M.: 1979, ApJ, 232, 236.
Statler, T. S.: 1987, ApJ, 321, 113.

APPENDIX 4

SELF-ORGANIZING MAPS (SOMs)

4.1 Introduction

The self-organizing map (SOM) method invented by T. Kohonen (Kohonen 1997) is a neural network method. The Kohonen (1997) definition states: "SOM [is a] result of a nonparametric regression process that is mainly used to represent high-dimensional, nonlinearly related data items in an illustrative, often two-dimensional display, and to perform unsupervised classification and clustering". Thus it is closely related to cluster analysis (partitioning) and other methods of data analysis (cf. Murtagh & Hernandez-Pajeres 1995).

The SOM method includes a set of iterative procedures for associating a finite number of object vectors (inputs) with a finite number of representational points (that should be viewed as bins or clusters). These representational points should respect the proximity relations between the inputs, and can be arranged, for example, in a planar grid. It is important to note that the SOM approach is representative of an *unsupervised learning* approach: cluster properties are estimated or learned without usage of prior information.

The SOM method can be condensed in the following three points (Murtagh 1995):

1. Each item in a multidimensional input data set is assigned to a cluster center.
2. The cluster centers are themselves ordered by their proximities.
3. The cluster centers are arranged in some specific output representational structure, for example a regularly spaced grid.

The output representational grid of cluster centers w_i (that are initially randomly valued) is structured through the imposing of neighborhood relations (Murtagh 1995, Murtagh & Hernandez-Pajeres 1995):

- | | |
|--------|----------------------------------------------------------------------------------------------|
| Step 1 | Set $t = 0$. Consider an input vector x from the set of inputs. |
| Step 2 | Determine the cluster center $c = i$ such that $\ x - w_i^{(t)}\ $ is minimum over all i . |
| Step 3 | For all clusters centers i : |

$$w_i^{(t+1)} = \begin{cases} w_i^{(t)} + \alpha^{(t)}(x - w_i^{(t)}) & \text{if } i \in N_c(t) \\ w_i^{(t)} & \text{if } i \notin N_c(t) \end{cases}$$

- | | |
|--------|-----------------------------------------------------------------------|
| Step 4 | Increment t . Go to Step 1, unless a stopping condition is reached. |
|--------|-----------------------------------------------------------------------|

An iteration in this algorithm is the assignment (or re-assignment) of an input vector to a cluster center. An epoch is the assignment (or re-assignment) of all inputs. Murtagh (1995) found that 5 or 6 epochs are enough to attain convergence. After some testing, in the code that I have applied I decided to use 10 epochs as a reasonable number that provides a balance between the time needed for one orbit SOM extraction and the quality of the extraction. Here, $\alpha^{(t)}$ is a small fraction that is used for controlling convergence, $N_c(t)$ is the neighborhood of the lattice element c . The weight vector $w_i^{(t)}$ is calculated for a lattice element i at iteration number t . The neighborhood is made to decrease with iterations, towards the best "winner" (defined in Step 2) cluster center.

Note that the initial cluster centers are randomly valued and are of the same dimensionality as the input data vectors.

4.2 Application

I have applied the aforementioned algorithm and wrote a FORTRAN program based on Murtagh & Hernandez-Pajeres (1995) that extracts positions and velocities from the orbit libraries that I had previously generated (for calculation of orbits see Appendix 3). As an input to the SOM routine for every calculated orbit I have a file that includes projected radius (r , through x and y coordinate) and line-of-sight velocity and as an output the following is calculated: for a selected number of points on the grid, projected radius (r , through x and y coordinate), line-of-sight velocity and the occupation weight (using notation of Rix et al. (1997): w_{xyv} , for which the following normalization is valid ($\sum_{xyv} w_{xyv} = 1$)).

In the following several plots I provide examples of calculated orbits and the SOM reconstruction. These examples were done using a tube orbit but similar results are obtained for a box orbit. Fig. 2 gives the tube orbit (presented in Fig. 1) projected using inclination angle of 50° . To show the SOM extraction of occupation weights from this plot, I presented in Fig. 3 numbers representing occupation weight at each given point. Note that the total number of points is 15,000. It is obvious that the SOM method manages to extract orbital weights successfully in 10 epochs. Using SOMs the storage of the necessary data is drastically reduced making them easily accessible for further calculations. Needless to say, one orbit library, with appropriate scaling, can be used in multiple cases after a projection procedure for a desired inclination angle.

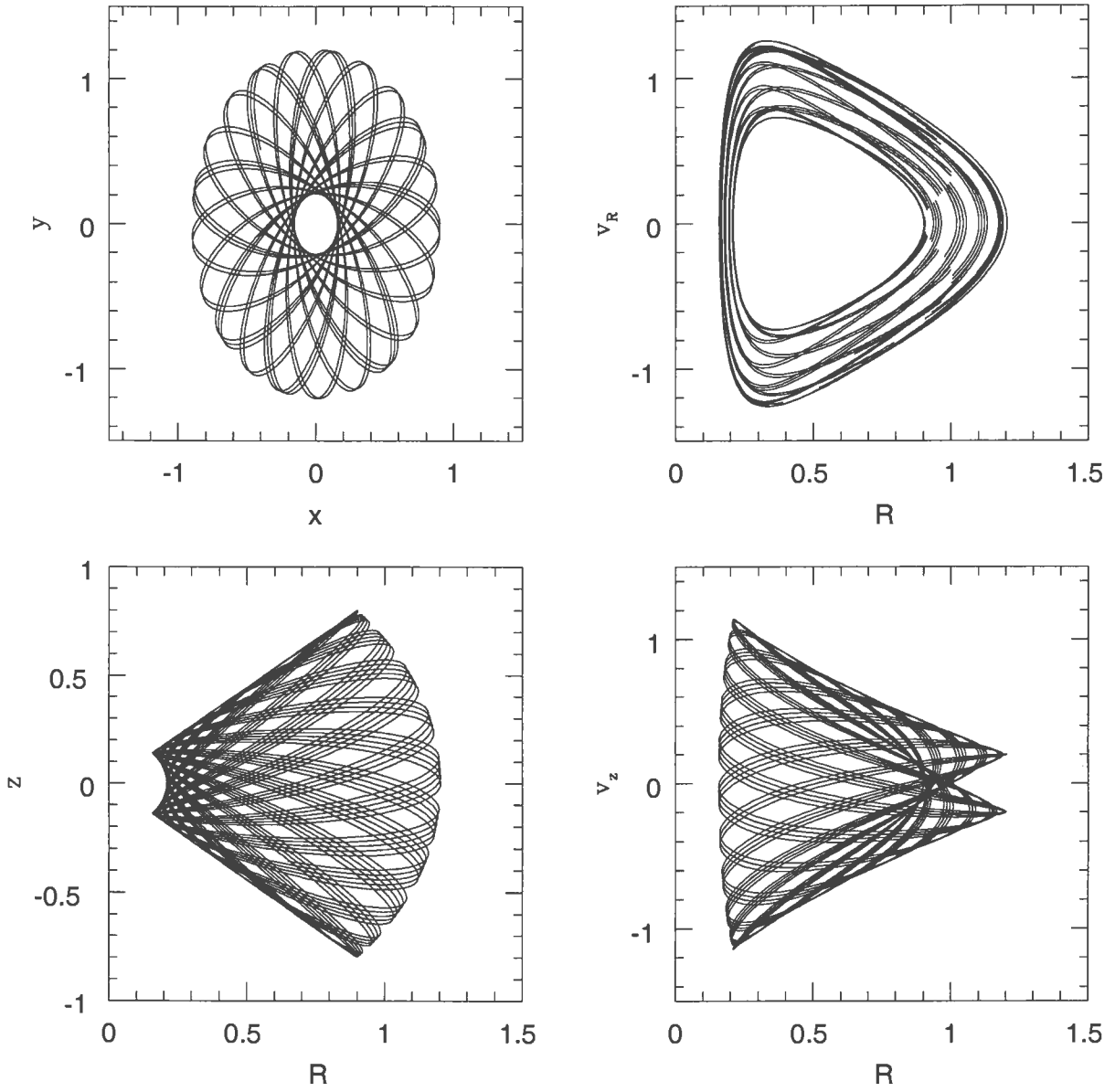


Figure 1: Tube orbit calculated in the axisymmetric logarithmic potential. Initial conditions were: $x = 0.9$, $y = 0.0$, $z = 0.8$, $v_x = 0.0$, $v_y = 0.3$, and $v_z = 0.0$. Potential velocity scale was 1.0, the value of the core radius was $R_c = 0.2$, and the flattening of the potential was $q = 0.9$. Note that the orbit extends out to larger radius with respect to the orbit plotted in Figure 3 (from Appendix 3), because of different initial conditions. Clockwise from the top left corner: dependence of y coordinate on x coordinate, dependence of v_R component of the velocity \mathbf{v} on R coordinate, dependence of v_z component of the velocity \mathbf{v} on R coordinate and dependence of z coordinate on R coordinate. Discontinuities in $v_R - R$ plot are due to the fact that values in the plot are taken only in the case when $z > 0$. Without this condition the whole region of surface of section will be filled (see Chapter A3.1.6).

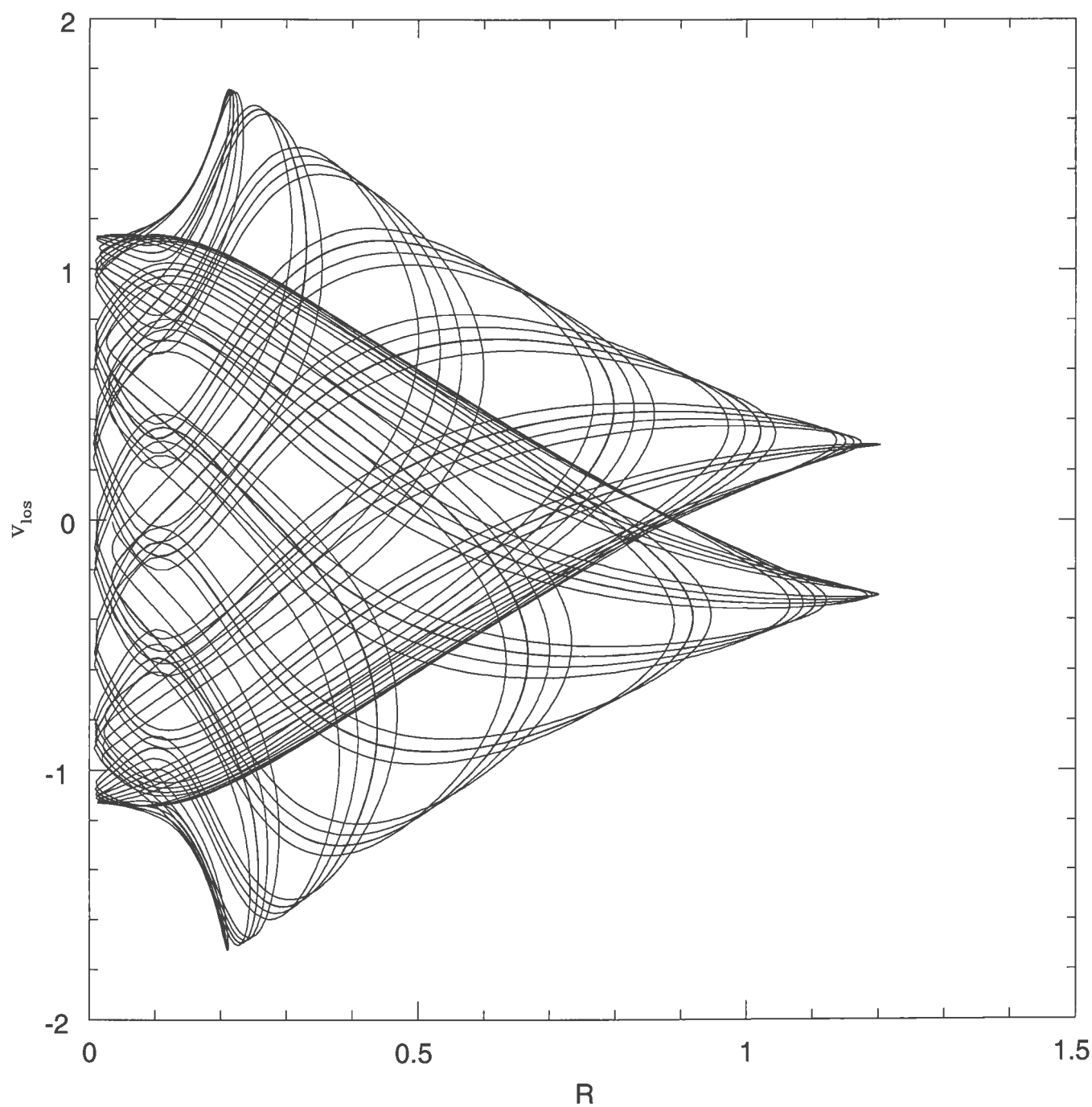


Figure 2: Tube orbit calculated in the axisymmetric logarithmic potential. x -axis is now R coordinate and y -axis is the velocity along the line-of-sight (v_{los}). Inclination is 50° .

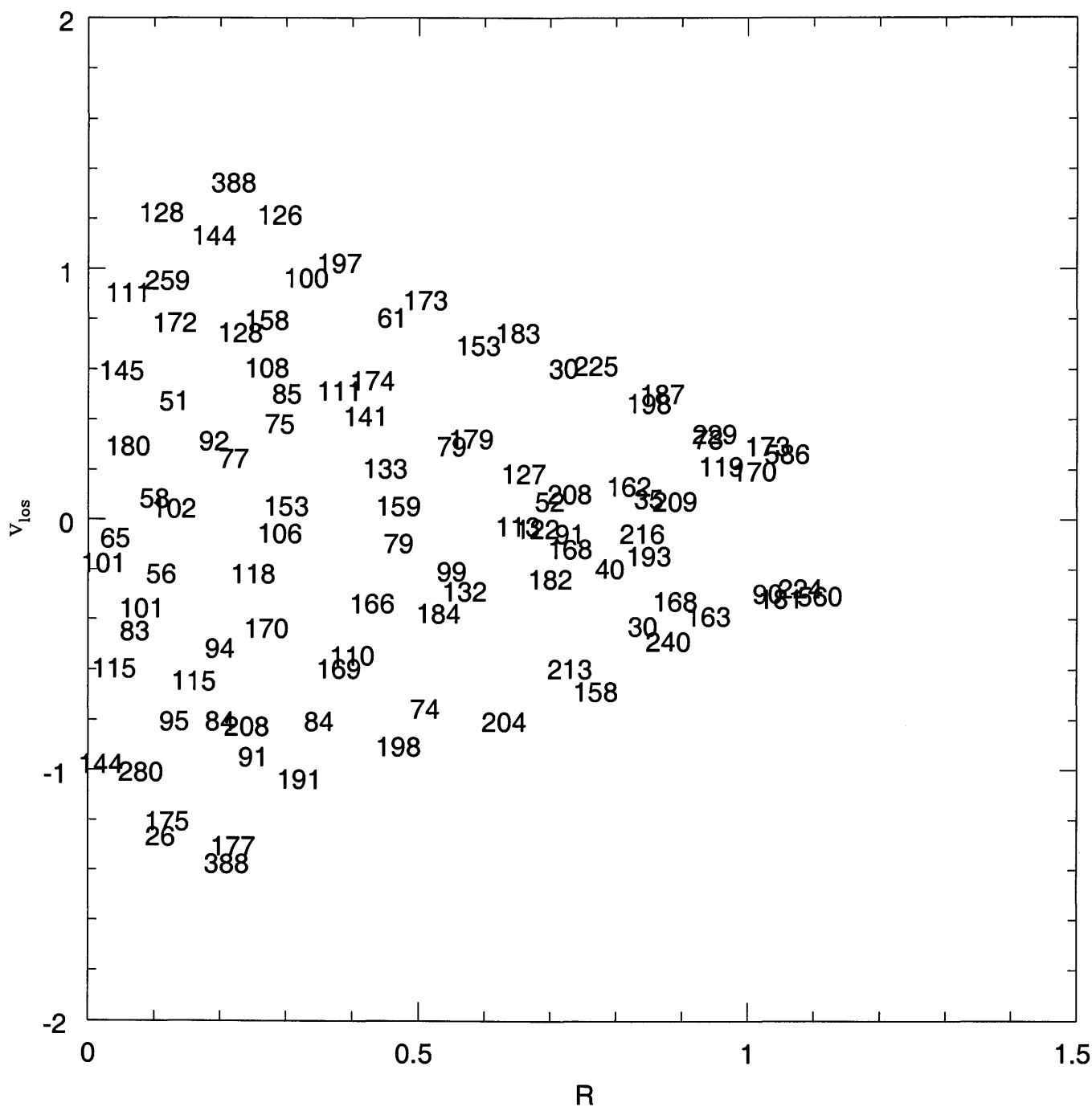


Figure 3: SOM reconstruction of the orbit from Fig. 2. Occupation weights are given in plot as numbers.

REFERENCES

- Kohonen, T.: 1997, *Self-Organizing Maps*, Springer-Verlag.
- Murtagh, F.: 1995, Pattern Recognition Letters, 16, 399.
- Murtagh, F. & Hernandez-Pajeres, M.: 1995, Journal of Classification, 12, 165.
- Rix et al.: 1997, ApJ, 488, 702.

APPENDIX 5

TABLES

5. 1 STELLAR KINEMATICS

TABLE A5-1

IC1459: MAJOR AXIS

r	velocity	err	σ	err	h_3	err	h_4	err
-89.608	95.698	25.135	169.480	24.391	-0.068	0.133	0.133	0.133
-75.794	102.597	19.720	163.257	16.297	-0.079	0.106	0.241	0.107
-65.327	121.165	17.883	183.567	22.703	-0.199	0.094	0.239	0.094
-58.974	76.006	16.481	234.049	15.407	-0.019	0.058	0.069	0.063
-53.963	61.948	14.635	241.966	13.329	0.007	0.049	0.075	0.054
-49.787	81.218	13.897	231.859	12.874	-0.032	0.050	0.075	0.054
-46.163	110.24	15.757	262.035	13.837	0.018	0.046	0.080	0.054
-42.810	124.364	13.676	242.944	12.458	-0.057	0.046	0.071	0.051
-39.725	66.984	13.232	255.728	14.135	0.024	0.041	-0.015	0.048
-37.223	67.771	14.594	278.077	12.821	0.028	0.039	0.076	0.048
-34.981	48.423	13.359	270.989	12.674	0.065	0.038	0.030	0.044
-32.739	56.906	10.967	258.893	10.091	0.005	0.033	0.058	0.038
-30.785	38.417	12.847	267.527	11.879	0.002	0.036	0.051	0.043
-29.112	69.605	12.108	268.088	10.983	0.024	0.034	0.060	0.040
-27.428	61.859	13.102	275.242	12.066	-0.010	0.035	0.050	0.042
-25.748	52.271	12.670	274.420	12.825	0.014	0.034	-0.001	0.041
-24.355	70.152	14.619	287.086	13.682	-0.003	0.037	0.040	0.045
-23.234	35.261	12.820	279.566	11.885	0.038	0.034	0.044	0.041
-22.114	20.275	11.958	266.581	11.656	0.003	0.034	0.024	0.040
-20.994	19.439	12.491	280.641	11.685	-0.004	0.033	0.041	0.039
-19.873	21.448	10.453	291.712	9.357	0.024	0.026	0.066	0.032
-18.753	30.122	12.012	286.600	11.272	0.031	0.031	0.037	0.037
-17.634	36.696	10.995	283.593	10.608	0.017	0.028	0.022	0.034
-16.513	20.862	11.180	301.964	10.874	0.059	0.027	0.011	0.032
-15.680	12.527	12.161	308.807	12.062	0.020	0.027	0.008	0.033
-15.120	18.488	13.908	302.048	13.638	0.063	0.033	0.005	0.040
-14.560	0.628	16.895	305.528	17.641	0.054	0.040	-0.037	0.048
-14.000	20.766	12.372	293.623	12.266	0.020	0.030	0.005	0.036
-13.440	22.538	11.843	289.379	11.235	0.027	0.030	0.031	0.036
-12.880	18.442	14.275	312.678	13.395	0.040	0.032	0.045	0.041
-12.320	13.073	13.877	309.492	14.580	0.026	0.031	-0.034	0.038
-11.760	20.24	12.140	318.476	11.560	0.042	0.026	0.039	0.034
-11.200	7.132	13.393	310.274	12.989	0.058	0.031	0.016	0.037
-10.640	11.204	12.971	308.312	11.974	0.075	0.031	0.044	0.038
-10.080	1.964	11.344	316.647	10.728	0.050	0.025	0.040	0.032
-9.520	14.763	11.508	308.410	10.749	0.042	0.026	0.045	0.033
-8.960	-11.319	10.450	307.970	9.865	0.065	0.024	0.032	0.030

IC1459: MAJOR AXIS (CONTINUED)

r	velocity	err	σ	err	h_3	err	h_4	err
-8.400	2.195	11.973	315.360	11.706	0.052	0.027	0.015	0.033
-7.840	-0.192	11.165	326.330	11.215	0.081	0.024	-0.011	0.029
-7.280	-11.324	10.741	315.678	9.805	0.053	0.024	0.063	0.031
-6.720	-14.223	11.613	322.202	11.122	0.093	0.026	0.018	0.031
-6.160	-18.614	11.714	341.184	11.177	0.067	0.024	0.052	0.031
-5.600	-19.66	12.040	338.357	11.596	0.091	0.026	0.029	0.031
-5.040	-32.463	11.824	341.004	11.608	0.077	0.024	0.025	0.030
-4.480	-44.091	11.259	338.169	10.803	0.104	0.025	0.023	0.029
-3.920	-50.476	11.266	334.689	10.751	0.097	0.025	0.029	0.030
-3.360	-51.924	11.881	338.544	11.498	0.089	0.025	0.027	0.031
-2.800	-59.817	10.187	330.681	9.706	0.104	0.023	0.022	0.027
-2.240	-56.934	10.723	341.247	10.165	0.117	0.024	0.027	0.028
-1.680	-56.246	11.498	346.636	10.854	0.101	0.024	0.048	0.030
-1.120	-34.563	12.155	343.103	11.845	0.076	0.025	0.034	0.031
-0.560	-11.207	13.910	341.779	13.939	0.077	0.029	0.009	0.034
0.000	0.000	13.584	335.607	13.451	0.059	0.028	0.021	0.035
0.560	64.773	13.550	330.543	13.831	-0.019	0.027	0.003	0.034
1.120	41.025	12.329	327.415	12.543	-0.029	0.025	0.001	0.031
1.680	72.978	12.977	324.131	13.110	-0.010	0.027	0.006	0.033
2.240	93.515	13.384	317.287	13.243	-0.022	0.029	0.014	0.036
2.800	88.161	12.975	315.420	12.818	-0.051	0.029	0.008	0.035
3.360	94.115	13.326	319.895	13.020	-0.059	0.029	0.017	0.036
3.920	83.247	13.626	311.288	13.196	-0.052	0.031	0.020	0.038
4.480	77.888	12.533	311.528	12.755	-0.016	0.028	-0.008	0.034
5.040	50.191	13.194	319.595	13.135	-0.006	0.028	0.013	0.035
5.600	57.395	13.182	321.551	13.124	-0.007	0.028	0.015	0.035
6.160	30.099	12.318	311.903	12.207	-0.018	0.027	0.010	0.034
6.720	45.402	11.682	315.057	11.229	0.031	0.026	0.032	0.032
7.280	49.54	11.678	320.937	11.378	0.020	0.025	0.028	0.031
7.840	38.143	11.796	309.733	11.779	0.016	0.026	0.004	0.032
8.400	50.055	13.290	316.146	12.994	0.053	0.029	0.015	0.036
8.960	48.897	13.160	327.410	13.156	0.037	0.027	0.013	0.034
9.520	27.645	12.004	306.298	12.232	0.022	0.027	-0.012	0.033
10.080	14.984	11.952	311.881	11.556	0.043	0.027	0.023	0.033
10.640	17.1	11.947	303.106	11.402	0.063	0.028	0.023	0.034
11.200	18.861	11.859	316.752	12.039	0.033	0.026	-0.006	0.031
11.760	2.951	11.570	316.747	11.553	0.046	0.025	0.003	0.031
12.320	10.752	12.174	311.036	12.311	0.028	0.027	-0.005	0.033
12.880	-4.117	10.728	301.099	10.872	0.046	0.025	-0.013	0.031
13.440	-7.849	10.265	302.861	9.980	0.040	0.024	0.016	0.029
14.000	-1.452	12.259	316.277	12.168	0.020	0.026	0.012	0.033
14.560	-0.432	11.647	305.249	11.583	0.016	0.026	0.005	0.032
15.120	-3.782	13.528	314.441	12.288	0.052	0.031	0.066	0.040
15.680	15.954	10.125	304.898	10.658	0.050	0.024	-0.042	0.029
16.240	2.923	12.771	296.385	12.075	0.045	0.031	0.031	0.038
17.073	-3.435	10.380	301.319	9.704	0.043	0.025	0.040	0.030
18.194	-16.026	10.976	299.967	10.196	0.046	0.026	0.043	0.032
19.314	-26.115	10.609	302.258	9.316	0.055	0.026	0.080	0.033
20.436	-27.453	12.201	308.059	11.141	0.068	0.029	0.054	0.036

IC1459: MAJOR AXIS (CONTINUED)

r	velocity	err	σ	err	h_3	err	h_4	err
21.551	-28.393	12.007	303.493	10.798	0.055	0.029	0.064	0.036
22.674	-33.819	10.082	292.630	8.810	0.084	0.026	0.072	0.032
23.795	-41.113	11.382	294.164	10.656	0.090	0.029	0.025	0.034
24.915	-33.013	12.538	298.468	11.986	0.039	0.030	0.026	0.037
27.988	-36.619	12.789	287.368	11.879	0.040	0.033	0.042	0.039
29.669	-42.04	10.953	297.999	10.392	0.076	0.027	0.022	0.032
31.350	-33.386	11.511	300.428	10.263	0.096	0.029	0.058	0.035
33.303	-46.175	10.867	277.943	10.008	0.045	0.029	0.047	0.035
35.541	-48.5	12.146	275.367	11.475	0.106	0.036	0.019	0.040
37.782	-61.208	11.763	273.917	10.507	0.049	0.033	0.065	0.039
40.294	-57.907	12.915	260.229	11.573	0.106	0.041	0.058	0.045
43.106	-76.088	9.915	234.690	9.735	0.032	0.035	0.045	0.038
46.136	-54.036	11.510	234.418	12.348	0.085	0.043	-0.004	0.047
49.795	-51.694	13.862	255.001	11.893	0.097	0.045	0.091	0.051
53.928	-89.869	14.058	200.652	26.597	0.238	0.071	0.177	0.069
58.963	-97.594	15.891	199.162	27.492	0.158	0.075	0.173	0.075
65.327	-120.835	17.883	183.567	22.703	0.199	0.094	0.239	0.094
73.939	-82.389	23.726	135.026	32.675	0.007	0.142	0.522	0.148
86.244	-108.638	37.625	118.830	69.486	-0.020	0.247	0.398	0.234

TABLE A5-2
IC3370: MAJOR AXIS

r	velocity	err	σ	err	h_3	err	h_4	err
-118.709	-97.283	33.982	108.359	47.825	-0.102	0.306	-0.009	0.346
-76.994	-98.17	13.729	149.995	15.174	-0.020	0.082	0.054	0.088
-58.261	-108.416	13.138	172.560	12.817	0.040	0.065	0.070	0.068
-46.710	-131.07	10.158	157.412	11.417	0.093	0.060	0.023	0.064
-38.513	-118.186	9.072	161.628	10.925	0.077	0.052	-0.015	0.058
-31.791	-111.942	9.111	152.370	10.386	0.086	0.056	0.027	0.059
-26.880	-148.232	10.553	138.989	16.823	0.072	0.080	-0.138	0.112
-23.520	-97.746	9.498	157.489	10.566	0.043	0.054	0.035	0.058
-20.160	-94.81	10.537	186.111	11.442	0.047	0.048	0.000	0.051
-16.800	-77.852	10.333	183.333	9.788	0.047	0.048	0.066	0.049
-13.440	-82.048	10.792	193.314	11.130	0.033	0.046	0.015	0.048
-10.080	-70.944	9.994	189.044	9.632	0.036	0.044	0.050	0.045
-6.720	-69.167	11.289	205.146	10.671	0.007	0.044	0.041	0.045
-3.360	-60.06	11.441	208.147	10.757	0.011	0.044	0.040	0.045
0.000	0.000	11.151	208.537	10.793	0.050	0.043	0.025	0.044
3.360	67.06	10.770	199.582	10.236	0.026	0.044	0.044	0.045
6.720	96.202	11.002	199.779	11.602	-0.028	0.045	-0.001	0.048
10.080	113.86	10.915	204.124	10.313	-0.041	0.043	0.041	0.044
13.440	114.294	9.822	185.917	10.724	-0.024	0.045	0.000	0.048
16.800	125.151	9.606	185.910	11.544	-0.038	0.045	-0.045	0.051
20.160	127.636	9.426	181.309	11.575	-0.013	0.045	-0.047	0.052
23.520	127.365	8.849	170.744	10.957	-0.059	0.047	-0.041	0.054
26.880	129.717	9.302	168.540	11.390	-0.023	0.049	-0.028	0.056
30.240	139.625	9.165	156.671	12.257	-0.092	0.058	-0.066	0.068
35.141	133.451	8.889	148.509	10.985	-0.010	0.055	0.005	0.062
41.864	121.188	8.819	146.365	12.311	0.008	0.057	-0.051	0.071
50.100	146.844	8.659	154.099	12.364	-0.034	0.054	-0.083	0.069
61.694	135.349	9.836	145.376	14.707	0.033	0.067	-0.091	0.088
79.294	122.278	12.685	124.982	15.916	0.073	0.097	0.033	0.104
116.432	124.591	18.182	99.847	30.532	0.093	0.184	-0.102	0.247

TABLE A5-3
IC3370: MINOR AXIS

r	velocity	err	σ	err	h_3	err	h_4	err
-80.156	41.732	15.472	185.858	20.348	-0.170	0.103	-0.305	0.149
-61.574	30.78	17.496	233.660	11.910	-0.133	0.065	0.170	0.068
-50.043	54.865	15.371	183.722	13.351	-0.067	0.071	0.107	0.073
-41.662	1.02	21.828	201.291	20.062	-0.058	0.089	0.057	0.091
-35.373	29.818	19.630	232.101	18.222	-0.243	0.093	-0.038	0.080
-30.240	34.231	14.851	186.155	13.909	-0.105	0.070	0.062	0.070
-26.880	21.567	14.278	182.174	11.897	0.016	0.065	0.133	0.068
-23.520	40.021	14.302	183.965	12.714	0.056	0.066	0.096	0.067
-20.160	48.205	15.211	230.440	16.886	0.035	0.052	-0.050	0.057
-16.800	37.463	15.702	216.157	17.973	-0.020	0.058	-0.051	0.065
-13.440	35.915	13.037	205.530	15.336	-0.081	0.056	-0.064	0.061
-10.080	36.775	15.706	220.740	18.126	-0.078	0.061	-0.070	0.067
-6.720	34.023	12.548	216.791	13.353	0.033	0.046	-0.020	0.049
-3.360	35.387	12.093	206.551	12.634	0.025	0.047	-0.002	0.050
0.000	0.000	11.312	223.119	10.956	0.072	0.041	0.011	0.041
3.360	-15.449	11.714	216.859	10.655	0.043	0.043	0.047	0.044
6.720	-32.512	11.494	208.624	11.032	0.038	0.044	0.032	0.045
10.080	-52.446	10.533	193.031	10.462	0.051	0.046	0.033	0.047
13.440	-45.915	11.340	202.402	12.168	-0.040	0.046	-0.011	0.049
16.800	-54.17	11.744	188.615	12.172	-0.051	0.053	0.019	0.055
20.160	-38.137	14.072	213.722	15.152	-0.073	0.055	-0.028	0.057
23.520	-40.025	15.812	210.258	15.055	-0.002	0.060	0.035	0.062
26.880	-78.507	13.215	178.116	13.214	0.035	0.063	0.051	0.066
30.240	-44.075	21.753	245.018	17.623	0.011	0.067	0.079	0.070
35.131	-52.099	13.435	181.799	13.803	0.070	0.064	0.030	0.066
41.859	-32.566	14.869	201.688	14.593	0.076	0.062	0.025	0.063
50.024	-42.578	14.372	174.449	13.211	0.020	0.070	0.098	0.072
62.955	6.104	17.907	212.082	19.989	0.084	0.073	-0.046	0.077
87.898	-14.423	17.562	156.723	22.006	-0.072	0.106	-0.024	0.120

TABLE A5-4
IC3370: INTERMEDIATE AXIS

r	velocity	err	σ	err	h_3	err	h_4	err
-59.788	-97.318	11.334	180.295	16.307	0.052	0.059	-0.142	0.082
-46.693	-103.027	9.992	133.376	11.399	0.006	0.068	0.069	0.072
-38.494	-103.169	10.171	147.593	14.390	-0.018	0.066	-0.062	0.083
-31.754	-100.368	9.884	157.162	12.581	0.079	0.060	-0.037	0.068
-26.880	-99.208	10.273	166.574	14.369	0.027	0.057	-0.095	0.074
-23.520	-102.625	10.907	156.696	13.198	0.038	0.063	-0.004	0.071
-20.160	-87.717	10.239	162.518	14.397	0.064	0.061	-0.100	0.077
-16.800	-84.928	10.636	174.007	14.551	0.078	0.059	-0.107	0.073
-13.440	-87.972	10.301	170.535	12.116	0.051	0.054	-0.016	0.059
-10.080	-81.43	9.921	169.085	11.912	0.061	0.053	-0.025	0.059
-6.720	-74.647	10.695	173.391	12.346	0.053	0.055	-0.012	0.060
-3.360	-47.07	11.336	190.177	12.093	0.047	0.050	0.002	0.053
0.000	0.000	11.413	198.156	12.091	0.077	0.049	-0.008	0.051
3.360	48.517	10.996	196.522	13.149	0.021	0.047	-0.053	0.054
6.720	94.703	10.941	188.287	12.965	-0.019	0.049	-0.040	0.056
10.080	107.835	10.712	183.460	13.909	-0.019	0.051	-0.078	0.063
13.440	115.963	10.342	185.005	13.115	-0.036	0.049	-0.069	0.058
16.800	132.163	9.937	176.510	13.251	-0.002	0.050	-0.082	0.063
20.160	133.392	9.804	175.128	13.410	-0.053	0.052	-0.100	0.066
23.520	129.282	9.888	169.665	14.142	-0.083	0.058	-0.134	0.076
26.880	128.456	9.650	169.223	14.866	-0.017	0.056	-0.177	0.084
31.771	139.59	9.432	159.740	14.169	-0.005	0.057	-0.129	0.080
38.494	139.441	9.034	142.028	11.807	-0.149	0.067	-0.047	0.074
46.683	140.017	10.226	150.049	14.515	-0.091	0.069	-0.089	0.086
59.581	134.721	12.377	163.816	15.429	-0.152	0.079	-0.067	0.085
84.130	115.096	12.181	144.219	17.536	-0.150	0.094	-0.128	0.116

TABLE A5-5

NGC1336: MAJOR AXIS

r	velocity	err	σ	err	h_3	err	h_4	err
-16.735	-18.592	37.439	78.257	55.978	-0.109	0.440	-0.152	0.602
-6.386	-21.773	13.465	89.392	15.367	0.046	0.125	0.026	0.131
-2.617	-13.72	9.048	91.756	10.478	0.009	0.081	0.022	0.086
-0.910	-1.815	9.183	91.497	8.703	-0.002	0.081	0.113	0.082
0.000	0.000	10.134	100.126	10.012	0.021	0.084	0.086	0.083
0.910	-1.478	8.907	96.390	9.001	-0.026	0.076	0.078	0.076
2.249	-6.818	7.028	93.551	6.235	-0.002	0.061	0.144	0.062
4.440	3.631	7.727	76.800	7.871	-0.179	0.088	0.073	0.089
8.180	13.251	12.526	75.136	13.568	-0.177	0.146	0.041	0.154
19.703	51.156	63.643	40.820	141.717	-0.938	2.092	-0.175	2.480

TABLE A5-6

NGC1339: MAJOR AXIS

r	velocity	err	σ	err	h_3	err	h_4	err
-25.742	-94.743	22.695	134.458	16.413	0.520	0.287	-0.476	0.303
-17.480	-111.953	12.207	75.172	11.303	-0.222	0.146	0.114	0.153
-13.053	-117.659	7.751	101.705	7.262	0.117	0.065	0.068	0.063
-9.929	-129.029	6.559	99.831	5.974	0.073	0.054	0.094	0.054
-7.699	-111.261	8.081	119.588	8.357	0.086	0.058	0.031	0.056
-5.868	-99.337	6.740	128.511	6.474	0.095	0.046	0.059	0.043
-4.550	-71.191	6.395	136.939	6.492	0.084	0.041	0.039	0.039
-3.640	-61.163	6.098	149.073	7.438	0.079	0.037	-0.037	0.039
-2.730	-48.896	7.170	157.476	9.638	-0.004	0.040	-0.072	0.048
-1.820	-38.789	6.579	165.892	8.376	0.043	0.035	-0.058	0.040
-0.910	-21.133	6.201	172.602	7.512	0.029	0.031	-0.038	0.034
0.000	0.000	5.861	174.987	7.127	0.008	0.028	-0.040	0.032
0.910	21.724	5.864	173.035	6.838	0.002	0.028	-0.021	0.031
1.820	39.686	5.531	166.422	6.791	-0.026	0.029	-0.039	0.032
2.730	57.038	6.473	156.475	7.520	-0.046	0.036	-0.012	0.037
3.640	72.192	5.589	145.910	6.245	-0.004	0.032	0.011	0.033
4.550	81.129	5.815	143.540	6.723	-0.041	0.035	-0.004	0.036
5.460	97.88	6.954	139.692	7.243	-0.108	0.045	0.022	0.043
6.776	106.814	5.935	121.410	6.198	-0.063	0.041	0.032	0.040
9.034	124.889	5.154	115.339	4.817	-0.115	0.039	0.066	0.037
12.161	122.955	7.434	120.445	6.607	-0.104	0.053	0.091	0.051
16.197	118.14	8.421	94.826	6.760	-0.059	0.072	0.172	0.077
22.679	131.216	13.618	127.333	10.591	-0.059	0.091	0.160	0.091
35.049	133.738	24.404	117.745	19.926	-0.120	0.180	0.129	0.175

TABLE A5-7
NGC1373: MAJOR AXIS

r	velocity	err	σ	err	h_3	err	h_4	err
-32.824	7.214	52.102	106.468	37.297	-0.534	0.777	-0.433	0.784
-10.954	7.102	8.473	75.902	8.484	-0.059	0.090	0.102	0.101
-7.159	9.676	6.315	85.218	7.601	-0.021	0.060	-0.020	0.069
-4.945	17.341	5.729	91.327	6.227	0.017	0.050	0.025	0.053
-3.640	19.185	6.782	110.464	5.431	-0.020	0.050	0.156	0.052
-2.730	10.607	5.044	96.357	4.877	0.013	0.042	0.075	0.043
-1.820	9.967	5.050	97.436	5.202	-0.010	0.041	0.046	0.042
-0.910	7.414	4.732	94.230	5.345	0.021	0.040	0.006	0.043
0.000	0.000	3.485	90.562	3.795	0.004	0.031	0.025	0.033
0.910	-4.025	2.927	89.411	3.131	0.010	0.026	0.033	0.028
1.820	-5.595	2.680	88.067	2.942	0.015	0.024	0.022	0.026
2.730	-6.238	3.511	81.374	3.529	0.046	0.034	0.077	0.038
3.640	-10.881	4.108	80.626	4.403	-0.032	0.041	0.045	0.046
4.550	-7.639	6.087	85.431	6.176	-0.054	0.057	0.061	0.061
5.851	-12.728	6.517	88.276	7.788	-0.049	0.060	-0.022	0.067
8.064	-9.953	8.120	81.012	12.069	0.037	0.086	-0.144	0.125
11.834	-13.691	14.856	83.622	13.563	0.258	0.171	0.048	0.166
16.543	-27.347	48.526	145.338	32.566	-0.131	0.304	0.234	0.315

TABLE A5-8
NGC1374: MAJOR AXIS

r	velocity	err	σ	err	h_3	err	h_4	err
-26.939	-57.611	30.424	114.178	37.117	0.169	0.268	-0.066	0.274
-17.962	-47.56	16.999	134.089	22.601	0.127	0.126	-0.082	0.142
-13.065	-43.008	11.989	143.066	13.917	0.056	0.074	0.008	0.077
-9.930	-55.522	10.645	157.363	11.902	0.057	0.059	0.014	0.061
-7.694	-56.133	9.601	163.833	9.097	0.118	0.053	0.070	0.051
-5.862	-46.672	8.958	159.571	8.335	0.067	0.048	0.090	0.048
-4.550	-63.018	9.524	162.250	9.163	0.125	0.053	0.062	0.052
-3.640	-64.943	10.422	188.411	9.097	0.060	0.046	0.098	0.047
-2.730	-52.424	11.462	202.537	9.629	0.044	0.046	0.106	0.048
-1.820	-40.744	10.421	187.258	9.232	0.055	0.047	0.092	0.047
-0.910	-20.41	11.040	201.617	10.030	0.056	0.045	0.070	0.046
0.000	0.000	10.103	184.430	10.135	0.008	0.046	0.043	0.047
0.910	27.026	9.453	174.201	10.318	-0.032	0.046	0.015	0.048
1.820	43.939	9.187	156.135	9.719	-0.051	0.051	0.039	0.052
2.730	48.49	8.751	151.891	9.321	-0.090	0.052	0.032	0.051
3.640	30.511	9.484	163.355	9.705	-0.044	0.050	0.049	0.050
4.550	40.101	9.607	160.424	9.248	-0.123	0.054	0.063	0.053
5.868	53.032	9.151	138.085	8.992	-0.030	0.057	0.081	0.056
7.699	43.762	9.707	135.940	8.344	0.037	0.061	0.140	0.060
9.937	54.533	10.305	149.730	10.522	-0.180	0.068	0.022	0.064
13.480	54.652	11.499	119.739	10.684	-0.131	0.086	0.092	0.081
19.154	44.85	19.196	109.795	17.579	-0.140	0.155	0.096	0.147
30.536	58.845	61.594	146.638	73.102	-0.102	0.500	-0.368	0.756

TABLE A5-9
NGC1379: MAJOR AXIS

r	velocity	err	σ	err	h_3	err	h_4	err
-27.414	-37.638	26.266	84.144	29.456	0.193	0.294	-0.019	0.295
-17.864	-30.576	12.878	90.752	14.091	0.204	0.137	-0.021	0.133
-13.084	-35.328	9.933	77.046	11.534	-0.058	0.107	0.041	0.118
-9.935	-26.562	9.367	96.713	9.119	-0.103	0.083	0.088	0.081
-7.696	-36.17	9.835	118.130	9.880	0.045	0.071	0.078	0.071
-5.860	-25.16	8.067	103.744	7.898	0.009	0.065	0.095	0.065
-4.550	-23.787	8.249	109.633	8.732	-0.009	0.064	0.060	0.064
-3.640	-24.055	7.737	114.886	7.704	0.061	0.058	0.080	0.057
-2.730	-15.61	8.461	125.739	8.579	0.035	0.058	0.073	0.058
-1.820	-9.037	7.374	113.555	8.749	-0.002	0.056	0.014	0.059
-0.910	-5.116	7.489	111.421	7.633	0.011	0.057	0.075	0.057
0.000	0	8.205	99.870	8.156	-0.029	0.069	0.089	0.068
0.910	3.801	9.410	108.872	11.584	0.005	0.075	0.001	0.080
1.820	16.739	10.116	109.554	12.447	-0.004	0.080	0.001	0.086
3.138	19.829	10.067	111.362	9.526	0.067	0.077	0.103	0.076
4.970	28.732	9.627	99.779	11.808	-0.056	0.084	-0.004	0.089
7.210	8.949	9.837	95.435	9.048	0.010	0.085	0.129	0.085
10.355	10.738	10.791	84.713	10.734	-0.015	0.104	0.106	0.106
15.076	26.726	15.407	80.422	18.253	0.059	0.160	0.022	0.176
24.776	31.714	23.826	81.533	39.904	-0.050	0.275	-0.223	0.449
49.381	2.922	60.072	88.758	50.863	-0.091	0.562	0.179	0.568

TABLE A5-10

NGC1399: MAJOR AXIS

r	velocity	err	σ	err	h_3	err	h_4	err
-57.866	-56.932	28.389	186.720	33.541	0.101	0.141	-0.037	0.150
-34.004	-44.194	21.697	263.389	20.368	-0.013	0.060	0.039	0.067
-23.828	-48.451	26.690	265.557	27.482	0.063	0.077	-0.014	0.082
-18.032	-31.729	18.278	210.741	17.697	0.018	0.070	0.048	0.075
-13.979	-33.779	17.142	243.371	19.832	0.081	0.059	-0.078	0.068
-10.848	-32.732	17.815	253.375	20.222	0.113	0.062	-0.094	0.069
-8.615	-23.84	18.614	240.227	19.851	0.079	0.063	-0.025	0.068
-6.793	-36.237	21.843	264.060	23.903	0.038	0.062	-0.041	0.069
-5.460	3.885	25.089	288.781	22.179	0.084	0.066	0.057	0.071
-4.550	-15.904	21.980	285.350	26.589	0.063	0.062	-0.156	0.085
-3.640	-43.939	24.524	278.302	24.373	-0.024	0.063	0.009	0.069
-2.730	-26.106	26.837	314.417	25.249	0.091	0.065	0.021	0.066
-1.820	-18.244	24.138	297.469	23.973	0.103	0.064	-0.012	0.063
-0.910	1.204	25.296	307.789	26.199	0.046	0.059	-0.015	0.061
0.000	0.000	26.829	318.740	29.269	0.017	0.059	-0.036	0.062
0.910	-14.935	27.587	314.022	29.412	0.047	0.063	-0.030	0.065
1.820	25.378	26.884	307.782	29.042	0.002	0.061	-0.032	0.065
2.730	20.336	27.599	291.960	29.897	0.042	0.069	-0.039	0.074
3.640	-2.417	25.858	299.042	27.112	-0.015	0.061	-0.018	0.065
4.550	7.407	22.832	278.705	24.721	0.044	0.060	-0.039	0.066
5.460	32.475	26.527	297.061	28.291	0.039	0.064	-0.030	0.068
6.370	-9.957	26.312	282.230	30.246	0.090	0.076	-0.104	0.087
7.702	18.435	20.548	242.598	22.727	0.051	0.067	-0.039	0.075
9.524	26.225	23.907	256.182	25.238	-0.056	0.072	-0.022	0.078
11.757	33.544	17.898	238.130	20.274	0.050	0.060	-0.049	0.068
14.500	33.286	19.607	252.804	21.725	0.029	0.059	-0.042	0.067
18.033	41.765	15.772	199.916	17.242	-0.029	0.066	0.003	0.071
23.805	21.854	17.721	237.931	22.407	0.069	0.065	-0.154	0.092
33.462	7.361	17.882	214.600	18.993	0.059	0.069	0.000	0.074
66.315	27.565	36.641	212.475	47.827	0.055	0.176	-0.280	0.310

TABLE A5-11
NGC1404: MAJOR AXIS

r	velocity	err	σ	err	h_3	err	h_4	err
-79.230	-67.908	35.671	170.194	35.648	-0.292	0.257	-0.101	0.234
-67.148	-66.976	27.246	145.061	39.868	0.034	0.180	-0.181	0.275
-56.551	-85.784	22.325	179.746	26.729	-0.028	0.104	-0.040	0.115
-44.822	-78.145	17.516	166.335	20.560	0.157	0.106	-0.076	0.109
-34.710	-65.477	19.448	192.650	23.450	0.113	0.094	-0.082	0.103
-28.977	-63.873	19.392	194.510	20.242	0.047	0.081	0.006	0.084
-24.934	-76.662	19.792	204.481	23.400	0.025	0.079	-0.051	0.088
-21.787	-73.017	19.593	192.370	21.551	0.149	0.098	-0.050	0.097
-19.543	-88.97	21.312	193.010	22.469	0.084	0.094	-0.004	0.095
-17.723	-60.481	19.772	195.616	23.287	0.109	0.092	-0.069	0.099
-15.900	-62.848	22.611	219.149	23.825	0.070	0.084	-0.016	0.087
-14.077	-57.908	20.830	203.490	21.607	0.068	0.084	0.000	0.086
-12.740	-66.113	21.690	225.700	24.900	0.086	0.082	-0.066	0.089
-11.830	-60.627	20.810	219.085	23.730	0.112	0.085	-0.071	0.090
-10.920	-81.796	21.739	212.467	25.163	0.082	0.087	-0.059	0.095
-10.010	-74.736	22.695	231.514	25.583	0.119	0.088	-0.078	0.093
-9.100	-65.053	22.672	228.310	24.830	0.076	0.081	-0.040	0.086
-8.190	-70.622	24.176	242.353	27.892	0.078	0.082	-0.077	0.092
-7.280	-53.125	24.332	238.015	26.102	0.059	0.081	-0.031	0.085
-6.370	-41.985	24.883	241.758	27.432	0.070	0.083	-0.048	0.089
-5.460	-32.67	24.751	245.101	26.705	0.051	0.078	-0.035	0.084
-4.550	-26.696	25.522	247.036	26.909	0.070	0.082	-0.029	0.085
-3.640	-22.327	24.603	249.490	25.131	0.057	0.076	-0.012	0.079
-2.730	-19.154	24.786	242.072	26.857	0.041	0.079	-0.033	0.085
-1.820	-7.683	24.578	242.723	26.016	0.034	0.077	-0.022	0.082
-0.910	-1.999	23.345	232.569	25.728	0.030	0.078	-0.035	0.085
0.000	0.000	22.845	226.077	25.761	0.017	0.079	-0.041	0.087
0.910	-0.464	24.044	229.634	26.563	0.046	0.083	-0.037	0.089
1.820	3.951	25.089	238.422	26.493	0.051	0.082	-0.022	0.086
2.730	11.678	25.523	240.624	27.740	0.029	0.081	-0.033	0.088
3.640	30.664	25.167	243.186	27.373	-0.006	0.078	-0.032	0.085
4.550	41.524	25.382	239.067	26.887	-0.007	0.080	-0.019	0.086
5.460	32.838	26.256	241.279	28.648	-0.005	0.082	-0.033	0.090
6.370	46.561	25.360	243.891	25.980	0.005	0.078	-0.006	0.083
7.280	61.767	24.287	231.353	26.501	-0.031	0.081	-0.030	0.088
8.190	63.565	24.536	237.202	27.020	-0.005	0.079	-0.035	0.086
9.100	76.874	22.275	222.214	25.892	-0.020	0.079	-0.053	0.089
10.010	79.801	21.837	215.010	23.682	-0.010	0.080	-0.018	0.085
10.921	89.696	22.518	215.494	23.762	-0.034	0.082	-0.008	0.087
11.830	93.1	21.457	209.028	21.591	-0.079	0.085	0.008	0.085
12.740	90.926	20.635	204.205	21.075	-0.065	0.083	0.007	0.084
13.650	89.024	19.502	195.113	21.907	-0.070	0.084	-0.030	0.089
14.987	80.048	20.457	201.418	22.251	-0.023	0.081	-0.012	0.086
16.812	92.978	20.550	211.731	21.897	-0.038	0.077	-0.011	0.081
18.633	80.826	19.696	198.656	17.907	0.007	0.079	0.064	0.081
20.877	98.042	20.974	205.081	21.186	-0.080	0.085	0.008	0.085
23.609	86.675	20.127	196.115	18.547	0.028	0.082	0.059	0.084

NGC1404: MAJOR AXIS (CONTINUED)

r	velocity	err	σ	err	h_3	err	h_4	err
26.751	77.569	18.888	189.532	19.628	-0.042	0.081	0.012	0.084
31.203	82.592	19.020	186.533	21.525	-0.056	0.086	-0.025	0.091
38.184	92.712	17.412	168.845	20.488	-0.102	0.094	-0.044	0.099
52.192	101.68	18.176	169.521	24.888	0.019	0.094	-0.100	0.121
67.123	241.99	42.197	207.255	27.489	0.080	0.178	0.234	0.197

TABLE A5-12
NGC1419: MAJOR AXIS

r	velocity	err	σ	err	h_3	err	h_4	err
-6.521	0.024	17.809	113.962	25.817	-0.029	0.142	-0.069	0.173
-4.023	-15.093	13.940	110.476	10.743	0.173	0.114	0.193	0.112
-2.730	-16.604	12.411	122.926	12.931	0.028	0.087	0.064	0.087
-1.820	16.003	11.973	126.676	12.193	0.107	0.086	0.060	0.083
-0.910	-8.81	10.837	111.608	11.892	0.152	0.092	0.010	0.088
0.000	0.000	9.044	106.235	11.431	0.033	0.074	-0.011	0.080
0.910	5.598	9.235	104.526	11.035	-0.033	0.076	0.011	0.080
1.820	-9.225	9.446	114.905	12.436	0.013	0.073	-0.026	0.081
2.730	-5.819	11.340	107.952	16.569	0.026	0.095	-0.073	0.117
3.640	3.304	9.793	88.596	10.736	0.054	0.092	0.050	0.096
4.941	5.946	12.755	107.210	12.159	0.016	0.100	0.106	0.099
7.140	-3.687	21.883	107.995	27.116	-0.152	0.199	-0.054	0.205
10.857	-67.488	32.059	125.815	20.233	-0.376	0.279	0.295	0.279

TABLE A5-13
NGC4339: MAJOR AXIS

r	velocity	err	σ	err	h_3	err	h_4	err
-29.382	-56.039	21.360	51.647	39.225	0.467	0.462	0.000	0.623
-13.443	-55.628	10.087	61.333	13.922	-0.146	0.146	0.062	0.203
-9.268	-56.091	7.161	72.821	7.709	0.120	0.081	0.044	0.098
-7.026	-43.412	6.504	87.364	6.266	-0.024	0.057	0.073	0.062
-5.579	-51.131	6.931	89.253	6.488	0.027	0.060	0.085	0.064
-4.396	-38.795	6.124	107.542	6.092	0.013	0.045	0.051	0.045
-3.540	-29.805	5.633	91.803	5.447	0.001	0.047	0.067	0.050
-2.950	-25.508	5.551	107.796	5.474	0.084	0.042	0.043	0.041
-2.360	-20.547	4.737	106.737	4.970	0.048	0.036	0.026	0.035
-1.770	-16.284	4.767	116.225	4.659	0.036	0.033	0.058	0.032
-1.180	-15.468	4.234	114.615	4.568	0.016	0.030	0.023	0.029
-0.590	-12.232	4.595	117.255	5.024	-0.020	0.032	0.019	0.032
0.000	0.000	4.290	114.959	4.745	0.011	0.030	0.014	0.030
0.590	3.27	4.918	115.513	5.363	0.036	0.035	0.017	0.034
1.180	13.646	4.909	117.557	6.200	-0.007	0.035	-0.032	0.037
1.770	29.471	6.161	108.380	5.758	-0.036	0.045	0.075	0.045
2.360	34.194	7.030	117.596	7.187	0.020	0.049	0.043	0.047
3.211	48.644	5.960	96.788	6.421	-0.027	0.048	0.016	0.049
4.401	51.343	8.112	95.894	8.804	0.073	0.068	0.003	0.069
5.833	67.687	7.542	85.695	6.904	-0.069	0.069	0.100	0.075
8.085	63.709	7.545	76.335	8.227	0.047	0.078	0.027	0.093
12.514	68.394	11.090	64.667	12.393	-0.029	0.136	0.210	0.171
25.312	80.162	27.611	75.533	17.626	-0.120	0.349	0.670	0.459

TABLE A5-14
NGC3379: MAJOR AXIS

r	velocity	err	σ	err	h_3	err	h_4	err
-25.879	63.194	8.513	162.073	7.368	-0.090	0.045	0.109	0.046
-14.051	68.302	7.637	179.704	7.898	-0.073	0.036	0.028	0.037
-8.753	56.908	4.830	176.622	5.180	-0.012	0.023	0.022	0.024
-6.255	52.234	5.303	183.786	5.603	0.015	0.024	0.024	0.025
-4.809	51.106	5.572	199.728	5.931	-0.015	0.023	0.014	0.024
-3.624	42.337	5.403	207.183	5.545	0.002	0.021	0.026	0.022
-2.773	45.139	5.834	214.089	5.978	-0.011	0.022	0.023	0.023
-2.183	39.724	5.935	219.934	5.964	-0.019	0.021	0.029	0.023
-1.593	35.234	5.928	225.600	6.096	-0.010	0.021	0.016	0.022
-1.003	29.393	5.767	224.304	5.916	-0.003	0.020	0.018	0.022
-0.413	19.156	5.681	217.610	5.945	0.016	0.021	0.012	0.022
-0.177	5.516	5.703	223.417	6.094	0.013	0.020	0.001	0.022
0.767	-3.167	5.601	217.749	5.619	0.016	0.020	0.030	0.022
1.357	-9.204	5.750	208.990	5.938	0.024	0.022	0.022	0.023
1.947	-11.184	6.080	203.897	6.422	0.040	0.024	0.013	0.026
2.798	-18.15	5.505	201.697	5.764	0.028	0.022	0.019	0.023
3.983	-24.77	5.559	196.204	5.828	0.032	0.023	0.021	0.024
5.428	-29.387	5.263	184.628	5.622	0.010	0.023	0.020	0.025
7.704	-30.205	4.881	175.466	5.150	0.025	0.023	0.028	0.024
12.261	-45.279	5.224	171.950	5.111	0.027	0.025	0.060	0.026
20.582	-60.748	7.666	155.531	8.560	0.033	0.042	0.011	0.043

TABLE A5-15
NGC4105: MAJOR AXIS

r	velocity	err	σ	err	h_3	err	h_4	err
-22.585	31.695	62.504	260.281	84.348	0.134	0.246	-0.143	0.310
-14.673	4.87	33.698	234.433	42.807	0.095	0.136	-0.051	0.154
-10.619	35.136	23.159	253.402	27.209	0.072	0.081	-0.026	0.090
-8.165	12.979	19.660	259.904	21.912	0.069	0.066	-0.008	0.071
-6.519	24.065	17.210	262.390	18.105	0.016	0.055	0.020	0.058
-5.356	27.889	14.490	262.859	17.444	0.027	0.047	-0.039	0.055
-4.347	20.754	14.195	257.176	15.235	-0.010	0.047	0.017	0.050
-3.520	11.619	15.405	285.667	17.093	0.021	0.044	-0.021	0.049
-2.847	21.285	14.241	284.228	15.041	0.025	0.041	0.001	0.044
-2.173	15.245	14.320	283.497	14.142	0.027	0.041	0.031	0.043
-1.680	10.452	16.009	310.394	16.202	-0.001	0.040	0.004	0.044
-1.344	4.165	15.589	307.387	15.176	0.032	0.040	0.022	0.042
-1.008	3.815	16.464	298.603	18.045	0.055	0.045	-0.028	0.050
-0.672	7.031	16.050	298.183	16.030	-0.003	0.042	0.017	0.046
-0.336	15.546	14.806	304.751	16.300	-0.022	0.039	-0.030	0.044
0.000	0.000	14.837	298.764	18.337	-0.020	0.041	-0.079	0.051
0.336	1.583	17.086	313.825	18.558	-0.039	0.043	-0.031	0.049
0.672	-5.221	15.298	306.415	16.960	-0.044	0.040	-0.037	0.046
1.008	14.739	15.538	308.173	15.828	-0.067	0.041	-0.003	0.044
1.344	28.992	15.082	285.592	14.677	-0.013	0.042	0.036	0.045
1.680	28.555	15.058	299.200	17.439	-0.058	0.042	-0.054	0.049
2.016	4.331	16.399	301.758	18.116	-0.026	0.043	-0.030	0.049
2.352	50.178	14.001	278.795	16.299	0.001	0.042	-0.036	0.048
2.688	32.482	13.129	254.500	13.943	-0.020	0.044	0.023	0.046
3.181	38.352	13.591	277.016	14.385	0.043	0.041	0.004	0.044
3.855	21.539	14.533	295.552	16.118	-0.029	0.040	-0.028	0.045
4.528	28.619	14.184	273.435	16.533	-0.032	0.044	-0.034	0.050
5.356	41.094	15.362	280.693	16.450	-0.001	0.045	-0.001	0.049
6.516	26.132	14.800	261.816	17.802	0.032	0.049	-0.038	0.056
8.017	31.639	17.392	279.589	19.685	0.032	0.052	-0.026	0.058
9.996	31.828	18.018	262.988	21.318	0.045	0.059	-0.033	0.067
12.943	40.285	25.093	262.602	27.882	0.075	0.083	-0.010	0.089
18.002	66.794	33.495	249.708	45.852	0.014	0.120	-0.085	0.154
27.268	49.384	45.562	248.060	63.312	0.018	0.166	-0.092	0.216

TABLE A5-16

NGC4105: MINOR AXIS

r	velocity	err	σ	err	h_3	err	h_4	err
-9.613	66.253	56.865	287.610	63.660	-0.164	0.240	-0.404	0.377
-6.800	-11.076	27.873	243.361	32.630	0.106	0.106	-0.024	0.114
-5.167	41.767	37.886	309.688	28.733	0.076	0.099	0.139	0.105
-4.009	22.206	24.338	283.535	34.077	0.001	0.075	-0.136	0.109
-3.180	9.865	28.872	315.807	26.594	0.044	0.071	0.041	0.075
-2.504	25.53	15.694	288.956	15.782	-0.036	0.044	0.018	0.047
-2.016	25.516	18.632	284.057	22.655	0.073	0.057	-0.070	0.068
-1.680	68.354	23.839	327.022	16.758	0.100	0.060	0.175	0.066
-1.344	2.133	16.576	303.480	16.686	-0.044	0.043	0.008	0.047
-1.008	11.083	18.115	317.555	19.687	0.075	0.046	-0.041	0.052
-0.672	14.812	14.372	288.949	13.448	-0.047	0.040	0.049	0.042
-0.336	-7.478	15.040	318.497	13.816	-0.052	0.037	0.040	0.039
0.000	0.000	14.757	303.940	15.209	0.015	0.038	0.000	0.042
0.336	-3.794	15.515	312.880	13.146	-0.034	0.039	0.082	0.041
0.672	-5.044	19.103	327.555	17.912	-0.008	0.044	0.030	0.048
1.008	-13.082	17.626	301.887	15.988	-0.019	0.046	0.057	0.048
1.344	-31.054	15.749	277.036	16.262	0.006	0.046	0.017	0.049
1.680	-30.863	17.706	305.189	19.507	0.005	0.046	-0.030	0.052
2.169	-7.328	24.048	292.992	18.893	-0.001	0.066	0.133	0.069
2.844	-55.537	53.998	238.476	26.755	0.057	0.277	0.760	0.297
3.668	-5.908	17.948	280.591	24.505	-0.008	0.055	-0.115	0.076
4.829	16.595	19.588	267.684	23.580	0.046	0.063	-0.045	0.073
6.466	58.218	30.208	278.722	34.763	-0.070	0.093	-0.039	0.104
9.289	14.762	67.459	223.187	108.529	0.019	0.327	-0.293	0.556
16.996	63.552	89.328	199.778	151.321	-0.076	0.487	-0.237	0.759

5. 2 LINE STRENGTH INDICES

TABLE A5-17
IC1459: MAJOR AXIS

r	Mg2	err	Fe5270	err	Fe5335	err	<Fe>	err
-78.960	0.283	0.015	2.888	0.018	1.844	0.051	2.366	0.051
-76.160	0.286	0.014	2.994	0.018	1.960	0.050	2.477	0.050
-73.360	0.291	0.014	2.990	0.017	1.979	0.048	2.484	0.048
-70.560	0.294	0.013	3.000	0.017	2.017	0.046	2.508	0.046
-67.760	0.298	0.013	3.037	0.016	2.097	0.044	2.567	0.044
-64.960	0.300	0.012	3.065	0.016	2.146	0.043	2.605	0.043
-62.160	0.303	0.012	3.081	0.015	2.175	0.041	2.628	0.041
-59.360	0.305	0.012	3.324	0.015	2.515	0.040	2.920	0.040
-56.560	0.308	0.011	3.243	0.014	2.411	0.038	2.827	0.038
-53.760	0.310	0.011	3.175	0.014	2.314	0.037	2.745	0.037
-50.960	0.313	0.010	3.094	0.013	2.171	0.036	2.633	0.036
-48.160	0.315	0.010	3.072	0.013	2.103	0.034	2.588	0.034
-45.360	0.316	0.009	3.095	0.012	2.068	0.032	2.581	0.032
-42.560	0.316	0.009	3.139	0.011	2.089	0.031	2.614	0.031
-39.760	0.315	0.008	3.227	0.011	2.171	0.029	2.699	0.029
-36.960	0.315	0.008	3.290	0.010	2.248	0.028	2.769	0.028
-34.160	0.316	0.007	3.526	0.009	2.595	0.025	3.060	0.025
-31.360	0.317	0.007	3.584	0.009	2.699	0.024	3.141	0.024
-28.560	0.319	0.006	3.653	0.008	2.866	0.022	3.259	0.022
-25.760	0.321	0.006	3.675	0.007	2.983	0.020	3.329	0.020
-22.960	0.326	0.005	3.672	0.007	3.139	0.018	3.405	0.018
-20.160	0.331	0.005	3.658	0.006	3.209	0.016	3.434	0.016
-17.360	0.342	0.004	3.653	0.005	3.234	0.014	3.443	0.014
-14.560	0.350	0.004	3.668	0.004	3.201	0.012	3.435	0.012
-11.760	0.359	0.003	3.704	0.004	3.117	0.010	3.411	0.010
-8.960	0.364	0.003	3.883	0.003	3.343	0.009	3.613	0.009
-6.160	0.367	0.002	3.906	0.003	3.256	0.008	3.581	0.008
-3.360	0.367	0.002	3.914	0.003	3.206	0.007	3.560	0.007
-0.560	0.367	0.002	3.920	0.003	3.435	0.007	3.678	0.007
2.240	0.365	0.002	4.085	0.003	3.392	0.007	3.738	0.007
5.040	0.362	0.002	3.922	0.003	3.338	0.008	3.630	0.008
7.840	0.359	0.003	3.920	0.003	3.027	0.009	3.473	0.009
10.640	0.354	0.003	3.914	0.004	3.017	0.011	3.466	0.011
13.440	0.350	0.004	3.909	0.004	3.032	0.012	3.471	0.012
16.240	0.343	0.004	3.749	0.005	2.819	0.015	3.284	0.015
19.040	0.337	0.005	3.751	0.006	2.856	0.016	3.303	0.016
21.840	0.330	0.006	3.752	0.007	2.895	0.019	3.324	0.019
24.640	0.324	0.006	3.747	0.007	2.905	0.021	3.326	0.021
27.440	0.313	0.007	3.722	0.008	2.902	0.023	3.312	0.023
30.240	0.305	0.007	3.688	0.009	2.896	0.024	3.292	0.024
33.040	0.292	0.008	3.609	0.010	2.881	0.026	3.245	0.026
35.840	0.285	0.008	3.541	0.010	2.863	0.027	3.202	0.027
38.640	0.278	0.008	3.435	0.011	2.820	0.029	3.128	0.029

IC1459: MAJOR AXIS (CONTINUED)

r	Mg2	err	Fe5270	err	Fe5335	err	<Fe>	err
41.440	0.276	0.009	3.237	0.011	2.561	0.031	2.899	0.031
44.240	0.276	0.009	3.187	0.012	2.533	0.033	2.860	0.033
47.040	0.278	0.010	3.181	0.012	2.525	0.034	2.853	0.034
49.840	0.282	0.010	3.213	0.013	2.528	0.036	2.870	0.036
52.640	0.286	0.011	3.259	0.014	2.534	0.037	2.896	0.037
55.440	0.292	0.011	3.352	0.014	2.544	0.039	2.948	0.039
58.240	0.296	0.012	3.414	0.015	2.550	0.040	2.982	0.040
61.040	0.299	0.012	3.474	0.015	2.559	0.042	3.016	0.042
63.840	0.300	0.013	3.482	0.016	2.567	0.043	3.024	0.043
66.640	0.298	0.013	3.187	0.016	2.209	0.045	2.698	0.045
69.440	0.296	0.013	3.167	0.017	2.209	0.046	2.688	0.046
72.240	0.292	0.014	3.144	0.018	2.196	0.048	2.670	0.048
75.040	0.291	0.014	3.134	0.018	2.178	0.049	2.656	0.049
77.840	0.290	0.015	3.126	0.019	2.149	0.051	2.638	0.051
80.640	0.289	0.015	3.123	0.019	2.132	0.052	2.627	0.052
83.440	0.287	0.016	3.002	0.020	1.981	0.054	2.492	0.054

TABLE A5-18
IC3370: MAJOR AXIS

r	Mg2	err	Fe5270	err	Fe5335	err	<Fe>	err
-87.92	0.19	0.04	2.45	0.06	2.07	0.16	2.26	0.16
-85.12	0.18	0.04	2.47	0.06	2.14	0.15	2.30	0.15
-82.32	0.17	0.04	2.53	0.05	2.21	0.15	2.37	0.15
-79.52	0.16	0.04	2.57	0.05	2.26	0.14	2.42	0.14
-76.72	0.16	0.04	2.65	0.05	2.32	0.14	2.49	0.14
-73.92	0.16	0.04	2.70	0.05	2.36	0.13	2.53	0.13
-71.12	0.16	0.04	2.78	0.05	2.44	0.13	2.61	0.13
-68.32	0.16	0.03	2.86	0.04	2.53	0.12	2.69	0.12
-65.52	0.16	0.03	2.94	0.04	2.64	0.12	2.79	0.12
-62.72	0.17	0.03	3.01	0.04	2.69	0.11	2.85	0.11
-59.92	0.17	0.03	3.01	0.04	2.69	0.10	2.85	0.10
-57.12	0.18	0.03	2.93	0.04	2.63	0.10	2.78	0.10
-54.32	0.18	0.03	2.79	0.03	2.53	0.09	2.66	0.09
-51.52	0.19	0.03	2.67	0.03	2.45	0.09	2.56	0.09
-48.72	0.19	0.02	2.52	0.03	2.35	0.09	2.43	0.09
-45.92	0.19	0.02	2.44	0.03	2.30	0.08	2.37	0.08
-43.12	0.19	0.02	2.38	0.03	2.24	0.08	2.31	0.08
-40.32	0.19	0.02	2.39	0.03	2.22	0.07	2.30	0.07
-37.52	0.19	0.02	2.43	0.02	2.24	0.07	2.34	0.07
-34.72	0.20	0.02	2.49	0.02	2.25	0.06	2.37	0.06
-31.92	0.20	0.02	2.60	0.02	2.29	0.06	2.45	0.06
-29.12	0.21	0.01	2.73	0.02	2.35	0.05	2.54	0.05
-26.32	0.21	0.01	2.87	0.02	2.50	0.05	2.69	0.05
-23.52	0.22	0.01	2.93	0.01	2.50	0.04	2.71	0.04
-20.72	0.22	0.01	2.99	0.01	2.54	0.03	2.77	0.03
-17.92	0.22	0.01	3.02	0.01	2.59	0.03	2.80	0.03
-15.12	0.23	0.01	3.10	0.01	2.69	0.03	2.89	0.03
-12.32	0.23	0.01	3.12	0.01	2.68	0.03	2.90	0.03
-9.52	0.23	0.01	3.16	0.01	2.66	0.02	2.91	0.02
-6.72	0.24	0.01	3.20	0.01	2.75	0.02	2.98	0.02
-3.92	0.24	0.01	3.18	0.01	2.60	0.02	2.89	0.02
-1.12	0.24	0.01	3.15	0.01	2.56	0.03	2.86	0.03
1.68	0.24	0.01	3.13	0.01	2.49	0.03	2.81	0.03
4.48	0.24	0.01	3.06	0.01	2.37	0.03	2.71	0.03
7.28	0.23	0.01	3.03	0.01	2.28	0.04	2.66	0.04
10.08	0.23	0.01	3.02	0.02	2.25	0.04	2.63	0.04
12.88	0.23	0.01	3.02	0.02	2.23	0.05	2.62	0.05
15.68	0.22	0.02	3.00	0.02	2.10	0.05	2.55	0.05
18.48	0.21	0.02	2.97	0.02	2.02	0.06	2.49	0.06
21.28	0.21	0.02	2.98	0.02	1.99	0.06	2.48	0.06
24.08	0.19	0.02	2.98	0.03	1.97	0.07	2.48	0.07
26.88	0.18	0.02	2.96	0.03	1.96	0.07	2.46	0.07
29.68	0.16	0.02	2.92	0.03	1.97	0.08	2.45	0.08
32.48	0.16	0.02	2.89	0.03	1.97	0.08	2.43	0.08
35.28	0.15	0.03	2.85	0.03	1.96	0.09	2.41	0.09
38.08	0.14	0.03	2.84	0.03	1.95	0.09	2.40	0.09
40.88	0.13	0.03	2.85	0.04	1.94	0.10	2.39	0.10

IC3370: MAJOR AXIS (CONTINUED)

r	Mg2	err	Fe5270	err	Fe5335	err	<Fe>	err
43.68	0.13	0.03	2.86	0.04	1.94	0.10	2.40	0.10
46.48	0.12	0.03	2.88	0.04	1.98	0.11	2.43	0.11
49.28	0.11	0.03	2.86	0.04	2.00	0.11	2.43	0.11
52.08	0.10	0.03	2.77	0.04	2.04	0.12	2.40	0.12
54.88	0.09	0.03	2.71	0.04	2.04	0.12	2.37	0.12
57.68	0.08	0.04	2.58	0.05	2.01	0.13	2.30	0.13
60.48	0.08	0.04	2.50	0.05	1.98	0.13	2.24	0.13
63.28	0.08	0.04	2.44	0.05	1.87	0.14	2.15	0.14
66.08	0.08	0.04	2.43	0.05	1.76	0.14	2.09	0.14
68.88	0.07	0.04	2.44	0.05	1.62	0.15	2.03	0.15
71.68	0.07	0.04	2.42	0.05	1.57	0.15	1.99	0.15
74.48	0.07	0.04	2.36	0.06	1.55	0.16	1.95	0.16

TABLE A5-19
IC3370: MINOR AXIS

r	Mg2	err	Fe5270	err	Fe5335	err	<Fe>	err
-81.20	0.20	0.05	2.15	0.07	1.84	0.19	2.00	0.19
-78.40	0.20	0.05	2.28	0.07	1.88	0.19	2.08	0.19
-75.60	0.20	0.05	2.39	0.07	1.82	0.18	2.11	0.18
-72.80	0.20	0.05	2.39	0.06	1.73	0.18	2.06	0.18
-70.00	0.20	0.05	2.31	0.06	1.56	0.17	1.93	0.17
-67.20	0.19	0.05	2.25	0.06	1.48	0.17	1.87	0.17
-64.40	0.17	0.04	2.21	0.06	1.52	0.16	1.87	0.16
-61.60	0.16	0.04	2.23	0.06	1.64	0.16	1.94	0.16
-58.80	0.14	0.04	2.27	0.05	1.84	0.15	2.05	0.15
-56.00	0.14	0.04	2.31	0.05	1.92	0.14	2.11	0.14
-53.20	0.13	0.04	2.30	0.05	1.94	0.13	2.12	0.13
-50.40	0.13	0.04	2.24	0.05	1.88	0.13	2.06	0.13
-47.60	0.13	0.03	2.18	0.04	1.77	0.12	1.98	0.12
-44.80	0.13	0.03	2.14	0.04	1.70	0.11	1.92	0.11
-42.00	0.14	0.03	2.12	0.04	1.60	0.10	1.86	0.10
-39.20	0.14	0.03	2.14	0.03	1.59	0.10	1.87	0.10
-36.40	0.14	0.03	2.25	0.03	1.66	0.09	1.95	0.09
-33.60	0.15	0.02	2.35	0.03	1.75	0.09	2.05	0.09
-30.80	0.15	0.02	2.52	0.03	1.94	0.08	2.23	0.08
-28.00	0.16	0.02	2.62	0.03	2.03	0.08	2.32	0.08
-25.20	0.17	0.02	2.70	0.03	2.11	0.07	2.41	0.07
-22.40	0.17	0.02	2.78	0.02	2.15	0.06	2.47	0.06
-19.60	0.18	0.02	2.82	0.02	2.26	0.06	2.54	0.06
-16.80	0.19	0.01	2.82	0.02	2.22	0.05	2.52	0.05
-14.00	0.19	0.01	2.85	0.02	2.23	0.04	2.54	0.04
-11.20	0.20	0.01	2.90	0.01	2.26	0.04	2.58	0.04
-8.40	0.21	0.01	3.04	0.01	2.36	0.03	2.70	0.03
-5.60	0.22	0.01	3.11	0.01	2.40	0.03	2.75	0.03
-2.80	0.23	0.01	3.23	0.01	2.46	0.03	2.84	0.03
0.00	0.24	0.01	3.30	0.01	2.59	0.03	2.95	0.03
2.80	0.24	0.01	3.31	0.01	2.54	0.03	2.92	0.03
5.60	0.25	0.01	3.29	0.01	2.55	0.03	2.92	0.03
8.40	0.25	0.01	3.27	0.01	2.55	0.03	2.91	0.03
11.20	0.25	0.01	3.19	0.01	2.46	0.03	2.82	0.03
14.00	0.25	0.01	3.15	0.01	2.41	0.04	2.78	0.04
16.80	0.25	0.01	3.12	0.02	2.40	0.05	2.76	0.05
19.60	0.24	0.02	3.04	0.02	2.44	0.05	2.74	0.05
22.40	0.24	0.02	2.93	0.02	2.37	0.06	2.65	0.06
25.20	0.23	0.02	2.75	0.02	2.43	0.07	2.59	0.07
28.00	0.23	0.02	2.69	0.03	2.49	0.07	2.59	0.07
30.80	0.22	0.02	2.64	0.03	2.59	0.08	2.62	0.08
33.60	0.21	0.02	2.64	0.03	2.62	0.08	2.63	0.08
36.40	0.20	0.03	2.64	0.03	2.65	0.09	2.65	0.09
39.20	0.19	0.03	2.63	0.03	2.62	0.09	2.62	0.09
42.00	0.18	0.03	2.57	0.04	2.47	0.10	2.52	0.10
44.80	0.17	0.03	2.51	0.04	2.34	0.11	2.42	0.11
47.60	0.16	0.03	2.42	0.04	2.13	0.12	2.28	0.12

IC3370: MINOR AXIS (CONTINUED)

r	Mg2	err	Fe5270	err	Fe5335	err	<Fe>	err
50.40	0.15	0.03	2.41	0.04	2.02	0.12	2.21	0.12
53.20	0.14	0.04	2.49	0.05	1.95	0.13	2.22	0.13
56.00	0.13	0.04	2.56	0.05	1.94	0.14	2.25	0.14
58.80	0.13	0.04	2.65	0.05	1.97	0.14	2.31	0.14
61.60	0.13	0.04	2.68	0.05	1.98	0.15	2.33	0.15
64.40	0.12	0.04	2.60	0.06	2.00	0.16	2.30	0.16
67.20	0.11	0.05	2.46	0.06	1.98	0.16	2.22	0.16
70.00	0.10	0.05	2.17	0.06	1.88	0.17	2.02	0.17
72.80	0.09	0.05	1.93	0.06	1.77	0.18	1.85	0.18
75.60	0.08	0.05	1.58	0.07	1.66	0.19	1.62	0.19
78.40	0.07	0.05	1.39	0.07	1.65	0.19	1.52	0.19
81.20	0.06	0.06	1.28	0.07	1.76	0.20	1.52	0.20

TABLE A5-20
IC3370: INTERMEDIATE AXIS

r	Mg2	err	Fe5270	err	Fe5335	err	<Fe>	err
-81.20	0.21	0.05	2.47	0.06	1.28	0.18	1.87	0.18
-78.40	0.21	0.05	2.48	0.06	1.28	0.17	1.88	0.17
-75.60	0.21	0.04	2.36	0.06	1.22	0.16	1.79	0.16
-72.80	0.20	0.04	2.23	0.06	1.17	0.16	1.70	0.16
-70.00	0.18	0.04	2.08	0.05	1.13	0.15	1.61	0.15
-67.20	0.16	0.04	2.04	0.05	1.18	0.14	1.61	0.14
-64.40	0.15	0.04	2.10	0.05	1.40	0.14	1.75	0.14
-61.60	0.14	0.04	2.22	0.05	1.62	0.13	1.92	0.13
-58.80	0.14	0.03	2.38	0.05	1.98	0.13	2.18	0.13
-56.00	0.14	0.03	2.50	0.04	2.16	0.12	2.33	0.12
-53.20	0.14	0.03	2.58	0.04	2.31	0.11	2.45	0.11
-50.40	0.14	0.03	2.59	0.04	2.32	0.11	2.45	0.11
-47.60	0.15	0.03	2.62	0.04	2.29	0.10	2.45	0.10
-44.80	0.15	0.03	2.65	0.03	2.27	0.10	2.46	0.10
-42.00	0.16	0.03	2.69	0.03	2.27	0.09	2.48	0.09
-39.20	0.16	0.02	2.72	0.03	2.30	0.08	2.51	0.08
-36.40	0.16	0.02	2.73	0.03	2.35	0.08	2.54	0.08
-33.60	0.16	0.02	2.72	0.03	2.37	0.07	2.55	0.07
-30.80	0.16	0.02	2.70	0.02	2.41	0.07	2.55	0.07
-28.00	0.17	0.02	2.68	0.02	2.40	0.06	2.54	0.06
-25.20	0.17	0.02	2.67	0.02	2.39	0.06	2.53	0.06
-22.40	0.18	0.01	2.73	0.02	2.40	0.05	2.56	0.05
-19.60	0.18	0.01	2.78	0.02	2.51	0.04	2.64	0.04
-16.80	0.19	0.01	2.81	0.01	2.48	0.04	2.64	0.04
-14.00	0.20	0.01	2.88	0.01	2.52	0.03	2.70	0.03
-11.20	0.21	0.01	2.94	0.01	2.57	0.03	2.75	0.03
-8.40	0.22	0.01	3.09	0.01	2.70	0.03	2.90	0.03
-5.60	0.22	0.01	3.15	0.01	2.72	0.03	2.94	0.03
-2.80	0.23	0.01	3.24	0.01	2.74	0.02	2.99	0.02
0.00	0.24	0.01	3.29	0.01	2.85	0.02	3.07	0.02
2.80	0.24	0.01	3.26	0.01	2.72	0.02	2.99	0.02
5.60	0.25	0.01	3.22	0.01	2.69	0.03	2.96	0.03
8.40	0.25	0.01	3.19	0.01	2.64	0.03	2.91	0.03
11.20	0.25	0.01	3.10	0.01	2.51	0.03	2.80	0.03
14.00	0.25	0.01	3.03	0.01	2.42	0.04	2.73	0.04
16.80	0.25	0.01	2.98	0.02	2.38	0.04	2.68	0.04
19.60	0.24	0.01	2.90	0.02	2.37	0.05	2.64	0.05
22.40	0.23	0.02	2.83	0.02	2.26	0.05	2.54	0.05
25.20	0.23	0.02	2.72	0.02	2.22	0.06	2.47	0.06
28.00	0.22	0.02	2.71	0.02	2.21	0.06	2.46	0.06
30.80	0.21	0.02	2.73	0.03	2.18	0.07	2.45	0.07
33.60	0.21	0.02	2.75	0.03	2.13	0.08	2.44	0.08
36.40	0.20	0.02	2.78	0.03	2.06	0.08	2.42	0.08
39.20	0.19	0.02	2.80	0.03	2.01	0.09	2.40	0.09
42.00	0.18	0.03	2.82	0.03	1.95	0.09	2.38	0.09
44.80	0.18	0.03	2.84	0.04	1.91	0.10	2.38	0.10
47.60	0.16	0.03	2.85	0.04	1.89	0.11	2.37	0.11

IC3370: INTERMEDIATE AXIS (CONTINUED)

r	Mg2	err	Fe5270	err	Fe5335	err	<Fe>	err
50.40	0.16	0.03	2.83	0.04	1.90	0.11	2.36	0.11
53.20	0.15	0.03	2.79	0.04	1.95	0.12	2.37	0.12
56.00	0.14	0.03	2.73	0.04	1.99	0.12	2.36	0.12
58.80	0.14	0.04	2.63	0.05	2.03	0.13	2.33	0.13
61.60	0.13	0.04	2.63	0.05	2.02	0.13	2.33	0.13
64.40	0.13	0.04	2.69	0.05	1.96	0.14	2.33	0.14
67.20	0.12	0.04	2.78	0.05	1.91	0.15	2.34	0.15
70.00	0.11	0.04	2.93	0.05	1.85	0.15	2.39	0.15
72.80	0.10	0.04	2.96	0.06	1.82	0.16	2.39	0.16
75.60	0.09	0.05	2.86	0.06	1.81	0.16	2.34	0.16
78.40	0.09	0.05	2.70	0.06	1.81	0.17	2.26	0.17
81.20	0.09	0.05	2.44	0.06	1.84	0.17	2.14	0.17

TABLE A5-21
NGC3379: MAJOR AXIS

r	Mg2	err	Fe5270	err	Fe5335	err	<Fe>	err
-19.470	0.253	0.012	2.836	0.015	1.765	0.042	2.300	0.042
-18.290	0.255	0.011	2.848	0.014	1.827	0.038	2.338	0.038
-17.110	0.257	0.010	2.959	0.013	2.002	0.035	2.480	0.035
-15.930	0.259	0.009	2.971	0.012	2.057	0.032	2.514	0.032
-14.750	0.261	0.009	2.982	0.011	2.105	0.030	2.544	0.030
-13.570	0.262	0.008	2.992	0.010	2.147	0.027	2.570	0.027
-12.390	0.264	0.007	3.002	0.009	2.183	0.025	2.593	0.025
-11.210	0.265	0.007	3.011	0.009	2.214	0.024	2.613	0.024
-10.030	0.267	0.006	3.020	0.008	2.240	0.022	2.630	0.022
-8.850	0.268	0.006	3.028	0.008	2.262	0.021	2.645	0.021
-7.670	0.270	0.006	3.036	0.007	2.280	0.020	2.658	0.020
-6.490	0.271	0.006	3.157	0.007	2.469	0.019	2.813	0.019
-5.310	0.272	0.005	3.164	0.007	2.483	0.018	2.823	0.018
-4.130	0.273	0.005	3.170	0.006	2.496	0.018	2.833	0.018
-2.950	0.275	0.005	3.176	0.006	2.507	0.017	2.841	0.017
-1.770	0.276	0.005	3.181	0.006	2.516	0.017	2.849	0.017
-0.590	0.277	0.005	3.186	0.006	2.525	0.017	2.855	0.017
0.590	0.278	0.005	3.190	0.006	2.533	0.017	2.861	0.017
1.770	0.279	0.005	3.193	0.006	2.540	0.017	2.866	0.017
2.950	0.280	0.005	3.196	0.006	2.546	0.017	2.871	0.017
4.130	0.281	0.005	3.198	0.007	2.552	0.018	2.875	0.018
5.310	0.281	0.005	3.200	0.007	2.558	0.019	2.879	0.019
6.490	0.282	0.006	3.085	0.007	2.384	0.019	2.735	0.019
7.670	0.283	0.006	3.085	0.007	2.390	0.020	2.738	0.020
8.850	0.283	0.006	3.085	0.008	2.396	0.021	2.740	0.021
10.030	0.284	0.007	3.083	0.008	2.402	0.023	2.743	0.023
11.210	0.285	0.007	3.081	0.009	2.409	0.024	2.745	0.024
12.390	0.285	0.008	3.079	0.010	2.418	0.026	2.748	0.026
13.570	0.286	0.008	3.076	0.010	2.429	0.029	2.753	0.029
14.750	0.287	0.009	3.073	0.011	2.444	0.031	2.758	0.031
15.930	0.288	0.010	3.070	0.012	2.463	0.034	2.767	0.034
17.110	0.290	0.011	3.070	0.014	2.489	0.037	2.779	0.037
18.290	0.293	0.012	2.969	0.015	2.377	0.041	2.673	0.041
19.470	0.298	0.013	2.977	0.017	2.424	0.046	2.700	0.046

TABLE A5-22
NGC4105: MAJOR AXIS

r	Mg2	err	Fe5270	err	Fe5335	err	<Fe>	err
-21.50	0.19	0.03	2.41	0.04	1.90	0.11	2.16	0.11
-19.49	0.19	0.03	2.43	0.04	1.92	0.10	2.17	0.10
-17.47	0.19	0.03	2.53	0.03	1.94	0.09	2.24	0.09
-15.46	0.20	0.03	2.62	0.03	1.93	0.09	2.28	0.09
-13.44	0.20	0.02	2.70	0.03	1.93	0.08	2.32	0.08
-11.42	0.20	0.02	2.73	0.03	1.95	0.07	2.34	0.07
-9.41	0.21	0.02	2.79	0.02	1.98	0.06	2.39	0.06
-7.39	0.22	0.01	2.83	0.02	2.00	0.05	2.42	0.05
-5.38	0.23	0.01	2.92	0.01	2.06	0.04	2.49	0.04
-3.36	0.24	0.01	3.00	0.01	2.15	0.03	2.58	0.03
-1.34	0.25	0.01	3.11	0.01	2.22	0.02	2.66	0.02
0.67	0.26	0.01	3.15	0.01	2.23	0.02	2.69	0.02
2.69	0.26	0.01	3.15	0.01	2.16	0.02	2.66	0.02
4.70	0.26	0.01	3.10	0.01	2.14	0.03	2.62	0.03
6.72	0.25	0.01	3.04	0.02	2.08	0.05	2.56	0.05
8.74	0.25	0.02	3.01	0.02	2.05	0.06	2.53	0.06
10.75	0.24	0.02	2.98	0.02	1.98	0.07	2.48	0.07
12.77	0.23	0.02	2.98	0.03	1.96	0.08	2.47	0.08
14.78	0.22	0.02	2.97	0.03	1.95	0.08	2.46	0.08
16.80	0.21	0.03	2.92	0.03	1.94	0.09	2.43	0.09
18.82	0.21	0.03	2.86	0.04	1.90	0.10	2.38	0.10
20.83	0.20	0.03	2.83	0.04	1.87	0.11	2.35	0.11

TABLE A5-23
NGC4105: MINOR AXIS

r	Mg2	err	Fe5270	err	Fe5335	err	<Fe>	err
-21.50	0.14	0.04	2.11	0.06	1.45	0.15	0.00	1.78
-19.49	0.14	0.04	2.05	0.05	1.86	0.14	0.00	1.95
-17.47	0.15	0.04	1.94	0.05	2.08	0.13	0.00	2.01
-15.46	0.16	0.03	1.91	0.04	1.92	0.12	0.00	1.91
-13.44	0.16	0.03	1.86	0.04	1.52	0.10	0.00	1.69
-11.42	0.17	0.02	1.91	0.03	1.50	0.08	0.00	1.71
-9.41	0.19	0.02	2.21	0.03	1.90	0.07	2.05	0.07
-7.39	0.21	0.02	2.43	0.02	2.12	0.06	2.27	0.06
-5.38	0.24	0.01	2.82	0.02	2.28	0.04	2.55	0.04
-3.36	0.25	0.01	2.97	0.01	2.32	0.03	2.65	0.03
-1.34	0.27	0.01	3.13	0.01	2.29	0.02	2.71	0.02
0.67	0.27	0.01	3.17	0.01	2.30	0.02	2.73	0.02
2.69	0.27	0.01	3.19	0.01	2.27	0.03	2.73	0.03
4.70	0.26	0.01	3.15	0.02	2.28	0.04	2.72	0.04
6.72	0.25	0.02	3.08	0.02	2.29	0.06	2.69	0.06
8.74	0.24	0.02	3.01	0.03	2.28	0.07	2.65	0.07
10.75	0.23	0.02	2.80	0.03	2.21	0.08	2.50	0.08
12.77	0.22	0.03	2.68	0.04	2.16	0.10	2.42	0.10
14.78	0.22	0.03	2.44	0.04	1.97	0.11	2.21	0.11
16.80	0.21	0.04	2.29	0.05	1.82	0.13	2.06	0.13
18.82	0.20	0.04	2.02	0.05	1.56	0.17	1.79	0.17
20.83	0.19	0.05	1.91	0.06	1.57	0.36	1.74	0.36

TABLE A5-24

NGC4339: MAJOR AXIS

r	Mg2	err	Fe5270	err	Fe5335	err	<Fe>	err
-19.47	0.21	0.04	2.77	0.06	2.29	0.16	2.53	0.16
-18.29	0.21	0.04	2.79	0.05	2.29	0.15	2.54	0.15
-17.11	0.22	0.04	2.80	0.05	2.28	0.13	2.54	0.13
-15.93	0.22	0.04	2.81	0.05	2.27	0.12	2.54	0.12
-14.75	0.22	0.03	2.82	0.04	2.26	0.12	2.54	0.12
-13.57	0.19	0.03	2.28	0.04	2.24	0.11	2.26	0.11
-12.39	0.19	0.03	2.34	0.04	2.25	0.10	2.30	0.10
-11.21	0.20	0.03	2.40	0.03	2.26	0.09	2.33	0.09
-10.03	0.20	0.03	2.48	0.03	2.30	0.09	2.39	0.09
-8.85	0.20	0.02	2.52	0.03	2.30	0.08	2.41	0.08
-7.67	0.20	0.02	2.57	0.03	2.31	0.08	2.44	0.08
-6.49	0.20	0.02	2.63	0.03	2.34	0.08	2.48	0.08
-5.31	0.21	0.02	2.69	0.03	2.36	0.07	2.53	0.07
-4.13	0.21	0.02	2.73	0.03	2.36	0.07	2.55	0.07
-2.95	0.21	0.02	2.78	0.03	2.46	0.07	2.62	0.07
-1.77	0.21	0.02	2.81	0.03	2.46	0.07	2.63	0.07
-0.59	0.21	0.02	2.84	0.03	2.45	0.07	2.65	0.07
0.59	0.21	0.02	2.86	0.03	2.45	0.07	2.66	0.07
1.77	0.21	0.02	2.88	0.03	2.45	0.07	2.66	0.07
2.95	0.21	0.02	2.89	0.03	2.44	0.07	2.67	0.07
4.13	0.22	0.02	2.88	0.03	2.35	0.07	2.61	0.07
5.31	0.22	0.02	2.86	0.03	2.31	0.07	2.59	0.07
6.49	0.22	0.02	2.87	0.03	2.30	0.08	2.59	0.08
7.67	0.22	0.02	2.85	0.03	2.27	0.08	2.56	0.08
8.85	0.22	0.02	2.85	0.03	2.26	0.09	2.55	0.09
10.03	0.22	0.03	2.82	0.03	2.22	0.09	2.52	0.09
11.21	0.22	0.03	2.82	0.04	2.20	0.10	2.51	0.10
12.39	0.22	0.03	2.81	0.04	2.18	0.10	2.49	0.10
13.57	0.21	0.03	2.80	0.04	2.15	0.11	2.47	0.11
14.75	0.21	0.03	2.78	0.04	2.12	0.12	2.45	0.12
15.93	0.21	0.04	2.75	0.05	2.09	0.13	2.42	0.13
17.11	0.21	0.04	2.72	0.05	2.06	0.14	2.39	0.14
18.29	0.21	0.04	2.67	0.06	2.02	0.15	2.34	0.15
19.47	0.21	0.05	2.62	0.06	1.98	0.17	2.30	0.17

LIST OF FIGURES

INTRODUCTION

1. The Hubble tuning-fork diagram 2

CHAPTER 1

1. Reduced central spectrum of the galaxy IC3370 and template star 12

2. Various combinations of h_3 and h_4 14

3. Photometric profiles for IC3370 (in the B-band) 17

4. Kinematic profiles for the major axis of IC3370 19

5. Kinematic profiles for the intermediate and minor axes of IC3370 20

6. Photometric profiles for IC1459 (in the V-band).
 Kinematic profiles for the major axis of IC1459 (comparison) 21

7. Stellar kinematics of IC1459 (major and minor axis) 23

8. Photometric profiles of NGC1336 in the B-band.
 Stellar kinematics of NGC1336 30

9. Photometric profiles of NGC1339 in the B-band.
 Stellar kinematics of NGC1339 31

10. Photometric profiles of NGC1373 in the B-band.
 Stellar kinematics of NGC1373 32

11. Photometric profiles of NGC1374 in the B-band.
 Stellar kinematics of NGC1374 33

12. Photometric profiles of NGC1379 in the B-band.
 Stellar kinematics of NGC1379 34

13. Photometric profiles of NGC1399 in the B-band.
 Stellar kinematics of NGC1399 35

14. Photometric profiles of NGC1404 in the B-band.
 Stellar kinematics of NGC1404 36

15. Photometric profiles of NGC1419 in the B-band.
 Stellar kinematics of NGC1419 37

16. Photometric profiles of NGC4339 in the B-band.
 Stellar kinematics of NGC4339 38

17. Photometric profiles of NGC3379 in the B-band. Stellar kinematics of NGC3379.....	39
18. Stellar kinematics of NGC3379 (major and minor axis). Taken from Statler & Smecker-Hane (1999)	40
19. Photometric profiles of NGC4105 in the R-band.	41
20. Stellar kinematics of NGC4105 (major and minor axis).	42
21. Stellar kinematics of NGC2434 (major axis). Taken from Carollo et al. (1995)	43
22. Stellar kinematics of NGC3706 (major axis). Taken from Carollo et al. (1995)	44
23. Stellar kinematics of NGC5018 (major axis). Taken from Carollo et al. (1995)	45

CHAPTER 2

1. Flowchart of two-integral modeling procedure.....	49
2. Predictions of the two-integral models for IC3370 (major and minor axis).....	52
3. Predictions of the two-integral models for IC3370 (intermediate axis).....	53
4. Predictions of the two-integral models for IC1459 (major and minor axis).....	56
5. Predictions of the two-integral models for IC1459 (corrected velocity and velocity dispersion, major axis)	57
6. Parameters of the LOSVD along the major axis for a remnant, a typical 3:1 merger. Taken from Bendo & Barnes (2000)	58
7. Predictions of the two-integral models for NGC3379 (major and minor axis).....	59
8. Predictions of the two-integral models for NGC4105 (major and minor axis).....	61
9. Flowchart of three-integral modeling procedure.	62
10. Reference systems of the ellipsoid and the observer. Taken from Simonneau et al. (1998)	68
11. Predictions of the three-integral modeling for IC3370 for the major axis.	73
12. Predictions of the three-integral modeling for IC1459 for the major axis.	75
13. Predictions of the three-integral modeling for NGC1336 for the major axis.	76
14. Predictions of the three-integral modeling for NGC1339 for the major axis.	77
15. Predictions of the three-integral modeling for NGC1373 for the major axis.	78
16. Predictions of the three-integral modeling for NGC1374 for the major axis.	80
17. Predictions of the three-integral modeling for NGC1379 for the major axis.	81
18. Predictions of the three-integral modeling for NGC1399 for the major axis.	82
19. Predictions of the three-integral modeling for NGC1404 for the major axis.	84

20. Predictions of the three-integral modeling for NGC1419 for the major axis. 85

21. Predictions of the three-integral modeling for NGC4339 for the major axis. 86

22. Predictions of the three-integral modeling for NGC3379 for the major axis. 88

23. Predictions of the three-integral modeling for NGC4105 for the major axis. 89

24. Modeling results for the sample of Carollo et al. (1995).
 Taken from Carollo et al. (1995). 90

25. Predictions of the three-integral modeling for NGC2434 for the major axis. 91

26. Predictions of the three-integral modeling for NGC3706 for the major axis. 92

27. Predictions of the three-integral modeling for NGC5018 for the major axis. 93

CHAPTER 3

1. The observed and azimuthally averaged electron density profile $n(r)$ in NGC 4472.
 Typical temperature profiles for several bright E galaxies.
 Taken from Mathews & Brighenti (2003) 97

2. Mass-to-light ratios of four galaxies with X-ray haloes from my sample:
 IC1459, NGC1399, NGC4105 and NGC1404 101

3. Mass-to-light ratios of a galaxy with X-ray halo from my sample: NGC3379. 102

CHAPTER 4

1. The corrections for the iron indices for IC3370. 109

2. Mg_2 and iron indices (Fe5270, Fe5335, and $\langle Fe \rangle$) for the major axis of IC3370. 112

3. Mg_2 and iron indices (Fe5270, Fe5335, and $\langle Fe \rangle$) for the minor axis of IC3370. 112

4 Mg_2 and iron indices (Fe5270, Fe5335, and $\langle Fe \rangle$) for the intermediate axis of IC3370. ... 113

5. Mg_2 and iron indices (Fe5270, Fe5335, and $\langle Fe \rangle$) for the major axis of IC1459. 114

6. Mg_2 and iron indices (Fe5270, Fe5335, and $\langle Fe \rangle$) for the major axis of NGC3379. 115

7. Mg_2 and iron indices (Fe5270, Fe5335, and $\langle Fe \rangle$) for the major axis of NGC4339. 116

8. Mg_2 and iron indices (Fe5270, Fe5335, and $\langle Fe \rangle$) for the major axis of NGC4105. 117

9. Mg_2 and iron indices (Fe5270, Fe5335, and $\langle Fe \rangle$) for the minor axis of NGC4105. 117

10. Mass-Metallicity relation for the galaxies in my samples. 118

11. Modeling of Mg_2 index and $\langle Fe \rangle$ for IC3370. 119

12. Modeling of Mg_2 index and $\langle Fe \rangle$ for IC1459. 120

13. Modeling of Mg_2 index and $\langle Fe \rangle$ for NGC3379 121

14. Modeling of Mg_2 index and $\langle Fe \rangle$ for NGC4339 122

15. Modeling of Mg_2 index and $\langle Fe \rangle$ for NGC4105	123
-------------------------------------------------------------------------	-----

APPENDIX 1

1. L-curve in case of orbits in triaxial logarithmic potential for which $p = q = 0.9$	138
-----------------------------------------------------------------------------------------------	-----

APPENDIX 3

1. Example of an orbit in the Hernquist potential.	145
2. Example of an orbit in the logarithmic axisymmetric potential.	150
3. Example of an orbit in the logarithmic axisymmetric potential using cylindrical coordinates.	151
4. Example of an orbit in the logarithmic triaxial potential ($p = q = 0.9$).	154
5. Example of an orbit in the logarithmic triaxial potential using cylindrical coordinates.	155
6. Scheme of leapfrog integration.	157

APPENDIX 4

1. Tube orbit calculated in the axisymmetric logarithmic potential.	161
2. Tube orbit calculated in the axisymmetric logarithmic potential (line-of-sight velocity vs. R coordinate).	162
3. SOM reconstruction of the orbit from Fig. 2.	163

LIST OF TABLES

CHAPTER 1

1. Graham et al. (1998) sample. 24

CHAPTER 3

1. X-ray and mass properties of galaxies with X-ray haloes.....98

CHAPTER 4

1. Definitions of indices used in this thesis. 106

2. Comparison of calculations of integrals of analytic functions..... 107

3. Comparison with the Worthey’s calculations. 107

CHAPTER 5

1. Results of dark matter research in early-type galaxies using different methodologies. 129

APPENDIX 3

1. Potential density pairs for spherical potentials. 144

2. Potential density pairs for flattened potentials 147

APPENDIX 5

1. Stellar kinematics of IC1459 (major axis) 165

2. Stellar kinematics of IC3370 (major axis) 168

3. Stellar kinematics of IC3370 (minor axis) 169

4. Stellar kinematics of IC3370 (intermediate axis) 170

5. Stellar kinematics of NGC1336 (major axis) 171

6. Stellar kinematics of NGC1339 (major axis) 171

7. Stellar kinematics of NGC1373 (major axis) 172

8. Stellar kinematics of NGC1374 (major axis) 173

9. Stellar kinematics of NGC1379 (major axis) 174

10. Stellar kinematics of NGC1399 (major axis) 175

11. Stellar kinematics of NGC1404 (major axis) 176

12. Stellar kinematics of NGC1419 (major axis).....	177
13. Stellar kinematics of NGC4339 (major axis).....	178
14. Stellar kinematics of NGC3379 (major axis).....	179
15. Stellar kinematics of NGC4105 (major axis).....	180
16. Stellar kinematics of NGC4105 (minor axis).....	181
17. Line strength indices of IC1459 (major axis).....	182
18. Line strength indices of IC3370 (major axis).....	184
19. Line strength indices of IC3370 (minor axis)	186
20. Line strength indices of IC3370 (intermediate axis).....	188
21. Line strength indices of NGC3379 (major axis)	190
22. Line strength indices of NGC4105 (major axis)	191
23. Line strength indices of NGC4105 (minor axis)	192
24. Line strength indices of NGC4339 (major axis)	193